



TECHNICAL REPORT
NATICK/TR-92/004

AD A243 018

EFFECT OF COATINGS AND PROCESSING ON FAILURE MECHANISMS OF POLYCARBONATE MATERIAL - PHASE I

By
R.D. Eisler
A.K. Chatterjee
G. Burghart
A.H. Koivu
C.D. Newlander
S.F. Stone

Mission Research Corporation
Costa Mesa, CA 92626

and
E. Healy*

November 1991

FINAL REPORT
December 1988 - June 1989

APPROVED FOR PUBLIC RELEASE;
DISTRIBUTION UNLIMITED

Prepared for
UNITED STATES ARMY NATICK
RESEARCH, DEVELOPMENT AND ENGINEERING CENTER
NATICK, MASSACHUSETTS 01760-5000

*SOLDIER SCIENCE DIRECTORATE

DISCLAIMERS

The findings contained in this report are not to be construed as an official Department of the Army position unless so designated by other authorized documents.

Citation of trade names in this report does not constitute an official endorsement or approval of the use of such items.

DESTRUCTION NOTICE

For Classified Documents:

Follow the procedures in DoD 5200.22-M, Industrial Security Manual, Section II-19 or DoD 5200.1-R, Information Security Program Regulation, Chapter IX.

For Unclassified/Limited Distribution Documents:

Destroy by any method that prevents disclosure of contents or reconstruction of the document.

REPORT DOCUMENTATION PAGE			Form Approved OMB No. 0704-0188	
Public reporting burden for this collection of information is estimated to average 1 hour per response, including the time for reviewing instructions, searching existing data sources, gathering and maintaining the data needed, and completing and reviewing the collection of information. Send comments regarding this burden estimate or any other aspect of this collection of information, including suggestions for reducing this burden, to Washington Headquarters Services, Directorate for Information Operations and Reports, 1215 Jefferson Davis Highway, Suite 1204, Arlington, VA 22202-4302, and to the Office of Management and Budget, Paperwork Reduction Project (0704-0188), Washington, DC 20503.				
1. AGENCY USE ONLY (Leave blank)		2. REPORT DATE November 1991	3. REPORT TYPE AND DATES COVERED Final December 1988 - June 1989	
4. TITLE AND SUBTITLE EFFECT OF COATINGS AND PROCESSING ON FAILURE MECHANISMS OF POLYCARBONATE MATERIAL - PHASE I			5. FUNDING NUMBERS DAAK60-89-C-0011	
6. AUTHOR(S) R.D. EISLER, A.K. CHATTERJEE, G. BURGHART, A.H. KOIVU, C.D. NEWLANDER, S.F. STONE, E. HEALY *				
7. PERFORMING ORGANIZATION NAME(S) AND ADDRESS(ES) Mission Research Corporation 3505 Cadillac Avenue - Building H Costa Mesa, California 92626			8. PERFORMING ORGANIZATION REPORT NUMBER	
9. SPONSORING/MONITORING AGENCY NAME(S) AND ADDRESS(ES) U.S. Army Natick Research, Development and Engineering Center Kansas Street, Attn: STRNC-YSM Natick, MA 01760-5000			10. SPONSORING/MONITORING AGENCY REPORT NUMBER NATICK/TR-92/004	
11. SUPPLEMENTARY NOTES *Professional affiliation: US Army Natick RD&E Center, Natick, MA 01760 This project was a DoD Small Business Innovation Research (SBIR) Program				
12a. DISTRIBUTION/AVAILABILITY STATEMENT Approved for public release; distribution unlimited.			12b. DISTRIBUTION CODE	
13. ABSTRACT (Maximum 200 words) The subject effort identified the first order damage mechanisms and governing parameters contributing to the occurrence of a ductile to brittle transition in the mechanical behavior of ballistically impacted polycarbonate materials with protective coatings. Polycarbonate embrittlement is associated with a severe reduction in impact resistance as well as extensive in-plane cracking and rear surface debris. In-plane cracking can severely block the visual surface and target debris can cause debilitating eye injury. The current effort included: (1) Definition of contact pressures associated with the impact of polycarbonate material with and without protective coatings; (2) Definition of polycarbonate substrate and coating configurations of interest; (3) Stress wave response analysis; (4) Structural and fracture mechanics analysis; and, (5) Fabrication, quasistatic penetration, and ballistic testing of polycarbonate materials with and without protective coatings. Hardening recommendations designed to mitigate the influence of damage mechanisms identified as contributing to the brittle failure of polycarbonate were also rendered.				
14. SUBJECT TERMS COATINGS FAILURE(MECHANICS) FRACTURE(MECHANICS) CRACKS POLYCARBONATES TENSILE STRESS IMPACT SHOCK BALLISTICS TENSILE STRENGTH BALLISTIC IMPACT			15. NUMBER OF PAGES 206	
			16. PRICE CODE	
17. SECURITY CLASSIFICATION OF REPORT Unclassified	18. SECURITY CLASSIFICATION OF THIS PAGE Unclassified	19. SECURITY CLASSIFICATION OF ABSTRACT Unclassified	20. LIMITATION OF ABSTRACT	

GENERAL INSTRUCTIONS FOR COMPLETING SF 298

The Report Documentation Page (RDP) is used in announcing and cataloging reports. It is important that this information be consistent with the rest of the report, particularly the cover and title page. Instructions for filling in each block of the form follow. It is important to *stay within the lines* to meet optical scanning requirements.

Block 1. Agency Use Only (Leave blank).

Block 2. Report Date. Full publication date including day, month, and year, if available (e.g. 1 Jan 88). Must cite at least the year.

Block 3. Type of Report and Dates Covered. State whether report is interim, final, etc. If applicable, enter inclusive report dates (e.g. 10 Jun 87 - 30 Jun 88).

Block 4. Title and Subtitle. A title is taken from the part of the report that provides the most meaningful and complete information. When a report is prepared in more than one volume, repeat the primary title, add volume number, and include subtitle for the specific volume. On classified documents enter the title classification in parentheses.

Block 5. Funding Numbers. To include contract and grant numbers; may include program element number(s), project number(s), task number(s), and work unit number(s). Use the following labels:

C - Contract	PR - Project
G - Grant	TA - Task
PE - Program Element	WU - Work Unit Accession No.

Block 6. Author(s). Name(s) of person(s) responsible for writing the report, performing the research, or credited with the content of the report. If editor or compiler, this should follow the name(s).

Block 7. Performing Organization Name(s) and Address(es). Self-explanatory.

Block 8. Performing Organization Report Number. Enter the unique alphanumeric report number(s) assigned by the organization performing the report.

Block 9. Sponsoring/Monitoring Agency Name(s) and Address(es). Self-explanatory.

Block 10. Sponsoring/Monitoring Agency Report Number. (If known)

Block 11. Supplementary Notes. Enter information not included elsewhere such as: Prepared in cooperation with...; Trans. of...; To be published in.... When a report is revised, include a statement whether the new report supersedes or supplements the older report.

Block 12a. Distribution/Availability Statement. Denotes public availability or limitations. Cite any availability to the public. Enter additional limitations or special markings in all capitals (e.g. NOFORN, REL, ITAR).

DOD - See DoDD 5230.24, "Distribution Statements on Technical Documents."

DOE - See authorities.

NASA - See Handbook NHB 2200.2.

NTIS - Leave blank.

Block 12b. Distribution Code.

DOD - Leave blank.

DOE - Enter DOE distribution categories from the Standard Distribution for Unclassified Scientific and Technical Reports.

NASA - Leave blank.

NTIS - Leave blank.

Block 13. Abstract. Include a brief (*Maximum 200 words*) factual summary of the most significant information contained in the report.

Block 14. Subject Terms. Keywords or phrases identifying major subjects in the report.

Block 15. Number of Pages. Enter the total number of pages.

Block 16. Price Code. Enter appropriate price code (*NTIS only*).

Blocks 17. - 19. Security Classifications. Self-explanatory. Enter U.S. Security Classification in accordance with U.S. Security Regulations (i.e., UNCLASSIFIED). If form contains classified information, stamp classification on the top and bottom of the page.

Block 20. Limitation of Abstract. This block must be completed to assign a limitation to the abstract. Enter either UL (unlimited) or SAR (same as report). An entry in this block is necessary if the abstract is to be limited. If blank, the abstract is assumed to be unlimited.

Table of Contents

<u>Section</u>	<u>Page</u>
List of Figures	iv
List of Tables	xi
Preface	xii
Acknowledgments	xiii
1.0 SUMMARY	1
1.1 Program Motivation	7
1.2 Phase I Work Plan	9
2.0 TECHNICAL APPROACH	9
2.1 Task 1 - Definition of Ballistic Threats & Contact Forcing Functions	24
2.2 Task 2 - Definition of Polycarbonate and Coating Configurations	31
2.3 Task 3 - Stress Wave Response Analysis	31
2.4 Task 4 - Fracture Mechanics and Structural Analysis	50
2.5 Task 5 - Fabrication of Polycarbonate Materials and Testing	59
2.6 Task 6 - Hardening Recommendations	69
3.0 PHASE I CONCLUSIONS	76
4.0 REFERENCES	78
APPENDICES	87
A STRESS WAVE ANALYSIS	89
A.1 One Dimensional Stress Wave Analysis	91
A.2 Two Dimensional Stress Wave Analysis	105
B STRUCTURAL ANALYSIS	151
B.1 Static Analysis	153
B.2 Frequency Analysis	163
C BALLISTIC TEST DATA	167
C.1 Natick RD&E Center Coated Ballistic Goggle Lenses	169
C.2 MRC Uncoated Polycarbonate Flat Sheet Specimens	175
C.3 MRC PMMA-Clad Polycarbonate Specimens	179

List of Figures

<u>Figure</u>		<u>Page</u>
1	Brittle Failure Mode of Ballistic Goggle Subject to Edge Impact	5
2	Typical Failure Modes of Polycarbonate Samples Laminated with PMMA	6
3	Phase I Task Schedule	9
4	Ductile Failure in Monolithic Polycarbonate	11
5	Equivalent Mass-Spring Model	13
6	Velocity Reduction as a Function of Effective Target Mass for Different Tensile Strains	14
7	Velocity Reduction as a Function of Tensile Strain for Prescribed Target Mass	15
8	Brittle Failure Modes Associated with Crack Initiation	17
9	Unstable Crack Geometries	17
10	Ballistic Test Data for 15.7 FSP on Injection Molded PC	19
11	Ballistic Behavior of PMMA/PC Laminates without Interlayer	21
12	Variation of Stress Intensity for a Ductile-Brittle Succession of Material Phases (Phase I 30%, Phase II 10% plasticized)	23
13	Variation of Stress Intensity for a Brittle-Ductile Succession of Material Phases (Phase I 10%, Phase II 30% plasticized)	23
14	(P,v) Hugoniot for Collision of Two Materials of Finite Thickness	25
15	Force-Time History on Substrate for Nominal Projectile Length: (a) Acoustically Thin Coating; (b) Acoustically Thick Coating; and, (c) Uncoated Substrate.	27
16	Plastic Strain Accumulation during Stress Reversals	27
17	Effect of Load Spectrum on Crack Growth	29
18	MRC Equation-of-State Model	35
19	Finite Difference Model: (a) Global Model; and, (b) Enlarged Detail of Global Model.	36
20	Pressure and Stress at Target Point 5 subject to Low Velocity Impact	39
21	Reflected and Transmitted Waves Resulting from Impact with Two Layer Sample	40
22	Amplitude Ratios for the Reflection of a P-wave	41
23	Relative Amplitude of P-wave for Various Values of Poisson Ratio	41
24	Relative Magnitude of P-wave Terms	43
25	Relative Magnitude of P-wave Terms (Continued)	43
26	Relative Amplitude of P-wave Terms (Concluded)	44
27	Relative Amplitude Ratio of P-wave	44
28	Incident versus Refracted Angle	46
29	Critical Angle versus Velocity	46

List of Figures (Continued)

<u>Figure</u>		<u>Page</u>
30	Normalized Radial Stress versus Incident Angle for Poisson Ratio = 0.19	47
31	Normalized Radial Stress versus Incident Angle for Poisson Ratio = 0.38	48
32	Normalized Stress vrs Time for a Generic Field Point; Poisson Ratio = 0.19	48
33	Normalized Stress vrs Time for a Generic Field Point; Poisson Ratio = 0.38	49
34	Comparison of Interface Stress for: (a) PMMA on the Impact Surface which is Fusion Bonded and Adhesively Bonded to PC; (2) PC on the Impact Surface which is Fusion Bonded and Adhesively Bonded to PMMA.	52
35	Attenuation of Stress Associated with 2D Effects.	53
36	Influence of Material Interphase on Crack Propagation	53
37	Quasistatic Growth of Mode III Cracks Approaching an Interface.	55
38	Stress Intensity Factor of a Surface Crack in a Homogeneous Plate Subject to a Lateral Load.	56
39	Ballistic Goggle Finite Element Model.	58
40	Static Test of Ballistic Goggles with Conical Indenter.	60
41	Static Test of PC Sheet and Ballistic Goggles with Fragment Simulating Indenter.	61
42	Geometry of Brittle Failure Associated with Debris Impact Near a Lateral Free Surface	65
43	Diffacted Stress Field for an Incident Wave Interacting with a Spherical Cavity	65
44	Stages in Radial Crack Formation in PMMA Impact Layer	66
45	Brittle Failure Induced by Circumferential Cracking	68
46	Brittle Failure Induced by Radial Cracking	68
47	Fracture due to Stress Waves	71
48	Formation of Off-Axis Microcracks and Directional Stability	72
49	Deformation Mechanisms in Amorphous Polymers	74
50	Shear Yielding and Crazing Envelopes in Amorphous Polymers	75

List of Figures (Continued)

<u>Figure</u>	APPENDIX A.1 - One Dimensional Stress Wave Analysis	<u>Page</u>
A.1	Predicted One Dimensional Stress Wave Response for 0.25 inch PC Impacted by 0.05 inch Steel Flyer Plate Incident at 600 cm/sec	93
A.2	Predicted One Dimensional Stress Wave Response for 0.25 inch PC Impacted by 0.05 inch Steel Flyer Plate Incident at 6,000 cm/sec	94
A.3	Predicted One Dimensional Stress Wave Response for 0.25 inch PC Impacted by 0.05 inch Steel Flyer Plate Incident at 60,000 cm/sec	95
A.4	Predicted One Dimensional Stress Wave Response for 0.25 inch PC Impacted by 0.25 inch Steel Flyer Plate Incident at 600 cm/sec	96
A.5	Predicted One Dimensional Stress Wave Response for 0.25 inch PC Impacted by 0.25 inch Steel Flyer Plate Incident at 6,000 cm/sec	97
A.6	Predicted One Dimensional Stress Wave Response for 0.25 inch PC Impacted by 0.25 inch Steel Flyer Plate Incident at 60,000 cm/sec	98
A.7	Predicted One Dimensional Stress Wave Response for 0.25 inch PC Impacted by 1.25 inch Steel Flyer Plate Incident at 600 cm/sec	99
A.8	Predicted One Dimensional Stress Wave Response for 0.25 inch PC Impacted by 1.25 inch Steel Flyer Plate Incident at 6,000 cm/sec	100
A.9	Predicted One Dimensional Stress Wave Response for 0.25 inch PC Impacted by 1.25 inch Steel Flyer Plate Incident at 60,000 cm/sec	101
A.10	Predicted One Dimensional Stress Wave Response for 0.25 inch PC with 0.05 inch PMMA Coating Impacted by 1.25 inch Steel Flyer Plate Incident at 6,000 cm/sec	102
A.11	Predicted One Dimensional Stress Wave Response for 0.25 inch PC with 0.20 inch PMMA Coating Impacted by 1.25 inch Steel Flyer Plate Incident at 6,000 cm/sec	103
A.12	Predicted One Dimensional Stress Wave Response for 0.25 inch PC with 0.20 inch PMMA Coating and 0.01 inch RS1305 Silicone Adhesive Impacted by 1.25 inch Steel Flyer Plate Incident at 6,000 cm/sec	104

List of Figures (Continued)

<u>Figure</u>	APPENDIX A.2.1 - 2D Stress Wave Analysis for High Velocity Impact	<u>Page</u>
A.13	Location of Target Points for Post Processing of High Velocity Impact Analysis	107
A.14	Projectile Particle Velocities in Impact Direction: (a) Near Impact Surface; and, (b) Near Back Surface of Projectile.	108 109
A.15	Comparison of Particle Velocities in Impact and Radial Directions for Coated and Uncoated PC near Impact Surface	110
A.16	Comparison of Particle Velocities in Impact and Radial Directions for Coated and Uncoated PC near Near the Midplane of the Substrate	111
A.17	Comparison of Particle Velocities in Impact and Radial Directions for Coated and Uncoated PC Near the Midplane and Back Surface of the Substrate	112
A.18	Comparison of Particle Velocities in Impact and Radial Directions for Coated and Uncoated PC Near the Back Surface of the Substrate and along the Midplane of the Substrate Outside the Impact Region	113
A.19	Comparison of Pressure and Stress in the Projectile along the Impact and Radial Directions.	114
A.20	Calculated Pressure for Coated and Uncoated PC through the Target Thickness.	115
A.21	Calculated Stress for Coated and Uncoated PC through the Target Thickness along the Radial and Impact Directions.	116
A.22	Calculated Stress for Coated and Uncoated PC through the Target Thickness along the Radial and Impact Directions.	117

List of Figures (Continued)

<u>Figure</u>	APPENDIX A.2.2.1 - 2D Stress Wave Analysis for Low Velocity Impact without Defects	<u>Page</u>
A.23	Location of Target Points for Post Processing of Low Velocity Impact Analysis	121
A.24	Projectile Particle Velocities in Impact Direction: (a) Near Impact Surface; and, (b) Near Back Surface of Projectile.	122
A.25	Projectile Pressures: (a) Near Impact Surface; and, (b) Near Back Surface of Projectile.	123
A.26	Stress Components in Projectile Near Impact Surface: (a) Impact Direction; and, (b) Radial Direction.	124
A.27	Stress Components Near Back Surface of Projectile: (a) Impact Direction; and, (b) Radial Direction.	125
A.28	Pressure in PC Substrate near Impact Surface	126
A.29	Radial Stress Near Impact Surface of PC Substrate	127
A.30	Stress in Impact Direction Near Impact Surface of PC	128
A.31	Pressure near Midplane of PC Substrate	129
A.32	Stress Component at Midplane of PC Substrate in Impact Direction	130
A.33	Stress Component at Midplane of PC Substrate in Radial Direction	131
A.34	Pressure near Rear Surface of PC Substrate	132
A.35	Stress Component near Rear Surface of PC Substrate in Impact Direction	133
A.36	Stress Component near Back Surface of PC Substrate in Radial Direction	134
A.37	Pressure near Midplane of PC Substrate Outside of Impact Region	135
A.38	Stress Component near Midplane of PC Substrate Outside of Impact Region in Impact Direction	136
A.39	Stress Component near Back Surface of PC Substrate Outside of Impact Region in Radial Direction	137

List of Figures (Continued)

<u>Figure</u>	APPENDIX A.2.2.2 - 2D Stress Wave Analysis for Low Velocity Impact with Pre-Existing Geometric Discontinuity	<u>Page</u>
A.40	Pressure near Midplane of PC Substrate: (a) No PMMA Cladding; and, (b) Thin PMMA Cladding.	141
A.41	Stress Components at Midplane of PC Substrate: (a) No PMMA Cladding in Impact Direction; (b) Thin PMMA Cladding in Impact Direction; (c) No PMMA Cladding in Radial Direction; and, (d) Thin PMMA Cladding in Radial Direction.	142
A.42	Pressure near Rear Surface of PC Substrate	143
A.43	Stress Components near Rear Surface of PC Substrate: (a) No PMMA Cladding in Impact Direction; (b) Thin PMMA Cladding in Impact Direction; (c) No PMMA Cladding in Radial Direction; and, (d) Thin PMMA Cladding in Radial Direction.	144
A.44	Pressure near Rear Surface of PC Substrate	145
A.45	Stress Components near Rear Surface of PC Substrate: (a) No PMMA Cladding in Impact Direction; (b) Thin PMMA Cladding in Impact Direction; (c) No PMMA Cladding in Radial Direction; and, (d) Thin PMMA Cladding in Radial Direction.	146
A.46	Pressure near Midplane of PC Substrate outside Impact Region	147
A.47	Stress Components near Midplane of PC Substrate outside of Impact Region: (a) No PMMA Cladding in Impact Direction; (b) Thin PMMA Cladding in Impact Direction; (c) No PMMA Cladding in Radial Direction; and, (d) Thin PMMA Cladding in Radial Direction.	148
A.48	Pressure near Rear Surface of PC Substrate outside Impact Region	149
A.49	Stress Components near Rear Surface of PC Substrate outside of Impact Region: (a) No PMMA Cladding in Impact Direction; (b) Thin PMMA Cladding in Impact Direction; (c) No PMMA Cladding in Radial Direction; and, (d) Thin PMMA Cladding in Radial Direction.	150

List of Figures (Concluded)

<u>Figure</u>	APPENDIX B.1 - Static Analysis	<u>Page</u>
B.1	Finite Element Soln using Different Grid Refinements for: (a) Radial Stress in Uncoated PC; and, (b) Circumferential Stress in Uncoated PC.	155 156
B.2	Large Displacement Correction Factors for: (a) Uncoated Plate; and, (b) Coated Ballistic Lens.	157
B.3	Comparison of Small Displacement Solns for: (a) Circumferential Stress in Coated and Uncoated Ballistic Lens; and, (b) Radial Stress in Coated and Uncoated Ballistic Lens	158
B.4	Maximum Principal Stress for Static Point Load Applied at the Center of the: (a) Uncoated Lens; and, (b) Coated Ballistic Lens	159
B.5	Maximum Principal Stress for Static Point Load Applied at the Edge of the: (a) Coated Lens; and, (b) Uncoated Lens	160 161

APPENDIX B.2 - Frequency Analysis

B. 6	First Two Mode Shapes and Frequencies For Coated and Uncoated Ballistic Lens	164
B. 7	Third, Fourth and Fifth Mode Shapes and Frequencies	165

APPENDIX C.1 - Ballistic Test Data on Coated Ballistic Goggles

C.1	Ballistic Test Data on Coated PC Ballistic Goggles Supplied by Natick	171
-----	--	-----

APPENDIX C.2 - Ballistic Test Data on PC Flat Sheet Specimens

C.2	Ballistic Test Data on Uncoated PC Flat Plate Samples	175
-----	---	-----

APPENDIX C.3 - Ballistic Test Data on PMMA Clad PC Targets

C.3	Ballistic Test Data on PC Flat Samples with PMMA Cladding	179
C.4	Ballistic Damage to PMMA Impact Layer	180
C.5	Ballistic Damage to PC Substrate	181
C.6	Ballistic Damage to Rear Surface PMMA Cladding	182
C.7	Posttest Residual Cracks in Sample 2-30	183
C.8	Posttest Residual Cracks in Sample 2-31	184
C.9	Posttest Residual Cracks in Sample 2-32	185
C.10	Posttest Residual Cracks in Sample 2-33	186
C.11	Posttest Residual Cracks in Sample 2-34	187
C.12	Posttest Residual Cracks in Sample 2-35	188
C.13	Posttest Residual Cracks in Sample 2-61	189
C.14	Posttest Residual Cracks in Sample 2-64	190
C.15	Posttest Residual Cracks in Sample 2-65	191

List of Tables

<u>Table</u>		<u>Page</u>
1	Comparison of Polycarbonate versus Plexiglass (PMMA) Mechanical Properties	16
2	10 Pound Steel Plummets Drop Tests Results on Polycarbonate	20
3	Contributing Damage Mechanisms	24
4	Bulk Sound Speed, Density, and Calculated Impedance for Steel, Polycarbonate, and PMMA	25
5	Transmission and Reflection Factors for Different Interfaces	26
6	Comparison of Analytical Methods Employed for Prediction of Peak Contact Pressures	30
7	Comparison of Analytical Predictions for Peak Contact Pressure	30
8	Parametric One-Dimensional Hydrocode Calculations	32
9	Processing Conditions for MRC PC Targets	59
10	Mitigation of Damage Mechanisms	69

PREFACE

Mission Research Corporation's (MRC) Survivable Structures Technologies Division in Costa Mesa, California was awarded a Phase I Small Business Innovative Research (SBIR) program by the U.S. Army's Natick Research, Development, and Engineering Center (Contract DAAK60-89-0011 dated 30 December 1988) in response to Department of Defense solicitation 88.1 dated 8 January 1987, SBIR Topic A88-140. The published description of SBIR topic A88-140 is included below.

Polycarbonate (PC), used in ballistic protection, is extremely sensitive to processing. PC behaves as a ductile polymer when subjected to impact (e.g., from a shell fragment). Under certain conditions it behaves in a brittle fashion and cracks and spalls under ballistic impact. This often is associated with the presence of protective coatings on the PC. It is desirable to investigate the mechanisms underlying this brittle failure and the relative contributions on the various factors (e.g., crack initiation, crack propagation, crazing, surface degradation, moisture effects, etc.) and to recommend ways to prevent it.

The Background section is divided into three subsections. Section 1.1 discusses the motivation for the subject Phase I research and development effort. Section 1.2 summarizes the work plan proposed by MRC [Eisler, Jan. 1988 and May 1988] and Section 1.3 summarizes technical effort by task.

Section 2 begins with an introductory discussion of phenomenology and summary of technical accomplishments followed by technical discussions of each of the first six of seven tasks in Section 2.1 through 2.6 respectively. Section 3 summarizes Phase I conclusions.

Three appendices are provided which include results from Stress Wave Analysis (Appendix A), Structural Analysis (Appendix B), and Ballistic Test Data (Appendix C).

Appendix A is divided into two subsections. The first section of Appendix A, A.1, includes analytical results for one dimensional stress wave analysis employing the MRC version of the PUFF-74® stress wave response code. The cases considered include 0.127 to 3.175 cm thick steel flyer plates impacting 0.635 cm thick polycarbonate targets with and without various coatings and interfacial bonding layers. Impact velocities ranged from 600 cm/sec (19.6 ft/sec) to 60,000 cm/sec (1968 ft/sec). The purpose of this analysis was to examine phenomenology and develop a credible equation-of-state model for polycarbonate which could be used in subsequent analysis. The second subsection of Appendix A, A.2, includes two-dimensional stress wave analysis employing the AUTODYN® finite difference code. Results are presented for the normal impact of steel cylinders approximating the geometry of the 5.7 grain Fragment Simulating Projectile (FSP) against 2 mm thick polycarbonate targets with and without coatings. Results for impacts of 20,000 cm/second (656 ft/sec) are presented in Section A.2.1 and results for 2,000 cm/sec (65.6 ft/sec) are presented in Section A.2.2. The low velocity impacts considered in Section A.2.2 are further divided into analysis which does not include a preexisting defect in Section A.2.2.1 and results for a preexisting geometric discontinuity in Section A.2.2.2.

Appendix B is divided into two subsections. Section B.1 includes results from the stress analysis of ballistic goggles supplied by Natick RD&E Center subject to a static 1 Newton point load applied at different locations on the lens. A detailed three dimensional geometry model is employed using the COSMOS/M® finite element code. Section B.2 employs the geometry model employed in

Section B.1 to conduct a frequency analysis for the first five modes of the ballistic goggle lens.

Ballistic impact data employing 5.7 grain FSPs is presented in Appendix C. Test data generated by MRC for coated ballistic goggles supplied by Natick RD&E Center is presented in Section C.1. Data for flat uncoated polycarbonate samples is presented in Section C.2 and data for PMMA (polymethylmethacrylate) clad polycarbonate targets is presented in Section C.3.

ACKNOWLEDGEMENTS

This report constitutes the final deliverable (CDRL A002) for contract DAAK60-89-C-0011. This contract originated from a Phase I Small Business Innovative Research Proposal awarded by the Science and Advanced Technology Directorate of the U.S. Army Natick Research, Development and Engineering Center in January 1989. The Technical monitor was Dr. Edward Healy/STRNC-YSC who was assisted by Philip Cuniff/STRNC-ITFR from the Individual Protection Directorate. Other people at Natick were also extremely helpful, including William Kohlman/STRNC-YSM who supplied data relative to the ballistic impact of 15.7 grain fragment simulating projectiles on injection molded polycarbonate and Peter Dehmer/U.S. Army Materials Technology Laboratory, who rendered advice relative to the processing of polycarbonate.

The citation of trade names in this report does not constitute an official endorsement or approval of the use of an item.

The contributions of the following Mission Research Corporation (MRC) scientists also deserve to be highlighted. Mr. C. D. Newlander was responsible for developing the equation-of-state model for polycarbonate and conducting one dimensional stress wave analysis using the MRC version of the PUFF74® stress wave response code. Dr. A. K. Chatterjee was responsible for much of the fracture mechanics analysis and insight. Mr. M. N. West was responsible for conducting the quasistatic penetration tests and developing the static response model using the COSMOS/M® finite element code. Dr. S. F. Stone was responsible for setting up the two dimensional stress wave response model using the AUTODYN® finite difference code. Dr. Stone also provided much insight relative to the sensitivities of reflection coefficients in multilayered materials. Mr. Albert Koivu was responsible for fabricating polycarbonate test specimens and Mr. G. Burghart conducted ballistic tests using 5.7 grain fragment simulating projectiles, which involved developing a new sabot design.

1.0 SUMMARY

Task 1 - Definition of Ballistic Threats and Contact Forcing Functions of Interest. Projectile-target interface pressures were analytically determined for: (1) The impact of steel flyer plates 0.127 to 3.175 cm thick (0.05 to 1.25 inches) impacting uncoated and coated PC targets 0.635 cm thick (0.25 inches) at incident velocities of 600, 6,000 and 60,000 cm/sec (19.7 to 1968.5 ft/sec); and, (2) The impact of steel cylinders representing the impact of 5.7 grain fragment simulating projectiles on 2 mm thick PC targets with and without PMMA coatings of various thicknesses at incident velocities of 2,000 and 20,000 cm/sec (65.7 to 657 ft/sec).

In the case of nonpenetrating steel flyer plates impacting uncoated PC, peak contact pressures as calculated by the PUFF74 stress wave response code scaled linearly with velocity for incident velocities between 600 and 6,000 cm/sec. At 60,000 cm/sec material behaved nonlinearly, producing peak pressures approximately 16 times greater than what would be predicted based on linear elastic theory. Impacts of 600, 6K, and 60K cm/sec resulted in peak contact pressures of 0.15, 1.5, and 25 Kbars respectively.

For the impact of PMMA-coated PC targets which do not result in penetration of the coating on the impact surface, closed-form linear elastic analytical solutions indicate peak contact pressures between the target and projectile which are approximately 80% larger for a nominal PMMA-coated PC target than the corresponding uncoated PC target.

For the low velocity impact (2,000 cm/sec) of PMMA coated PC with 5.7 grain steel cylinders, analysis employing the AUTODYN finite difference code indicated contact pressures between the target and projectile of approximately 0.3 Kbars for the uncoated and 0.5 Kbars for the thinly coated PC. The PMMA coating on the thinly coated PC (coating thickness was 0.007 cm on impact and rear surfaces) was severely degraded at 0.7 microseconds and completely penetrated by 1 microsecond. At a corresponding location in the uncoated PC target, penetration did not occur till 4 microseconds. AUTODYN calculations for the thick PMMA coated PC targets (0.035 cm PMMA coating on impact surface and 0.007 cm coating on rear surface) indicate a total projectile penetration of approximately 30% of the coating thickness, which occurs at about 0.4 microseconds. The predicted contact pressure is on the order of 0.5 Kbars. AUTODYN analysis for the high velocity impact condition did not indicate significant differences in contact pressure between the thinly coated PC and uncoated PC targets.

Task 2 - Definition of Polycarbonate and Coating Combinations of Interest. The PC coating configuration of primary interest corresponds to a ballistic goggle with a thin coating rigidly attached to the front and back surface of a 2 mm thick PC substrate. The threat specification consists of a 5.7 grain fragment simulating projectile traveling at velocities up to 650 ft/sec. Coating thickness and mechanical properties are the primary free parameters since rigidly attached thicker coatings incorporating different materials are currently being developed for future applications. Other coating configurations which manifested ductile to brittle transitions corresponding to existing experimental data from the literature were also investigated. This included thick PC targets (0.25 inches) with coatings and interlayer material of various thicknesses and types subject to both ballistic and plummet drop tests.

Task 3 - Stress Wave Response Analysis. Accomplishments relative to defining the role of stress wave response in promoting a ductile to brittle transition were fourfold. First, based on existing experimental data from the Los Alamos National Laboratory [Marsh, 1980] and the Stanford Research Institute [Curran and Shockley, 1973], an equation-of-state material response model for polycarbonate was developed. This model describes equilibrium states of the material in terms of pressure, density, and internal energy. This model was then used to perform subsequent stress wave response analysis employing the PUFF74 code and the AUTODYN finite difference code.

The second effort concerned employing the MRC version of the PUFF74 code to evaluate the one dimensional impact of steel flyer plates of various thicknesses on 0.25 inch thick polycarbonate targets with and without PMMA coatings of various thicknesses and interlayer types. Key observations from this analysis were that: (1) Resulting stress histories were dependent on the impedance mismatch between layer materials; and, (2) Interlayer materials significantly altered the structure and magnitude of the incident stress pulse and resulting stress fields. Results from this effort are included in Appendix A.1 and discussed in more detail in Section 2.3.

The third effort involved implementing two-dimensional stress wave models for a 0.02 and 0.002 cm/microsecond impact of a 5.7 grain cylindrical steel fragment on rigidly attached PMMA coatings and uncoated 2 mm thick polycarbonate using the AUTODYN finite difference code and closed form elastic solutions. For the high velocity case the PMMA coating thickness was 0.007 cm on the front and back surfaces of the PC target. For the low velocity case, a thick PMMA coating equal to 0.035 cm was included on the impact surface with a thin 0.007 cm coating on the back face of the PC target. A thinly coated case was also evaluated.

Analytical results for the high velocity impact did not indicate significant differences in the stress states of thinly coated and uncoated PC targets. Additionally, the depths and rates of penetration were comparable; i.e., approximately 35 % of the substrate was penetrated in about 0.8 microseconds. Employing data from Rice [1980] and Curran and Shockley [1973] which indicate dynamic tensile strengths of 1 Kbar for PMMA and 1.6 Kbars for PC, it is very clear that the high rate of penetration associated with high incident velocity conditions is due to the fact that significant amounts of target material are failing in advance of the projectile arrival time.

In general, the high velocity impact produced tensile stress close to the impact surface of the substrate which was on the order of 1.5 to 5 Kbars in the radial direction and 6 to 7.5 Kbars in the impact directions. A very high compressive stress was also indicated in the circumferential direction of the substrate. Based on these results, the expected damage would be predicted to occur prior to penetration by the projectile and be propagated in the circumferential direction of the substrate. This was what was observed during the ballistic testing in Task 5.

These high tensile radial stresses develop at the acoustic velocity of the material and can be shown to promote the development of large diameter circumferential cracks on either side of the impact region. The large diameter circumferential cracks extend and eventually intersect, resulting in a large diameter plug of material being formed in the substrate. As the projectile begins to penetrate the substrate the large diameter plug displaces as a rigid body and travels at the same velocity as the projectile. Since shear forces at the projectile-target interface are not developed through this process, ductile penetration of the target by the projectile does not occur or is arrested resulting in a premature brittle failure of the target. Results from this effort are included in Appendix A.2.1 and discussed in Section 2.3.

Results for the low velocity impact indicate significant differences between the behavior and stress states developed in the PC substrates of coated and uncoated targets. For PMMA-coated PC the predominate tensile stress is in the circumferential direction and occurs in advance of the projectile penetration. This stress state would tend to promote radial fracture as opposed to the circumferential fractures associated with the higher velocity impact conditions. This is what was observed during the low velocity ballistic testing implemented in Task 5. Analysis also indicates that the stress components in the impact and radial directions are compressive which is also consistent with this hypothesis. The thin coating tends to produce higher dilatational stresses (i.e., pressures) than the thick coating. This is presumably due to the fact that the sample with the thick coating does not evidence any penetration into the substrate requiring bulk volume changes whereas the sample with the thin coating evidences penetration through 5% of the substrate thickness at about 0.7 to 1 microsecond. The individual stress components of the sample with the thick coating however tend to manifest higher tensile values than the thinly coated PC target. In general, tensile stresses in the PC substrate relative to the dynamic tensile strength of PC are much lower for the low velocity impact than the high velocity impact. This suggests that for the low velocity case, brittle failure initiates in the target coating as a radial crack, which then dynamically propagates through the substrate. Empirical data on crack trajectories from ballistic testing implemented in Task 5 is very suggestive of this mechanism. Analytical results for this effort are included in Appendix A.2.2.1 and discussed in Section 2.3.

The fourth effort concerns two dimensional stress wave analysis of uncoated and thinly coated PC in the presence of a geometric discontinuity. This discontinuity was placed on the impact surface of the PC for the uncoated target and on the impact surface of the PMMA for the coated target approximately 6 mm from the centerline of the impact location. A three to fourfold increase was calculated for the amplitude and pulse length associated with the pressure and radial stress components in the substrate. The stress component in the impact direction is largely unaffected however. More significantly, the sign of the pressure and radial component of stress for the two cases evaluated were opposite. This is due to the different signs associated with the reflection coefficients of a PC-air and PMMA-air interface (see Table 6 in Section 2.3). For the uncoated PC target the pressure pulse remains positive and the radial stress component is tensile. For the thinly coated PC target the pressure pulse becomes negative and the radial stress component becomes compressive. In the case of the uncoated PC, these results suggest circumferential crack propagation as the predominate damage mechanism as opposed to the coated PC where spallation is suggested by the stress wave analysis results. Detailed results from this effort are included in Appendix A.2.2.2 and discussed in Section 2.3.

Task 4 - Fracture Mechanics and Structural Analysis. The effort accomplished under this task was fourfold and included: (1) Assessment of the dynamic stress intensity factor associated with multilayered media with different material phases and interface conditions; (2) Static analysis for the stress field resulting from the application of 1 Newton point loads at different locations on the lens; and, (3) Frequency response analysis for the first five modes of the ballistic goggles supplied by Natick.

Preliminary work associated with the first effort related to determining the dynamic stress intensity factor ahead of a stationary crack situated in the coating of a coating-interlayer-PC assembly was initiated. Both experimental and analytical evidence was cited which indicates that the dynamic stress intensity factor for a crack proceeding from a brittle material phase to a ductile phase is significantly more severe than the case of a crack proceeding from a ductile material phase into a

brittle phase. This phenomenon can be related to cracks which initiate in the brittle coating of an impacted target and promote premature brittle failure of the specimen by subsequent crack propagation through the thickness of the target.

Detailed static stress and frequency analyses employing the COSMOS finite element code and closed form analytical solutions were performed as part of the second and third efforts implemented under this task. The static analysis did not indicate significant differences between a thinly coated and uncoated polycarbonate specimen (see Section 2.4). As the coating thickness is increased, however, bending deformation decreases. This reduced deformation for a thick-coated sample leads to enhanced stress in the impact region. The frequency analysis indicates a fundamental frequency on the order of 529.89 Hz for the uncoated ballistic goggles and 550.9 Hz for a coated version of the goggles. As the coating thickness is increased the fundamental frequency also increases. The period corresponding to these frequencies, however, is on the order of 10^{-3} seconds compared with the force-time history associated with the impact which is on the order of microseconds, 10^{-6} seconds. This suggests that the steady-state response of the material in terms of stress and displacement may be predicted with static analysis and the transient response is dictated by the stress wave behavior.

Task 5 - Fabrication of PC Materials Employing Processing Variations and Testing. Quasistatic penetration tests on ballistic goggles supplied by Natick and uncoated polycarbonate samples fabricated at Mission Research were conducted. Two failure modes were manifested during these tests (see Section 2.5). A ductile punch plug failure produced by high shear stresses was evident with a penetrator identical to the 5.7 grain fragment simulating projectile and a ductile "petaling" failure produced by high tensile bending stresses was evident with a rounded conical penetrator. For the fragment simulating indenter, the target material appeared to initially fail in shear. When the residual thickness of target material was sufficiently thin, the remaining ligament of target material failed in tension, producing a dish - shaped plug.

During the static penetration tests the coated ballistic goggles also evidenced fine circumferential cracks in the front surface coating and fine radial cracks were evident in the rear surface coating. These cracks were observed almost immediately after load application. In some cases large crazes were evident in the substrate toward the rear coating-substrate interface. In uncoated flat polycarbonate samples less pronounced rear surface crazing was evident (see Section 2.5).

Thirty-three ballistic tests were accomplished in Task 5 using 5.7 grain cylindrical steel fragment-simulating projectiles (FSP) with incident velocities of 368 to 847 ft/sec. Ballistic targets included uncoated and PMMA-clad flat polycarbonate specimens fabricated by MRC, and coated polycarbonate lens supplied by Natick RD&E center. Both ductile and brittle failures were observed in polycarbonate (PC) samples with and without protective coatings.

Brittle failures assumed one of three modes. For impacts near the edge of the ballistic goggles supplied by Natick RD&E center, a circumferential crack propagated outside the impact region and intersected the edge of the lens causing a large region of the lens to separate from the target (see Figure 1). For the PMMA-clad polycarbonate impacted at high velocities, circumferential cracks (with different radii of curvature) propagated in the polycarbonate substrate outside of but concentric with the impact region. At the intersection of the circumferential cracks a large relatively undeformed plug (approximately 4 to 6 projectile diameters) with a rough fracture surface was removed from the polycarbonate substrate (see Figure 2). The third brittle failure mode observed

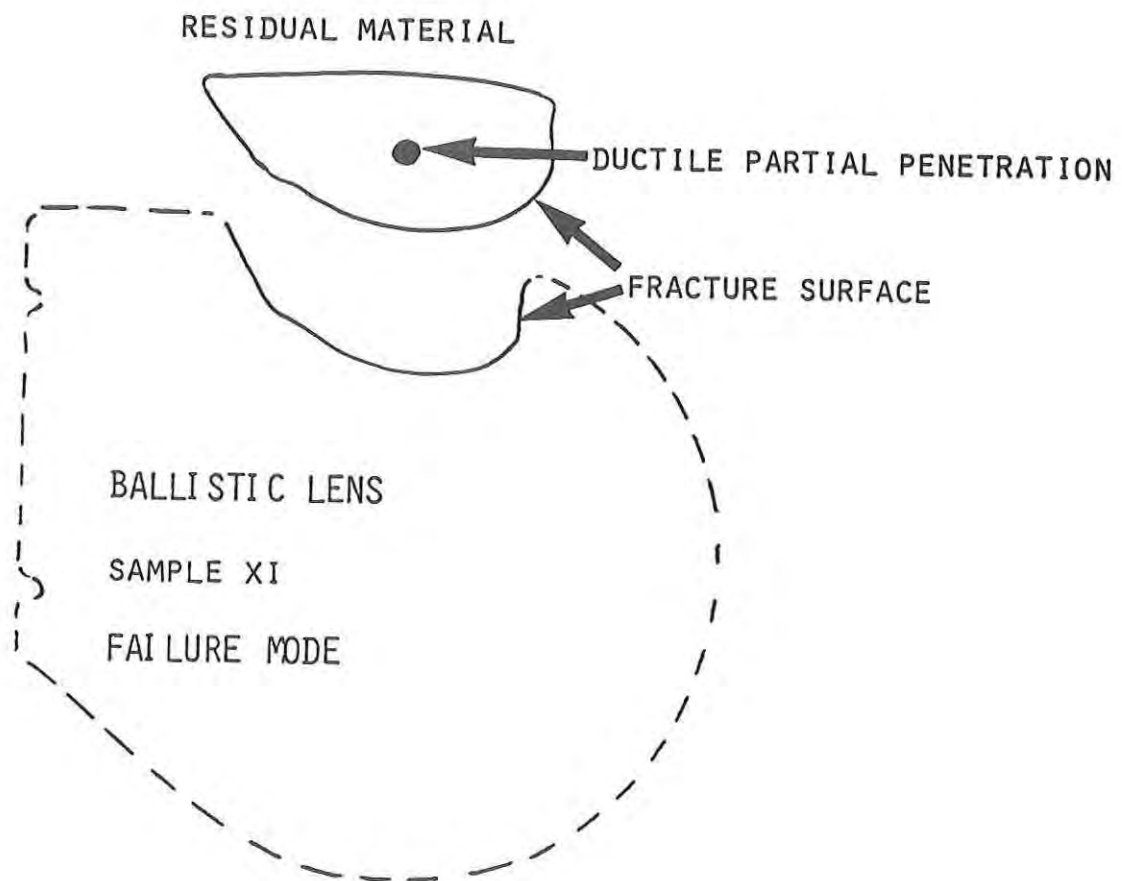
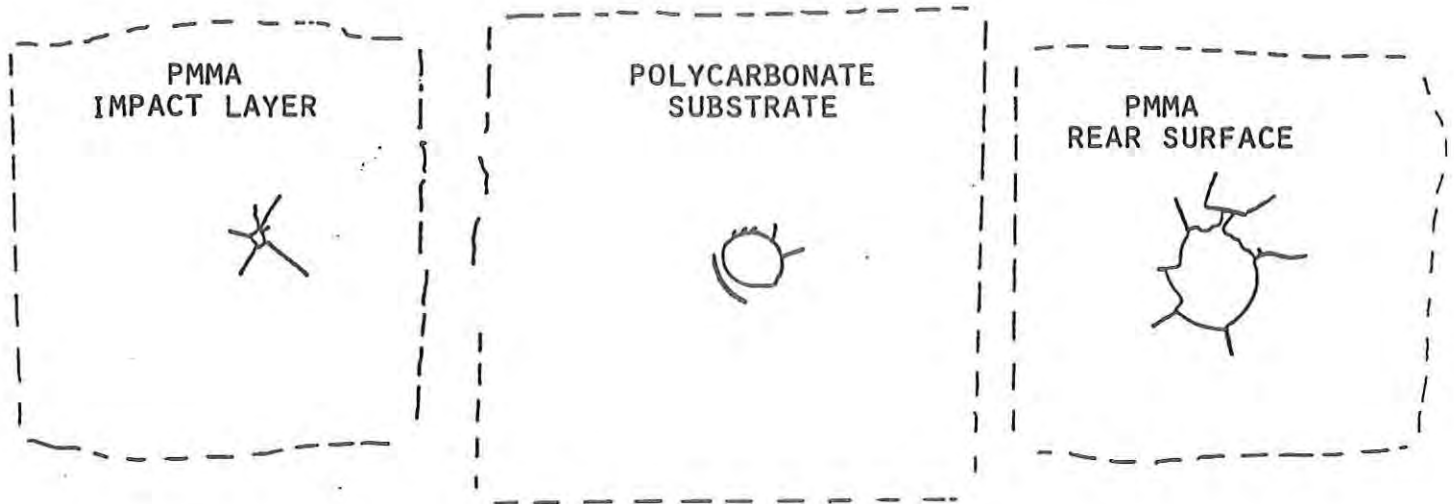


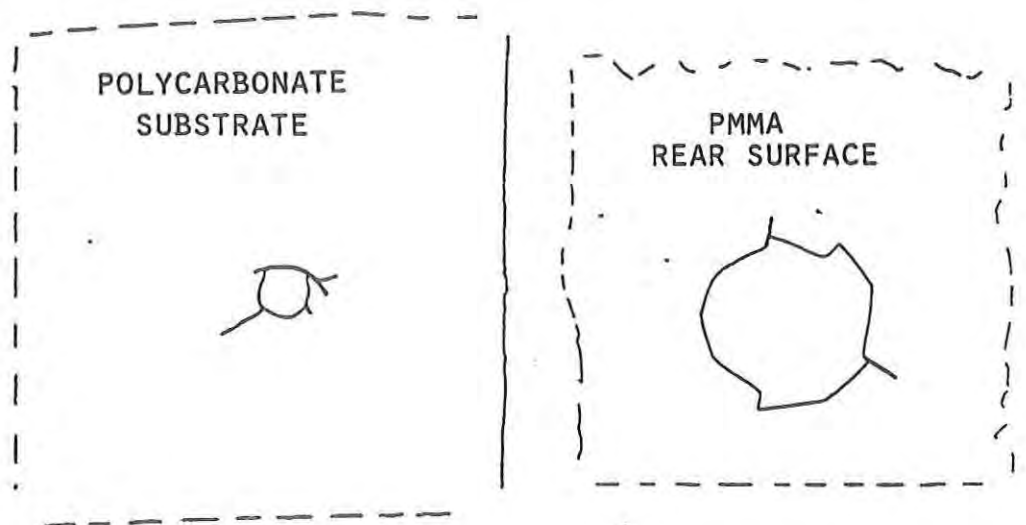
Figure 1. Brittle Failure Mode of Ballistic Goggle Subject to an Edge Impact.



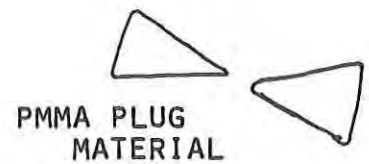
SUBSTRATE PLUG



SAMPLE 34



SAMPLE 31



PMMA PLUG
MATERIAL

Figure 2. Typical Failure Modes of Polycarbonate Samples Laminated with PMMA.

during testing in Task 5 concerned low velocity impacts, which resulted in very shallow penetrations of the PMMA-clad polycarbonate. These samples evidenced a significant amount of radial cracking, which propagated through the thickness of the target.

Ductile failures were observed on all of the uncoated polycarbonate targets and impacts in the central region of the ballistic goggles supplied by Natick. The ductile failure consisted of a dish shaped "Punched Plug" Failure (PPF) approximately the same diameter as the projectile. In general, a ductile failure results in very localized damage, which requires much higher projectile energies for penetration.

Task 6 - Hardening Recommendations. Damage mechanisms and governing parameters that promote a ductile to brittle transition in coated PC were identified along with potential hardening strategies. These recommendations are discussed in Section 2.6.

Task 7 - Final Report

1.1 Program Motivation

According to a U.S. Army clothing and equipment statement of need approved by the Army Chief of Staff [Smith, 1984]:

Eye injuries are common and disabling during combat, training, garrison, and athletic events. Recent combat statistics indicate that between 7 and 10 percent of all wounded in action are eye wound casualties. Virtually all of these eye wounds can be prevented by the wearing of a ballistic protective eye covering. Additionally, such an item could be worn during peacetime while conducting training, maintenance, and athletic activities, further reducing the number of eye injuries sustained by soldiers.

Transparent ballistic protection materials also have a variety of other military and civilian applications including automotive, aircraft, and helicopter windshields, goggles for Army tank crews, head and face protection of military personnel, shop workers, chemical laboratory personnel, specialty vehicle operators, police, and riot control personnel, lectern protection of important people, and hardened windows on structural assets that may be targets for terrorist or military action (e.g., embassies). Transparent ballistic protection materials also afford the opportunity to harden optical sensors against debris impact.

Material requirements for transparent ballistic protection include optical clarity over a range of wavelengths, impact resistance, and manifestation of ductile failure when the component is subject to impact. This last requirement includes resistance to crack propagation, spallation, or radial or conchoidal fractures and the predominance of local area or "punched plug failure". Punched Plug Failure (PPF) is local yielding about the contact area resulting in a hole without associated in-plane cracking. This failure mode results in optical components retaining clarity over most of the optical surface except in regions local to the contact area and also mitigates the tendency for ocular injury due to expelled target debris, which is often associated with the brittle failure of a target during penetration.

Consistent with the above, organic plastics have distinct advantages over inorganic glasses for ballistic protection. Glass shattering is obviously hazardous and in itself can cause injuries sometimes more serious than the threat missile. Plastics on the other hand can be designed not to shatter. Plastics can also be more easily formed, machined, and polished into intricate shapes than glass. Additionally, plastics can behave in a ductile manner when subject to impact conditions, thereby offering improved ballistic performance. Plastics are also lighter, can be made more transparent, and are more resistant than glasses to the accumulation of water vapor on optical surfaces. Among organic plastics, polycarbonate is a material of choice due to its excellent optical clarity and unexcelled resistance to ballistic penetration at acceptable thicknesses.

The main disadvantage of plastics and polycarbonate in particular is susceptibility to scratching and degradation of optical and mechanical properties from exposure to ultraviolet radiation or organic solvents. These disadvantages, however, can be mitigated by the inclusion of surface coatings. Under certain conditions, however, polycarbonate behaves in a brittle fashion and cracks and spalls under ballistic impact. This behavior is often associated with the presence of protective coatings on the polycarbonate. The purpose of the currently proposed effort is to investigate the mechanisms underlying the ductile to brittle transition in the mechanical behavior of polycarbonate subject to ballistic impact and recommend ways to prevent them.

1.2 Phase I Work Plan

The effort included seven tasks as shown in Figure 3 with a six month period of performance.

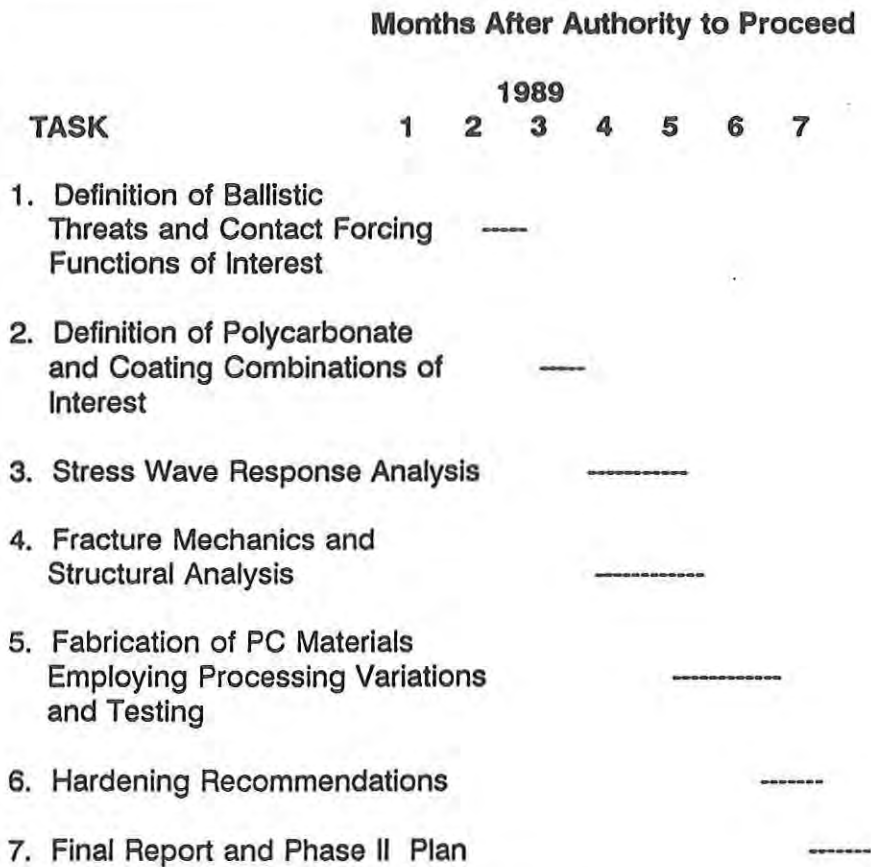


Figure 3. Phase I Task Schedule.

2.0 TECHNICAL APPROACH

As previously mentioned three types of brittle failure were observed during the ballistic testing conducted in Task 5. These failures included: (1) Circumferential fractures associated with high velocity impact on PMMA clad PC assemblies which led to the removal of large diameter plugs from the PC substrate; (2) Radial fractures which initiated in the PMMA cladding and propagated through the PC substrate leading to extensive in-plane and through-the-thickness cracking; and, (3) Circumferential fracture associated with impacts located within a critical distance to the lateral free surface (edge) of the Natick-supplied ballistic goggle leading to removal of a large hemispherically shaped segment of the goggle lens.

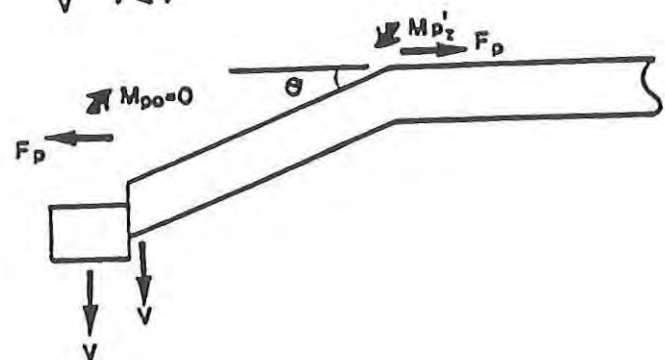
In general, all three types of brittle failure evidenced the beginning stages of a ductile Punched Plug Failure (PPF). For every case of brittle failure initiated by circumferential fracture; a ductile crater extending in depth approximately 30 to 75% of the substrate thickness was evident in the residual large diameter substrate plug recovered posttest. The incident velocities associated with brittle failure initiated by radial fracture were too low to result in perforation of the PMMA cladding; however, upon posttest examination following separation of the PMMA layers from the PC substrate, it was clear that the deformation of the PMMA had resulted in some very shallow local yielding in the PC substrate. In the case of the brittle failure associated with the ballistic goggles, a deep ductile crater was evident in the segment of lens removed from the goggle by the impact. As will be discussed in Section 2.3, it is the diffraction of stress waves reflected from the edge of the lens, about the residual crater, that promotes the circumferential fracture and consequent brittle failure of the ballistic goggle lens.

Ductile failures observed for the PC substrate during the ballistic testing consisted exclusively of punched plug failures and were associated with uncoated samples or impacts located within a central region of the thinly coated ballistic lens supplied by Natick. Ductile failure, as opposed to brittle failure, of the lens is desirable particularly for ballistic eye protection since: (1) Damage tends to be much more localized; (2) There tends to be less target debris and/or debris with much lower residual velocities yielding greatly reduced probability of eye injury; and, (3) In general, ductile failure requires much higher projectile energies for target perforation.

Figure 4 shows a schematic representation of a projectile impacting an infinite beam in 4(a) and two stages of PPF in Figures 4(b) and (c). During Stage I (Figure 4b) the projectile and plug of target material below the projectile slide at a velocity, V' , while the adjacent target material rotates at a velocity, V . Initially the projectile and target plug move faster than the adjacent target material (i.e., $V' > V$) resulting in shear at the projectile-target and plug-target material interfaces. With time V' decreases and V increases until they are equal, and sliding/shearing ceases, or the contact length, h , is reduced to zero and a plugging failure results. In the case where sliding ceases the plate continues to deform as a stretching membrane in Stage II, Figure 4(c), until a tensile separation of the plug results. Alternatively, if the velocity of the impacting penetrator is too low, deformation ceases and the velocity of the projectile is reduced to zero.

In the case of debris impact with a PC target, the principal deformation mode in terms of the absorption of projectile momentum by the target is membrane deformation as opposed to shear. This deformation is mainly due to two reasons. First, during an impact the distribution of pressure between the projectile and target surface is parabolically shaped with the maximum pressure coinciding with centerline of the projectile. Since debris particles tend to have low aspect ratios and sharp corners, stress concentrations associated with projectile edges will have sufficient extent to interact with the centerline of the projectile where peak contact pressures occur. This will produce a much more intense stress field when compared with the case of a projectile with a low aspect ratio where the stress concentrations associated with the projectile edges tend to be independent of the large contact pressures occurring toward the center of the projectile. For the debris particle, the large increase in interface pressure between the projectile and target will tend to fail target material in advance of projectile penetration, making penetration much easier. In the case of the 5.7 FSP employed in Task 5 of this effort, there is substantial evidence that this occurred based on posttest optical microscopic examination of recovered plug material following ballistic impact with PC targets.

PLUG SHEARING



- Figure 4. Ductile Punched Plug Failure (PPF) Process in Uncoated Polycarbonate.**

The net result is that the shear resistance/stiffness of the target will not be a major factor in the absorption of energy from debris impact. However, due to the exceptionally large 100 to 130% strain to failure of PC, the amount of energy absorption that can be accommodated by PC through membrane deformation dwarfs other plastic materials and deformation modes.

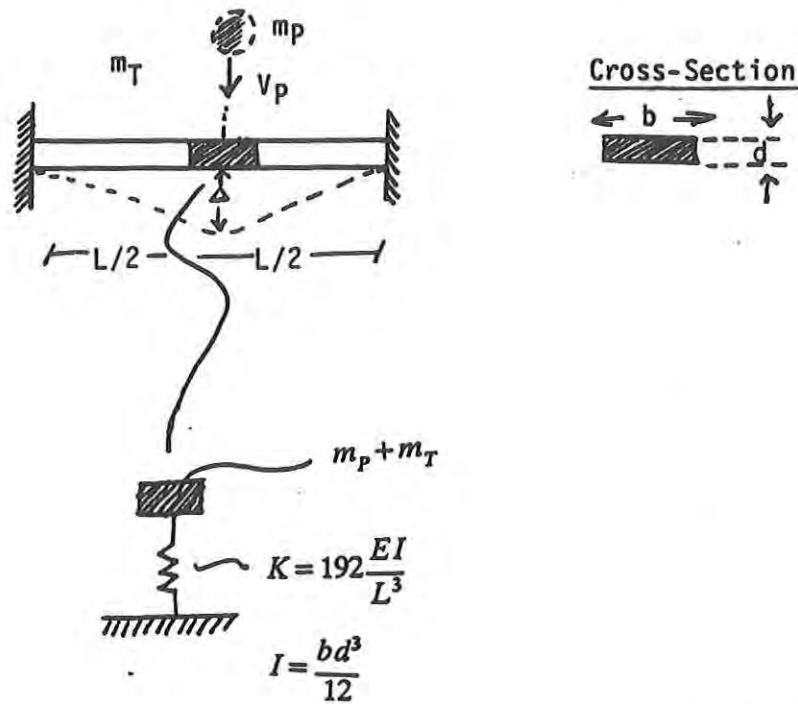
In order to begin understanding the relative importance of parameters governing the amount of energy dissipated in PC through membrane deformation, we formulated the spring-lumped mass model shown in Figure 5. The model describes the absorption of strain energy through bending deformation of a beam. The bending stiffness of the beam is equilibrated to the spring-coefficient of the model and the displacement of the spring by the lumped mass can be related to axial strain in the beam due to bending. The model includes two related free parameters which are the effective mass of target material, m_T , which interacts with the projectile during impact (generally on the order of the target plug, which is much less than the total mass of the target) and axial strain, ϵ , induced by the displacement of the spring, Δ . The strain energy absorbed by the spring-lumped mass system can then be equilibrated to the momentum imparted to the target by the projectile, as determined from conservation of momentum between the impacting mass and the sum of the projectile and effective target mass. The absorbed strain energy can then be related to the reduction in projectile momentum and hence residual velocity of the projectile. If the projectile velocity is reduced by 100%; i.e., projectile velocity equals 0, then the projectile will presumably not penetrate the target.

Figure 6 shows results for the velocity reduction of the projectile in terms of the target mass involved by the impact event for different values of axial strain. Figure 7 shows velocity reduction as a function of tensile strain for a prescribed effective target mass. In general, the effective target mass associated with the ductile penetration of polycarbonate is relatively small corresponding to target material within 1 to 1.25 projectile diameters. This fact in conjunction with Figures 6 and 7 indicates that the key parameter for the absorption of impact energy by PC during ductile penetration is the structural deformation and associated membrane strain which can accommodate very large elongations prior to failure (see Table 1).

It should be noted that the numerical entries for Figures 6 and 7 are for the beam model shown in Figure 5. Analogous results for plates of the same thickness, due to the higher bending stiffness associated with plates, tend to push the results in Figures 6 and 7 toward the ordinate axis in the respective plots.

For the purpose of the Phase I effort, a nonproprietary coating (PMMA) was employed as a nominal coating with properties that were presumably representative of PC coating materials. PMMA has been used on PC as a protective coating and is mechanically well characterized. Most importantly however is that PMMA coatings have been associated with the occurrence of a ductile to brittle transition in the mechanical behavior of PC substrates during impact. The static mechanical properties of PMMA (Plexiglass) and PC are compared in Table 1.

Impact Loading: Equivalent Mass - Spring Model Beam Analysis



ϵ = strain

m_p = Projectile Mass

m_T = Effective Target Mass

v_p = Projectile Striking Velocity

v = Combined Velocity of Projectile
+ Effective Target Mass

Conservation of Energy:

$$\frac{1}{2}(m_p + m_T)v^2 = \frac{1}{2}m_p v_p^2 - \frac{1}{2}K\Delta^2$$

which gives:

$$\frac{v}{v_p} = \sqrt{\frac{\left[1 - \frac{K\Delta^2}{v_p^2}\right]}{1 + \bar{m}}}$$

where:

$$\bar{m} = \frac{m_T}{m_p}$$

$$K = \frac{K}{m_p}$$

$$\Delta = L\sqrt{\epsilon^2 + 2\epsilon}$$

Figure 5. Equivalent Spring-Mass Model.

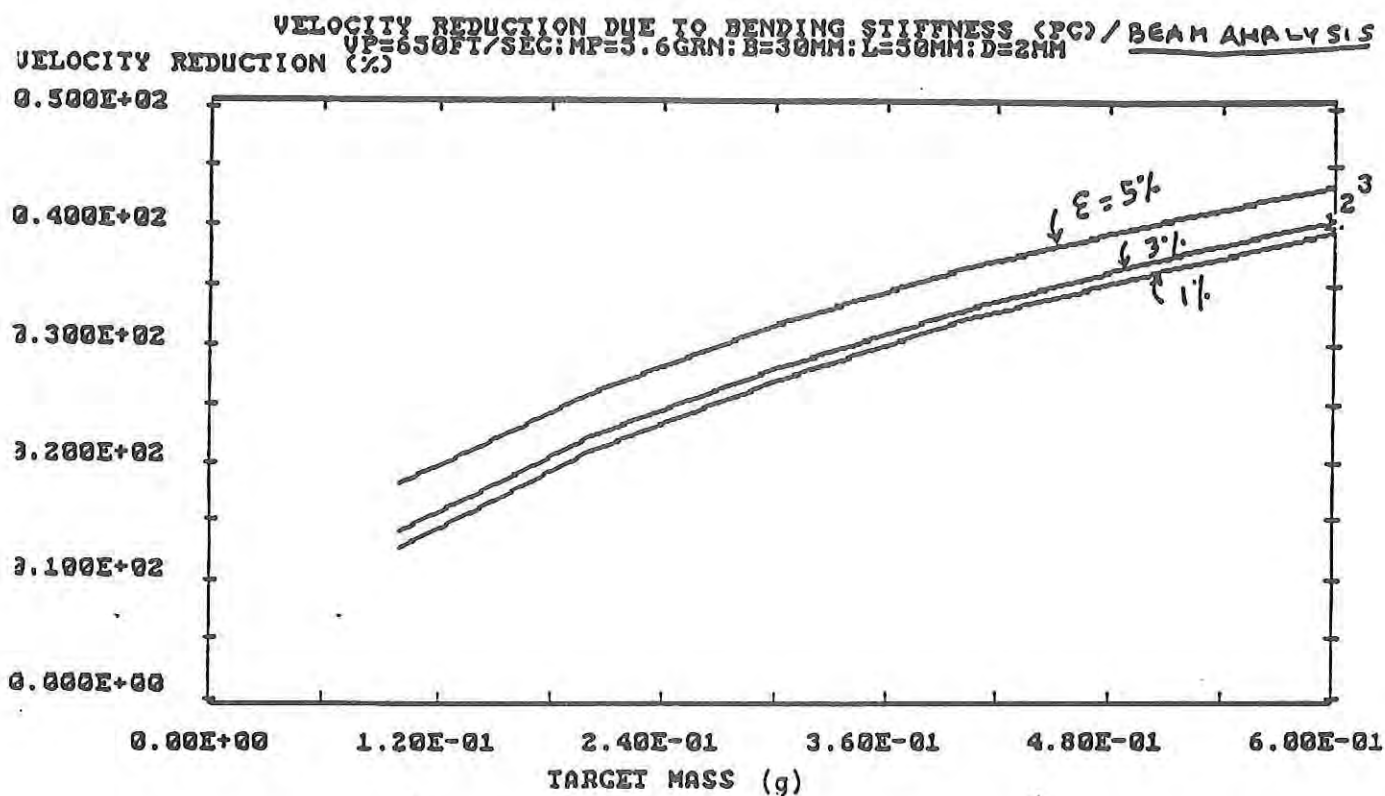


Figure 6. Velocity Reduction as a Function of Effective Target Mass for Different Tensile Strains.

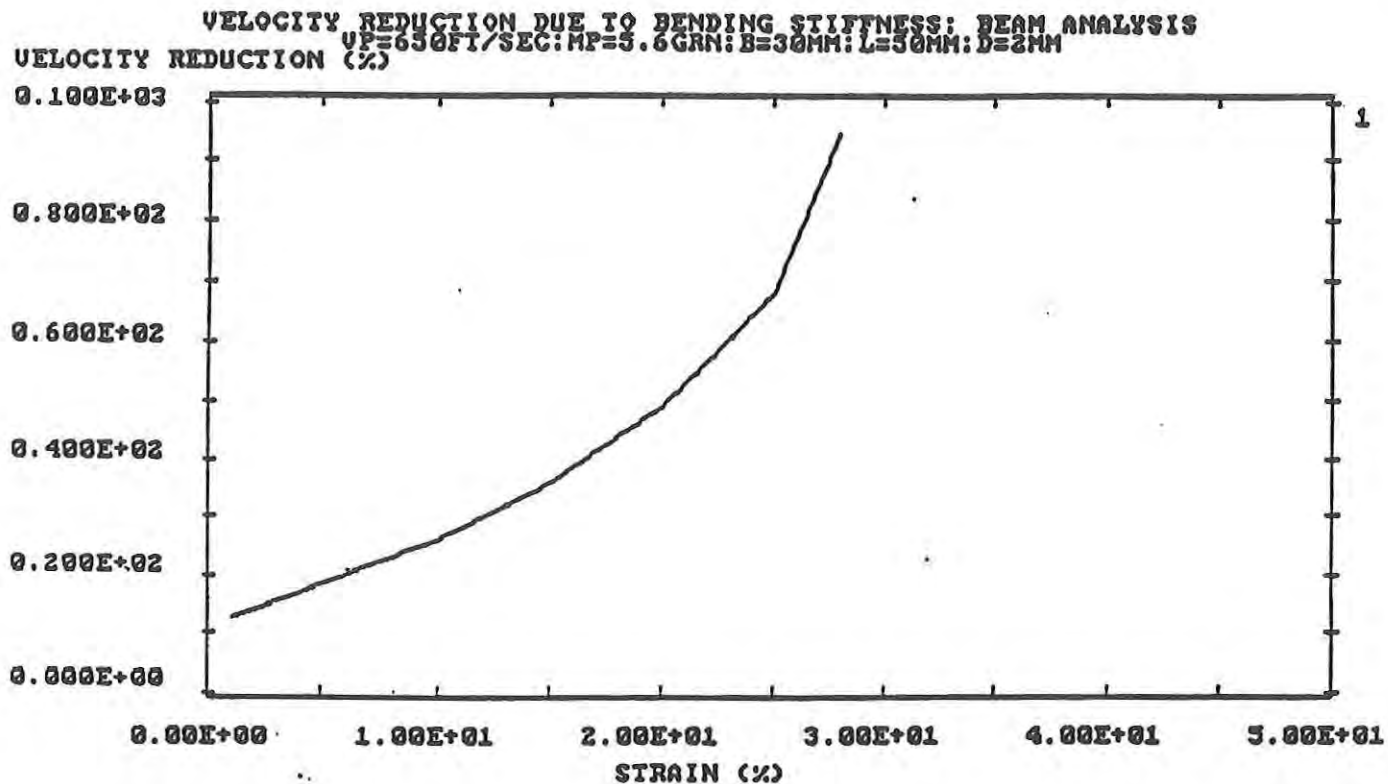


Figure 7. Velocity Reduction as a Function of Tensile Strain
for Prescribed Target Mass.

**Table 1. Comparison of Polycarbonate (PC) versus Plexiglass (PMMA)
Static Mechanical Properties**

	Tensile Strength (N/cm ²)	Elongation at Break (%)	Tensile Modulus (N/mm ²)	Ball Hardness (N/mm ²)	Notched Impact (ft-lb per inch notch)
PC	56/67	100/130	2100/2400	110	12/18
PMMA	50/77	2/10	2700/3200	180/200	0.3/0.5

It is clear from Table 1 that there is a displacement incompatibility between the coating and PC substrate due to the lower tensile modulus and higher strain-to-failure of the PC substrate in relation to the protective coating. As the coating/PC assembly deforms in response to the impact event, the deformation of the PC will be constrained and the coating due to its much lower strain-to-failure will manifest extensive cracking. Once the macrocracks form in the coating, they can be propagated into the PC substrate by one or both of the failure modes shown in Figure 8.

The first failure mode in Figure 8 shows a macrocrack in the coating being propagated into the substrate by tensile stress applied to crack faces producing an unstable crack geometry. The source of the tensile stress is threefold. First, tensile stress is induced by compressive stress waves from the impact event reflecting in tension from lateral free surfaces of the target or non-specular reflection from impedance mismatches at coating substrate interfaces. Second, bending deformation will induce tensile stress below the neutral axis of the target which is applicable to macrocracks induced in the rear surface coating by bending deformation. Finally, as the projectile penetrates, target material is radially pushed away from the projectile which induces tensile hoop stresses outside the crater. The unstable geometry of the macrocrack in conjunction with the direction of the predominate applied tensile stress results in through-the-thickness propagation of the crack.

Crack propagation can proceed in any direction depending on the predominate stress component and the energy required to create a new fracture surface. In general the most unstable crack geometries are those where tensile stress is applied normal to a crack face (see Figure 9). Hence, if the maximum principal tensile stress is in the radial direction then the development of circumferential cracks is encouraged. Similarly, if the predominate tensile stress component is circumferential then radial crack development is promoted. Cracking will occur if the energy associated with the applied stress field is greater than the energy required to create a new fracture surface. In general, it takes a factor of 2π more energy to create a circumferential fracture surface than the corresponding radial fracture surface of the same equivalent crack length. This is due to the larger fracture surface associated with the formation of circumferential cracks. It will therefore require significantly larger tensile stresses to create circumferential cracks compared to radial cracks of the same equivalent length.

The second failure mode in Figure 8 shows a macrocrack in the coating, which extends laterally due to the application of through-the-thickness tensile stress on the crack faces. Through-the-thickness tensile stress is caused by compressive stress waves from the impact event reflected in tension off coating-substrate interfaces. As the macrocrack extends laterally, it increases in velocity and interacts with microdefects, which causes the crack to bend and extend into the PC

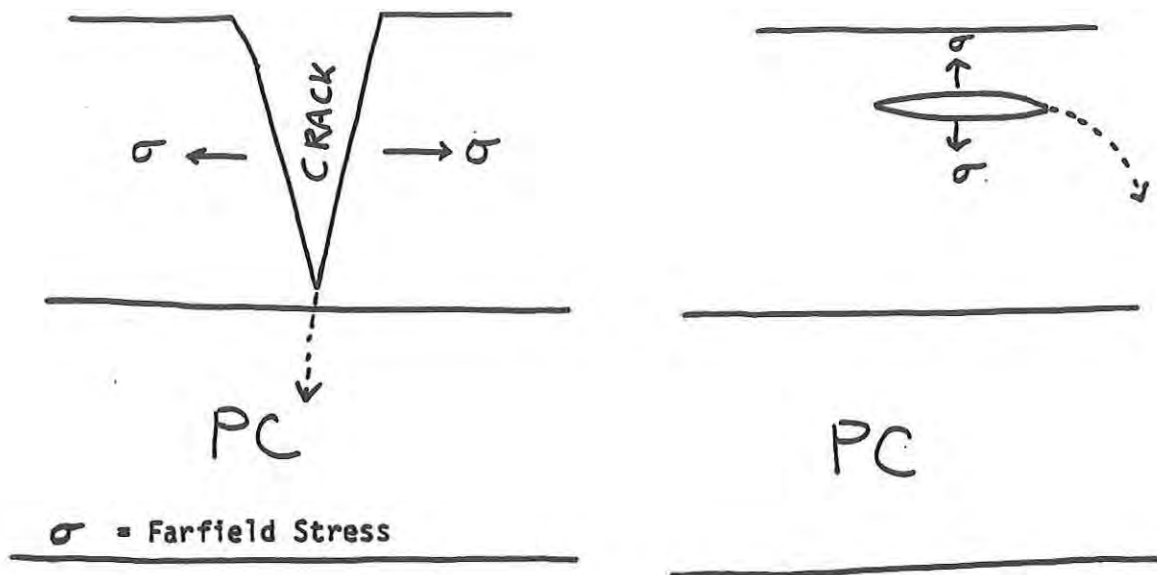


Figure 8. Brittle Failure Modes Associated with Crack Propagation Initiating in the Coating.

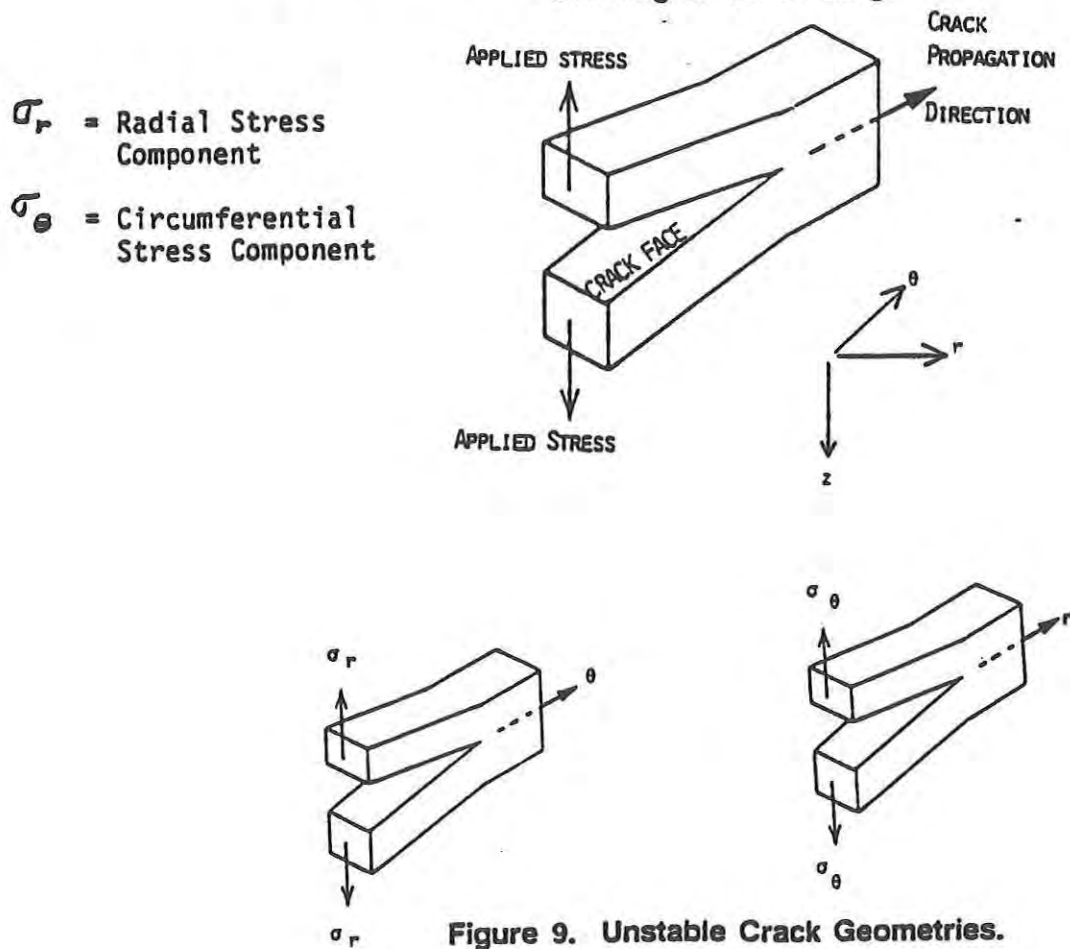


Figure 9. Unstable Crack Geometries.

substrate. This mechanism will be discussed in more detail in Section 2.4; however, there is substantial evidence for this mechanism both in the literature and from ballistic testing accomplished as part of Task 5 in the current effort.

Based on results from the ballistic testing accomplished in Task 5, radial crack propagation through the thickness of a PMMA-clad PC target appears significant in terms of instigating brittle failure for low velocity impacts; i.e., where projectile penetration into the PMMA cladding is minimal. At higher impact velocities where the resulting stress fields are more severe and the projectile partially penetrates into the PC substrate, damage in the PC substrate consists of predominately circumferential cracking, which begins due to high radial stresses occurring in the substrate.

Analytical results in Task 3 for two-dimensional stress wave models evaluating a 0.02 (656 ft/sec) and 0.002 cm/microsecond (65.6 ft/sec) impact of a 5.7 grain cylindrical steel fragment on PMMA coated and uncoated PC targets show reflected stress waves from coating interfaces at the higher impact velocities, which lead to large radial tensile stresses at very early time in the substrate as opposed to the predominately compressive stress field at corresponding locations in the uncoated sample (see Section 2.3). These high tensile stresses develop at the acoustic velocity of the material and can be shown to promote the development of large diameter circumferential cracks on either side of the impact region. The large diameter circumferential cracks extend and eventually intersect resulting in a large diameter plug of material being formed in the substrate. As the projectile begins to penetrate the substrate, the large diameter plug displaces as a rigid body and travels at the same velocity as the projectile. Since shear forces at the projectile-target interface are not developed through this process, ductile penetration of the target by the projectile does not occur or is arrested resulting in a premature brittle failure of the target.

At higher velocities, beyond the ballistic limit of the target where complete penetration of the target by the projectile occurs, the target material begins to behave hydrodynamically and target inertia is no longer involved in the projectile interaction with the target. For injection molded PC this fact is illustrated in Figure 10, based on data from Kohlman [1989] relative to the impact of 15.7 grain fragment simulating projectiles against polycarbonate sheets. Target areas on the polycarbonate sheet were rigidly clamped with one-inch diameter disks. Two phenomenological regions were identified relative to these test results. The first region corresponds with complete penetration and low incident and residual velocities of the projectile. In this region a large fraction of the projectile momentum (relative to the second region) was absorbed by the target material. The target response involves the entire inertia of the material, as evidenced by brittle cracking near the target boundaries, which are well outside the impact region. In the second region the behavior is more localized and the incident and residual velocity of the penetrator is increased. In this region the target material behaves hydrodynamically (i.e., provides minimal or no resistance to shear) absorbing a lower fraction of projectile momentum and involving lower amounts of material inertia. Coinciding with this observation is that no damage is seen except for the residual crater formed via a ductile punched plug failure.

It is clear from the above, that the ductile to brittle transition observed in PC substrates is very sensitive to the incident velocity and geometry of the projectile as well as the coating thickness and elastic properties relative to the PC substrate.

In terms of the phenomenology outlined above, additional contributing mechanisms were identified during the course of the Phase I effort. These mechanisms are of varying significance

15.7 Gn Frag Simulator Ballistic Data

Uncoated Polycarbonate - 0.139" Sheet

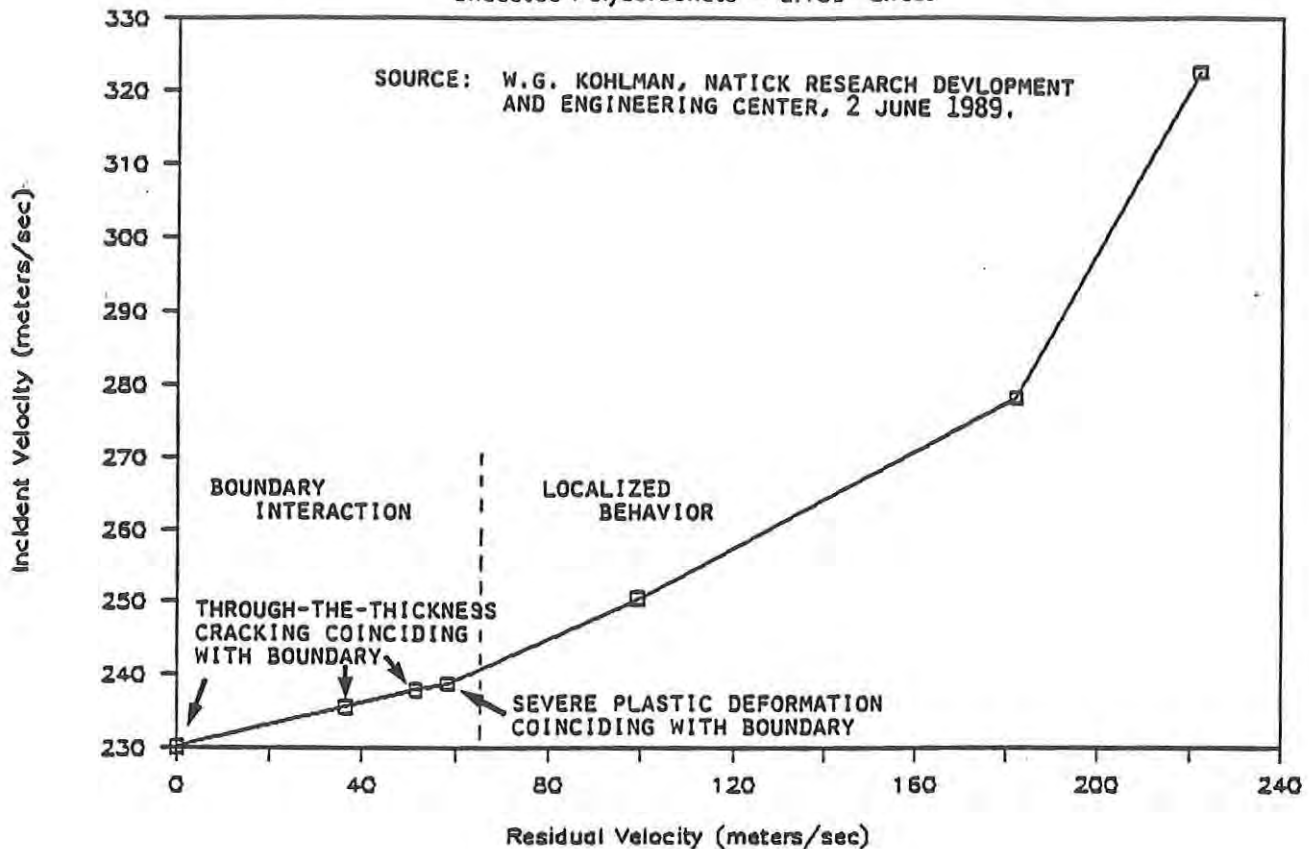


Figure 10. 15.7 grain Fragment Simulating Projectile Ballistic Data on Polycarbonate.

depending on variables specific to the impact event, such as projectile-target contact time, impact velocity, projectile and target material, projectile and PC target geometry, and interlayer properties between the coating and PC substrate, etc.

The first mechanism tends to occur for impact events with long contact times (relative to the fundamental mode of vibration and the acoustic thickness of the projectile and PC-coating assembly) or penetration problems with the associated long incident compressive pulse. Due to the long pulse width, the associated structural response tends to mimic or approach a static response. If the shear modulus and shear strength of the PC-coating interlayer tend to be high, then the PC-coating assembly will behave in a mechanically monolithic manner during the large deformations associated with an impact event. Since the coating is present to afford abrasion, environment, and/or UV protection for the PC, it tends to be stiff and brittle relative to the PC substrate, which is ductile. During large deformation, if the compliance and thickness of the coating-PC interlayer is insufficient to isolate the strains from adjacent material layers, an incompatibility in displacements can occur leading to rupture of the coating, failure of the interlayer, and/or premature crack propagation in the PC substrate.

Note that the end result of this first mechanism is different if the coating is on the impacted surface of the PC, both surfaces of the PC, or the back surface of the PC, or if the interlayer

debonds. If the coating is on the back surface, the coating will tend to break due to large displacements of the PC producing excessive flexural strains in the coating. If the PC-coating interlayer remains intact, the coating and the adjacent PC material will be in tension due to bending for some relatively long elapsed time. The coating will fail in tension and due to stress risers associated with cracks in the coating will tend to promote failure in the adjacent tensile regions of the PC material. If the coating is on the front surface, the PC substrate can accommodate coating displacements. The coating however will tend to fail in compression. This damage will not be easily promoted in the adjacent PC material since it will also tend to be in compression. This result is consistent with data shown in Figure 11 and Table 2.

Figure 11 [Illinger, 1972] shows the experimentally determined ballistic limit of two layer PMMA/polycarbonate configurations subject to 17-grain fragment simulating projectiles. The top curve corresponds to PMMA on the impact surface with different thickness of PC on the back surface. The bottom curve corresponds to different thicknesses of polycarbonate on the impact surface with PMMA on the back surface.

Table 2 is from data developed by Huyett and Wintermutte [1976] where the results of impact tests performed with long steel plummets and 1.5 inch hemispherical indenters (plummet was approximately 20 inches long) are reported. The tests were performed on 6x6 inch clamped specimens subject to a 20 pound plummet and 12x12 inch simply supported specimens subject to a 10 pound plummet. For 0.25 inch monolithic PC, failure occurred in the clamped specimen at a drop height of 28 feet and the simply supported specimen survived drop heights greater than 38 feet. Plummet tests (10 pounds) were also performed employing plexiglass coatings of various thicknesses (0.05 to 0.187 inches) on 12x12 specimens. In all cases the PC substrate was 0.25 inch thick and the coating was either fusion bonded with chemical solvents or bonded with silicone or urethane adhesives. In some cases the coating was placed on the impact surface, the rear surface, or both surfaces.

Table 2. 10 Pound Steel Plummet Drop Test Results on PC.

Specimen	Drop Height at Failure
Plexiglass fusion bonded on both sides	
0.001 inch Plex on impact surface, 0.05 inch Plex on rear surface	less than 4 feet
0.125 inch Plex on both sides	3-4 feet
0.187 inch Plex on both sides	less than 6 feet
0.187 inch Plexiglass fusion bonded on impact surface	8-10 feet
0.187 inch Plexiglass fusion bonded on rear surface	less than 4 feet
Adhesively bonded (interlayer thickness ranged from 0.002 to 0.1 inch) Plexiglass (0.062 to 0.125 inch thick) to impact or rear surface	Survived 38 feet although surface coating cracked

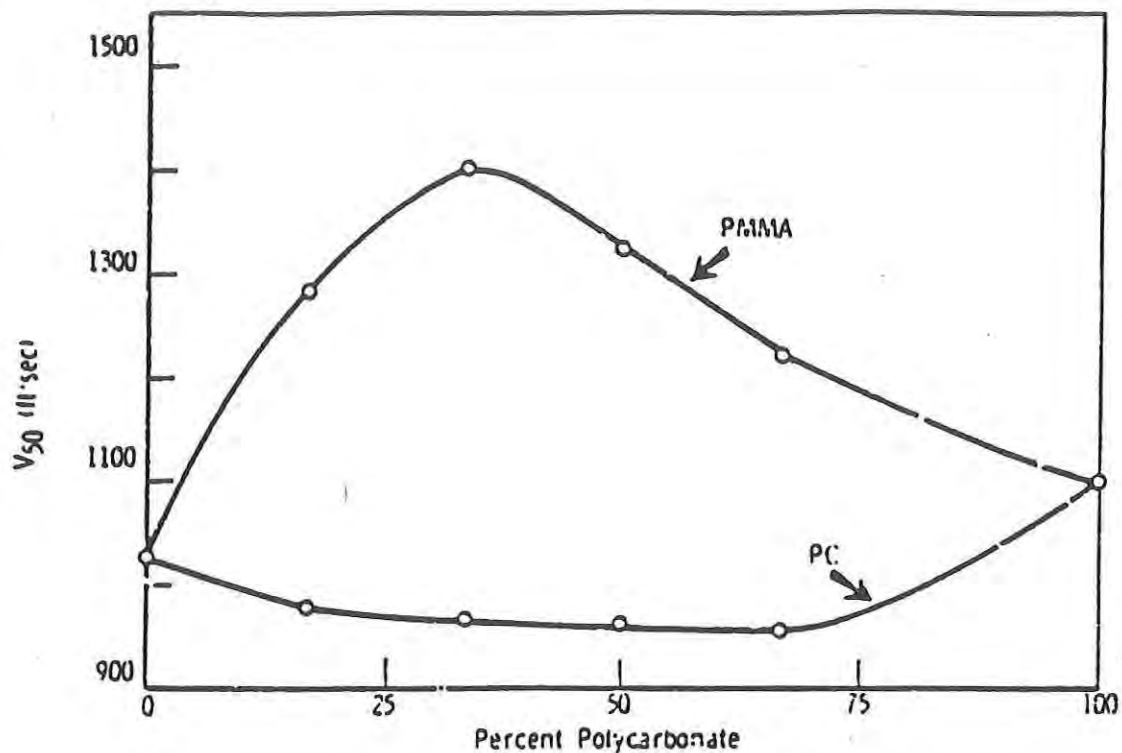


Figure 11. Ballistic Behavior of PMMA/PC Laminates without Interlayer.
(17-grain FSP, 0 degree obliquity, 38 oz/sq. ft.)

Although a detailed description of the failure mode and associated damage is not included with the experimental results reported above; in general, a large reduction in failure threshold indicates brittle behavior. Both sets of data indicate that when protective coatings are on the front surface of the PC target, ductile behavior is promoted. When the only coating is applied to the rear surface or both surfaces of the PC target, brittle behavior is manifested. Also, consistent with this first mechanism are the data in Table 2, which shows that rigid interlayers favor brittle behavior. When the interlayer is changed to a flexible interlayer, PC-coating configurations which had failed in a brittle mode no longer did so. Unfortunately for many applications, neither the use of flexible interlayers or the application of coatings to only the rear surface of the PC is acceptable due to other constraints associated with current and future applications.

The second mechanism is related to the difference in plane-strain versus plane-stress fracture toughness for PC. Fracture mechanics measurements on PC [McCrum, 1988] show a decrease in toughness from $G_c = 10 \text{ KJ/m}^2$ under plane-stress conditions (in relatively thin specimens, 3mm thick) to $G_{IC} = 1.5 \text{ KJ/m}^2$ under plane-strain conditions (in relatively thick specimens). In a thin sheet at the tip of a stressed crack, the thickness of the specimen decreases because of Poisson contraction resulting in plane-stress conditions at the crack tip. In a thick plate at the tip of a stressed crack, the thickness of the specimen is prevented from decreasing by the elastic restraint and consequent

through-the-thickness stress imposed by the surrounding material which offsets the Poisson contraction. Plain strain conditions therefore prevail at the crack tip. Since yielding is generated by shear components of stress and the stress state associated with plane-strain conditions tends to be pure triaxial tension, the shear components of stress and the extent of yielding at the crack tip is greatly reduced, resulting in reduced fracture toughness.

Given the occurrence of a through-the-thickness crack in the coating of a PC (produced by the impact or preexisting flaws) the stress state at the crack tip will be different depending on the interface. In a fusion bonded specimen, the rigid interface ahead of the flaw will tend to promote development of a plain-strain stress state with the associated low fracture toughness relative to a pliable adhesive interface, which would tend to promote plane-stress conditions and encourage the development of shear stress at the coating PC interface (depending on the shear modulus of the adhesive interlayer). Additionally, for an adhesive interlayer, the coating could debond ahead of the crack tip, resulting in a free surface which does not permit fracture propagation into the PC substrate.

A third mechanism is related to the build up of the dynamic stress intensity factor associated with a defect or crack in the coating. It can be shown that the order of the singularity and the rate at which the stress intensity factor increases with crack length is sensitive to interface properties as well as the properties of the materials on either side of the interlayer [Cook and Erodgan, 1972; Theocaris and Papis, 1983; Kuo, 1984; and Chatterjee and Knopoff, 1984]. Figures 12 and 13 [Theocaris and Papis, 1983] show this effect for an interface dividing a brittle to ductile succession of material separated by an interlayer. Figure 12 shows the variation of stress intensity factor as a function of crack length, $a(m)$, for a ductile to brittle succession of materials phases. Figure 13 shows the same results for a brittle-ductile succession of material phases. The brittle to ductile succession of material in Figure 13 is analogous to a brittle coating configured on a ductile PC.

Table 3 shows some additional factors that may aggravate the damage mechanisms described above. Crazing significantly reduces fracture toughness and if the crazing occurs in a preferential direction, it can result in a preferential direction of fracture propagation. The reduced fracture toughness can result in accelerated crack velocities, which are a necessary precondition of crack branching and curving. If a defect from the crazed region occurs within a critical radius and subtended angle of the crack tip then the direction of maximum stress can be perturbed such that it is not colinear with the crack. This can cause the propagation of the crack to curve or branch. Additionally, residual stress from fabrication can superimpose upon the applied stresses to reduce tensile strength and cause preferential crazing. Variations in molecular weight and density can also alter molecular free-volume and equation-of-state properties.

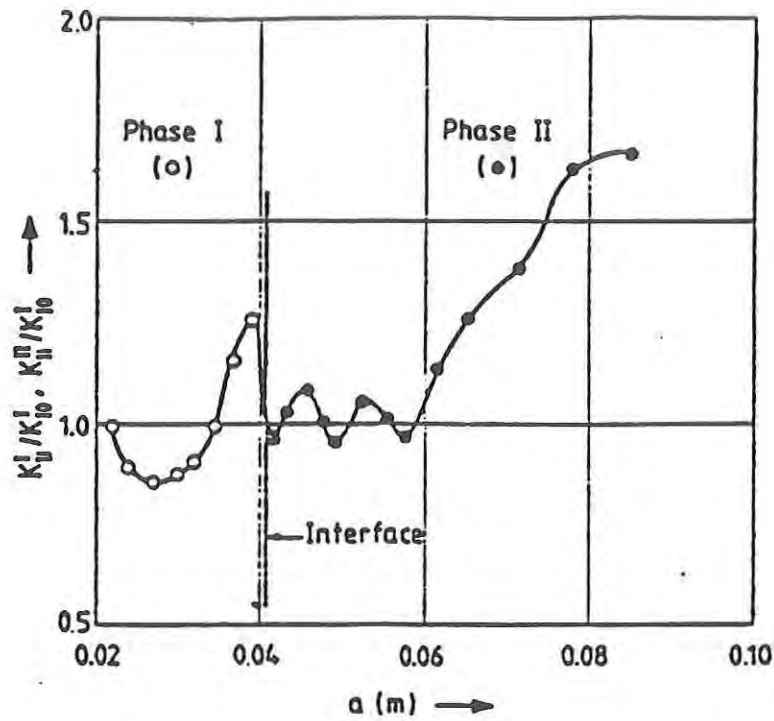


Figure 12. The Variation of the Stress Intensity Factor. Variations normalized at each phase to its initial value at the initiation of the crack in phase I (K_{I0}^I), as a function of the crack length a , in the case of a ductile-brittle succession (phase I 30%, phase II 10% plasticized).

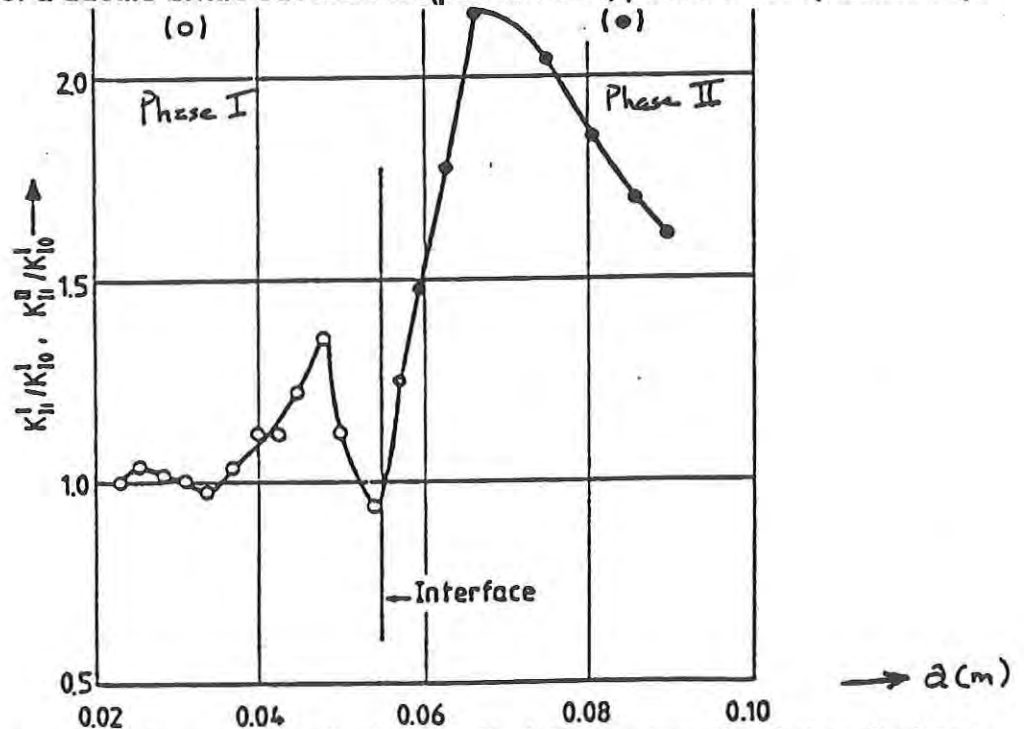


Figure 13. The Variation of the Stress Intensity Factor. Variations normalized at each phase to its initial value at the initiation of the crack in phase I (K_{I0}^I), as a function of the crack length a , in the case of a brittle-ductile succession (phase I 10%, phase II 30% plasticized).

Table 3. Contributing Damage Mechanisms.

CRAZING

- o Reduced Fracture Toughness
- o Accelerated Crack Velocities
- o Crack Curving/Branching and Preferential Propagation

RESIDUAL STRESSES FROM MANUFACTURING

- o Reduced Tensile Strengths
- o Preferential Crazing
- o Additional Source of Stress

VARIATIONS IN MOLECULAR WEIGHT AND DENSITY

- o Alters equation-of-state and resulting stress from impact
 - o Alters Molecular Free Volume
-

2.1 Task 1 - Definition of Ballistic Threats and Contact Forcing Functions.

Initial effort in this task was oriented toward understanding existing experimental data (see Plummert Test Data in Table 2) where an abrupt brittle to ductile transition in failure mode was observed. In general, the existing experimental literature concerned relatively thick PC substrates so the PC configurations and projectile properties initially selected for analysis were thicker than what was evaluated at later stages of the program. Contact pressure histories were determined for one dimensional impact employing the MRC version of the PUFF74 stress wave response code for the surface of coated and uncoated PC configurations ballistically impacted by steel flyer plates of various sizes and incident velocities. For this initial analysis the thickness of the PC substrate was taken to be 0.635 cm (0.25 inches). Plexiglass (PMMA) coatings of 0.05 and 0.2 inches as well as various interface conditions between the PMMA and PC substrate were employed (i.e., fusion bonded or 0.01 inches of silicone adhesive). The pressure histories were then used as input conditions for the stress wave analysis conducted in Task 3.

Pressure histories were determined later in the program on thinner PC configurations employing elastic analysis and the AUTODYN two dimensional stress wave finite difference code for the surface of coated and uncoated PC configurations employing the 5.7 grain fragment simulating projectile. In this analysis the PC coating was assumed to be 2 mm thick and the coating was nominally assumed to be PMMA which is a well characterized material with mature stress wave material response models. PMMA also has a high Brinnell hardness with properties representative of a PC coating that might be employed for abrasion resistance.

The elastic analysis assumes that the interface pressure generated from the collision of two finite thickness plates can be described by the intersection of two Hugoniot. A Hugoniot describes equilibrium states of the material in terms of internal energy, pressure, and specific volume. The Hugoniot may be rendered in several forms including pressure as a function of particle velocity. The Hugoniot associated with the target (material B) can be described in pressure versus particle velocity space by a straight line: $P = Z_B v$ where Z_B is the impedance (density multiplied by sound speed) of material B. The second Hugoniot associated with the impactor (material A) can be described by a straight line with a negative slope in particle velocity versus pressure space: i.e.,

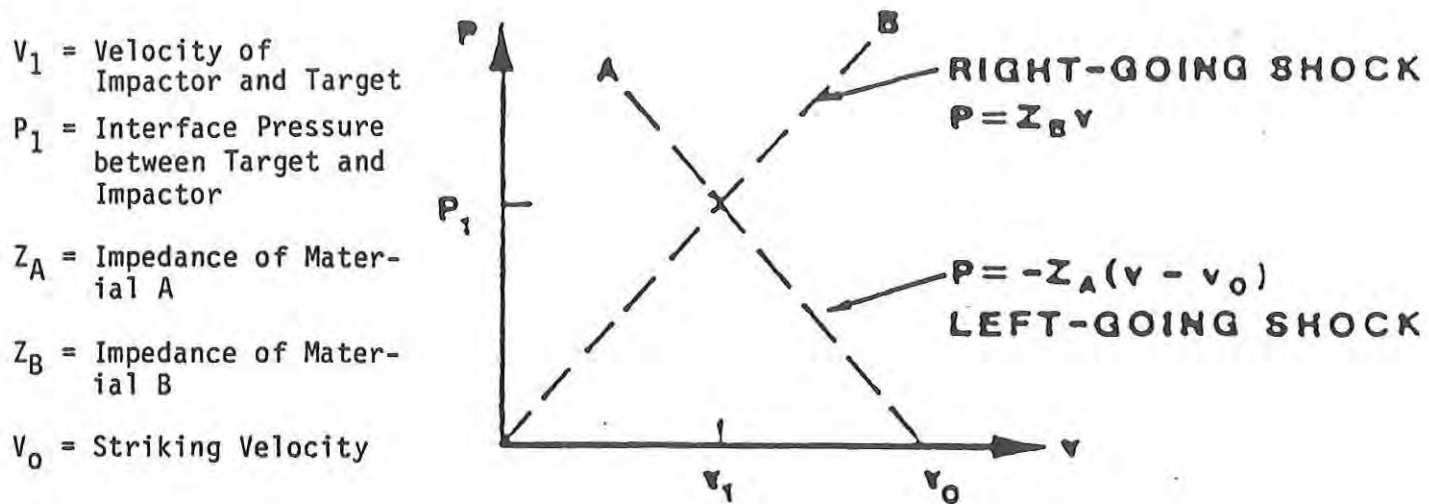


Figure 14. (P,v) Hugoniots for Collision of Two Materials of Finite Thickness.

$P = -Z_A(v - v_0)$ where Z_A is the impedance of material A and v_0 is the incident velocity (See Figure 14).

At the instant of impact, the particle velocities of materials A and B are equal to v_1 . Thus

(1a and b) $P_1/Z_B = v_1$ and $P_1 = -Z_A(P_1/Z_A - v_0)$.

Rearranging the terms above and solving for the interface pressure, P_1 , yields

(2) $P_1 = v_0 Z_A Z_B / (Z_A + Z_B)$.

The relevant material properties for steel, polycarbonate, and PMMA are shown in Table 4.

Table 4. Bulk Sound Speed, Density and Calculated Impedance for Steel, Polycarbonate, and PMMA.

	Bulk Sound Speed (10^5 cm/sec)	Density (gm/cc)	Impedance, Z (10^5 g/(sec-cm ²))
Steel	4.62	7.750	35.805
Polycarbonate	1.93	1.193	1.423
PMMA	2.22	1.184	2.63

For an incident velocity of 0.02 cm/microsec (656 ft/sec) using the properties shown in Table 4 and Equation 2, the interface stress associated with the impact of steel on polycarbonate is 2.74 kbar as compared with 4.9 kbar (79% difference) associated with the impact of steel on PMMA. For the PMMA/PC interface (front surface) the transmission and reflection coefficients

for the stress waves are calculated to be 0.702 and -0.298, respectively, as compared with the PC/PMMA interface (rear surface) where the transmission and reflection coefficients are determined to be 1.298 and 0.298 respectively. The net result is a 25% larger compressive stress in the substrate at the PMMA/PC interface (3.43 kBar) as compared with the corresponding location in the uncoated PC (i.e., at the front surface of the PC, 2.74 kbar).

In the coating, 1.46 kbar of the original stress pulse would be reflected back into the coating. This reflection and transmission process will continue in the coating and result in a high frequency component to the force-time history impinging on the substrate. This high frequency component will have amplitudes which decrease monotonically with time in proportion to the coating-substrate interface reflection and transmission coefficients. If the acoustic length (bulk sound speed multiplied by contact time) of the coating and projectile are related by a low integral number, the stress wave reflected off of the free surface of the projectile could superimpose constructively or destructively with reflected stress waves in the coating. These cases are schematically compared with the force time history that would be evident on an uncoated polycarbonate sample (see Figure 15).

The reflection and transmission coefficients of the various interfaces are shown in Table 5. If s_o is the stress level from the incident wave, a_s and b_s are the stress levels for the corresponding transmitted and reflected waves. This indicates that the steel/PMMA interface will transmit approximately twice the stress from each traversal of the stress wave reflected from the free surface of the projectile to the contact region as compared with the steel/PC interface. Ignoring contributions from reflected waves in the coating, the force time history in the coated sample will indicate high interface pressures which dissipate rapidly as compared with uncoated polycarbonate.

Table 5. Transmission and Reflection Factors for Different Interfaces.

Interface	PMMA/PC	PC/PMMA	Steel/PC	Steel/PMMA
Transmission, a	0.702	1.298	0.0765	0.137
Reflection, b	-0.298	0.298	-0.923	-0.863
Impact Stress, s_i	----	----	2.74 kbar	4.9 kbar
Transmitted Stress, s_t	3.43 kbar	----	----	----
Reflected Stress, s_r	1.46 kbar	----	----	----

If the amplitudes of the high frequency component of the force time history are sufficiently high and the imposed strain rates sufficiently low, plastic strain can accumulate with each cycle of the forcing function. This is indicated schematically in Figure 16. The stress, s , during the n th cycle can be represented by Equation (3).

$$(3) \quad s^{(n)} = s_e^{(n)} + s_p^{(n)};$$

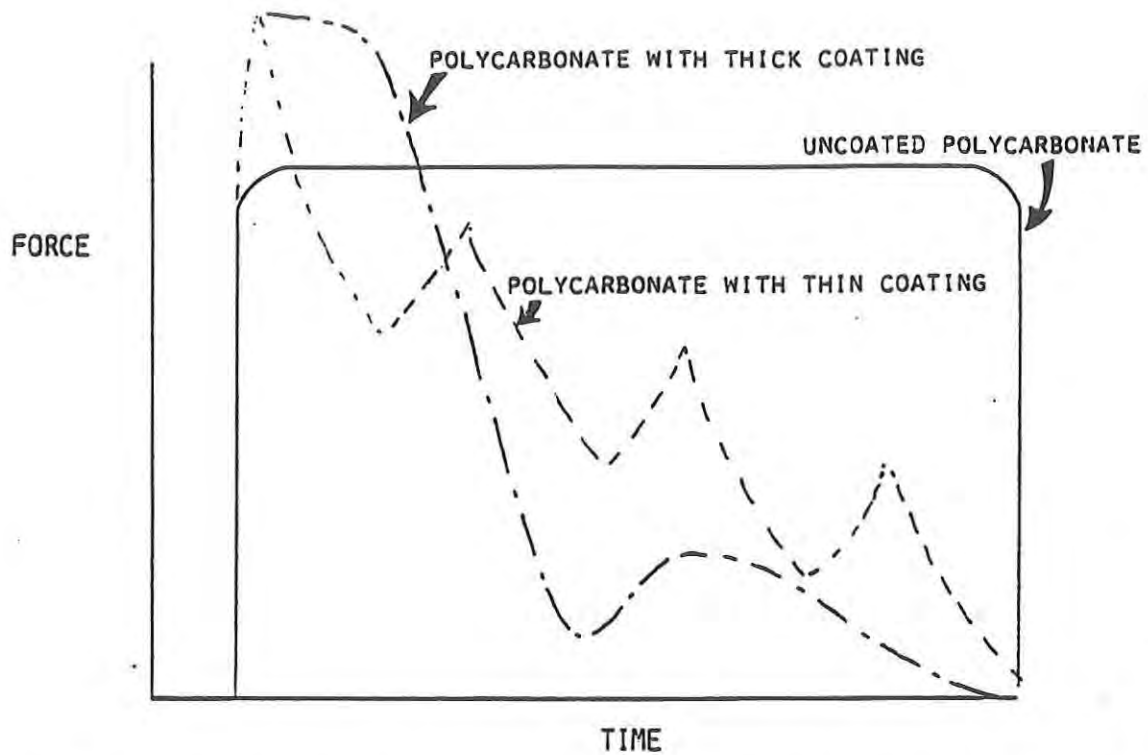


Figure 15. Force-Time History on Polycarbonate for Nominal Projectile Length: (a) Acoustically Thin Coating; (b) Acoustically Thick Coating; and, (c) Uncoated Polycarbonate.

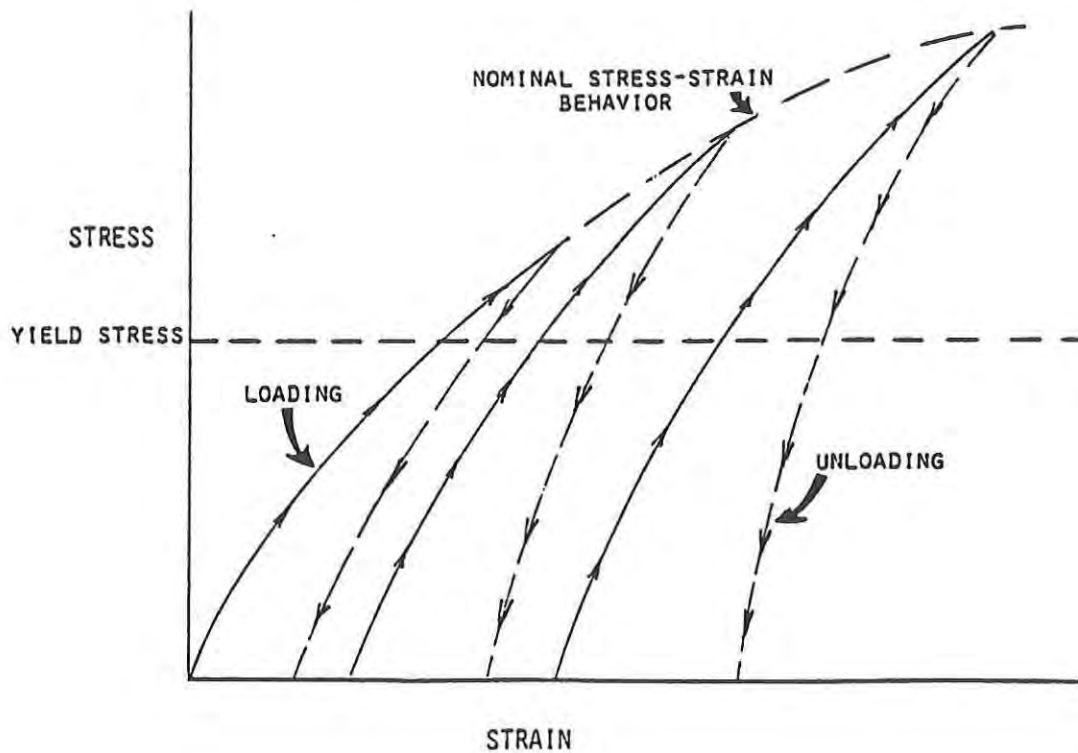


Figure 16. Plastic Strain Accumulation during Stress Reversals.

where the subscripts 'e' and 'p' represent elastic and plastic contributions to total stress. As the number of cycles which exceed the yield stress, s_y , increase, the plastic strain increases, resulting in a locally elevated stress state. This argument assumes: (1) That the incident velocity is sufficiently low that material inertia is governing the penetration process -- i.e., low residual velocity of the projectile following penetration; and, (2) The strain rate is sufficiently low that the material can "flow" inelastically.

The material will fracture if $s^{(n)} > s^{(c)}$ where $s^{(c)}$ is a critical fracture strength. Rewriting Equation (3),

$$(4) \quad s_p^{(n)} > s^{(c)} - s_e^{(n)}.$$

In Equation 4, the first term can increase with n if $s^{(n)}$ is greater than the strain rate sensitive s_y , the second term decreases (due to material degradation) or remains approximately constant, and the third term remains constant. For a nominal projectile and high impedance coating material (compared to polycarbonate), a high peak stress will be evident in the force time history, which can initiate cracking. This high peak stress will be followed by lower amplitude stress reversals which can promote inelastic strain accumulation. This is as opposed to the force time history associated with an uncoated polycarbonate specimen which will tend to manifest a lower stress level with a long pulse duration. If the coating material is sufficiently thin that the frequency of the stress reversals results in a strain rate where the material can not inelastically flow then $s_p^{(n)}$ may not increase with n and the differences associated with the force time histories associated with coated and uncoated polycarbonate samples may not be consequential.

The implications of the above are alluded to in Figure 17 based on experimental data [Wheeler, 1972 and Knopoff, 1989] which shows the effect of superimposing occasional overloads and/or underloads on a nominal load spectrum in terms of crack growth as a function of load application (i.e., increasing n). The nominal load spectrum results in inelastic strain accumulation and gradually increasing stress levels, consistent with the hysteresis effect shown in Figure 16. Crack growth therefore follows a fairly well defined curve. An overload has the effect of raising the critical fracture stress, $s^{(c)}$, of the material. This is because the stress level at the crack tip is proportional to the crack length. In an overload situation the crack extends beyond the length it would have had at the nominal stress level. When the stress is suddenly reduced, the stress associated with the crack tip is reduced well below the critical level necessary for crack extension at the longer crack length associated with the overload condition. In order for the crack to extend at the reduced stress levels associated with the nominal spectrum, inelastic strain must accumulate at the crack tip such that the local crack tip stress levels exceed the critical stress at the overload condition. The interval of load applications where plastic strain accumulates corresponds to the plateau shown in Figure 17 between the first and second overload. When sufficient plastic strain has accumulated such that the associated stress exceeds the critical stress in the overload condition, crack extension will resume at an accelerated rate. In an underload situation, the crack is larger than it would otherwise be at the lower stress level. The critical stress required for crack growth is therefore less than the nominal value. When the higher stress levels associated with the nominal spectrum are applied, crack growth proceeds at an elevated rate without interruption.

It should also be noted from Table 4 that the acoustic length of the fragment simulator (approximately a right circular cylinder 0.442 cm in length and 0.38 cm in diameter) and the polycarbonate substrate (nominally 2 mm thick or 2.032 mm thick with a coating on both sides) are

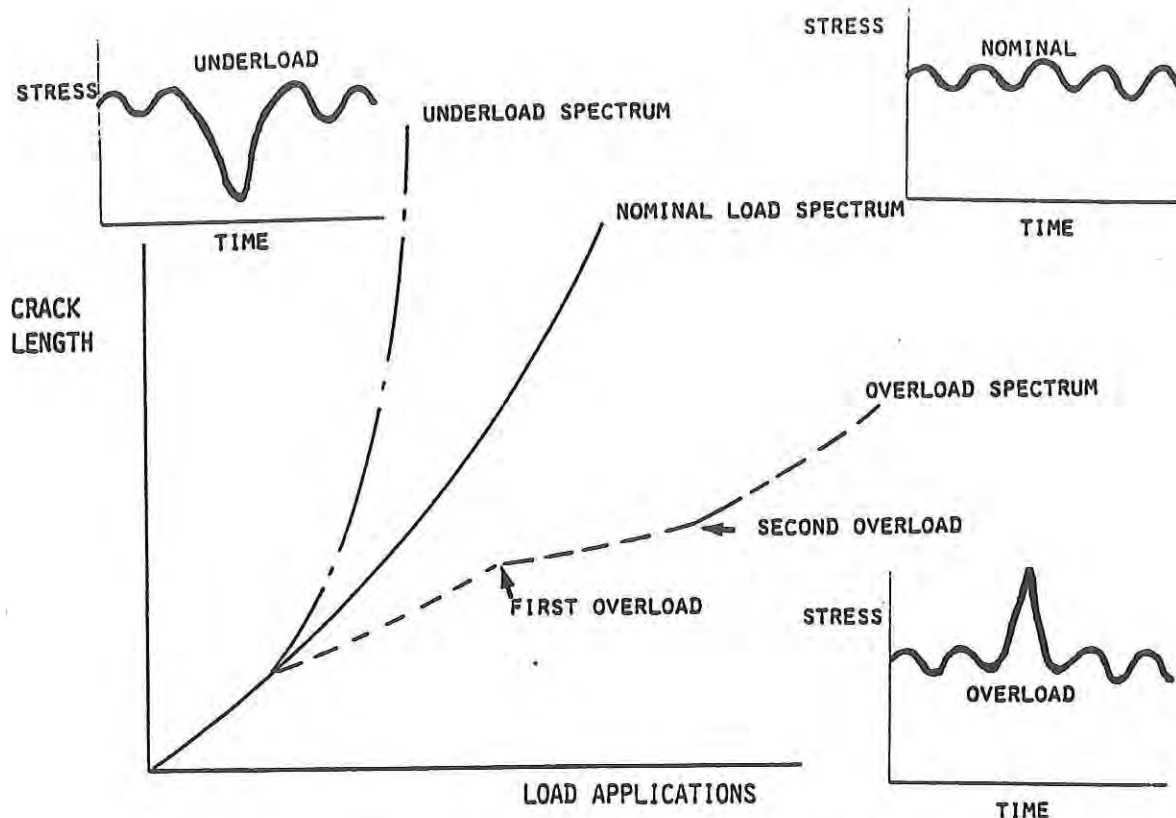


Figure 17. Effect of Load Spectrum on Crack Growth.

approximately the same. This means that the arrival time of the tensile pulse reflected off the rear free surface of the projectile and the tensile pulse reflected off the rear free surface of the polycarbonate target are approximately equal for a location in the middle of the substrate. This is an unusual situation which results in the two reflected tensile pulses superimposing and locally producing very high stresses creating a "worst case" situation from the standpoint of substrate damage.

Table 6 compares the various analytical tools employed to estimate contact pressure between the target and projectile. Table 7 presents results for the low and high velocity impact conditions on uncoated PC targets, PC targets with thin PMMA coatings, and PC targets with thick PMMA coatings on the impact surface. The results are remarkably consistent. The PUFF analysis typically yields the largest front surface pressures since it is one dimensional and employs a nonlinear Hugoniot. The AUTODYN analysis will yield lower front surface pressures than PUFF results since hydrodynamic attenuation of the stress pulse by two dimensional effects is included in the AUTODYN model. The AUTODYN analysis was also conducted employing the Shock equation-of-state which represents the shock velocity as a linear function of particle velocity as opposed to the Mie-Gruneisen equation-of-state employed in PUFF. The difference in these equation-of-state formulations is insignificant for the impact velocities being considered.

For the low velocity impacts investigated, the PMMA coated targets tend to give consistently higher contact pressures regardless of the analysis technique employed. For the high velocity impacts considered, the linear elastic and PUFF predictions for contact pressure yield substantially higher stress for the PMMA coated PC targets than the uncoated PC targets. This trend is not reflected in the corresponding AUTODYN results, however. This is presumably due to the fact that the

Table 6. Comparison of Analytical Methods Employed for Prediction of Contact Pressures.

Analytical Method	Linear Elastic Theory	PUFF74	AUTODYN
Model Assumptions - Material Response - Stress Field - Penetration	o Linear Elastic o One Dimensional o No Penetration	o Nonlinear Elastic o One Dimensional o No Penetration	o Elastic-Plastic o Two Dimensional o Models Penetration
Projectile - Material - Configuration - Size	o Steel o Infinite Half Space o N/A	o Steel o Infinite Plate o 0.05, 0.25, & 1.25 inches thick	o Steel o Cylinder o 5.7 grains
Targets	o Uncoated PC Infinite Thickness o PMMA coated PC Infinite Thickness o Interlayers of Various Types & Thicknesses	o Uncoated PC 0.25 inches thick o PMMA Coated PC .05 & .2 in. thick	o Uncoated PC 2 mm thick o PMMA Coated PC .007 & .035 cm thick
Incident Velocities (cm/sec)	o Contact Pressure Scales Linearly with Velocity	o 600 o 6,000 o 60,000	o 2,000 o 20,00

Table 7. Comparison of Analytical Predictions for Peak Contact Pressure.

Target	UNCOATED PC			THIN PMMA COATING			THICK PMMA COATING		
Analytical Method	Linear Elastic Theory	PUFF	AUTODYN	Linear Elastic Theory	PUFF	AUTODYN	Linear Elastic Theory	PUFF	AUTODYN
Resulting from Low Velocity Impact (2,000 cm/sec)									
Peak Contact Pressure (kbars)	0.3	0.4	0.3	0.5	0.5	0.5	0.5	Estimate 0.5	0.5
Resulting from High Velocity Impact (20,000 cm/sec)									
Peak Contact Pressure (kbars)	3	Estimate 7.4	5.4	5	Estimate 9.7	4.8	---	---	---

Linear Elastic and PUFF analysis was conducted without accounting for material damage; i.e., the respective targets had infinite strength.

The AUTODYN analysis employed a 1 kbar dynamic tensile strength for the PMMA coating. When regions of the coating are predicted to fail, the reflected tensile wave from the PMMA-PC interface causes failed segments of the coating to recoil from the PC target, which reduces the total momentum of the projectile and target system. Additionally, the failure process associated with the coating consumes a portion of the projectile energy deposited in the target material, which might otherwise be converted to stress.

If the coating was thicker such that it could not fail and/or the coating segments were not allowed to be detached from the substrate, then the results might be more consistent with the PUFF analysis. This is also consistent with experimental results from plummet tests conducted by Huyett and Wintermutte [1976] where PMMA coatings were bound to PC substrates employing different bonding techniques and agents. In the case where the bonding agent was sufficiently strong to prevent flyoff of the coating following coating failure, the drop height required to produce brittle failure was lower than the drop height required to cause brittle failure in targets where coating flyoff was not suppressed by the coating-substrate interface.

2.2 Task 2 - Definition of Polycarbonate and Coating Combinations.

Pursuant to guidance from the technical monitor, Dr. Healy, we have assumed a ballistic goggle lens as a nominal configuration for the polycarbonate and coating. This results in a 2 mm thick substrate with a coating estimated to be not more than 0.016 mm on each surface of the goggle. Because the coating employed on the goggles is proprietary, we have assumed for the purpose of our analysis that it is similar to PMMA, which is a mechanically, very well-characterized material, is often employed as a coating on polycarbonate, and presumably is representative of a coating material due to its high abrasion resistance. PMMA also has a low strain to failure, modulus and tensile strength, which is similar to polycarbonate, and facilitates a ductile to brittle failure transition in polycarbonate when used as a coating.

2.3 Task 3 - Stress Wave Response Analysis.

Efforts relative to defining the role of stress wave response in promoting a ductile to brittle transition were fourfold. First, based on existing experimental data from the Los Alamos National Laboratory [Marsh, 1980] and the Stanford Research Institute [Curran and Shockley, 1973], an equation-of-state material response model for polycarbonate was developed. The second effort concerned employing the MRC version of the PUFF74 code to evaluate the one dimensional impact of steel flyer plates of various thicknesses on 0.25 inch thick polycarbonate targets with and without PMMA coatings of various thicknesses and interlayer types. The third effort involved implementing two-dimensional stress wave models for a 0.02 and 0.002 cm/microsecond impact of a 5.7 grain cylindrical steel fragment on rigidly attached PMMA coatings and uncoated 2 mm thick polycarbonate using the AUTODYN finite difference code and closed form elastic solutions. Finally, two dimensional stress wave analysis of uncoated and thinly coated PC in the presence of a geometric discontinuity was implemented. These efforts are discussed in Sections 2.3.1 through 2.3.3.

2.3.1 Equation of State Modeling and One Dimensional Stress Wave Response. One-dimensional

hydrocode calculations were performed in order to: (1) Provide a data base for correlating and validating two-dimensional calculations; (2) Develop an understanding of the stress wave response of ballistically impacted polycarbonate and the influence of adhesively bonded and solvent fused coatings, and (3) Evaluate and modify existing material response models to include relevant physics models.

An initial set of calculations was performed using the PUFF74 material response code [Cecil and Newlander, 1976] and model parameters documented in a Stanford Research Institute (SRI) report [Curran and Shockey, 1973]. The PUFF74 code is a one-dimensional Lagrangian finite difference code, which solves the standard set of hydrodynamic equations. The code has models which calculate the effects of elastic-plastic, visco-elastic, visco-plastic, and porous behavior. The SRI response model was simply hydrodynamic, although it measured both longitudinal and shear wave acoustic velocities and a yield stress. The derived cubic fit to the hydrostat contained a negative quadratic term, which generally indicates that an elastic-plastic model may be more appropriate.

An initial set of calculations was completed as detailed in Table 8. These calculations investigated the stress wave response of a polycarbonate layer impacted by a steel projectile as a function of impactor velocity and thickness.

Table 8. Parametric One-Dimensional Hydrocode Calculation Configurations

Target Thickness (inch)	Projectile Thickness (inch)	Velocity (cm/sec)	Figure Number
0.250	0.05	600	A.1
0.250	0.05	6000	A.2
0.250	0.05	60000	A.3
0.250	0.25	600	A.4
0.250	0.25	6000	A.5
0.250	0.25	60000	A.6
0.250	1.25	600	A.7
0.250	1.25	6000	A.8
0.250	1.25	60000	A.9

The calculated stress-time histories at various locations within these configurations are shown in the indicated figures included in Appendix A.1. The histories are presented for the following locations: half-way through the steel impactor, at the steel/polycarbonate interface, one-third through the polycarbonate, and two-thirds through the polycarbonate. The results indicate relatively wide stress wave pulses, which travel through the thin polycarbonate layer without attenuation and whose details are dependent upon the specific thicknesses of the target and projectile. The calculations indicate that for the model used, the two lower impact conditions can be considered linear, in that the calculated stresses can be simply scaled by the impact velocities. In evaluating the calculations involving the higher velocity impact condition, it was determined that the SRI stress wave model was not accurate at the higher stress (> 10 kbars) conditions and greatly over predicted the unloading velocities (and hence potential hydrodynamic attenuation). This inaccuracy could lead to unrealistic stress histories in the target configurations.

Because the SRI model was not accurate at the higher velocities, and because it did not include the effects of yielding and plasticity, a small effort was initiated to develop a more satisfactory model. The new MRC model was based upon acoustic wave velocities and higher stress level Hugoniot data reported by Los Alamos National Laboratories [Marsh, 1980]. The MRC model is self-consistent, includes yielding, and matches the SRI model at low stress conditions and the LASL data at the higher stress conditions. The resulting Hugoniot is presented in Figure 18 in terms of stress versus condensation or change in density (ρ is density in Figure 18) and compared with existing models and data. The new MRC model will match the results from the SRI model at low impact velocities and will produce lower stress and more consistent results at the higher velocities.

Calculations were performed using the MRC model to investigate the effects of coatings and attachment techniques upon the generated polycarbonate stress wave response. Figure A.10 presents the stress-time histories in a configuration which included a 0.05 inch thick fused-bonded PMMA coating. The results show a tensile stress wave traveling through the polycarbonate which is the result of the shock impedance mismatch between the PMMA and the polycarbonate. This feature is also present in Figure A.11 where the PMMA thickness has been increased to 0.20 inches which suggests that this relatively high magnitude (> 0.5 kbar) tensile stress is independent of the PMMA coating thickness.

The results of a final calculation are presented in Figure A.12 which show the stresses for a 0.05 inch PMMA coating which is bonded to the polycarbonate with a thin (0.010 inch) silicone rubber adhesive layer. This layer disturbs the structure of the compressive stress wave and significantly reduces the tensile stress seen in Figures A.10 and A.11. These results clearly show that the one-dimensional stress histories are dependent upon the acoustic shock properties of the layer materials.

2.3.2 Two Dimensional Stress Wave Response. Two dimensional stress wave analysis was implemented using the AUTODYN finite difference code employing a 5.7 grain cylindrical steel projectile normally impacting a 2 mm polycarbonate target with and without PMMA coatings. The incident velocities considered were 0.02 and 0.002 cm/microsecond (i.e., 657 and 65.7 ft/sec). The target configurations evaluated were: (1) An uncoated polycarbonate material; (2) A 0.007 cm PMMA coating on both sides of the polycarbonate substrate; and, (3) A 0.035 cm PMMA coating on the impact surface and a 0.007 cm PMMA coating on the back surface of the PC target. The last configuration employing the thick front surface PMMA coating was evaluated only for the low velocity impact condition.

The projectile was modeled using a Lagrangian grid and the target was modeled using an Eulerian grid. A global and enlarged view of the model is shown in Figures 19(a) and (b). The "target points" or locations where the velocities, densities, and stresses were post processed are shown in Figure A.13 for the high-velocity impact and Figure A.23 for the low-velocity impact. The models were executed for a constant thickness but with material properties corresponding to PMMA for the first five and last five rows of elements, which represent the presence of a coating. For the uncoated model the PMMA properties were replaced with those of polycarbonate. The dynamic tensile strength of the PMMA is well established (about 1 kbar) and in the analysis was permitted to fail. The dynamic tensile strength and the appropriate failure condition of PC are not well established hence the PC was not allowed to fail. This prevention of failure was accomplished by prescribing an

infinite tensile strength for PC in the analysis. The aim of the analysis during Phase I was to gain some gross insight as to how the stress states in the PC substrate developed and how they might be correlated with the ductile to brittle transition in the mechanical behavior of PC subject to ballistic impact.

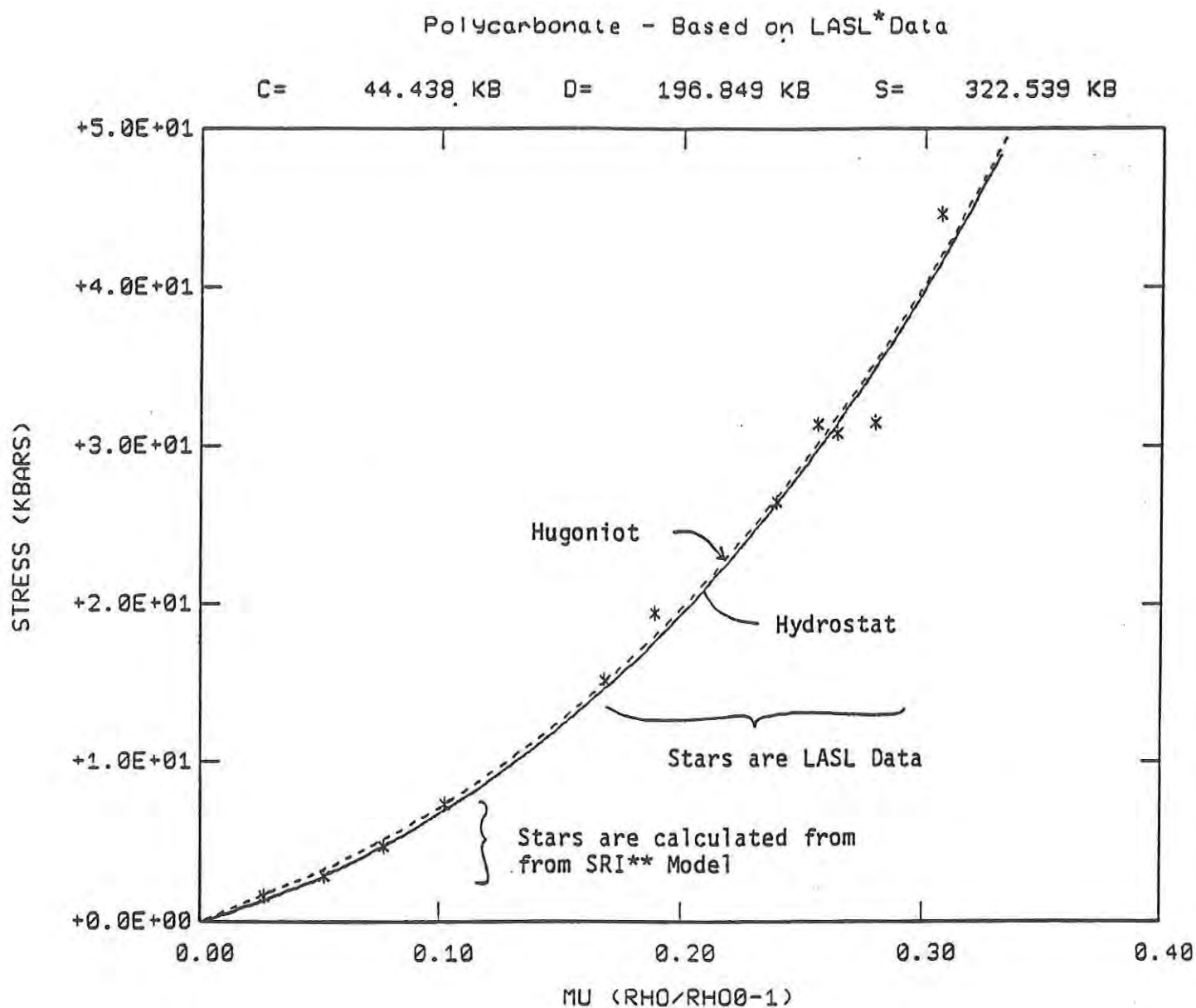


Figure 18. MRC Equation-of-State Model for Polycarbonate.

*Los Alamos Scientific Laboratory

**Stanford Research Institute

PROJECTILE/TARGET GEOMETRY

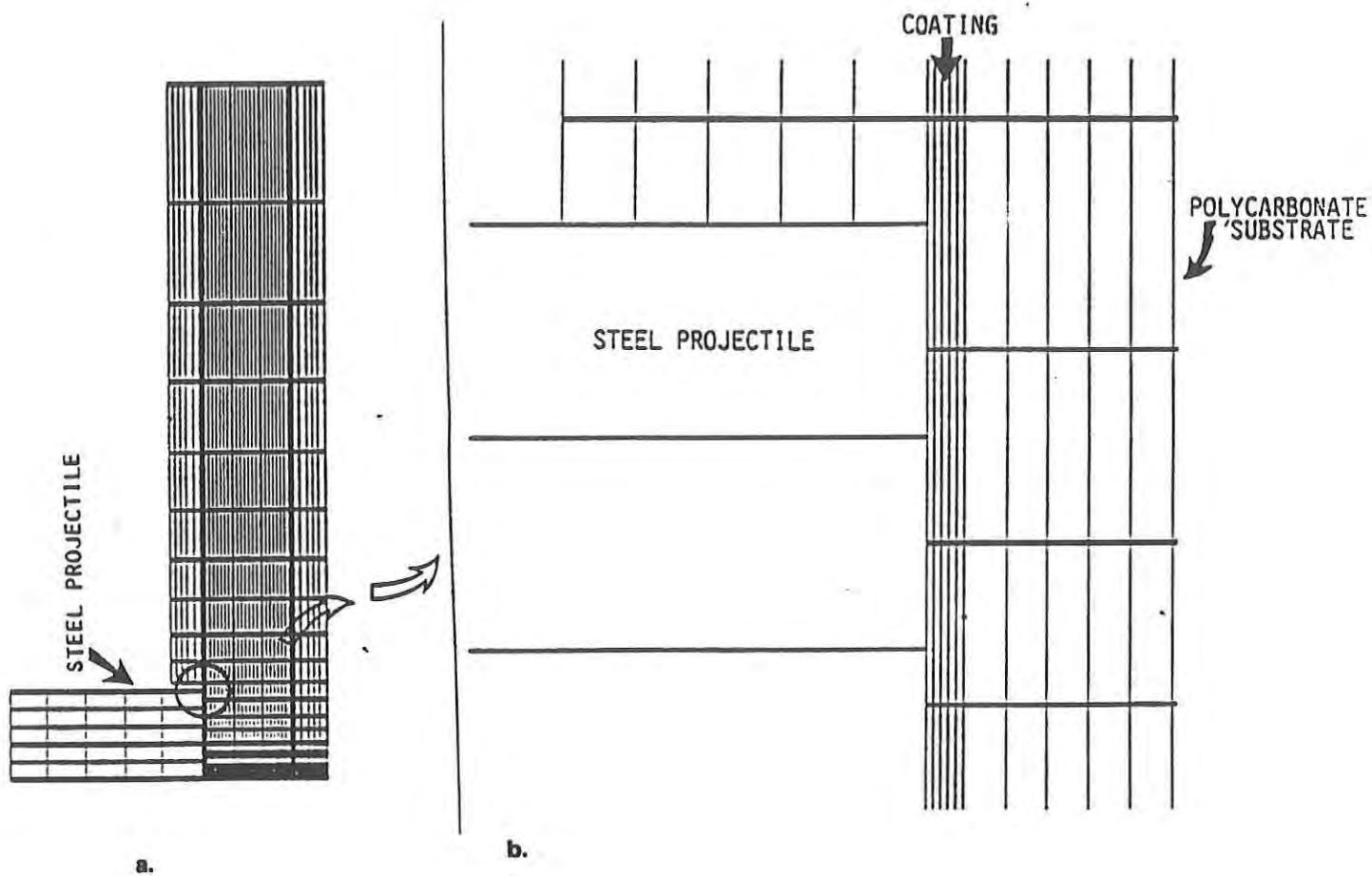


Figure 19. Finite Difference Model: (a) Global Model; and, (b) Enlarged Detail of Global Model.

HIGH VELOCITY IMPACT. Figures A.14(a) and (b) show particle velocities for the projectile in the impact direction corresponding to an incident velocity of 0.02 cm/microsecond. Target points 1 and 2 are toward the rear and impact surface of the projectile respectively. Time is represented in microseconds. Figures A.15(a) and (b) show a comparison between the particle velocities in the impact and radial directions associated with a target point located toward the rear of the PMMA impact surface. The radial particle velocity associated with the coated sample is considerably higher than the uncoated sample. As indicated in Table 4, this is due to the higher bulk sound speed of PMMA relative to PC. Corresponding results are shown in Figures A.15(c) and (d) for target point 6 located on the top surface of the substrate as well as target points 8 through 14 shown in Figures A.16, A.17, and A.18. For this condition, the results indicate that for both the uncoated and coated samples the velocity of the projectile will go to zero prior to complete penetration of the sample.

Figures A.19(a) through (f) show the pressure or dilatational component of stress as well as the in-depth (T_{xx}) and radial (T_{yy}) stress components in the projectile. Figure A.20(a) for target point 5 in the PMMA impact layer shows an initial pressure of about 5 kbars as compared with the corresponding location in the uncoated PC target which indicates an initial pressure of about 3 kbars. This initial difference in pressure between the two targets is due to the higher contact pressure generated in the PMMA coated target as compared with the uncoated PC target (see Section 2.1 and Table 7). The higher pressure in the coated specimen is rapidly truncated, however, due to the rapid penetration of the thin PMMA coating by the projectile. This mitigates the influence of the PMMA cladding and relieves coating stresses. Thus, Figure A.20 indicates that with the exception of this initial peak at the impact surface of the specimen the pressure or dilatational component of stress is significantly larger for the uncoated polycarbonate close to the impact surface. This is due to the fact that the PMMA coating fails dissipating some of the momentum and energy resulting from the projectile impact. The difference observed in the stresses near the impact surface of the two targets dissipates rapidly in-depth, as shown in Figures A.20(b) and (d) for target points 7 and 8 and Figures A.21 and A.22 for the in-depth (T_{xx}) and radial (T_{yy}) component of stress for target points 5, 6, 7 and 8.

In Figure A.21, the stress components for the PC substrate are shown in the impact and radial directions for both the uncoated and PMMA clad configurations. The stresses are shown to be well in excess of the assumed 1.6 kbar tensile strength of the PC material. Rearranging Equation 5,

$$\text{Pressure, } P = 1/3 (T_{\theta\theta} + T_{xx} + T_{yy}), \quad (5)$$

in terms of circumferential stress, i.e.,

$$T_{\theta\theta} = 3P - T_{xx} - T_{yy}; \quad (6)$$

it is clear given that the pressure, P, is positive at target points 5 and 6 (see Figure A.20) and the stress components in the impact (T_{xx}) and radial (T_{yy}) directions are tensile (see Figure A.21); the circumferential component of stress (T_{θθ}) will therefore be highly compressive. Since the principal tensile stresses are in the impact and radial directions, the most unstable direction in terms of crack propagation will be in direction perpendicular to these stress components, i.e., circumferential fracture (see Figure 9 and associated discussion).

This circumferential fracturing will occur on the order of the sound speed of the target

material (approximately 2 mm/microsec). At an incident velocity of 0.02 cm/microsec, the projectile will penetrate the target at a rate which is at least a factor of ten slower than the acoustic velocity of the target. Thus, the circumferential cracking will precede the arrival of the projectile. The large diameter circumferential cracks extend and eventually intersect resulting in a large diameter plug of material being formed in the substrate. As the projectile begins to penetrate the substrate, the large diameter plug displaces as a rigid body and travels at the same velocity as the projectile. Since shear forces at the projectile-target interface are not developed through this process, ductile penetration of the target by the projectile does not occur or is arrested resulting in a premature brittle failure of the target. This is consistent with posttest observations following ballistic testing in Task 5 (see Section 2.5 and Appendix C).

LOW VELOCITY IMPACT. AUTODYN results for the 0.002 cm/microsec impact indicate that the target material is behaving elastically and that pressures and stresses in the PMMA-clad PC targets are about 80% larger than the corresponding locations in the uncoated PC targets. This difference persists for several microseconds unlike results for the high velocity impact condition where the thin PMMA cladding is penetrated almost immediately, truncating the initially higher contact pressure in the PMMA-clad targets.

Figure 20 for target point 5 (see Figure A.23) and Figures A.28 through A.39 show that the pressures and principal components of stress for the uncoated PC targets are all below the tensile strength of the PC material. For the PC target with the thin PMMA cladding, Figure 20 shows for a location near the PMMA impact layer-PC substrate interface that the pressure is negative, and the stresses in the impact and radial directions are positive. This suggests in conjunction with Equation 6 that tensile stress well in excess of the PC strength will develop in the circumferential direction. This high tensile stress can easily explain the radial cracking observed in the low velocity ballistic test conducted in Task 5 on a thinly clad PC target. The effect, however, is extremely local to the interface as is suggested by the analytical results in Figures A.28 through A.39 which either do not show this effect or do not show this effect to as great an extent. The experimental results shown in Figures 12 and 13 also indicate the effect of the interface is extremely local.

Figure 20 also shows that the uncoated and thickly clad PC targets exhibit positive pressures and tensile stresses in the impact and radial directions. Using Equation 6, this fact results in compressive circumferential stresses. However, the tensile stress in the impact and radial directions for the thickly clad PC target, as opposed to the uncoated PC, exceed the tensile strength of the PC, suggesting that circumferential failure will also tend to occur in the PC substrate for low velocity impact conditions. This fact is different than the phenomenology associated with the thinly clad PC targets where brittle failure is promoted at low impact velocities due to radial cracking.

This is consistent with the results from ballistic testing in Task 5 on the three thickly clad samples. These samples are designated in Table C.3 as samples 2-61, 2-64, and 2-65 and were subject to impact velocities of 686, 708, and 675 ft/sec respectively. Table C.5 indicates that the substrate in the samples subject to impacts at 686 and 675 ft/sec behaved in a ductile manner. The small increase in impact velocity associated with sample 2-64, however, was sufficient to promote a brittle failure due to circumferential cracking. Apparently, the PMMA layer employed on the thickly clad targets in Task 5 was sufficiently thick that the strength of the stress wave due to geometric dispersion is severely dissipated by the time it arrives at the substrate. The magnitude of the stress wave does not exceed the strength of the PC substrate at the lower velocities and barely exceeds the strength of the PC substrate at the higher velocity. The small difference in incident velocities

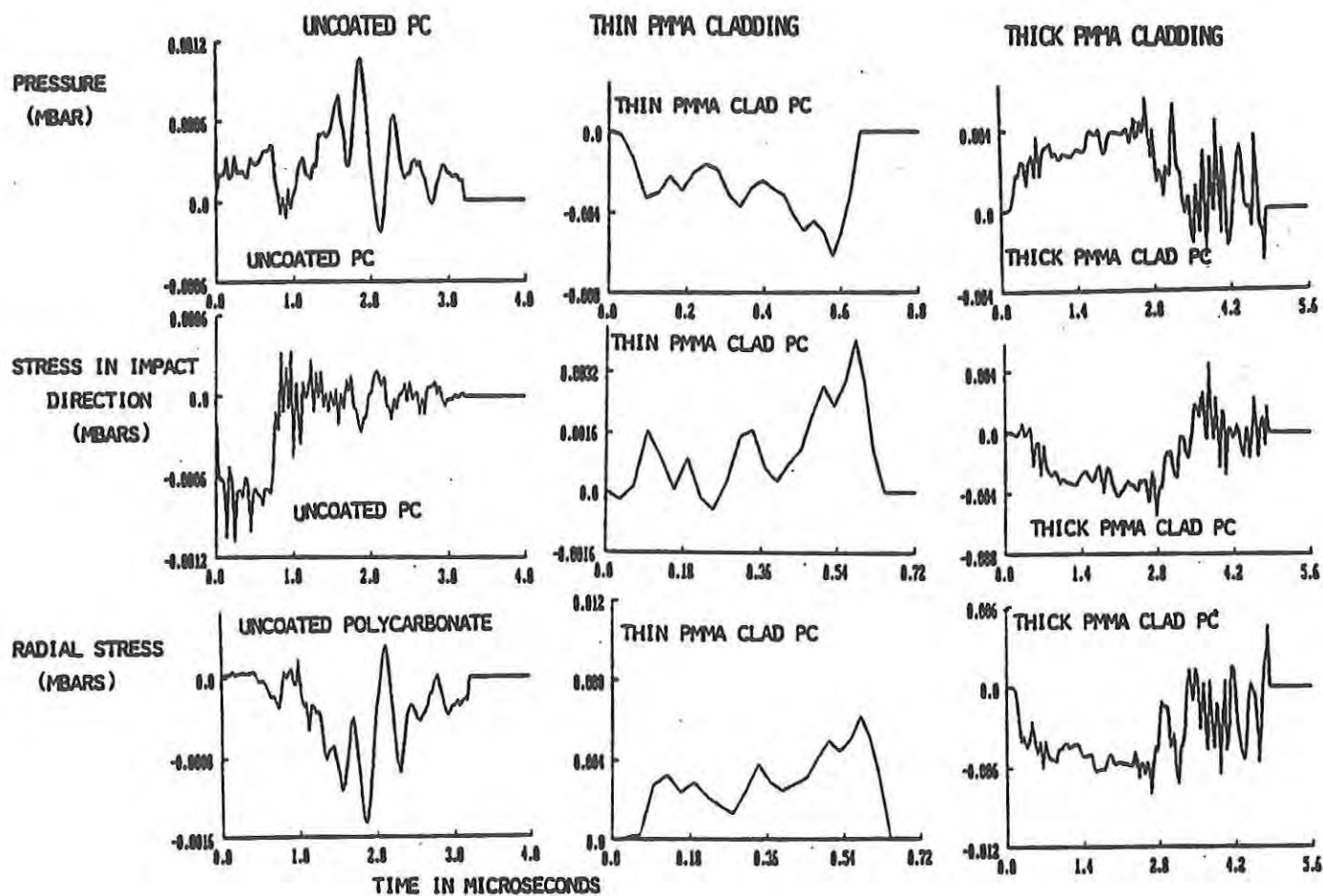


Figure 20. Pressure and Stress Components in the Radial and Impact Directions for 0.002 cm/sec Impact on Uncoated, Thinly Clad, and Thickly Clad PC Targets. Location is Adjacent to Impact Layer-PC Substrate Interface.

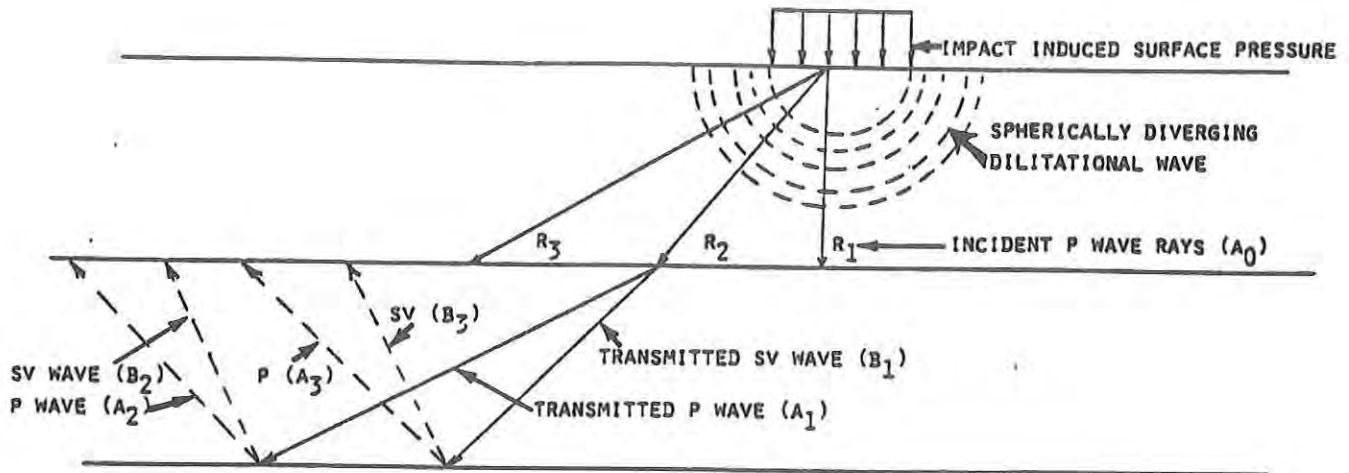


Figure 21. Reflected and Transmitted Waves Resulting from Impact with Two Layer Sample.

associated with the substrate behaving in a ductile versus a brittle manner suggests that intervening regime where radial cracking occurs (as observed analytically and experimentally for thinly clad targets) does not occur for more thickly clad targets.

To understand the source of the radial stresses discussed above, the problem shown in Figure 21 was considered. Figure 21 shows a two layer semi-infinite target. A cross-section of a compressive spherical pressure wave is shown propagating in the top medium which corresponds to the PMMA coating in our problem. Three rays, R_1 , R_2 , and R_3 , from the spherical pressure wave are shown. R_2 has an amplitude A_0 and is shown incident at the interlayer between the PMMA coating and polycarbonate substrate. In addition to reflected components of these p-waves (not shown), a compressive p- and sv-wave from the p-wave associated with R_2 is transmitted with amplitude A_1 and B_1 respectively and refracted some angle. Each of the transmitted waves are reflected as p- and sv-waves from the polycarbonate/rear PMMA layer interface. For a compressive wave incident at 90 degrees, the reflected wave at the rear PMMA/polycarbonate interface is in compression. The compressive wave then reflects off the PMMA impact layer/polycarbonate interface in tension (see Table 5).

There are three mechanisms associated with the above which directly affect the amplitudes of the radial components of the various stress waves reflected in the polycarbonate substrate. First, since R_2 is spherically diverging, the stress wave intensity associated with the p-wave incident at the interlayer between the polycarbonate substrate and PMMA impact layer will be inversely proportional to the square of the distance traversed, i.e., proportional to r^{-2} where r is the thickness of the PMMA layer. Since the thickness of the PMMA layer is constant, the intensity associated with the p-wave incident from the PMMA impact layer will be directly proportional to $\sin^2\theta$ where θ is the incident angle of the stress pulse (ignoring damping or viscoelastic effects).

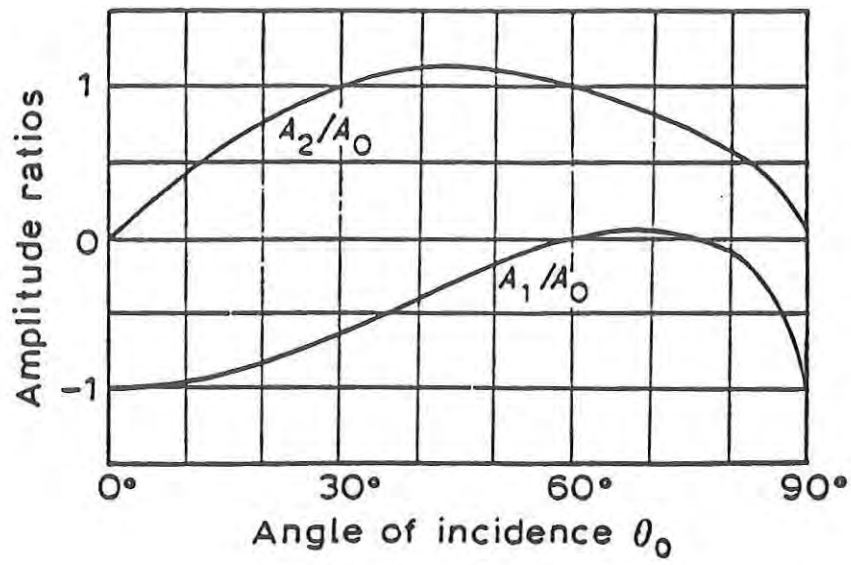


Figure 22. Amplitude ratios for the Reflection of a P-wave; Poisson ratio = 0.25. A_1/A_0 = relative amplitude of reflected P-wave. A_2/A_0 = relative amplitude of reflected SV-wave.

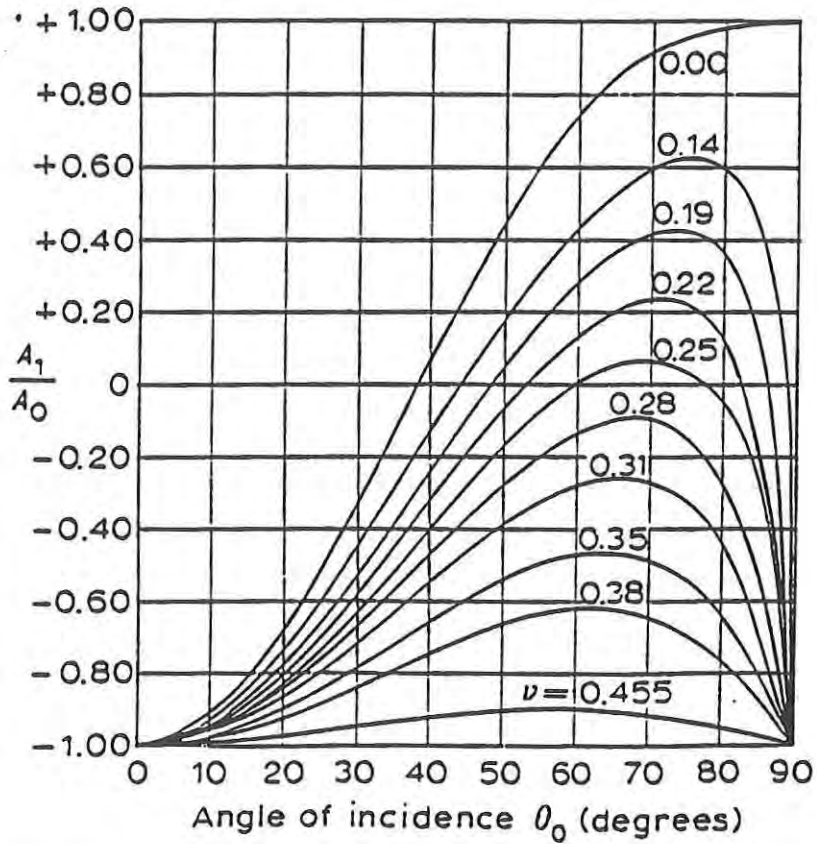


Figure 23. Relative Amplitude of P-wave for various values of Poisson Ratio, ν .

The second mechanism concerns the impedance at the interlayer, which is a function of incident angle and material properties as shown in Figures 22 and 23 from Arenberg [1948]. Figure 22 shows for an incident p-wave the amplitude ratio for reflection of a p- and sv wave from a free surface. In Figure 23 the Poisson ratio is constant at 0.25. Figure 23 shows the amplitude ratio of a reflected p-wave for different Poisson ratios.

It can be shown employing the respective potential functions [Achenbach, 1976; Brekhovskikh, 1980; and Ewing, 1957] that the radial component of reflected P-waves from the polycarbonate/rear PMMA layer interface is proportional to $[(c_s/c_l)^2 \cos^2 \theta - 0.5] V_{LL}$ where c_s and c_l are the respective shear and longitudinal wave velocities, θ is the incident angle (measured with respect to a normal vector from the surface), and V_{LL} is the reflection coefficient. Combining this expression with the attenuation due to spherical divergence yields for the radial stress component, S_r (derived from the P-wave) that it is proportional to

$$[(c_s/c_l)^2 \sin^2 \theta \cos^2 \theta - 0.5 \sin^2 \theta] V_{LL}. \quad (7)$$

The wave speeds are a function of the Poisson ratio, ν ; i.e., $(c_s/c_l)^2 = (1-2\nu)/[2(1+\nu)]$ and the reflection coefficients as previously shown (Figures 22 and 23) are a function of incident angle and Poisson ratio. Figure 24 shows a plot of the first two terms in brackets in Equation 7 assuming a Poisson ratio of 0.19. This ratio is suspect but is based on data in Curran and Shockey [1973]. According to data from Los Alamos National Laboratories [Carter, 1977 and Marsh 1980] the Poisson ratio is closer to 0.4. For high velocity impacts with low residual velocities, extensive plasticity occurs and the material is locally incompressible with Poisson ratios approaching 0.5. A Poisson ratio of 0.19, however, manifests the largest sensitivity for the first term in brackets from Equation 7.

Figure 24 shows for incident angles beyond 20 degrees that the second bracketed term in Equation 7 dominates. Figure 25 superimposes V_{LL} as a function of incident angle for different Poisson ratios on the plots shown in Figure 24. It is apparent that the angular dependence of V_{LL} at low Poisson ratios will dominate S_r in terms of developing tensile stresses. As the Poisson ratio increases, the sensitivity of the reflection coefficient to incident angle decreases.

Figure 26 superimposes the reflection factors as a function of incident angle for different Poisson ratios on plots of Equation 7 employing bounding values of Poisson ratio and divided by V_{LL} . The envelope associated with Equation 7 (without the influence of V_{LL}) is eclipsed by the apparent sensitivity of V_{LL} . Finally, Figure 27 plots Equation 7 in its entirety for different Poisson ratios to show the relative amplitude of P-wave radial stress components in the substrate relative to compressional P-waves incident on the PMMA impact surface.

For a layered medium, the reflection and transmission factors are functions of incident angle and impedances on adjacent material layers. However, the material properties associated with the layer impedances for a normal incidence angle are relatively constant at a specific point during the stress time history. This allows consideration of the amplitude ratios in terms of sensitivity to incident angle as is discussed above. The discussion above however ignores viscoelastic damping (or viscoelastic influence on Poisson ratio) and dispersion as well as the influence of the bond layer. The influence of the bond layer will be minimal however since the bond layer thickness relative to the incident pulse length is small. Finally, the argument above ignores angle changes due to refraction.

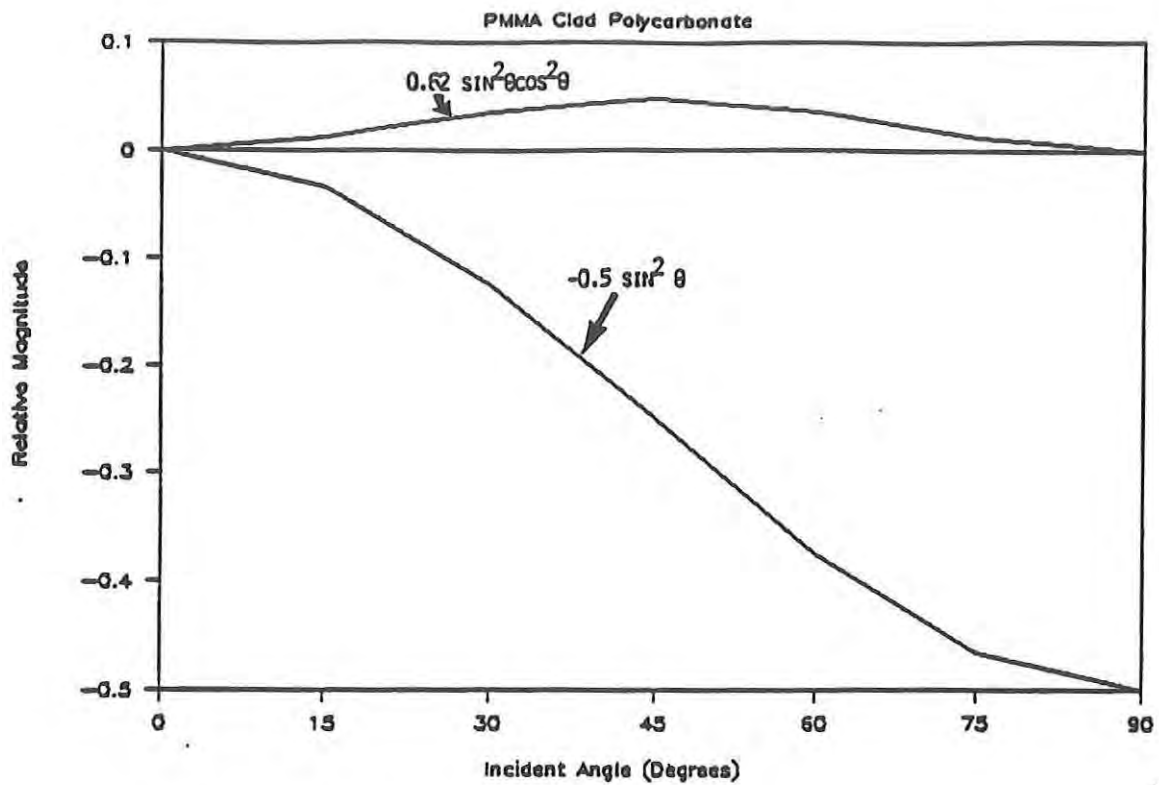


Figure 24. Relative Magnitude of P-wave Terms.

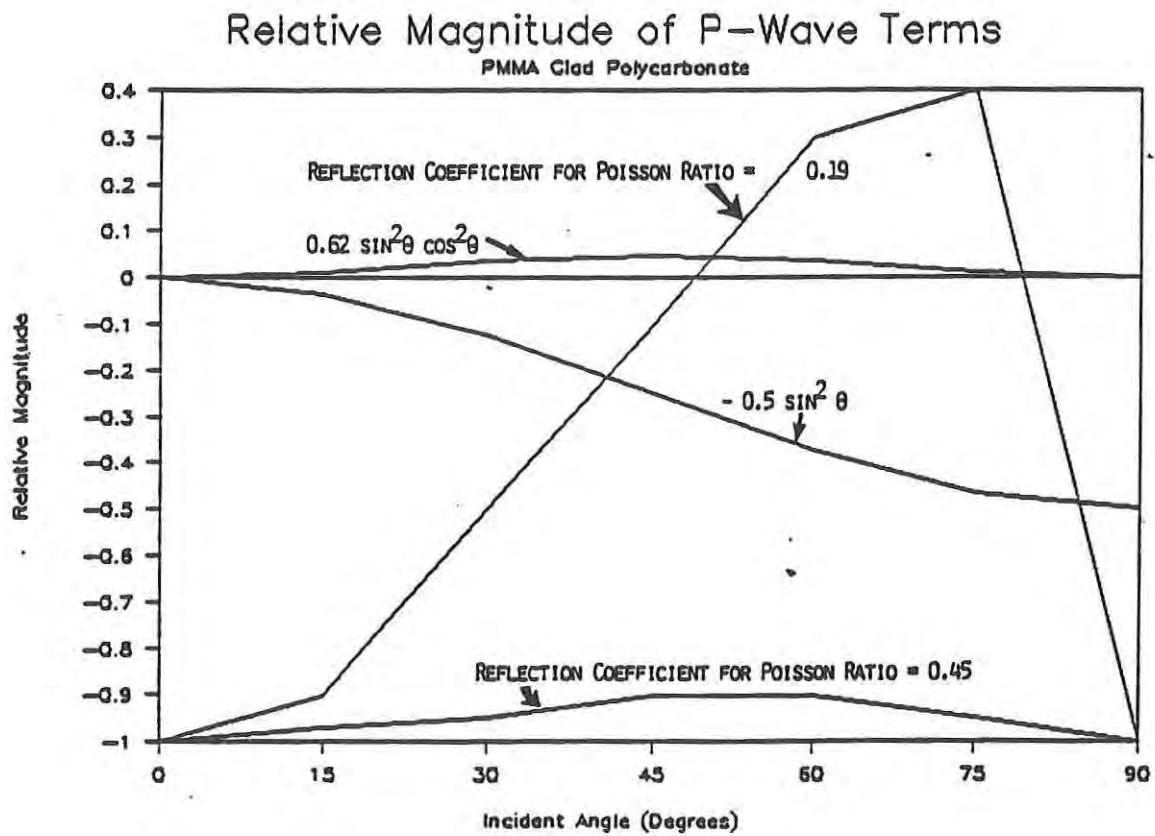


Figure 25. Relative Magnitude of P-wave Terms.

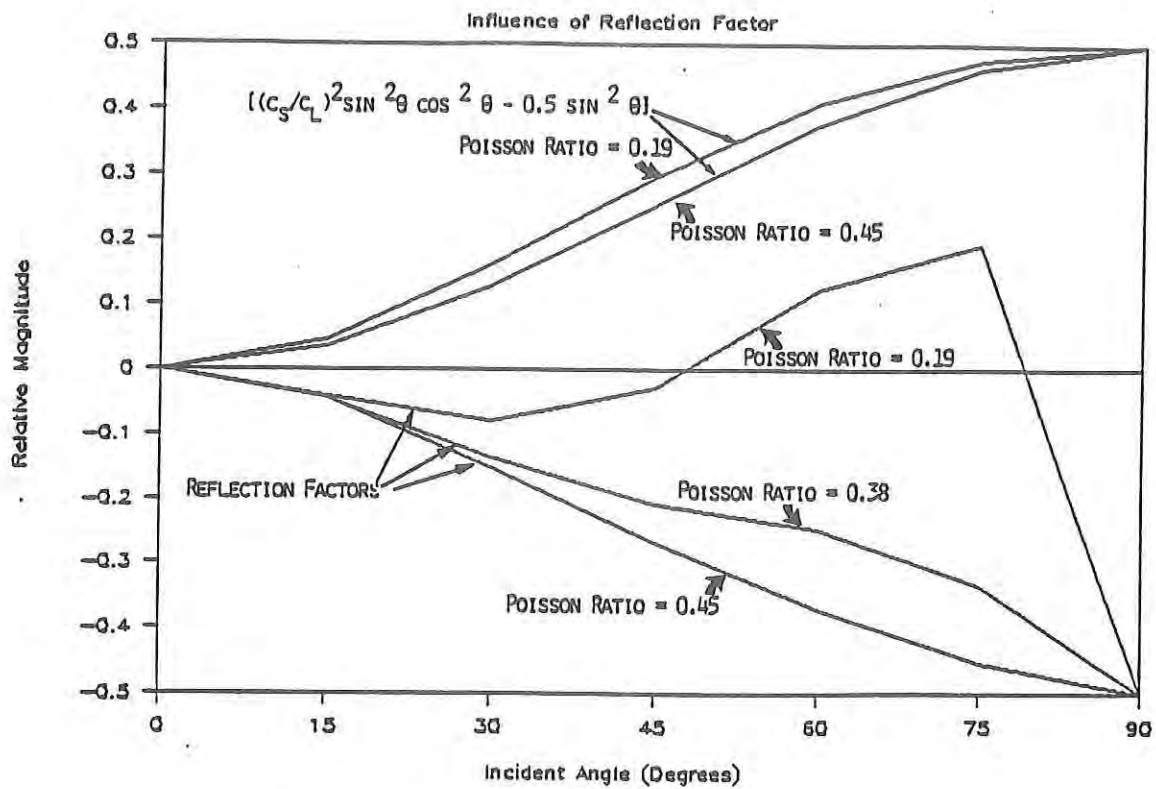


Figure 26. Relative Amplitude Ratio of P-wave Terms.

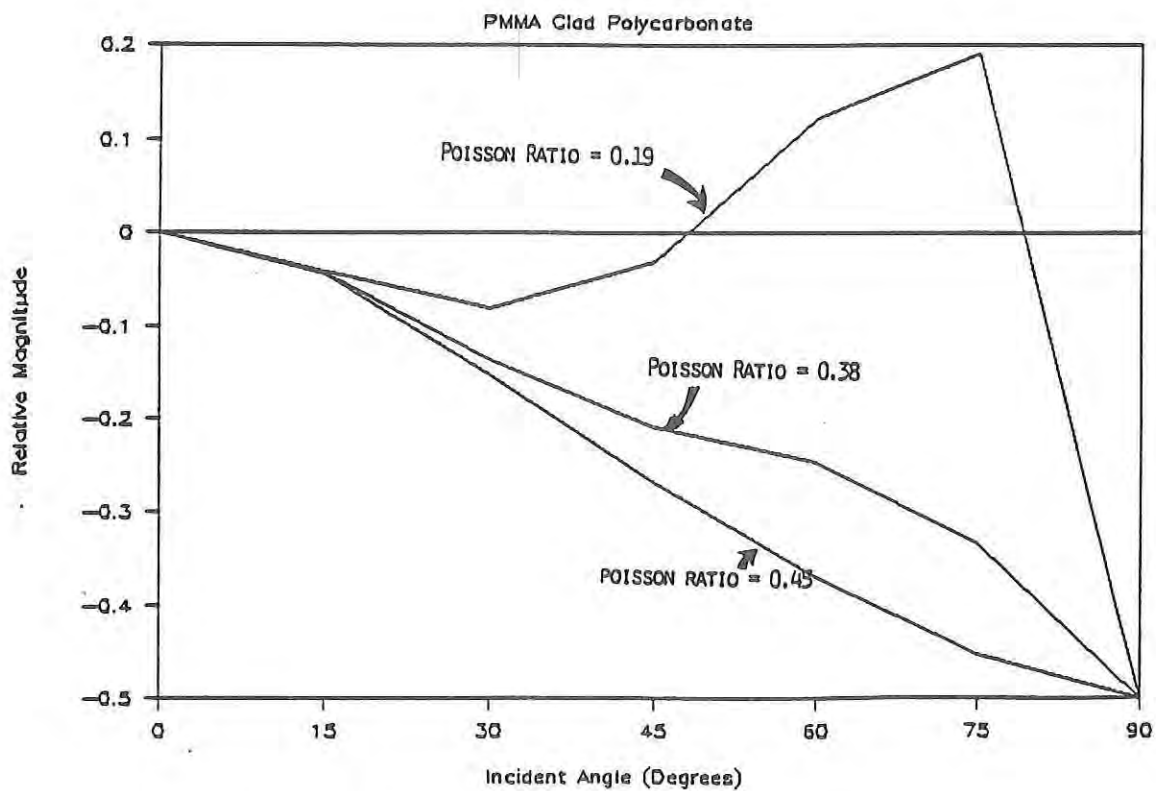


Figure 27. Relative Amplitude Ratio of P-wave.

The refracted angle in the polycarbonate substrate can be estimated from

$$\theta_{PC} = \arcsin[(c_p/c_{PMMA})\sin\theta_{PMMA}]. \quad (8)$$

Equation 8 is plotted in Figure 28 where it is observed for an incident angle of 90 degrees, which results in the largest incident stress at the PMMA impact layer/polycarbonate interface, that the refracted angle is approximately 60.5 degrees. This will result in a reflected angle at the rear PMMA layer/polycarbonate interface of about 60 degrees which from Figure 27 corresponds to a tensile S_{π} equal to about 40 to 45% of the transmitted contact pressure across the PMMA impact layer/polycarbonate interface. The peak tensile S_{π} will occur at an in-plane distance from the impact zone equal to the substrate thickness multiplied by the cotangent{60.45 degrees}. This corresponds to a distance equal to or less than 0.39 inches. If the critical fracture stress, S_{π}^c , is less than the peak tensile S_{π} than the circumferential fracture will occur at a distance farther from the impact zone corresponding to a lower critical incident angle, θ_c .

Figure 29 shows experimental values (determined from the ballistic testing in Task 5) for incident velocity (which is proportional to contact pressure on the impact surface) as a function of critical incident angle (see Section 2.5). The critical angle was determined by evaluating the expression: $\arctan\{(\text{thickness of PMMA impact layer} + \text{polycarbonate substrate})/(\text{rear surface polycarbonate substrate crater radius})\}$. Physically this corresponds to the closest distance from the impact region where the radial stresses exceed the fracture strength of the material. That is,

$$S_{\pi}(\theta_c) = S_{\pi}^c \quad (9)$$

For the one low velocity impact where the observed brittle failure was driven by the circumferential cracking in the polycarbonate substrate, it is evident from Figure 29 that the approximately 20% lower contact pressures on the impact surface result in a requirement for a higher critical angle where a larger percentage of the pressure pulse is developed as radial stresses in the polycarbonate substrate. At lower velocities, either the higher critical angles required to initiate circumferential failure are not possible or the contact pressure at the impact surface is too low to result in excursions of S_{π} above S_{π}^c . In this velocity regime, the mode of brittle failure transitions to radial cracking caused by the circumferential stress component. Although the circumferential stresses are lower, the energy required to create a radial fracture surface is lower than the energy require to created a circumferential fracture surface by approximately 2π .

An analytical model which considers a plane wave (similar to our problem at very early time only) with a unit step function time-dependent pressure pulse incident on a single semi-infinite layer was considered (as opposed to the ray model above). The sensitivity of reflection coefficients for radial stress components in a polycarbonate material 2 mm thick was assessed, including the conversion of incident waves into P- and SV components.

Figure 30 shows the peak reflected radial stress as a function of incident angle normalized with respect to the incident stress level. The solution is for a Poisson's ratio of 0.19, which was determined from wave speed measurements reported in Curran et al. [1973]. These data as

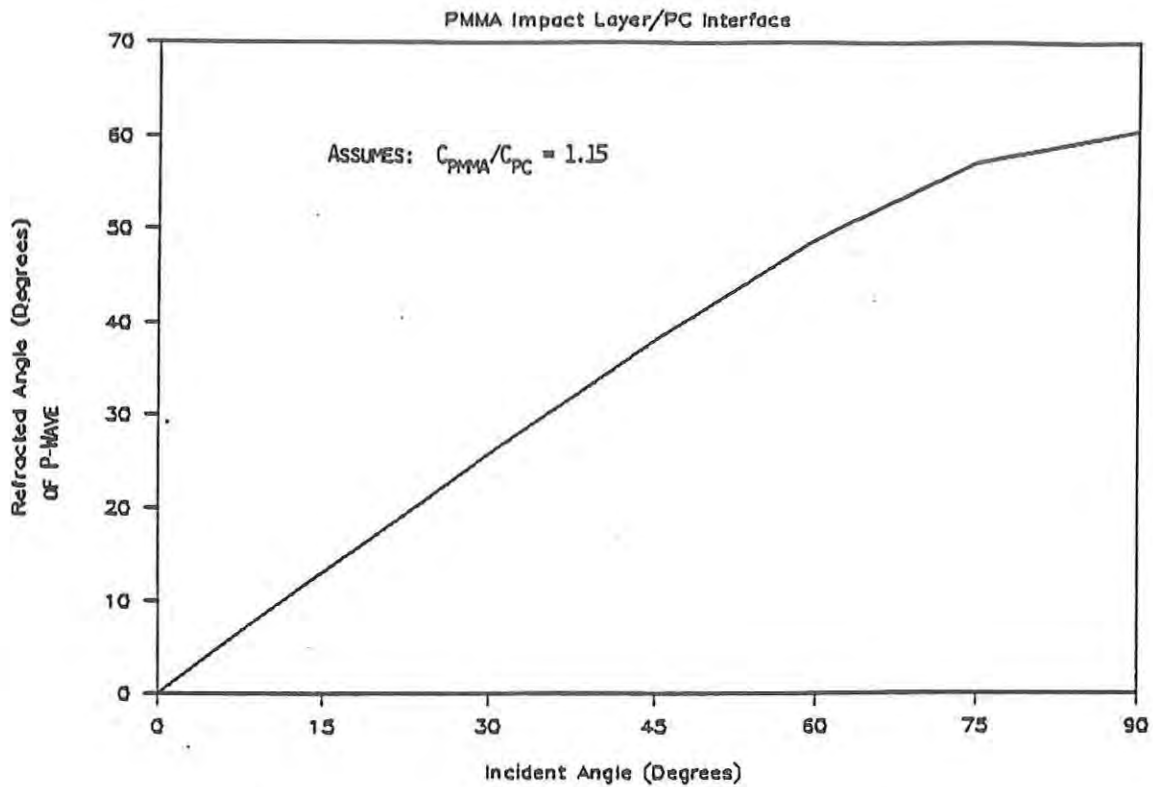


Figure 28. Incident versus refracted Angle.

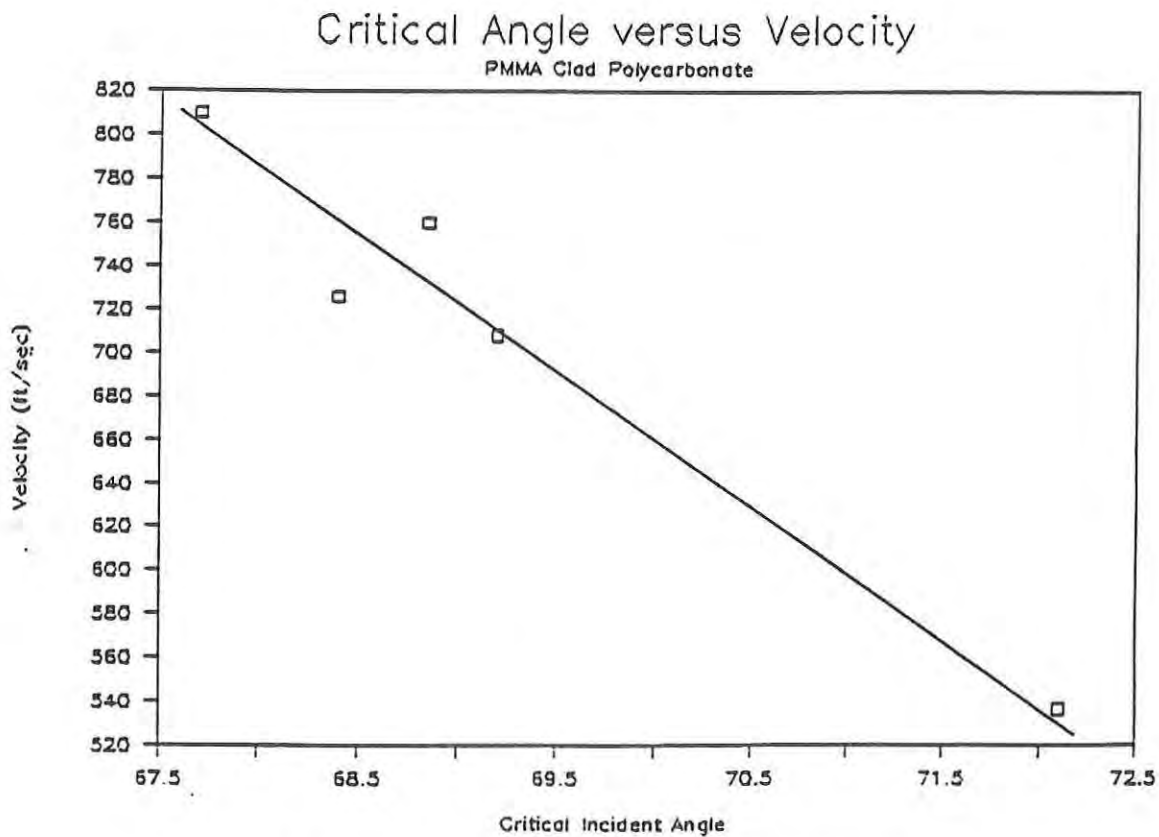


Figure 29. Critical Angle versus Velocity.

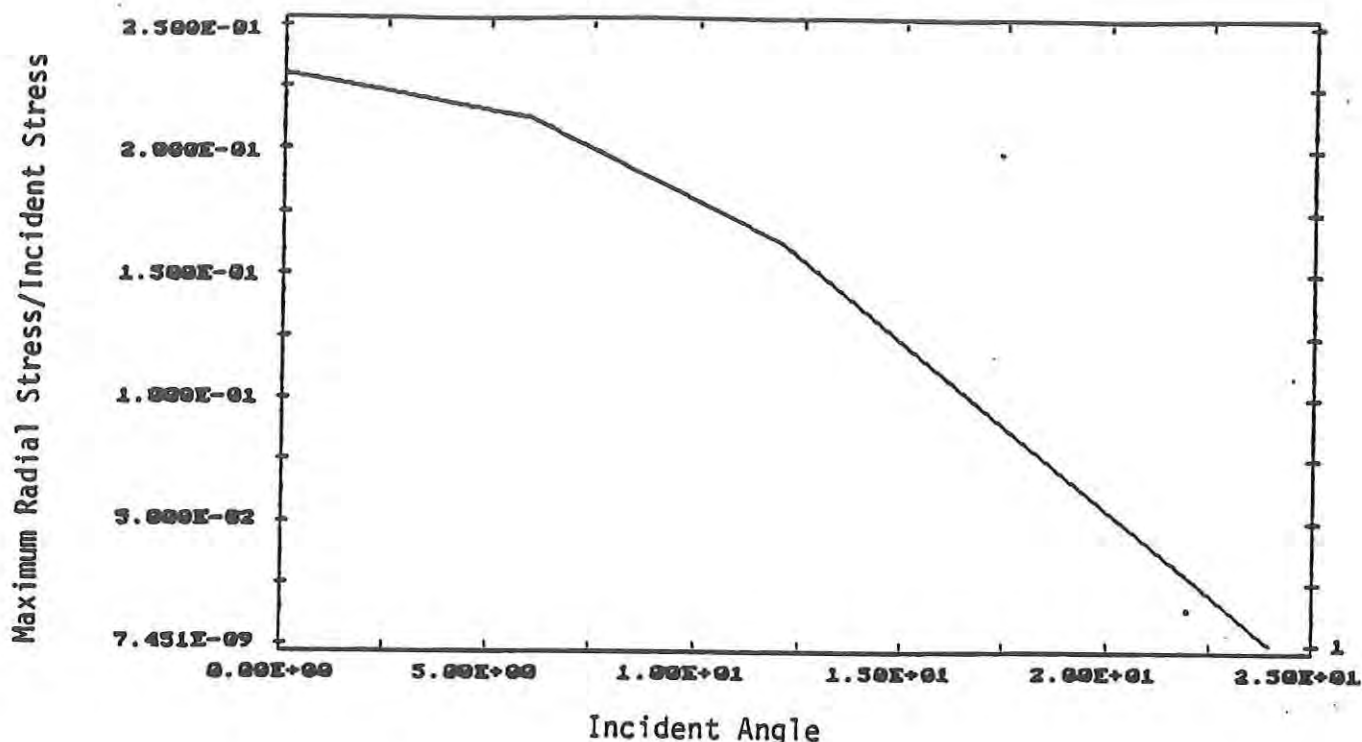


Figure 30. Normalized Radial Stress versus Incident Angle; Poisson Ratio = 0.19.

mentioned in Eisler et al. [March 1989] and Eisler and Chatterjee [April 1989] are questionable. Analysis was therefore conducted for a Poisson ratio of 0.38 which corresponds to a widely reported measured static value. Figure 31 shows the results for the higher value of Poisson's ratio where it is evident that the sensitivity of the reflection coefficient to incident angle is decreasing. The magnitudes of the stress pulse for a generic field point corresponding to the reflection coefficients employed in Figures 30 and 31 are shown in Figures 32 and 33 respectively. The different curves correspond to incident angles of 0, 17, 34, 51, and 68 degrees. The late time components corresponding to 68 degrees in Figure 32 and 51 and 68 degrees in Figure 33 are due to differences in reflection coefficients for the p- and sv-waves resulting in different arrival times at a field point producing different total stress states. A problem with polycarbonate is that the associated Poisson ratio is not known accurately. Further, due to viscoplastic effects the Poisson ratio for polycarbonate is a function of time as well as material state; i.e., in the plastic state polycarbonate becomes incompressible with a Poisson ratio approaching 0.5. For high velocity impacts, there is extensive plasticity underneath the impact region as opposed to the low velocity impacts where a substantial quantity of material behaves elastically.

The third mechanism involves trigonometry and the fact the incident and reflected angles of the respective stress waves are not identical. The reflection angle will dictate the relative proportion of the various stress components; e.g., for an incident wave traveling in the impact (z direction) and reflected at 45 degrees, the reflected wave will have both significant radial and z components.

The stress levels at a generic field point involve trade-offs between the competing mechanisms above. That is, the incident P-wave from the PMMA impact surface will be maximum for a normal incident angle at the PMMA/polycarbonate interlayer. However, the refraction angle,

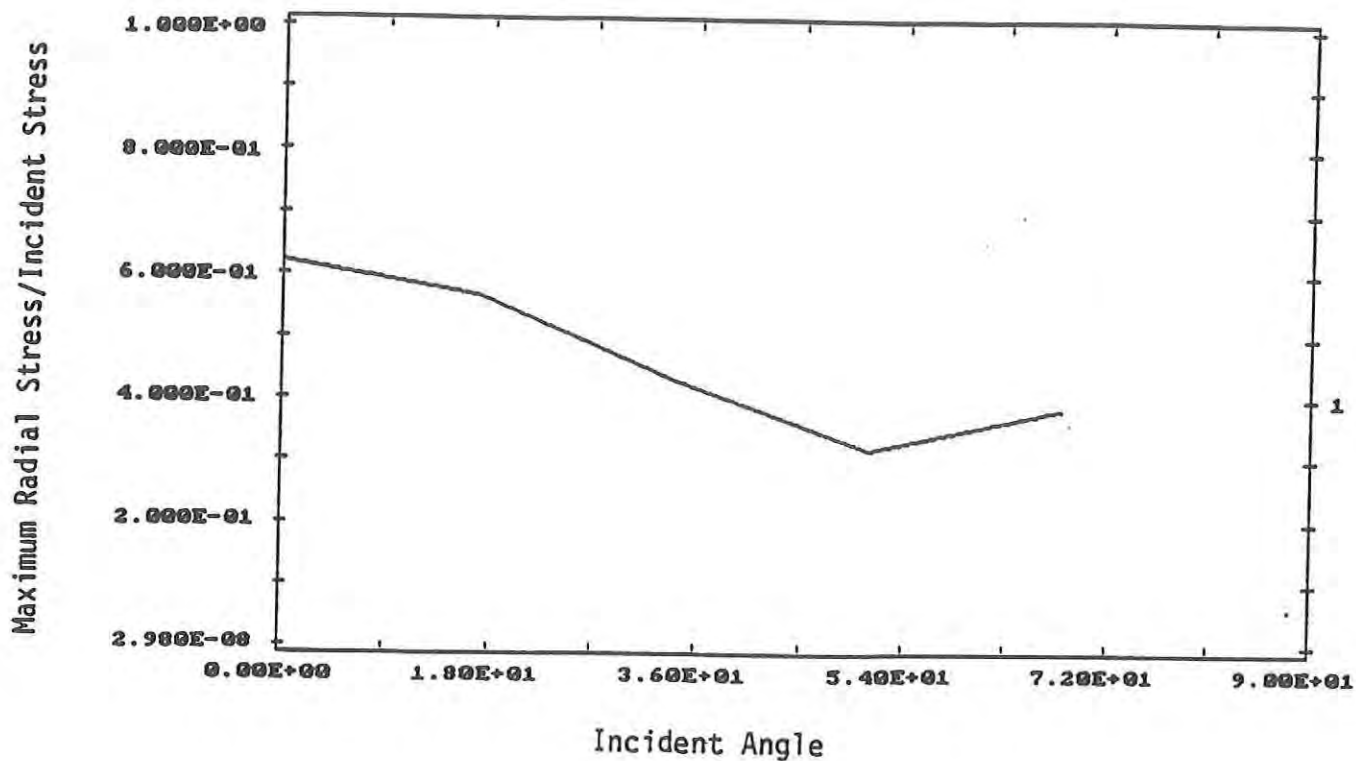


Figure 31. Normalized Radial Stress versus Incident Angle; Poisson Ratio = 0.38.

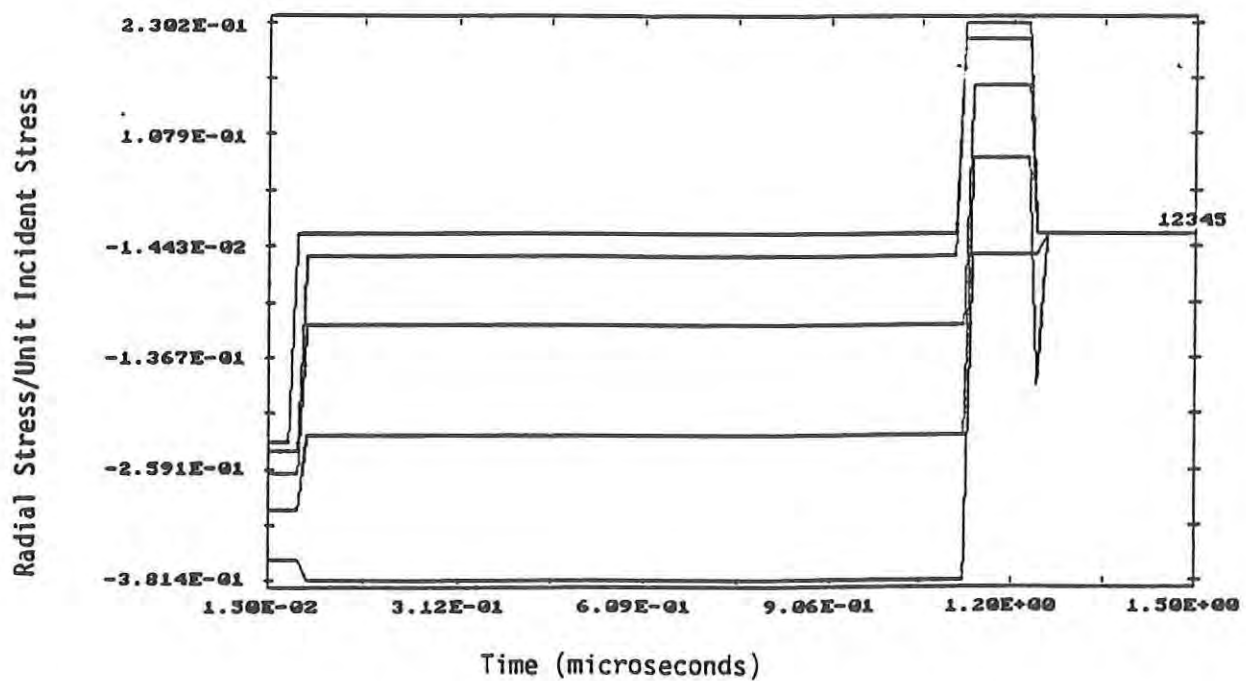
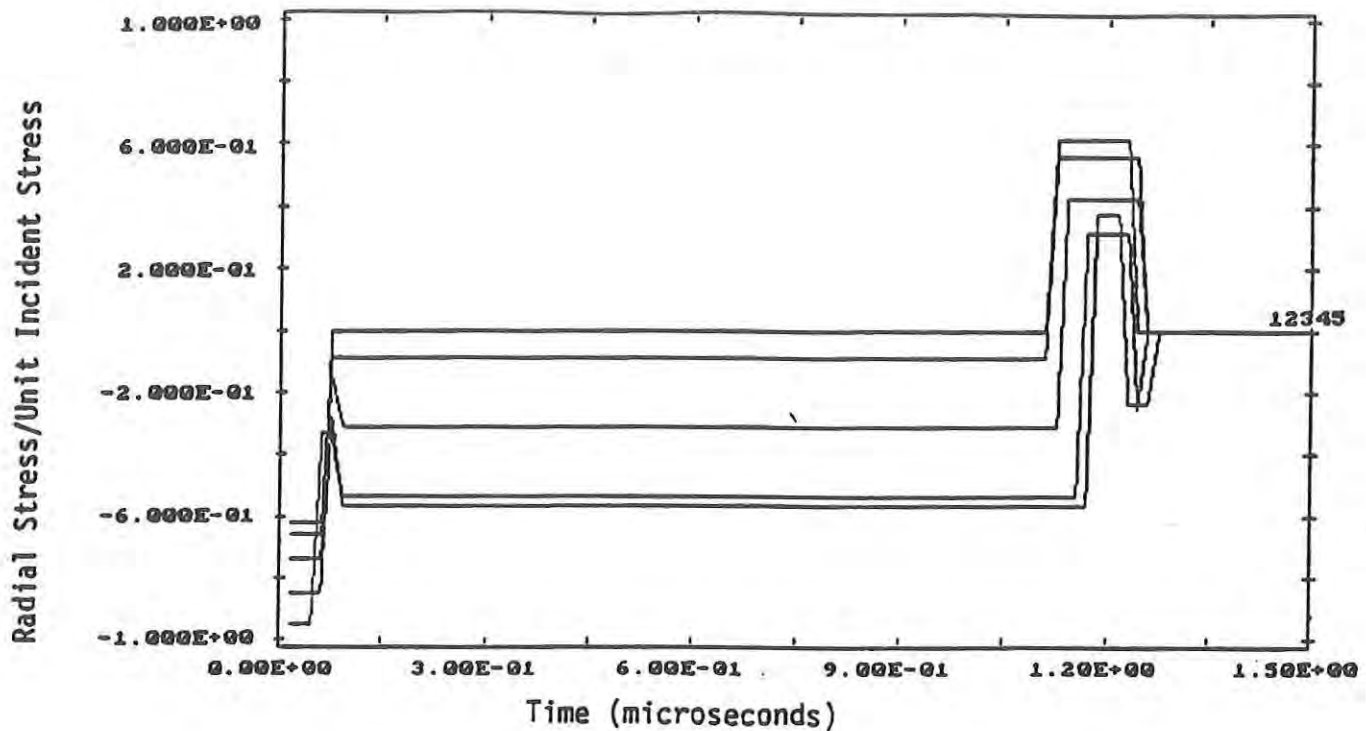


Figure 32. Normalized Radial Stress versus Time for a Generic Field Point; Poisson Ratio = 0.19.



**Figure 33. Normalized Radial Stress versus Time for a Generic Field Point;
Poisson Ratio = 0.38.**

and transmission coefficients as well as relative proportion of p- and sv-waves (which have different wave speeds) will also vary with angle affecting the compressive wave transmitted into the polycarbonate substrate. Even more significant is the sensitivity of the reflection coefficient at the Polycarbonate/rear PMMA interlayer to incident angle and Poisson ratio which dictate the magnitude and sign of the reflected wave. Finally, the relative proportion of the various stress components will be a function of the reflection angle.

The total stress state at a field point is a function of both the dilatational (P-wave) and deviatoric (shear wave) components. In general, the reflection and transmission coefficients for the P- and SV-waves are different leading to different arrival times and total stress levels. Additionally, the incident compressional waves are three dimensional so in reality the reflection coefficients are functions of the three incident angles and due to viscoplastic effects are also dependent on time and stress level. It is clear however that the radial stress component will tend to be a maximum for a reflection angle of approximately 65 degrees. This reflection angle results in peak radial stresses at a distance of 0.25 to 0.35 inches away from the impact zone which corresponds to the location of the observed circumferential cracking in the ballistic experiments. This argument also suggests that the ductile to brittle transition could occur at different incident velocities for different impact angles and that certain combinations of oblique impacts may be worse than normal impacts.

Other significant differences between the analytical results for the thin and thick PMMA cladding include: (1) The thin PMMA cladding is completely penetrated in about 0.7 microseconds whereas the thick PMMA cladding is never completely penetrated -- the corresponding location in the unclad PC target is penetrated in about 4 microseconds, and (2) Significantly longer pulse widths are associated with the thick PMMA-clad targets.

2.3.3 The Effect of a Geometric Discontinuity on Stress Wave Response. Two dimensional stress wave analysis in the presence of a pre-existing geometric discontinuity on the back surface of the target was accomplished for an uncoated and thin clad PC target. The discontinuity can represent a scratch, surface crazing, or other surface flaw. The results are shown in Appendix A.2.2.2. General observations include: (1) The stress component in the impact direction is relatively unaffected by the presence of the discontinuity; (2) The pressure and stress components in the radial and circumferential directions are greatly affected, and (3) For the affected stress components, the magnitude of reflected stresses are enhanced by up to a factor of 6 and the pulse width of the wave reflected from the free surface associated with the discontinuity is greatly lengthened relative to the incident wave. The most significant differences, however, relate to the sign of the reflected stress components and the behavior of the singularity associated with the flaw.

For the uncoated PC target, the interface associated with the discontinuity is PC-air resulting in a negative reflection coefficient. In the case of a thinly clad target the interface is PC-PMMA-Air. The PC/PMMA reflection coefficient is positive (see Table 5). The net result of this is that the reflected waves from the discontinuous region associated with the two targets will be of opposite signs.

Inspection of Figures A.40 through A.49 show that the reflected pressure for the uncoated PMMA tends to be positive while the reflected pressure from the thinly clad target is negative. Similarly, the radial component of the reflected stress wave tends to be negative for the uncoated target and positive for the thinly clad target. Using Equation 6, it is clear that the circumferential component of stress will be compressive for uncoated targets and severely tensile for thinly clad targets. For the PMMA clad targets subject to low velocity impact, failure will therefore tend to propagate in the radial direction consistent with what was observed during the ballistic testing conducted in Task 5.

From the results of the stress wave analysis, it is apparent that the chief effect of the discontinuity is to lower the threshold velocity at which the ductile to brittle transition occurs as opposed to altering the type of incipient damage. It should also be noted that the reflected stresses, particularly at locations near the discontinuous region, are more severely enhanced for the PMMA clad targets than the uncoated targets. This is due to the fact that the order of the singularity associated with the flaw is a function of: (1) Material properties associated with the surrounding media; and, (2) Geometric properties associated with the flaw. In the case of PMMA clad targets, the order of the singularity is a function of the material properties associated PMMA as well as the PC. In the case of uncoated targets the order of the singularity is a function of the flaw geometry and the material properties associated with PC only. The effect of multilayered media properties on stress intensities is considered in more detail in the fracture mechanics task (Task 4, Section 2.4).

2.4 Task 4 - Fracture Mechanics and Structural Analysis.

The effort accomplished under this task was fourfold and included: (1) Assessment of the dynamic stress intensity factor associated with multilayered media with different material phases and interface conditions; (2) Static analysis for the stress field resulting from the application of 1 Newton point loads at different locations on the lens; and, (3) Frequency response analysis for the first five modes of the ballistic goggles supplied by Natick. These efforts are discussed in Sections 2.4.1 through 2.4.3 respectively.

2.4.1 Dynamic Stress Intensity for Multilayered Media with Different Interface Conditions. This effort was motivated by the experimental results for the falling plummet tests presented in Table 2 and through which an approach for analysis of the stress intensity factor in the presence of an interlayer was developed.

In order to understand the falling plummet results in Table 2, elastic one dimensional stress wave analysis was undertaken. This was done to see whether the test results could be predicted on the basis of results from one-dimensional stress wave propagation through multiple layers. MRC has developed a one-dimensional multiple layered code based on ray theory that can calculate the stress history at any point inside a composite when the loading history is known [Stone and Chatterjee, 1989]. For a fictitious linear exponentially rising and decaying stress wave incident on a PC-plexiglass assembly, the stress history was calculated at the interface of the PC and coating. Figure 34 shows calculated results for the interface stress associated with a plexiglass coating (0.187 inch) fusion bonded to PC (0.250 inch) and plexiglass (0.187 inch) adhesively bonded (0.1 inch) to PC (0.250 inches). Except for some tensile waves generated in the case when urethane adhesive is used, no significant change in the interface stress is seen which can explain the observed reduction in impact strength.

To see the effect of stacking sequence reversal on the interface stress, the interface stress for the case of plexiglass (0.187 inch) on the impact surface fusion bonded to PC (0.250 inches) and PC (0.250) on the impact surface fusion bonded to plexiglass (0.187 inches) is compared in Figures 34(a) and (b). Both configurations generate a significant amount of tensile stress which may cause spallation at the back surface. This is also consistent with PUFF74 results for different interlayers (see Figure A.12). The two curves in Figure 34 primarily differ in phase which is due to different travel times in the two layers that make up the PC-coating assembly. One dimensional stress wave propagation alone can not explain the drop in the impact strength shown in Table 2 for these specimen configurations.

Attenuation associated with 2D effects may be responsible for such changes in the impact strength when the stacking sequence is reversed. This is explained in Figure 35. Assuming that the attenuation factor is proportional to $\exp(-\lambda t)$ where the t is the travel time of the wave after it is incident on the composite and λ is the attenuation coefficient, the travel time of tensile wave in case (a) is twice the corresponding travel time for case (b). If tensile waves are responsible for the brittle failures then greater damage would be expected in case (b) than in case (a). This possibility will be investigated in Phase II by estimating the reduction in impact strength based on the proper attenuation factor of polycarbonate when the acrylic surface is opposite the impact surface and fusion bonded to the PC.

Within this context, adhesive bonding is more successful in preserving the impact strength of the PC in comparison to fusion bonding. The stress intensity factor ahead of a crack developed in the brittle plexiglass layer is the driving mechanism for the crack to propagate through the PC substrate when the interface is fusion bonded. In the case where adhesive is used, the index of the stress intensity factor changes from the classical square root to a value that depends on the properties of the interphase adhesive layer. It has been analytically shown that for a crack propagating perpendicular to an interface of two layers, the stress singularity is dependent on the properties of the media in contact [Kuo, 1982]. Experimentally, it has been shown that the

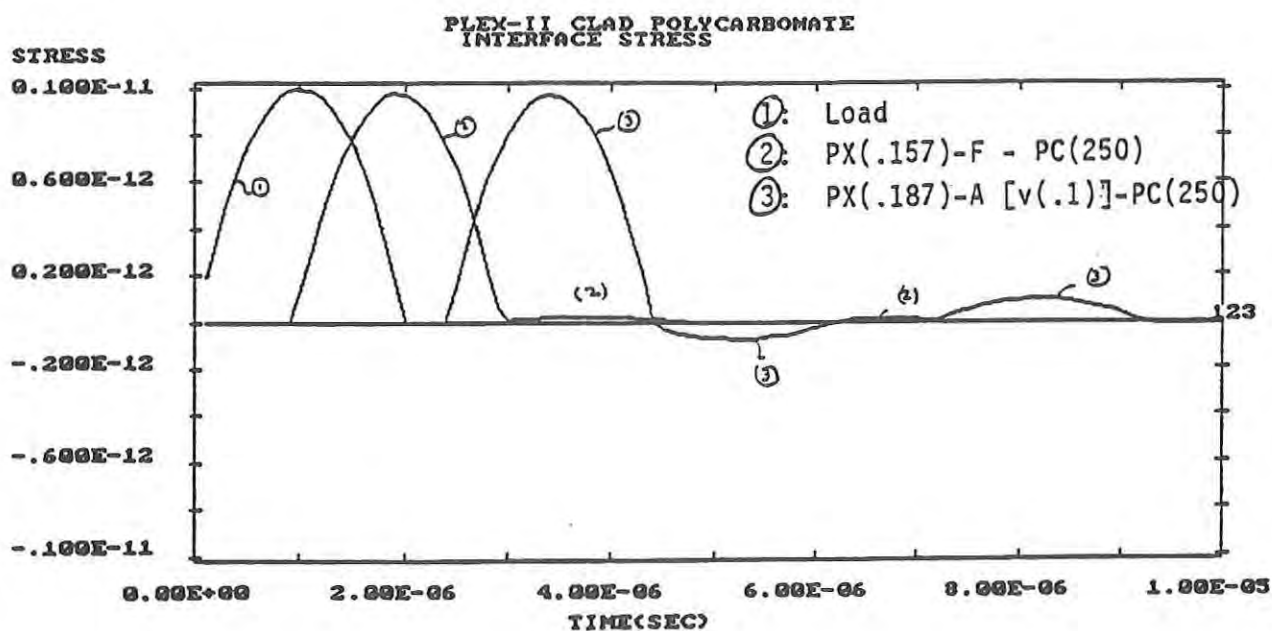
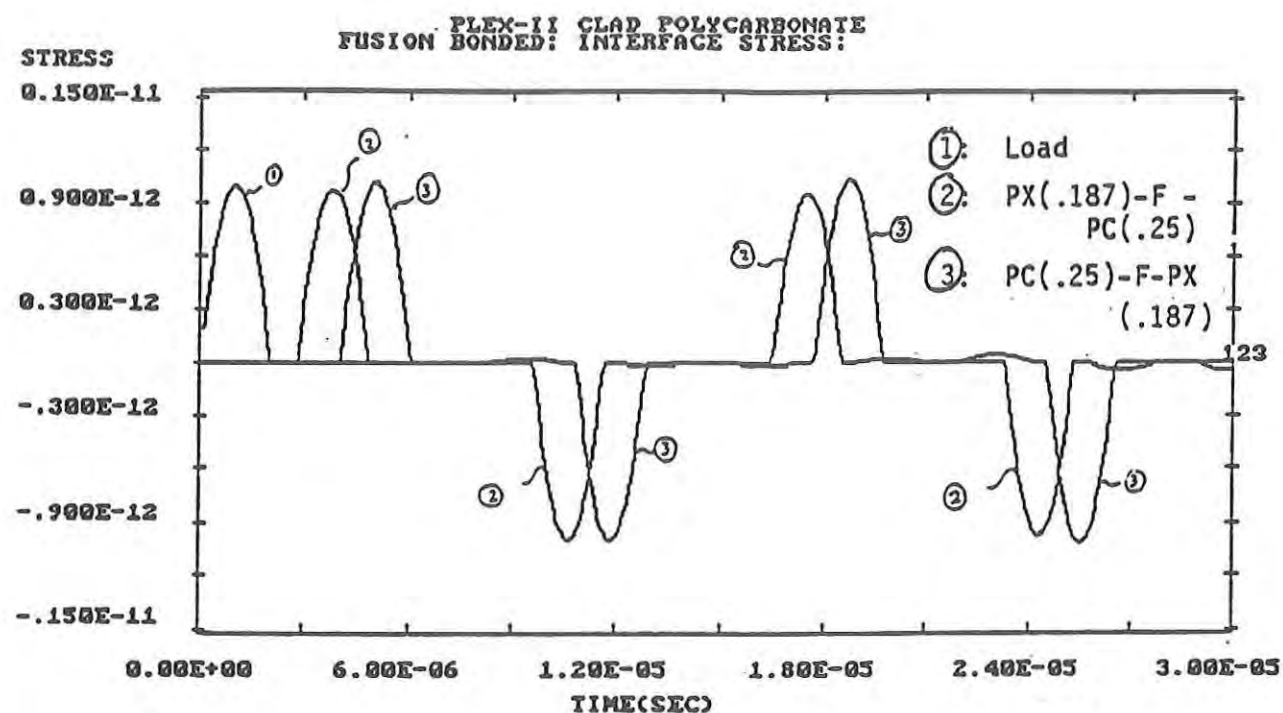
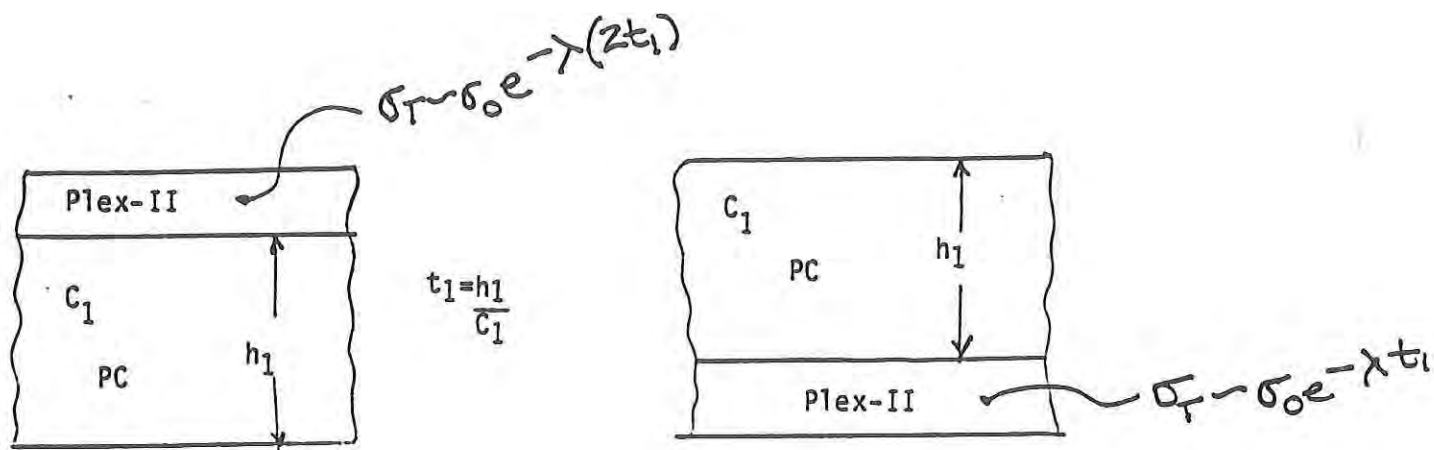


Figure 34. Comparison of Interface Stress for: (a) PMMA on the Impact Surface which is Fusion Bonded and Adhesively Bonded to PC; (b) PC on the Impact Surface which is Fusion Bonded and Adhesively Bonded to PMMA.



c_1 = Wave Speed in PC; σ_0 = Tensile Stress (No attenuation)

λ = Attenuation coefficient

Figure 35. Attenuation of Stress Associated with 2 Dimensional Effects.

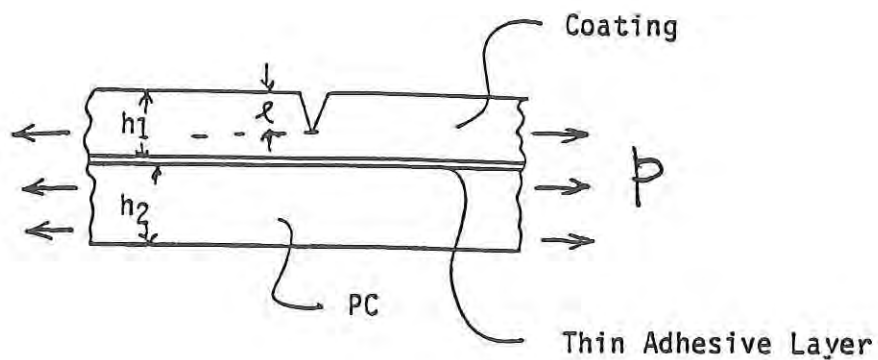


Figure 36. Influence of Material Interphase on Crack Propagation.

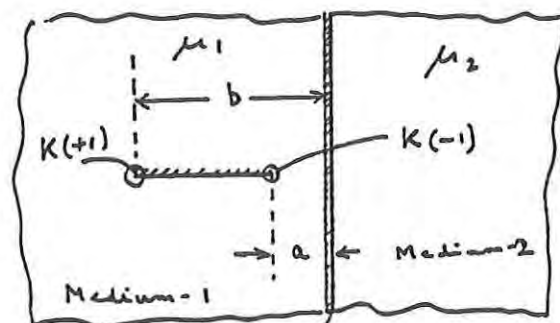
singularity changes significantly when a third interphase is present. An analytical solution, however, does not currently exist in the literature for this problem. In the presence of an adhesive, when a propagating crack reaches the interface, MRC postulates that the stress singularity ahead of the crack tip is reduced and stress redistribution occurs such that the crack no longer has the minimum threshold energy to be propagated into the polycarbonate substrate. During Phase II an estimate of the stress redistribution that occurs in the presence of adhesive layer will be developed.

Results obtained from plummet tests in Table 2 indicate that there is a significant drop in the fracture strength of polycarbonate when it is coated with fusion bonded plexiglass as opposed to the adhesively bonded plexiglass coating. This is a very significant result from the standpoint of fracture mechanics since it indicates a strong influence of the material interphase on the propagation of cracks initiating in the coating. An analytical model of this problem is given in Figure 36. For dynamic crack propagation through the coating-PC assembly, growth is controlled by the critical stress intensity factor ahead of the crack tip and the distribution of the critical stress intensity factor is assumed to be known through the thickness.

In this case, the experimental result alluded to above can be interpreted as a significant reduction of the stress intensity factor as the crack approaches the interface when an adhesive bond is present. Previous experiments that support the existence of this phenomena include those performed by Theocaris & Papis (1983), Dally et al. (1978), and Sereda et al. (1977).

Dally studied the mode-I tensile crack propagation in a composite composed of two materials bonded by a high-strength epoxy layer. It is observed that the stress intensity factor at the crack tip as well as the crack velocity decrease as the crack approaches the interface layer. Under constant loading, the crack has a significant delay before it enters into the substrate. The experiments by Sereda et al. (1977) exhibit a different behavior when the two materials were cast on each other without the presence of the intervening filler. In the latter experiments, the stress intensity factor increases as the crack is approaching the interface and no crack arrest mechanisms were observed. Thus the difference between the two experimental results can be attributed to the presence of the intermediate bonding layer in the first experiment and its absence in the second.

No effort has been made to date to develop analytical models capable of explaining the nature of the growth of a crack in the presence of a very thin intermediate layer connecting two materials. The main reason for the lack of such models is the complexity in analytical modelling of the effect of the third interphase, which has a microscopic influence on the growth of the crack. Chatterjee and Knopoff (1984) developed an analytical model where the effect of the intermediate layer is incorporated in the analysis of crack propagation by means of boundary conditions that relate the displacements and stresses on both sides of the bonding material. In this model, the boundary conditions at the interface are either one of perfect bonding or one which has an impedance boundary condition. The latter condition simulates imperfect bonding. The crack grows in the first medium and responds to the encounter of the interphase. An interphase parameter has been introduced to represent the property of the interphase so that it appears in the formalism only through boundary conditions at the interface. This model discusses the quasi-static growth of mode-III crack but the method is applicable to any mode of crack propagation as well. Results indicate that in the presence of the adhesive layer, the stress intensity factor decreases as the crack approaches the interface (as observed in the above experiments). One such result is given in Figure 37.



- μ_i = Shear Modulus of Material i
 λ_0 = Interface Parameter
 K = Mode III Stress Intensity Factor

Filler Interphase:
 Characterized by λ_0

SIF = Stress Intensity Factor

SIF: Two-phase Medium: ($\lambda_0 = -3$)

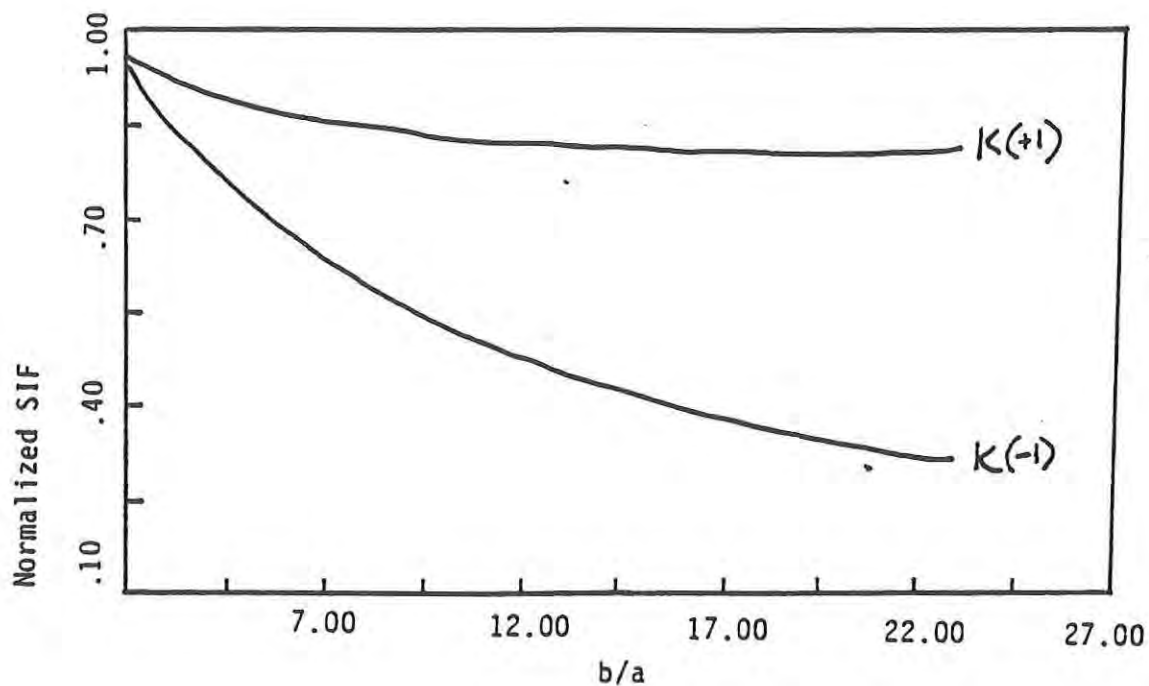


Figure 37. Quasistatic Growth of Mode III Cracks Approaching an Interface.

Using the above results and other established results in the literature, it is possible to develop an analytical equation for crack growth in polycarbonate composites. The procedure associated with this effort is shown below.

1. Determination of the tensile stress field generated during the impact of the polycarbonate composite. This tensile field will be used as loading in the analysis of crack growth in the composite and can be obtained by using existing codes on impact loading of composites in the absence of any fracture.
2. Calculate the static stress intensity factor in the case of a surface crack in a homogeneous plate subjected to lateral load as given by Cherepanov (1979, page 187, see Figure 38). This solution will be modified during Phase II to account for the presence a second and third layer of materials using analysis similar to that of Chatterjee and Knopoff [1984] mentioned above.

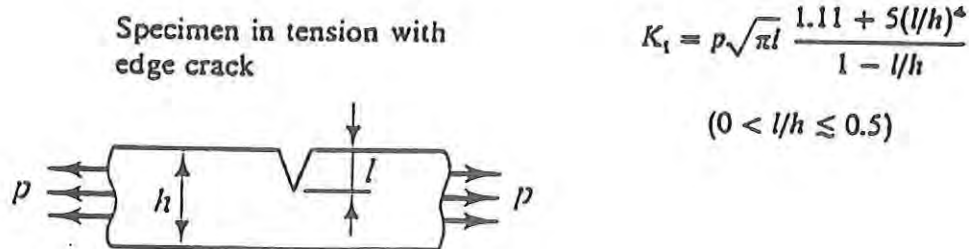


Figure 38. Stress Intensity Factor of a Surface Crack in a Homogeneous Plate Subject to a Lateral Load.

3. The critical stress intensity factor for polycarbonate will be used. This is given by Cherepanov [Op. Cit., page 199]:

$$K_{Ic} = (S_u E d)^{1/2};$$

where "d" is the maximum value of linear stretching before failure of the multimolecular formation, "E" is the Young's modulus and "S_u" is the applied stress when failure occurs.

4. The growth of the crack through the composite will then be determined by the application of the critical stress intensity factor criterion. This will be accomplished during Phase II.

Some other aspects of fracture mechanics that are of importance in the analysis of crack growth in polycarbonate materials also include, for example, the presence of fibrils between the crack surfaces. This increases the instability of the crack growth as the crack begins to propagate in the brittle phase. This is evident from the analysis of crack stability when resisting forces are present between the crack surfaces (Cherepanov, page 136) and is also observed by Morgan and Mones [1979]. The initial compressive forces present in the material when the composite is subjected to the impact load may be instrumental in accelerating the crack in a later phase due to lateral tensile

loading emanating from the edges of the specimen. This occurs by reducing the tensile strength of the material ("Greene effect", Cherepanov, page 173). Both mechanisms will further accelerate the crack beyond that predicted by the analytical models presented above.

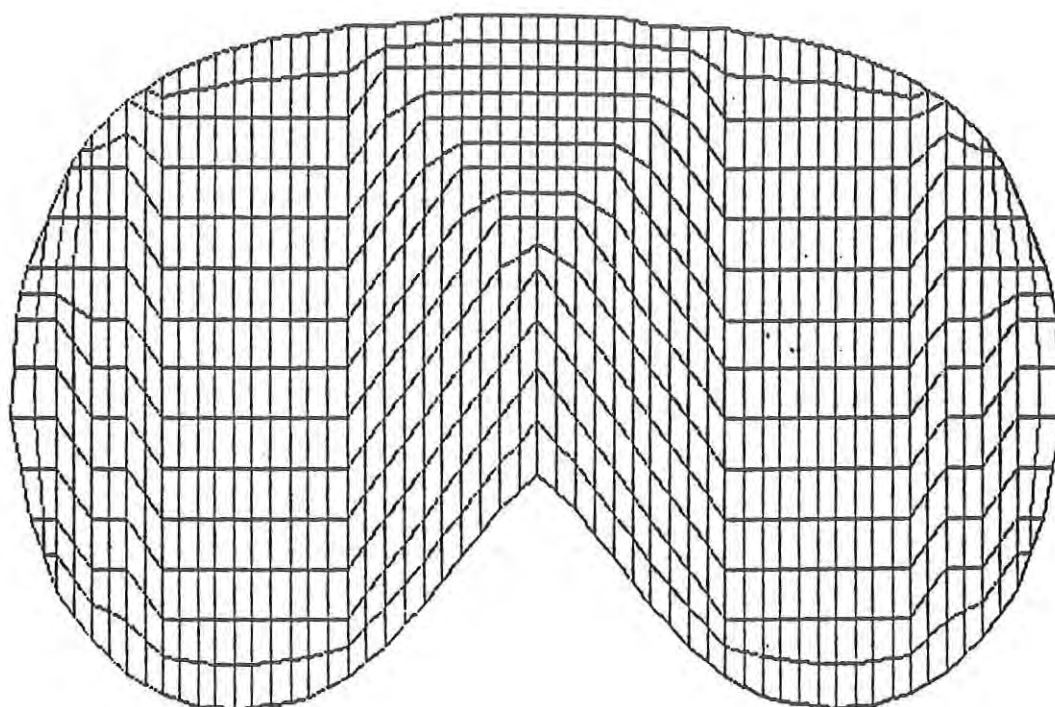
2.4.2. Static Analysis. Two linear elastic COSMOS plane stress finite element analyses were implemented. The models had very accurate representations of the goggle geometry including the goggle curvature. Static solutions for a 1 Newton point load using two grid refinements were implemented to establish error bounds on the solutions. A plan view of the refined grid is shown in Figure 39(a). An edge plot of the deformed shape of the lens is shown in Figure 39(b). Figures B.1(a) and (b) show solutions for radial and circumferential stress for two grid refinements associated with an uncoated ballistic lens. The results indicate very good agreement for radial distances in excess of 1 cm from the load application. For distances closer than 1 cm the finite element grid is not sufficiently refined to capture the large gradients associated with the application of the point load. To evaluate the solution in this region a classical solution of a circular plate will be implemented in Phase II using an equivalent lumped stiffness that results in solutions in agreement with the finite element solution at distances greater than 1 cm.

An additional problem associated with the finite element solution is the geometrically nonlinear character of the problem; i.e., due to the large strain capability of polycarbonate and the large displacements associated with the application of a point load, the analysis requires iterations in which the load is gradually applied and the analysis is conducted using the deformed geometry of the material as opposed to small deformation assumptions which are typically implemented. In small deformation linear elastic approaches the analysis is conducted in one load step using the undeformed geometry of the structure. The Phase I program resources do not permit running the existing COSMOS model to obtain a nonlinear geometric solution. To compensate for this short-coming, the small deformation results determined from the COSMOS code can be modified using a correction factor empirically determined as a function of displacement from load deflection experiments accomplished in Task 5. Large displacement correction factors were determined for the ballistic lens by comparison with the linear elastic small displacement finite element solution and for flat polycarbonate sheets by comparison with the classical small deformation linear elastic solution for a circular plate subject to a concentrically applied point load. The results from this comparison are shown for the coated ballistic lens and flat uncoated circular plate in Figures B.2(a) and (b). Figures B.3(a) and (b) show small displacement solutions for radial and circumferential stress on the impact and rear surfaces of the lens. Figures B.4 and B.5 show some typical contour plots of principal stress for uncoated and coated lenses. Figure B.4 shows results for a point load at the center of the lens and Figure B.5 shows analogous results for a point load near the lateral cylindrical surface.

During Phase II the correction factors shown in Figures B.2(a) and (b) will be applied to the small deformation solutions in B.3 to obtain approximate geometrically nonlinear static solutions for stress and strain.

2.4.3 Frequency Analysis. Frequency analysis was implemented using the geometry models developed with COSMOS. Deformed plots for the first three modes are compared for the coated and uncoated lens in Figures B.6 (a) through (d) and Figures B.7 (a) and c. Figures B.7 (b) and (d) show the shapes for the fourth and fifth modes associated with the uncoated lens.

The frequency analysis indicates a fundamental frequency on the order of 529.89 Hz for the uncoated ballistic goggles and 550.9 Hz for a coated version of the goggles. As the coating



FINITE ELEMENT GRID FOR STATIC ANALYSIS



EDGE PLOT OF DEFORMED SHAPE FOR 1" NEWTON POINT
LOAD AT CENTER OF LENS



Figure 39. Ballistic Goggle Finite Element Model.

thickness is increased the fundamental frequency also increases. The period corresponding to these frequencies, however, is on the order of 10^{-3} seconds compared with the force-time history associated with the impact which is on the order of microseconds, 10^{-6} seconds. This suggests that the steady-state response of the material in terms of stress and displacement may be predicted with static analysis and the transient response is dictated by the stress wave behavior.

2.5 Task 5 - Fabrication of PC Materials and Testing.

Effort in this task was threefold and included: (1) Fabrication of compression molded polycarbonate samples for static and ballistic testing; (2) Static penetration tests; and, (3) Ballistic testing employing 5.7 grain FSPs. These efforts are discussed in Sections 2.5.1 through 2.5.3 respectively.

2.5.1 Polycarbonate Fabrication. Six 13.5 inch x 13.5 inch 75 mil compression molded polycarbonate (high melt flow rate general purpose Calibre 300-22 with UV stabilizers from Dow Chemical Corporation) panels were fabricated by MRC. The raw polycarbonate pellets were dried for 3 hours at 250°F as per the manufacturer's recommendations. The specimens were fabricated at different combinations of temperature and pressure (see Table 9) within the ranges recommended by the manufacturer.

The specimens were cut into 3 inch x 3 inch samples. A subset of these samples were laminated with PMMA layers ranging in thickness between 15 and 60 mils using an Epoxy resin

Table 9. Fabrication Pressures and Temperatures.

Specimen	Temperature	Pressure	Specific Gravity
1	530 degrees F	800 gauge	1.24
2	450	900	1.23
3	550	300	1.16
4	450	300	1.19
5	500	800	1.2
6	513	600	1.21

(5 parts Products Research PR2045 and 1 part Hysol HD3490). The samples were then packaged in opaque airtight containers for ballistic testing.

2.5.2 Static Penetration Tests. Static penetration tests were accomplished on ballistic goggles and an uncoated polycarbonate sample fabricated by MRC. A rounded conical indenter (simulating a point load) and an indenter machined to represent the shape and dimensions of the 5.7 grain fragment simulating projectile were used. A load-displacement plot for the ballistic goggles (with unknown coating) subject to the conical indenter is shown in Figure 40. Corresponding results for the fragment simulating indenter on the ballistic goggles and an uncoated polycarbonate sheet of the same approximate thickness is shown in Figure 41(b). Figure 41(a) shows the crater depth as a function of load for the fragment simulating indenter. Each data point represents a separate test on a discrete sample to avoid hysteresis effects. Three regions were identified in Figure 41(a). The first region corresponds to a region where the beveled point of the indenter seats into the sample and

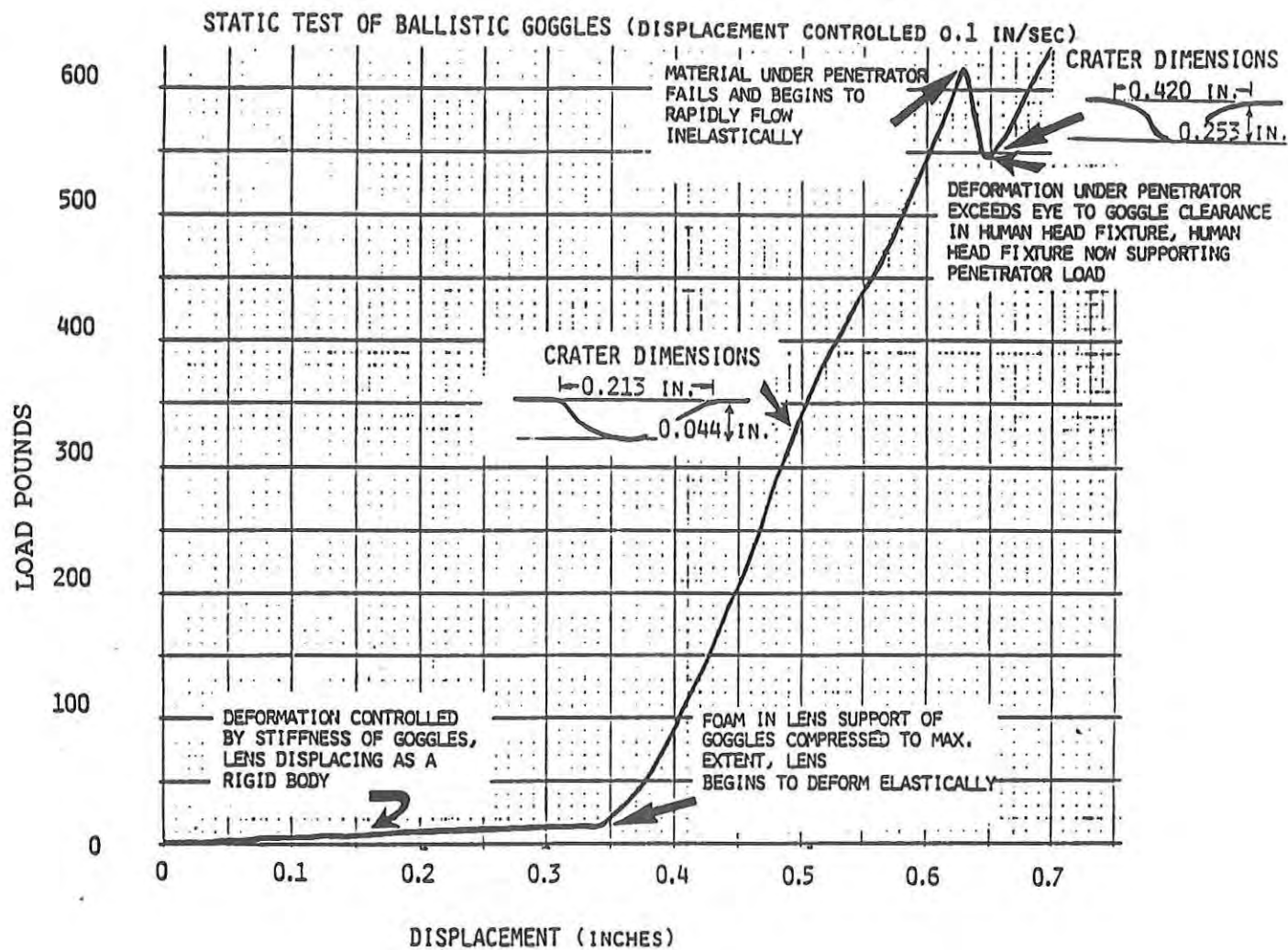
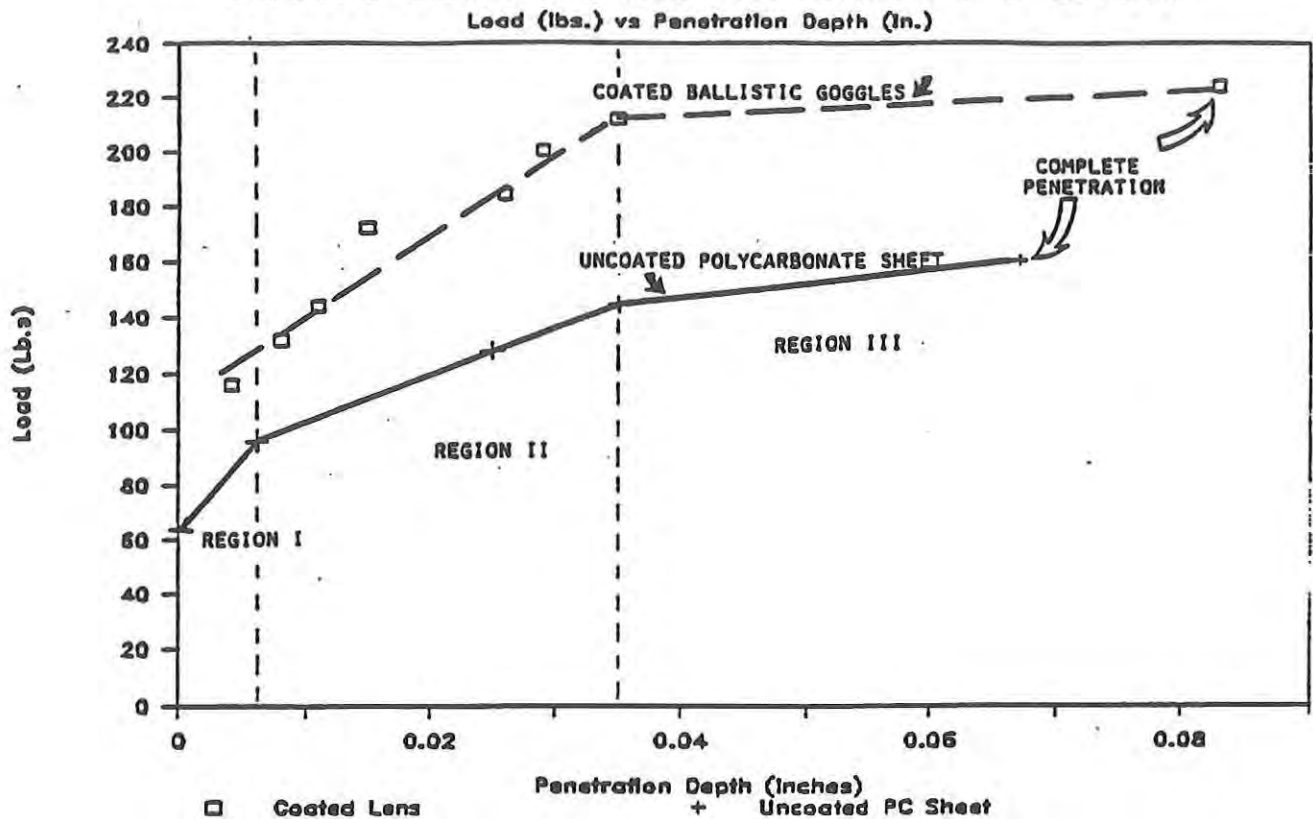


Figure 40. Static Test of Ballistic Goggles with Conical Indenter.

Coated Lens versus Uncoated PC Sheet



Load (Pounds) vs Displacement (Inches)

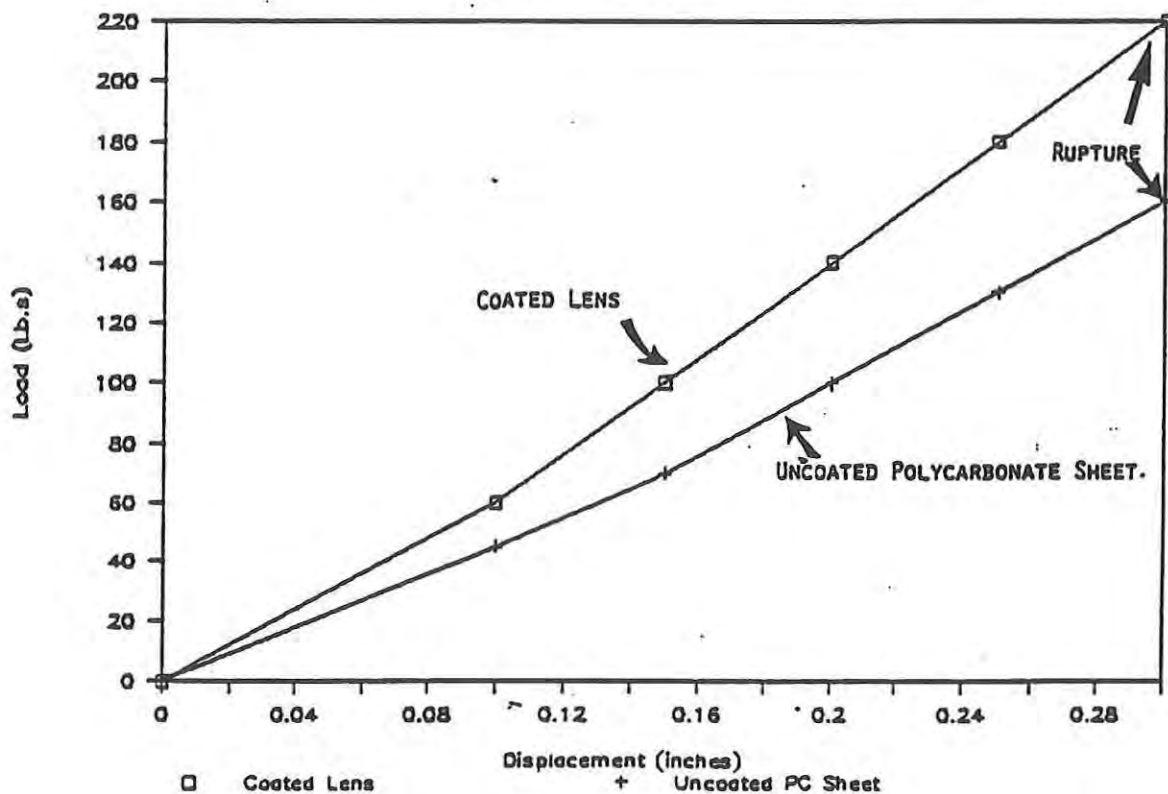


Figure 41. Static Test of Polycarbonate Sheet and Ballistic Goggles with Fragment Simulating Indenter.

material is failing in shear. The slope is very large due to the interaction of the stress concentrations on the corners of the indenter with the high stress underneath the centerline of the indenter failing material ahead of the indenter path making penetration easier. The conical penetrator did not manifest a region I, which corroborates this hypothesis.

The second region corresponds to depths where the entire point of the penetrator is immersed in the target material. Material is failing in shear and extensive plastic flow and larger contact areas between the advancing penetrator and target material permits a local redistribution of loads so that the effect of material failing in advance of the penetrator is somewhat mitigated. As the residual thickness of target material is decreased below the crater, the stress field is locally enhanced resulting in significant plastic flow in Region III. The eventual failure of the material is due to the tensile failure of the remaining ligament of target material beneath the crater resulting in a dish shaped ductile punched plug. The conical indenter resulted in a ductile petaling failure arising from local tensile bending stresses underneath the indenter.

The results from these tests will be used in Phase II to describe how the energy imparted to the target material by the penetrator is partitioned amongst the different damage mechanisms. Although the relation between quasistatic and dynamic penetration of polycarbonate at different strain rates is uncertain, the static case represents a ductile failure mode which is desirable to promote in the dynamic case and in some sense the static case represents an upper bound in terms of energy absorption for this mode. From this perspective, it is likely that some insight as to the nature of the ductile to brittle transition can be garnered by: (1) Comparing failure modes and energy absorbing mechanisms for static and ballistically impacted samples; and, (2) For those samples that failed in a brittle manner, determine why the static type of ductile "punched plug" failure mode did not occur.

2.5.3 Ballistic Testing. A 22 caliber smooth bore launch tube pumped by N₂ gas using a Lexan cylindrical sabot with a 5.7 grain fragment simulating projectile mounted with putty was set-up and tested. Redundant velocity measurements employing light screens and electrically conductive euler paper in front of the target and euler paper behind the target were implemented. A camera using an open shutter technique in conjunction with a xenon flash was used to photograph the projectile immediately prior to impact to verify projectile orientation. The results of trial testing indicated consistently normal impacts at incident velocities between 300 and 1000 ft/sec. The various military specifications and DoD standards listed in the Reference section of this report were also reviewed.

Since ballistic test data were not available to MRC for the ballistic goggles of concern to Natick and no ballistic data were available relative to the 5.7 grain fragment simulating projectile; the principal goal of the Phase I ballistic testing was to develop a mini-database to demonstrate phenomenology. Nine ballistic goggles were provided to MRC by Dr. Healy from Natick. One goggle was used for static testing leaving 8 goggles or 16 samples if each lens of the goggle were tested separately.

Five groups of ballistic tests with different goals were defined. The first group of ballistic tests employed the goggles supplied by Natick and determined the incident velocity corresponding to complete penetration of the goggle with a residual velocity as close to zero as possible. The purpose of this group of tests was to determine the incident velocity resulting in the maximum amount of energy input into the target. The second group of ballistic tests involved goggles that have been preconditioned with a shallow scratch penetrating the surface coating of the lens impacted at different

velocities. The purpose of these tests was to determine if different failure modes are evoked or the same failure mode at a different stress level (incident velocity).

The impacts associated with the first two groups of tests were designed to impact a central region of the ballistic lens. The third group of tests involved off-center impacts of the ballistic lens. The impacts were done at various distances from the lateral free surface of the lens to determine the influence of stress waves reflected from lateral free-surfaces. This third group of tests was the most interesting since for partial penetrations, the reflected stress wave from the lateral free surface must interact with the crater promoting a highly complex and locally intense stress field. Furthermore, in a debris environment, this region is more likely to be impacted.

The fourth and fifth group of tests are analogous to the first group of tests except that the specimens are flat polycarbonate samples fabricated by MRC. The thickness of the MRC samples are similar to the estimated thickness of the polycarbonate substrate in the ballistic goggles supplied by Natick. The ballistic goggles have an abrasion resistant coating on the front and back surfaces of the lens estimated to be on the order of 1 to 3 mils or up to 6 mils for both surfaces. The fourth group of ballistic tests will be on bare polycarbonate samples and the fifth group of tests will be on polycarbonate samples with various thicknesses of laminated plexiglass.

Thirty three ballistic tests employing the 5.7 grain FSP were conducted during Phase I. The ballistic test specimens included 16 ballistic goggle lenses supplied by Natick RD&E center, 1 PMMA sample, and seven uncoated and nine coated (with laminated PMMA) polycarbonate flat sheet samples. The specimens were mounted on a perforated foam fixture with double stick tape approximating the stiffness of the rubber supports on the ballistic goggles.

Tables C.1, C.2, and C.3 through C.15 describe the sample, test conditions, and residual damage for the ballistic goggle, uncoated polycarbonate, and laminated polycarbonate specimens. Tables C.4, C.5, and C.6 describe the residual damage to the PMMA impact surface, polycarbonate substrate, and PMMA rear surface for the laminated polycarbonate specimens. Figures 2 and 3 show typical brittle failure modes for the ballistic goggle lens and laminated polycarbonate sheets.

Of the 16 tests on the ballistic goggle lens, 15 resulted in ductile failures and in general met or exceeded Government specifications with respect to withstanding the specified projectile threat. One goggle failed in a brittle manner (sample XI) due to the propagation of a circumferential crack outside of the impact region. This behavior arises from stress waves reflected from the edge of the lens interacting with the residual crater formed by the projectile. This produces high radial stresses outside the impact region and is based on well established phenomenology.

All of the uncoated polycarbonate flat sheet samples manifested ductile behavior and for those samples which failed, a ductile dish shaped punched plug similar to what was observed in the static penetration tests was apparent (Section 2.5.2). An exception to this was sample 6A, which in addition to a dish-shaped plug, manifested cracking, which appeared to initiate from a surface defect. The penetration depths and residual velocities for the uncoated polycarbonate flat sheet samples were all very consistent and where not obviously affected by processing parameters.

All of the coated polycarbonate flat sheet samples failed in a brittle manner. A large area crater and extensive radial and circumferential cracking was observed on the rear PMMA layer. A small area crater approximately the diameter of the projectile with some radial cracks extending from

the edge of the crater is observed on the PMMA impact layer. The polycarbonate substrate evidences predominately circumferential cracking with secondary radial cracks. The crater in the substrate is intermediate in size between the craters in the PMMA layers and is formed by the intersection of two circumferential cracks with different radii of curvature which are asymmetrically located on either side of the projectile penetration area. In the center of the substrate plug there is evidence of a residual crater formed by the partial penetration of the projectile. The residual crater is ductile in nature, whereas the fracture surface of the substrate plug is very rough in appearance and shows evidence of substantial crack branching attempts.

Two exceptions to these general observations relative to the PMMA-clad samples concerned sample 31, which was impacted at 368 ft/sec. This sample did not evidence any projectile penetration; however, failure occurred due to radial cracking, which extended through-the-thickness into the PMMA and polycarbonate substrate layers. The other exception concerned samples 64 and 65 which had PMMA cladding, which was almost twice as thick as the remaining samples (except sample 61 which also had a thick coating but was impacted at a higher velocity than samples 64 and 65). Although the coatings on samples 64 and 65 failed with a phenomenology similar to the other PMMA-clad samples, the only damage evident in the polycarbonate substrate was a residual ductile crater formed by the partial penetration of the projectile.

Only two potential problem areas could be identified relative to the ballistic goggles. The first problem is related to why the brittle failure shown in Figure 2 occurred. During impact a spherical compressive pressure wave at the contact surface is developed which is reflected off of free surfaces in the medium as a tensile wave. For debris impact close to the edge of a lens, reflected tensile waves from the lateral free surface of the lens are diffracted around the residual crater formed by the complete or partial penetration of the projectile (see Figure 42). This penetration produces locally high radial stresses at a point, P, on the shadow side of the crater. The solution for the diffracted radial stresses interacting with a cylindrical cavity does not explicitly exist. However, the potential functions for this problem have been determined [Pao and Mow, 1973]. The radial stress field has the character shown in Figure 43, where the stress intensity is shown as a function of distance from the shadow side of the crater. The distance R in Figure 43 establishes the radial distance from the impact zone where the peak stress intensity occurs. The reflected stress wave spherically diverges from the edge of the lens, i.e., proportional to r^{-2} where r is the radial distance from the crater. The incident stress wave is therefore most intense for $\theta=0$ degrees where θ is the subtended angle with reference to a line which intersects P and is normal to T. In conjunction with R, this establishes the site at which the stress levels are most severe and where failure is expected to initiate. Since the reflected stress field for this scenario is predominately radial, the expected failure trajectory is circumferential (see Figure 9) and follows the maximum radial stress contour at this location (see Figure B.5).

As shown in Figure 2, this failure mode is observed experimentally (sample XI) and does not require a fully penetrating crater to evoke this response. This type of failure will also occur at lower incident velocities albeit at distances closer to the edge. As the impact occurs farther from the edge, the reflected tensile waves are more highly dispersed so that by the time the stress wave arrives at the crater, the incident intensity is sufficiently low that the resulting intensification of the stress level by the crater interaction is subcritical (as was the case for samples XII, XIII, and XIV). This problem will also presumably occur for impacts close to the nose bridge in the vicinity of the holes for the snaps, and at lower velocities if the lens is scratched close to an edge. It is also likely that near curved boundaries of the lens (e.g., the edge opposite to the impact region in Figure 2) the stress

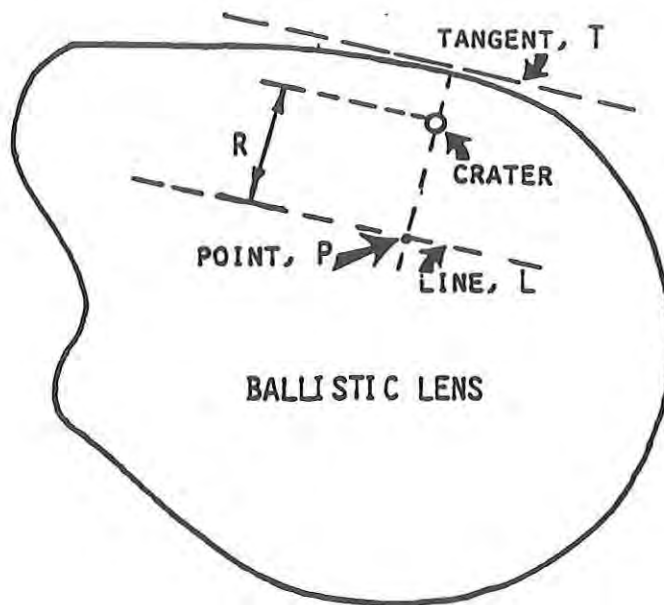


Figure 42. Geometry of Brittle Failure Associated with Debris Impact Near a Lateral Free Surface.

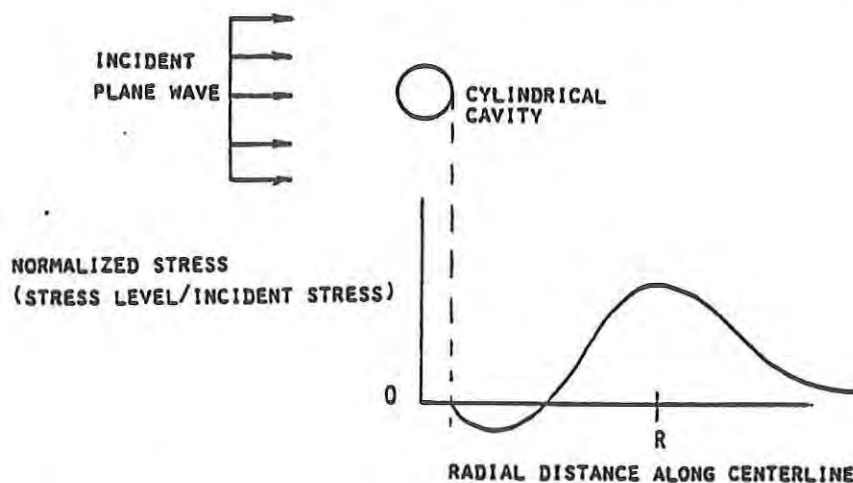


Figure 43. Diffracted Stress Field for an Incident Wave Interacting with a Cylindrical Cavity.

waves instead of spherically diverging could be focused, producing a much more vulnerable region. Unfortunately, Phase I resources did not permit a more thorough experimental demonstration of this problem. The vulnerable region for this failure mode at the specified velocity of 650 ft/sec (in the absence of scratches or other defects) is suspected to be roughly 30 to 40 % of the lens surface area.

The second problem area concerns the use of thicker coatings to mitigate the likelihood of scratches occurring. The ballistic lens currently employs a very thin coating, which cracks almost immediately following any sort of load application. If a thicker coating is employed to provide greater abrasion and/or scratch resistance, a failure mode similar to what was observed in the PMMA-coated polycarbonate samples would be expected. Some typical failure surfaces are shown in Figure 3 for these samples.

Following impact the PMMA layers fail first. The impact layer evidences a crater about the diameter of the projectile which in early time is rectangular since the front surface of the projectile tapers to a rectangle. Radial cracks extend outward from the crater coinciding with the corners of the projectile. These cracks are presumably due to stress concentrations at these locations along with enhanced circumferential stresses due to material being radially pushed out by the projectile. As the projectile penetrates deeper, the crater becomes circular (See Figure 44).

The rear PMMA surface fails due to bending which produces high radial and circumferential tensile stresses at the rear surface. Both radial and circumferential cracking occurs on the rear surface due to these high-bending stresses. When the incident stress wave is reflected off the rear free surface producing high tensile stresses normal to the plane of the PMMA layer, the back surface PMMA delaminates. When the PMMA delaminates the regions defined by the intersection of the radial and circumferential cracks are no longer attached to the polycarbonate substrate. Pie-shaped PMMA debris over a fairly large area is expelled off the rear surface of the sample with a fairly high residual velocity (see Figure 3). The pie-shaped PMMA spall fragments were recovered for some of the experiments.

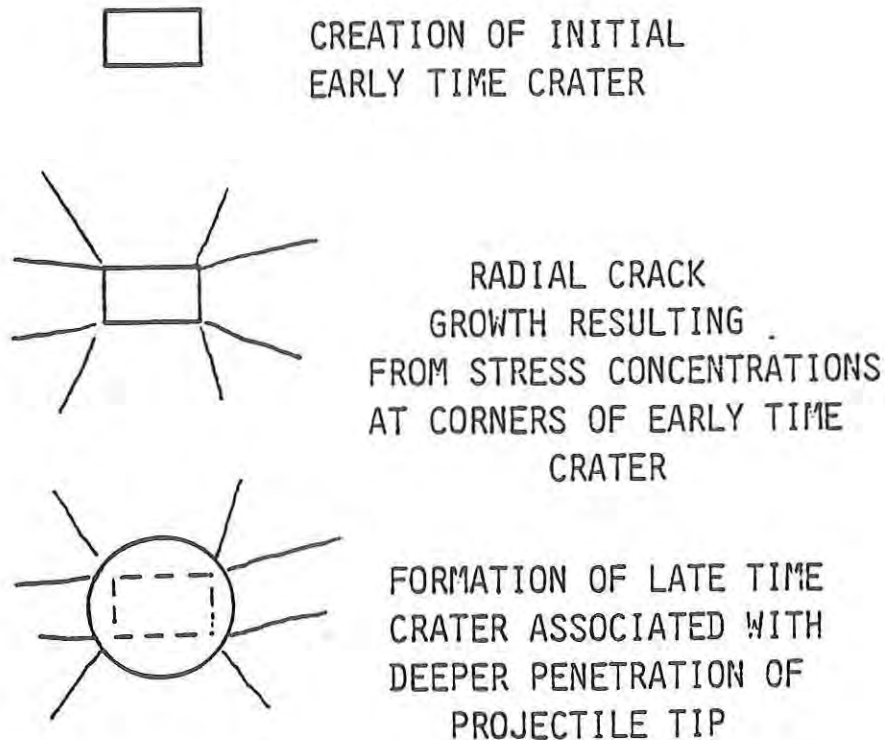


Figure 44. Stages in Radial Crack Formation on PMMA Impact Layer.

Several damage mechanisms are evident in the polycarbonate substrate of the PMMA-clad specimens. First, in all cases a partial crater about the diameter of the projectile was observed. This crater was caused by the ductile penetration of the projectile. Second, 1 to 3 rings of circumferential cracks asymmetrically located on either side of the crater and subtending an angle of 90 to 250 degrees were observed. Secondary radial cracks branching off the main circumferential cracks were also observed. In the velocity regime of approximately 600 to 800 ft/sec the polycarbonate substrate was penetrated due to the intersection of several circumferential cracks. For sample 2-35, in addition to the large diameter plug formed by the circumferential cracking, a secondary annular plug concentric with the first plug was formed by the intersection of a third circumferential crack intersecting the existing crater. In a few cases, a small amount of radial cracking is apparent in the plug. In general however the plug shows no evidence of damage except for the ductile residual crater and the rough fracture surface corresponding to the boundary of the circumferential cracking. The rough fracture surface is caused by cracking branching attempts. At lower velocities, the failure of the PMMA-clad sample was due to radial cracks, which propagated through the thickness of the sample (e.g., Sample 2-32).

Tables C.7 through C.15 document posttest observations relative to residual cracking on each sample. The first column on these tables entitled "Stress Concentration Group" associates groups of radial cracks with a common origin corresponding to a corner of the early time rectangular crater (which has four corners). The next three columns shows the subtended angle in degrees of radial cracks on each layer of the sample. The arrows associate multiple cracks corresponding to related cracks, which have propagated through the thickness of the sample. The difference in angle on the various layers for related cracks allude to the extent of crack curving.

In summary, two major brittle failure modes are observed to occur in polycarbonate which disrupt the ductile damage process and cause premature failure. The first mode shown in Figure 45 [Petrie, 1986] for an uncoated polycarbonate sample exposed to UV light impacted on the unexposed surface corresponds to the development of circumferential cracks caused by enhanced radial tensile stresses. When the plate is impacted on the exposed side, a ductile failure (also shown in Figure 45) is apparent. The second mode shown in Figure 46 [Petrie, 1985] for an uncoated polycarbonate with entrained moisture corresponds to the development of radial cracks which are propagated from the tensile surface of the specimen by circumferential stresses. Both failure modes are stress-related phenomena which occur at the acoustic velocity of the material. In the case of the MRC ballistic tests performed in Task 5, the acoustic velocity of the material is about an order of magnitude greater than the projectile velocity.

In the case of circumferential failure, the rear coating fails due to radial and circumferential cracks induced by bending strains. When the coating delaminates, the coating material is removed over the delaminated area. This all occurs in very early time. A circular region is then weakened at very early time in the substrate due to stress wave effects initiating circumferential cracks. The ductile penetration process begins in the substrate but due to the detachment of an annular ring of circumferentially cracked material, the plug displaces as a rigid body which arrests the ductile failure process.

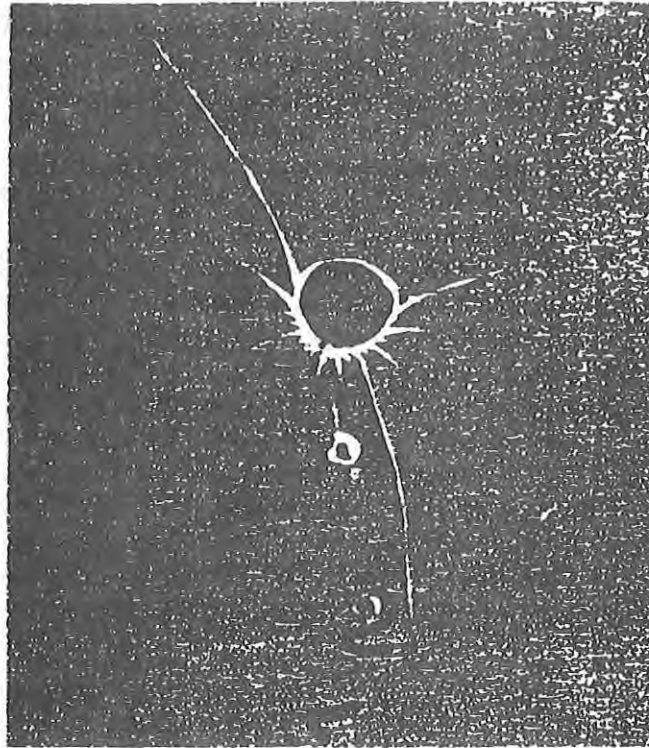


Figure 45. Brittle Failure induced by Circumferential Cracking.

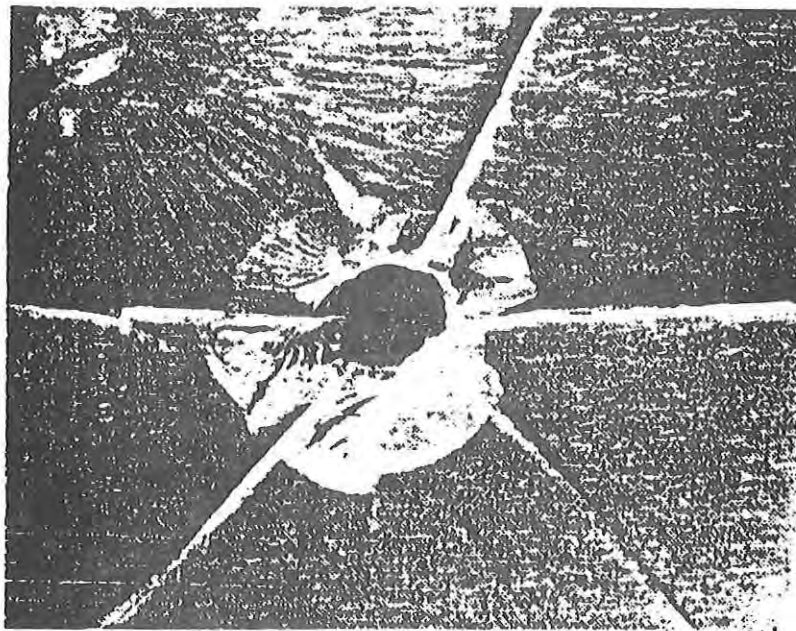


Figure 46. Brittle Failure induce by Radial Cracking.

2.6 Task 6 - Hardening Recommendations.

Strategies to mitigate the damage mechanisms discussed in Sections 2.0 through 2.5 are summarized in Table 10.

Table 10. Mitigation of Damage Mechanisms.

Damage Mechanism	Hardening Strategy
Flexural Deformation <ul style="list-style-type: none">o Low Elongation Coatingo High Modulus Coating	<ul style="list-style-type: none">o Promote Debondingo Strain Isolation<ul style="list-style-type: none">- Debonding- High Interlayer Shear Modulus- Interlayer Thickness- Adhesive Strength
Stress Wave <ul style="list-style-type: none">o Transverse Waveso Waves in Impact Direction	<ul style="list-style-type: none">o Geometry of Lateral Free Surfaceo Interlayer Impedance and Geometry
Fracture Mechanics <ul style="list-style-type: none">o Mitigate Crazingo Attenuate Stress Intensityo Crack Arrest	<ul style="list-style-type: none">o Promote Hydrostatic Stress Componento Residual Compressiono Interlayer Propertieso Allow Coating to Debond
Vibrations <ul style="list-style-type: none">o Shift Eigenfrequencies	<ul style="list-style-type: none">o Boundary Conditions<ul style="list-style-type: none">- Damping Material- Mass

Following impact, flexural deformation of a low elongation coating will result in rupture of the coating very shortly after load application. As was previously shown, particularly for low velocity impact on coated PC targets, this type of damage can lead to brittle failure promoted by radial crack propagation through the coating into the substrate. In this event, the ideal method to mitigate damage propagation from the coating into the substrate is to promote debonding of the coating. This can be accomplished by using bonding techniques which result in a weak coating substrate interface and by employing a sufficient impedance mismatch at the coating substrate interface that high tensile stresses normal to the plane of impact are developed in the coating.

Another alternative for this type of coating is to make the coating sufficiently thin such that the coating thickness is less than the critical crack length required for crack propagation. The stress intensity associated with a crack tip is proportional to crack length so that if the coating is sufficiently thin and fractures immediately, the coating will be relatively stress free and the stress intensity factor associated with the crack tip will be low, resulting in subcritical stresses from the perspective of crack propagation. This approach, however, compromises the abrasion resistance of the PC target and was apparently the approach implemented in the fabrication of the ballistic goggles supplied by Natick.

In the case that the coating is very stiff such that large strains or deformations are not developed except in regions very local to the impact, high stress and damage local to the impact region will be promoted. The appropriate mitigation strategy is to isolate the coating from the substrate. The most extreme method to accomplish this is through debonding. Less extreme methods include in-plane dispersal of the high stress associated with the coating by the selection of appropriate interlayers and bonding techniques or even providing a geometry at the interlayer, which favors in-plane reflection of stress waves. The key idea in all of these strategies is to attenuate high stress which develops in the coating such that at the interface between the coating-substrate-interlayer and the PC substrate, stresses have been severely attenuated. This can be accomplished by providing a coating and coating-substrate interlayer with very high longitudinal and shear wave speeds relative to the wave speed in the impact direction. Additional methods include providing an interlayer with a high shear modulus and sufficient interlayer thickness such that the displacement incompatibility between the coating and substrate can be accommodated. The interlayer can also be designed with material properties which result in attenuation of the dynamic stress intensity in front of a flaw in the coating (see Figures 12 and 13).

In terms of stress wave damage, the lateral free surface of the target can be designed such that the geometry of the target edges reflects in-plane stress waves away from the residual crater caused by the impact. This design will mitigate the effect of stress intensification caused by diffraction of transverse stress waves around residual craters. This damage mechanism led to the brittle failure observed in the ballistic goggles supplied by Natick. Stress waves in the impact direction can be attenuated by suitable selection of interlayer impedance and geometries.

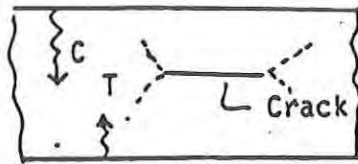
As previously discussed, there are two fundamental-fracture-mechanics related damage mechanisms that give rise to the ductile to brittle transition in coated PC (see Figure 47). In the first case a crack formed in the impact direction continues to propagate in a colinear manner through the substrate. This type of crack propagation is favored by transverse stress waves reflected from the target edges which apply tensile loads to the crack face. The second mechanism for which there was substantial evidence is the formation of an in-plane crack which branches and curves such that it eventually propagates through the substrate. This was observed in one dimensional flyer plate experiments on PC [Curran and Shockley, 1973] as well as during the ballistic testing conducted in Task 5 (see Tables C.7 through C.15).

A necessary condition established experimentally for crack branching/curving to occur in PC is that the crack velocity exceed $0.22 \times$ the dilatational wave speed of the material [Ramalu and Kobayahi, 1985]. Sufficient conditions which were also established experimentally for PC [Sun, et al., 1982; and Ramalu and Kobayahi, 1985] are based on the microstructure of the PC material. That is, the stress field at a characteristic distance, r_0 , from the crack tip must be perturbed such that the maximum principal tensile stress does not occur at $\theta = 0$ degrees (see Figure 48). This occurs if the crack tip is located beyond a critical radial distance within a critical subtended angle. This is the reason why MRC believes that crazing, surface flaws, entrained air and moisture during processing favor a ductile to brittle transition in PC.

As suggested in Table 10, there are three strategies to mitigate these fracture-mechanics-based failure mechanisms. In the most extreme case the crack can be arrested by allowing the coating to debond such that the crack cannot be propagated into the substrate. Secondly, the stress intensification factor can be attenuated by modifying interlayer properties (see Figures 12 and 13) such that crack branching does not occur (see Figure 48). Finally, crazing can be suppressed as a

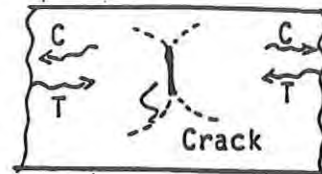
Fracture due to Stress Waves:

Notation: C \rightarrow Compressive; T \rightarrow Tensile



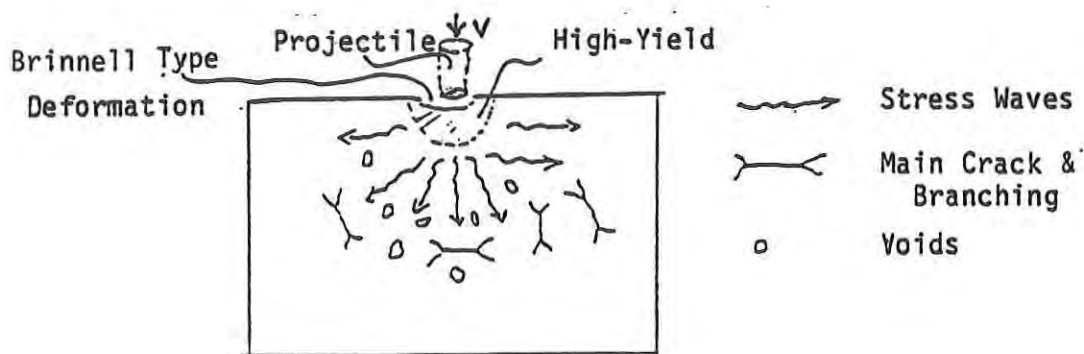
Transverse Cracking

— Main Crack
--- Branching



Longitudinal Cracking

Stress Waves due to Impact Loading



Polycarbonate

Crack Branching SIF: $3.2 \text{ MPa}\sqrt{\text{m}}$

Crack Branching Velocity: $0.22 \times \text{Dilatational Wave Speed}$
($\approx 3.5 \text{ mm}/\mu\text{sec}$)

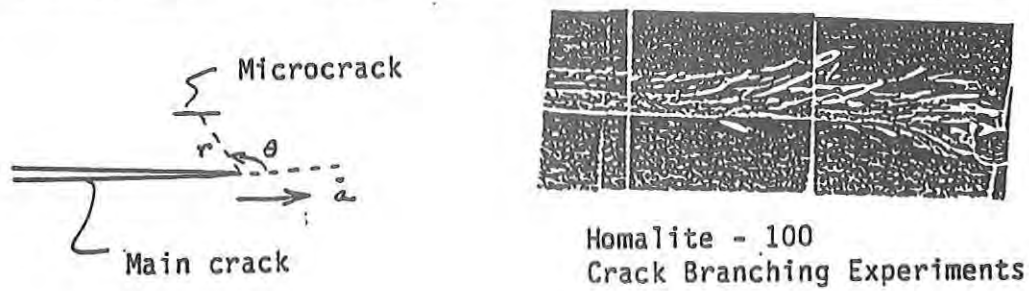
Fracture toughness:

10 KJ/m^2 (plane stress)

1.5 KJ/m^2 (plane strain)

Figure 47. Fracture due to Stress Waves.

Formation of off-axis microcracks and Directional Stability of a crack.



Angular coordinate of the microcrack depends on:

- Micro-structure of the material
- Stress at a characteristic distance r_0 from the crack tip

Necessary and sufficient condition for crack-branching.

$$\begin{array}{l} K_I \geq K_{I6} \\ r_0 \leq r_c \end{array} \quad \swarrow \searrow \quad \text{Material Properties}$$

Successful Branching:

$$2\theta > 20^\circ \text{ (Experimental)}$$

Branching Attempts \longrightarrow Rough crack face

Figure 48. Formation of Off-Axis Microcracks and Directional Stability.

principal deformation mechanism by promoting the hydrostatic stress component during processing or residual compression during fabrication.

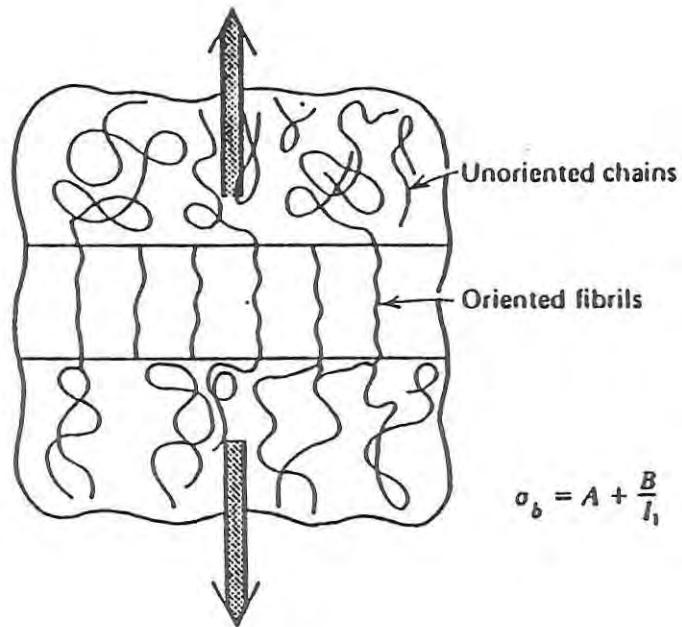
The two principal deformation mechanisms in amorphous polymers are shown in Figure 49. These mechanisms include shear yielding which is a function of the octahedral yield stress and crazing which is a function of the difference in principal stress, i.e., stress bias. Crazing as shown in Figure 50 will only occur for combinations of principal stress which result in a net normal tensile stress field. The determination of which deformation mechanism occurs depends upon whether the criteria associated with crazing ("normal stress yielding" in Figure 50) or the shear yielding is exceeded first. The analytical form of the criteria are shown in Figure 49.

In Figures 50(a) and (b) the locus associated with shear yielding is shown superimposed on two different crazing thresholds ("normal shear yielding"). In Figure 50(a) the crazing threshold is below the yield threshold in the first quadrant of the principal stress plot. For applied loads which result in stress fields corresponding to this first quadrant, crazing will tend to occur preferentially as opposed to shear yielding. In Figure 50(b) where the crazing threshold is larger than the yield locus, shear yielding will tend to occur preferentially for stress states laying in the first quadrant. When shear yielding is the principal deformation mechanism, ductile failure will tend to occur. Crazing on the other hand is shown experimentally to be almost invariably associated with brittle failure. We hypothesize that crazing results in a distribution of microflaws, which: (1) due to the associated reduction in fracture toughness result in accelerated crack velocities; and (2) promote crack branching consistent with the mechanism presented above. Thus, by encouraging the development of hydrostatic stress or residual compression during or after processing, the crazing threshold will intercept the yield locus for larger values of stress bias alleviating the tendency for crazing as a principal deformation mechanism.

The final mitigation strategy involves shifting resonant eigenfrequencies associated with vibration of the target by adding damping material to target supports or lumped mass to the target itself. Target response associated with vibrations was not seen to be a principal damage mechanism for targets investigated in Phase I (due to the relatively low natural frequencies of the Phase I targets). It is conceivably an effective strategy for stiffer targets with higher natural frequencies and/or forcing functions with thicker pulse widths (such as might occur with thicker targets or projectiles, or thicker targets with significant projectile penetration).

A goal of the Phase II research would be to quantify the effectiveness of the various mitigation strategies now that insight has been garnered relative to the various causes of the ductile to brittle transition in PC materials.

DEFORMATION MECHANISMS IN AMORPHOUS POLYMERS



$$\sigma_b = A + \frac{B}{I_1}$$

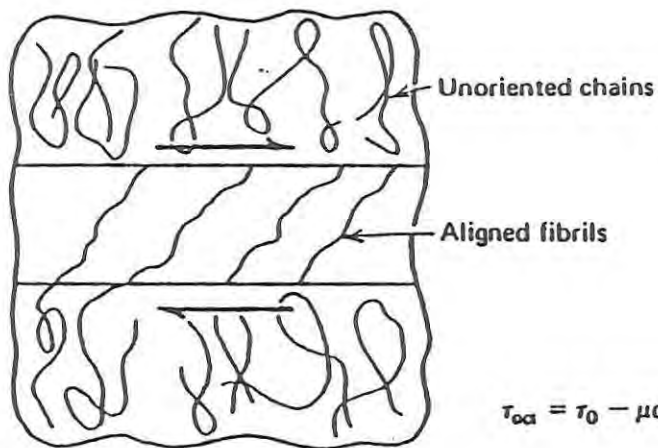
$$\sigma_b = |\sigma_1 - \sigma_2| = A(T) + \frac{B(T)}{I_1}$$

where

σ_b = stress bias given by the difference in principal stresses σ_1 and σ_2

$A(T), B(T)$ = temperature-dependent material constants

$I_1 = \sigma_1 + \sigma_2$, which must be positive to provide the necessary dilatation for craze formation



$$\tau_{oct} = \tau_0 - \mu \sigma_m$$

$$\tau_{oct} = \tau_0 - \mu \sigma_m$$

where

τ_{oct} = octahedral yield stress

τ_0 = rate- and temperature-dependent octahedral yield stress found for pure shear ($\sigma_m = 0$)

$$\sigma_m = (\sigma_1 + \sigma_2)/2$$

μ = material constant

Figure 49. Deformation Mechanisms in Amorphous Polymers.

DEFORMATION MECHANISMS IN AMORPHOUS POLYMERS

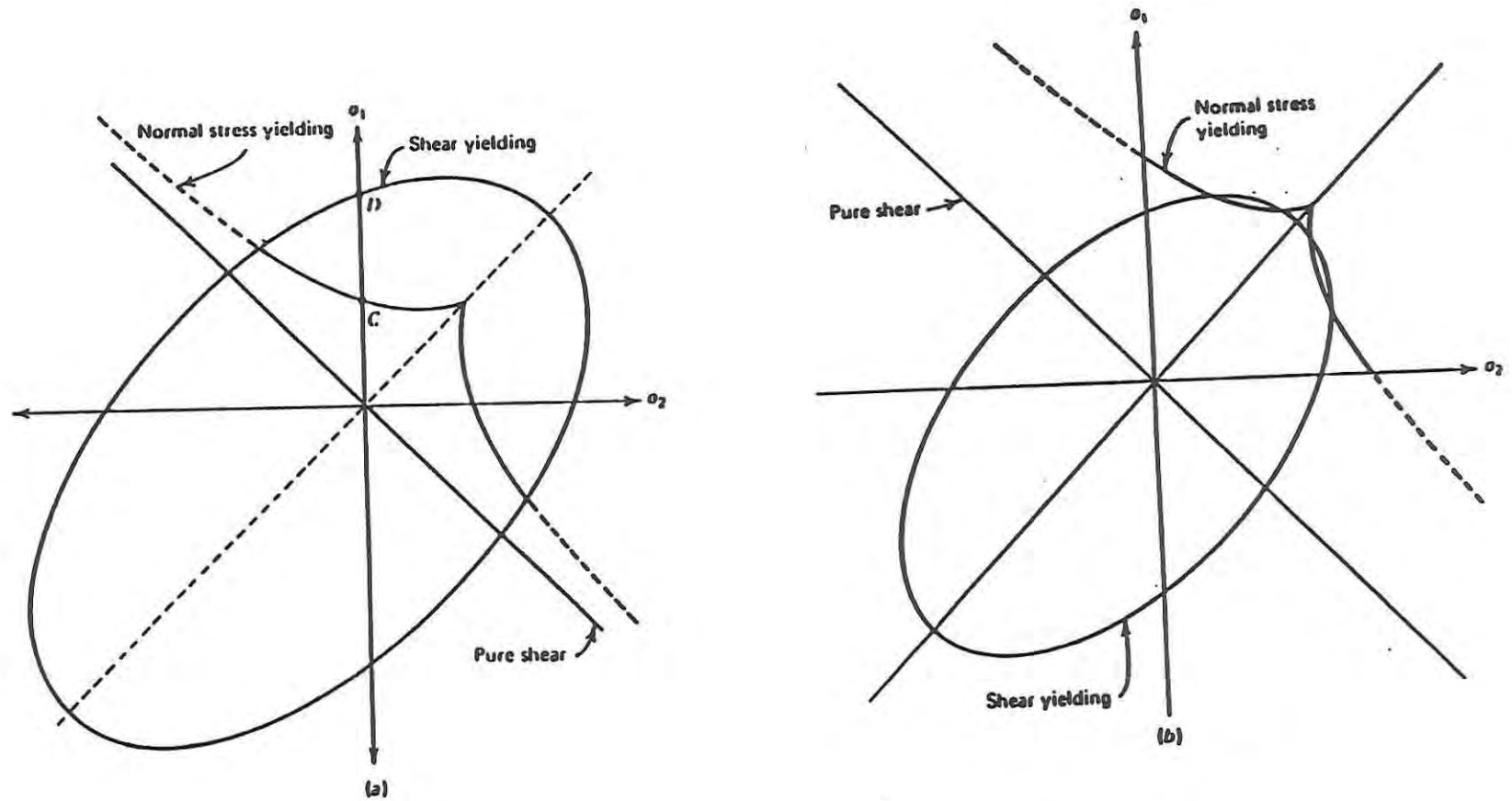


Figure 50. Shear Yielding and Crazing Envelopes in Amorphous Polymers.

3.0 PHASE I CONCLUSIONS

The ductile to brittle transition in the mechanical behavior associated with the impact response of coated PC targets were experimentally and analytically investigated as part of this Phase I effort. The brittle failure modes resulting from this ductile to brittle transition were seen to be of two generic types. The first mode resulted in extensive in-plane cracking and overall weakening of the coating-PC substrate assembly. The second mode resulted in circumferential failure of the PC substrate and removal of a large diameter plug from the target.

The first type of brittle failure tended to occur on coatings of moderate thickness at low impact velocities and was promoted by radial crack propagation, which initiated in the coating of the PC target and subsequently propagated through the PC substrate. The second type of transition was promoted by circumferential crack propagation engendered by reflected stress waves from the PC substrate-coating interface. This type of failure was promoted in coatings of moderate thickness at high impact velocities and in thick coatings at low and high impact velocities. Coatings that are very thin and which fail shortly after load application do not seem to affect the ductile to brittle transition in PC; however, the protective function of the coating is severely compromised.

The brittle failure observed following impact of the ballistic goggles was unrelated to the presence of a coating although failure occurred due to propagation of a large diameter circumferential fracture. The coating employed on the ballistic goggles was extremely thin and failed almost immediately following load application. The brittle failure occurred due to the interaction of stress waves reflected from the edge of the lens with the residual crater formed by the initial stages of ductile penetration by the projectile. This type of brittle failure results in detachment of a hemispherical region of lens material and requires the impact to be within a critical distance of the target edge. The surface area corresponding to this vulnerable distance represents something on the order of 30% of the lens surface.

Finally, a brittle failure occurred on an uncoated PC target subject to a low velocity impact. This failure occurred due to radial crack propagation originating from a surface flaw following fabrication.

In all cases of brittle failure, the initial stages of ductile crater formation were observed in the impact region suggesting that the rheological behavior of the PC material has not changed. Rather, alternative failure modes are excited and occur on a time scale much faster than the ductile failure process. Both stress waves and fractures are propagated at the acoustic velocity of the medium, which is substantially faster than the projectile penetration and the flow rate associated with shear yielding.

A new Equation-Of-State (EOS) model was developed for polycarbonate based on experimental results reported by the Los Alamos National Laboratory and the Stanford Research Institute. Stress wave analysis employing the new EOS formulation was conducted in one dimension employing closed form elastic solutions and the PUFF74 stress wave response code. Two dimensional stress wave analysis was conducted using the AUTODYN finite difference code. Parameter studies were conducted using different projectile and target thickness as well as various interlayers. High circumferential tensile stresses which promote radial crack propagation were analytically predicted for low velocity impact on coatings of moderate thickness. High radial stresses which promote circumferential failure were analytically predicted to occur for high velocity impact on moderately

thick coatings and high velocity impact on thick coatings. Analytical predictions correlated qualitatively with the results of ballistic testing in Task 5 and quantitatively with respect to the size of the damaged region.

Various fracture mechanics based mechanisms were discussed as contributing to the ductile to brittle impact behavior of PC. In the case of an in-plane crack initiating in the PC target coating following impact, crack branching/curving is required for propagation into the substrate. Experimental evidence from the literature was cited indicating that a critical distribution of microflaws was necessary to effect this behavior. Crazeing, entrained moisture, and/or surface flaws are seen as necessary conditions to achieve this distribution. In the case of colinear fracture propagation through the substrate, experimental evidence from the literature was cited indicating that interlayer properties are critical to effect this behavior. Preliminary analysis and a more in-depth approach to analytically model these two type of fracture propagation behaviors was defined in Task 4.

Both static analysis and frequency analysis using closed form small displacement elastic solutions and the COSMOS finite element code were implemented. Analytical results indicated that for the target configurations examined in Phase I that these effects were not of first order significance.

Finally, a number of countermeasures were proposed for all of the effects contributing to the occurrence of brittle failure in coated PC targets. These countermeasures are summarized in Table 10. Most of the countermeasures are easy to implement and there exist sufficient alternatives that where applications prohibit implementation of one countermeasure (for example allowing the coating to debond) alternative countermeasures are available.

4.0 REFERENCES

- Achenbach, J. D., *Wave Propagation in Elastic Solids*, North-Holland Publishing Company, New York, 1976.
- Arenberg, D. L., J. Acoustical Society of America, 20(1948), 1. Seen in Achenbach, J. D., *Wave Propagation in Elastic Solids*, North-Holland Publishing Company, New York, 1976.
- Beason, L. W. and Morgan, J. R., "Glass Failure Prediction Model," *Journal of Structural Engineering*, Vol. 110, No. 2, February 1984.
- Ball, G.L. et al., "Evaluation of Improved Transparent Materials and Adhesives for Ballistic and Impact Shields," AFML-TR-70-167, July 1970.
- Ballard, C.P., Jr., "A Transparent Ceramic Armor," SAND77-1736, Sandia Labs, Albuquerque, NM, May 1978.
- Bouchard, T., Olszewski, W.V., and LeGrand, D.G., "Nondestructive Evaluation of Residual Stresses and Orientation in Polycarbonate Resin", *ANTEC*, pp. 393-397, 1986.
- Brekhovskikh, L. M., *Waves in Layered Media*, Second Edition, Academic Press, New York, 1980.
- Broutman, Lawrence J., "The Control of Polymer Mechanical Behavior by Surface Modification", Illinois Institute of Technology, Chicago, IL, ARO 16425.3-MS, May 15, 1986.
- Buchdahl, R., "The Rheology of Organic Glasses," *Rheology: Theory and Applications*, Eirich, F. R. (ed.), Vol. II, Academic Press, New York, 1958.
- Buckley, C.P., et al., *Principles of Polymer Engineering*, Oxford University Press, New York, 1988.
- Carter, W.J., Marsh, S.P., "Hugoniot Equations of State of Polymers", Los Alamos Scientific Laboratory unpublished report LA-UR-77-2062 (1977) referenced in LASL Shock Hugoniot Data, Stanley P. Marsh, University of California Press, Los Angeles, CA, 1980.
- Cecil, R. A., Newlander, C. D., et al., *PUFF74: A Material Response Code*, AFWL-TR-76-43, Air Force Weapons Laboratory, Kirtland AFB, NM, June 1976.
- Celantano, J.T., et al., "Exploratory Development to Show Technical Feasibility of Automatic Fabrication of Spectacle Lenses in the Field", Life Systems Research Institute, Los Angeles, CA, 19 March 1971.
- Charest, J.A. and Lynch, C.S., "The Use of Commercial Piezofilms for Stress Wave Measurements", Dynasen Inc., Presented at the 38th ARA Meeting, Tokyo, Japan, October 6-9, 1987
- Chatterjee, A. K., and Knopoff, L., "On the Effect of Material Interface on Crack Propagation," Unpublished, University of California, Los Angeles, 1984.

Cherepanov, G. P., *Mechanics of Brittle Failure*, McGraw-Hill Inc., New York, 1979.

Curran, D. R., et al., *Impact Dynamics*, John Wiley & Sons, New York, 1982.

Curran, D.R. and Shockey, D.A., "Dynamic Fracture Criteria for Polycarbonate and Polyimide", Final Report, Contract DAAD05-71-C-0180, Stanford Research Institute, Menlo Park, CA, BRL-CR-91, USA Ballistic Research Laboratories, Aberdeen Proving Ground, MD, March 1973.

Dally, J. W., and Kobayashi, T., "Crack Arrest in Duplex Specimens," *Int. J., Solids Structures*, vol. 14, 1978.

Davis, A. and Sims, D., *Weathering of Polymers*, Applied Science Publishers, Barking Essex, England, 1983.

DeBona, B.T., "High Temperature Windshield/Canopy Materials Development", Allied Corporation, Morristown, NJ, AFML-TR-81-4178, January 1982.

Dekkers, M.E., Hobbs, S.Y., Watkins, V.H., "Toughened Blends of Poly(butylene terephthalate) and BPA Polycarbonate, Part 2-Toughening Mechanisms", *Journal of Materials Science*, 23, pp. 1225-1230, 1988.

Durelli, A.J. and Riley, W.F., "Experiments for the Determination of Transient Stress and Strain Distributions in Two-Dimensional Problems", *Journal of Applied Mechanics*, Vol. 22, No. 8, 1982.
Dynasen, Inc., "Shock Pressure Sensors and Impact Facilities", Goleta, CA, no date.

Eirich, Frederick R. (edited), et al., *Rheology, Theory and Applications*, Volume II, Academic Press Inc., New York, 1958.

Eisler, R. D., "Effect of Coatings and Processing on Failure Mechanisms of Polycarbonate Materials," Mission Research Corporation, Costa Mesa, CA, Phase I SBIR Proposal, MRC-COM-P-7103.60, 5 January 1988.

Eisler, R. D., "Clarification and Amendment of Phase I SBIR Proposal," Mission Research Corporation, Costa Mesa, California, MRC-COM-88-0169, 10 May 1988.

Eisler, R. D., Chatterjee, A. K., and Newlander, C. D., "Failure Mechanisms in Polycarbonate," First Progress Report for Contract DAAK60-89-C-0011, Mission Research Corporation, MRC-COM-R-89-0234, Costa Mesa, California, 14 March 1989.

Eisler, R. D., and Chatterjee, A. K., "Failure Mechanisms of Polycarbonate," Presentation at Natick RD&E Center, 13 April 1989.

Eisler, R. D., Chatterjee, A. K., and Koivu, A. H., "Failure Mechanisms in Polycarbonate," Second Progress Report for Contract DAAK60-89-C-0011, Mission Research Corporation, MRC-COM-R-89-0239, Costa Mesa, California, 15 July 1989.

Eisler, R. D., Burghart, G., and Stone, S. F., "Failure Mechanisms in Polycarbonate," Third Progress Report for Contract DAAK60-89-C-0011, Mission Research Corporation, MRC-COM-R-89-0241,

Costa Mesa, California, 31 July 1989.

Eringen, A. C. (editor), *Penetration Mechanics*, Pergamon Press, 1978.

Ewing, W. M., Jardetzky, W. S., and Press, F., *Elastic Waves in Layered Media*, McGraw-Hill Book Company, New York, 1957.

Fish, R.H., "The Penetration of Porous Projectiles in Aluminum and Plastic Targets," NASA TN D-4505, NASA Ames, Moffett Field, CA, April 1968.

Garey, H. E., "Scratch-Resistant Films for Glass and Plastics," *Polymer Plastics Technology and Engineering*, 28(1), 73-106 (1989).

Golden, J. H., et al., *Journal of Polymer Science*, 2A, 1964, p. 4787.

Goolsby, R.D., and Miller, J.M., "Instrumented Impact Fracture Toughness Testing of Polycarbonate", *ANTEC*, pp. 561-564, 1984.

Gover, J. and Browning, J., "Stress Wave Generation by Radiation Absorption", Sandia National Laboratories, Albuquerque, NM, June 1987.

Grigoryan, S. S., "Nature of 'Ultradeep' Penetration of Solid Microparticles into Solids", Scientific-Research Institute of Mechanics at the M.V. Lomonosov State University, Moscow, seen in American Institute of Physics, 1987.

Haddaoui, N., Chudnovsky, A., and Moet, A., "Ductile Fatigue Crack Propagation in Polycarbonate", *Polymer*, Vol. 27, September 1986.

Hansen, M.G., and Bland, D.G., "Impact Strength and Melt Viscosity of Bisphenol-A-Polycarbonate and Styrene-Maleic-Anhydride Copolymer Blends," *Polymer Engineering and Science*, Vol. 25, No. 14, p. 896, Mid-October, 1985.

Hassard, R. S., "Design Criteria Transparent Polycarbonate Plastic Sheet", Goodyear Aerospace Corp., Litchfield Park, AZ, Report No. AFML-TR-72-117, August 1972.

Hassett, R.J., et al., "Protective Eye Shield Against Small Fragments," NOLTR 70-202, US Naval Ordnance Lab, 1 June 1970.

Hayashi, Tsuyoshi; Kawata, Kozo; and Umekawa, Sokichi; "Progress in Science and Engineering of Composites, Volume 1", *Proceedings of the Fourth International Conference on Composite Materials*, ICCM-IV, Tokyo, Japan, 25-28 October 1982.

Heath, J.B.R., et al., "Comparison of Bullet Resistance of New and Aged Polycarbonate," AFWAL-TR-83-4154, *Conference on Aerospace Transparent Materials and Enclosures*, December 1983.

Henry, M. C., "Transparent Armor," *Ballistic Materials and Penetration Mechanics*, R.C. Laible (ed.),

Elsevier Scientific Publishing Co., New York, 1980.

Hertzberg, R. W., *Deformation and Fracture Mechanics of Engineering Materials*, Second Edition, John Wiley & Sons, New York, 1976.

Hillig, W.B., "Impact Response Characteristics of Polymeric Matrices," Final Report, AD-A015 131, General Electric, Schenectady, NY, August 1975.

Hillig, W.B., "Impact Response Characteristics of Polymeric Materials," Final Report, General Electric, Schenectady, NY, September 1976.

Hillig, W.B., "Dynamic Impact Response Behavior of Polymeric Materials," Final Report, General Electric, Schenectady, NY, August 1977.

Hull, D., *Polymeric Materials*, ASM, Metals Park, Ohio, 1975, P. 487.

Huyett, R. A., and Wintermute, G.E., "Environmental Resistance of Coated and Laminated Polycarbonate Transparencies", Goodyear Aerospace Corporation, Report No. AFML-TR-76-24, Litchfield Park, AZ, March 1976.

Hyakutake, Hiizu; and Nisitani, Hironobu; "Conditions for Ductile and Brittle Fracture in Notched Polycarbonate Bars", *JSME International*, Vol. 30, No. 259, 1987.

Jacobson, S.S., "Penetration of a Transparent Medium by Rigid Blunt-And-Conical-Nosed Bodies of Revolution," Picatinny Arsenal, Dover, NJ, December 1975.

Jacopi, A.V., and White, J.R., "Residual Stress, Aging and Fatigue Fracture in Injection-Molded Glassy Polymers. II. Polycarbonate", *Journal of Applied Polymer Science*, Vol. 33, 607-623, 1987.

Jones, H.L., and Yu, R., "The Quantitative Molding and Finishing Effects of Moisture in Polycarbonate on the Physical and Chemical Properties of Structural Foam," *Proc. of the S.P.I. 9th Annual Foam Conference*, 1981

Juran, R. (editor), et al., *Modern Plastics Encyclopedia*, McGraw Hill Inc., October 1989.

Kenig, S., et al., "Tensile Failure of Weathered Polycarbonate", *Polymer Engineering*, Mid-June, Kay, B.F., "Design, Test and Acceptance Criteria for Helicopter Transparent Enclosures," USARTL-TR-78-26, United Technologies Corp., Stratford, Conn, November 1978.

Kohlman, W.G., US Army Natick RD&E/STRNC-YSM, Correspondence to R.D. Eisler/Mission Research Corporation, Transmittal and description of 15.7 grain fragment simulating projectile test data on uncoated polycarbonate sheets, 1 June 1989.

Knopoff, L., Undocumented personal communication, University of California, Los Angeles, May 1989.

- Kuo, An-Yu, "Dynamic Analysis of Interfacial Cracks in Composite Materials," Ph.D Dissertation, Department of Theoretical and Applied Mechanics, University of Illinois at Urbana-Champaign, 1982.
- Laible, R.C. (editor), *Ballistic Materials and Penetration Mechanics*, Volume 5 of Methods and Phenomena: Their Applications in Science and Technology, Elsevier Scientific Publishing Company, 1980.
- Lee, O.S., "Tertiary Ductile Fracture Process in Polycarbonate (PC) Specimens", *Journal of Materials Science Letters*, 4, pp. 125-128, 1985.
- Marsh, S. P. (editor), *LASL Shock Hugoniot Data*, University of California Press, Los Angeles, CA, 1980.
- Margolis, J.M., *Engineering Thermoplastics, Properties and Applications*, Marcel Dekker, Inc., New York, 1985.
- Matsumoto, D.S., and Gifford, S.K., "Competing Fatigue Mechanisms in BPA- Polycarbonate", *Journal of Materials Science*, 4, pp. 4610-4616, 1985.
- McCrum, N. G., et al., *Principles of Polymer Engineering*, Oxford University Press, New York, 1988.
- McDonald, W. C., Plumer, J. R., "Evaluation of Scratch- and Spall-Resistant Windshields", Army Materials and Mechanics Research Center, Watertown, Mass, Report No. 76-22, December 1976.
- McDonough, T. B., and Rourke, J. E., "Application of Integral Theory of Impact to Improving Transparency Resistance to Ballistic Fragment Threats", Aeronautical Research Associates of Princeton, Inc., Report No. AFFDL-TR-79-3156, January 1980.
- Michalske, T. A. and Bunker, B. C., "The Fracturing of Glass," *Scientific American*, December 1987.
- "Military Standard, Nomenclature and Definitions in the Ammunition Area," MIL-STD-444, Notice 3, 31 March 1988.
- "Military Specification, Projectile, Calibers .22, .30, .50 and 20MM, Fragment - Simulating," MIL-P-46593A(MU), Amendment 1, 12 October 1964.
- "Military Standard, V50 Ballistic Test for Armor," MIL-STD-662E, 22 January 1987.
- "Military Specification, Visors, Shatter Resistant," MIL-V-85374(AS), Amendment 1 dated 9 January 1981.
- "Military Standard, Weapon Caliber and Ammunition, Metric System for Identification of", DOD-STD-396, 8 December 1977.
- Morgan, R. J., and O'Neal, J. E., "Modes of Deformation and Failure of Polycarbonate", *Polymer*, Vol. 20, March 1979.

Morgan, R. J., and O'Neal, J. E.; "The Effect of Thermal History on the Mechanical Properties and Crystallinity of Polycarbonate", McDonnell Douglas Research Laboratories, St. Louis, MO, Report No. MDRL 75-37, November 1975.

Morgan, R. J., and Mones, E. T.; "Environmentally Enhanced Crazing in Polymers", Lawrence Livermore Laboratory, Report UCRL-82488, March 29, 1979.

Morgan, R. J. and O'Neal, J. E., "The Relationship Between the Physical Structure and the Mechanical Properties of Polycarbonate", *Journal of Polymer Science*, Vol. 14, 1976.

Newlander, C. D., Technical Memorandum, Mission Research Corporation, Costa Mesa, CA, MRC-COM-87-0187, 29 July 1987.

Nimmer, R.P., Moran, H., and Tryson, G.R., "Impact Response of a Polymeric Structure - Comparison of Analysis and Experiment", *ANTEC*, 1984, pp 565 - 568

Pao, Y. H., and Mow, C. C., *Diffraction of Elastic Waves and Dynamic Stress Concentrations*, Rand Corporation, Crane, Russak & Company, Inc., New York, 1973.

Perepechko, I.I., *An Introduction to Polymer Physics*, Mir Publishers, Moscow, 1981.

Petrie, S.P., "The Brittle Failure of Polycarbonate in High Rate Impact", 630-633, *ANTEC*, 1985.

Petrie, S.P., "The Effect of UV Degradation on the Behavior of Polycarbonate in High Rate Impact", 605-609, *ANTEC*, 1986.

Pitman, G.L., Ward, I.M., and Duckett, R.A., "The Effects of Thermal Pre- Treatment and Molecular Weight on the Impact Behavior of Polycarbonate", *Journal of Materials Science*, 13, pp. 2092-2104, 1978.

Plumer, J. R., "Development of Scratch- and Spall-Resistant Windshields", Army Materials and Mechanics Research Center, Watertown, Mass, Report No. AMMRC TR 72-19, August 1974.

Recht, R. F., and Ipson, T. W., "Ballistic Perforation Dynamics", *Journal of Applied Mechanics*, pp. 384-390, September 1963.

Reed, P.E., and Turner, S, "Flexed Plate Impact Testing V: Injection Moulded Polycarbonate Discs", *Plastics and Rubber Processing and Applications*, 8, pp. 173-179, 1987.

Rice, M. H., "PUFF74 EOS Compilation," Final Report, AFWL Contract F29601-79-C-0026, Systems, Science and Software, La Jolla, CA, February 1980.

Roseblade, R. J., "The Effect of Injection Moulding Processing Parameters on the Environment" Materials Research Labs, Australia, August 1983.

Roy, Arabinda, "Pulse Generation in an Elastic Half Space by Normal Pressure", *Int. J. Engng Sci.*, 1975, Vol. 13, pp. 641-651, Pergamon Press.

Shelton, Ralph, "Transparent Polyolefin Film Armor", Swedlow, Inc., Garden Grove, CA, Report No. AMMRC TR 81-41, August 1981.

Singh, R.K., and Parihar, K.S., "The J-Integral as a Fracture Criterion for Polycarbonate Thermoplastic," *Journal of Materials Science*, 21, pp. 3921-3926, 1986.

Skidmore, I. C., An Introduction to Shock Waves in Solids, Atomic Weapons Research Establishment, Aldermaston, Berks, U.K., Applied Materials Research, pp. 131-147, July 1965.

Smith, Rodney W., "Statement of Need Clothing and Equipment, Ballistic Eye Protection for Emmetropes (BEPE)", U.S. Army, Action Control Number 70779, 24 June 1984.

Stokes, V.K., and Nied, H.F., "Lateral Strain Effects During the Large Extension of Thermoplastics," *Polymer Engineering and Science*, Vol. 28, No. 19, page 1209, Mid-October 1988.

Stone, S. F., Technical Memorandum, Mission Research Corporation, Costa Mesa, CA, MRC-COM-87-202, 21 August 1987.

Stone, S. F., and Chatterjee, A. K., "Modeling Techniques for Composites Subjected to Rapid Thermal Loading", Eighth Mission Research Progress Report for AFWAL Contract F33615-87-C-3247, MRC-COM-R-0219, Costa Mesa, CA, 10 February 1989.

Sun, Y.-J., et al., "Further Studies on Dynamic Crack Curving," *Selected Papers on the 11th Southwestern Conference in Theoretical and Applied Mechanics*, University of Alabama, Huntsville, 1982.

Takemori, M.T., "Fatigue Fracture of Polycarbonate," *Polymer Engineering and Science*, Vol. 22, No. 15, page 937, October 1982.

Thakkar, B.S., and Broutman, I.J., "Impact Strength of Polymers. 3: The Effect of Annealing on Cold Worked Polycarbonates", *Polymer Engineering and Science*, Vol. 21, No. 3, page 155, February 1981.

Theocaris, P. S., and Pazis, D., "Crack Deflection and Arrest Phenomena at an Oblique Bimaterial Interface," *Int. J. Solids and Structures*, vol 19, pp. 611-623, 1983.

Thermofil, Engineering Thermoplastics, "R2 Series Polycarbonate Alloys"

"US Army Test and Evaluation Command Test Operations Procedure, Ballistic Tests of Armor Materials, Final", US Army Aberdeen Proving Ground, Report No. TOP 2-2-710, 7 February 1984.

"US Army Test and Evaluation Command Test Operations Procedure, Projectile Velocity Measurements, Final", US Army Aberdeen Proving Ground, Report No. TOP 4-2-805, 21 September 1982.

Voss, D.L., "Urethane-Clad Polycarbonate," *SPE National Tech Conference on High Performance Plastics*, Cleveland, OH, 1976.

Voss, D.L., and Barham, S.A., "Impact Resistant Glass-Polycarbonate Glazing," *SPE Pacific Tech Conference*, 4th Annual, 1979.

Wheeler, O. E., "Spectrum Loading and Crack Growth," *J. Basic Engineering*, Transactions ASME, March 1972.

Wilde, A.F., et al., "Synthesis and Ballistic Evaluation of Selected Transparent Polyurethane Block Copolymers, Part III: Further Efforts to Optimize Ballistic Performance," AMMRC TR 76-31, Army Materials and Mechanics Research Center, Watertown, Mass, September 1976.

Yang, J. C. S., and Chun, D. S., "Application of the Hertz Contact Law to Problems of Impact in Plates", United States Naval Ordnance Laboratory, White Oak, MD, 5 September 1969.

APPENDICES

APPENDIX A: STRESS WAVE ANALYSIS

A.1 One-Dimensional Stress Wave Analysis

A.2 Two-Dimensional Stress Wave Analysis

A.2.1 High Velocity Impact

A.2.2 Low Velocity Impact

A.2.2.1 Without Preexisting Defect

A.2.2.2 With Preexisting Defect

APPENDIX A.1 - One Dimensional Stress Wave Analysis

<u>Figure</u>		<u>Page</u>
A.1	Predicted One Dimensional Stress Wave Response for 0.25 inch PC Impacted by 0.05 inch Steel Flyer Plate Incident at 600 cm/sec	93
A.2	Predicted One Dimensional Stress Wave Response for 0.25 inch PC Impacted by 0.05 inch Steel Flyer Plate Incident at 6,000 cm/sec	94
A.3	Predicted One Dimensional Stress Wave Response for 0.25 inch PC Impacted by 0.05 inch Steel Flyer Plate Incident at 60,000 cm/sec	95
A.4	Predicted One Dimensional Stress Wave Response for 0.25 inch PC Impacted by 0.25 inch Steel Flyer Plate Incident at 600 cm/sec	96
A.5	Predicted One Dimensional Stress Wave Response for 0.25 inch PC Impacted by 0.25 inch Steel Flyer Plate Incident at 6,000 cm/sec	97
A.6	Predicted One Dimensional Stress Wave Response for 0.25 inch PC Impacted by 0.25 inch Steel Flyer Plate Incident at 60,000 cm/sec	98
A.7	Predicted One Dimensional Stress Wave Response for 0.25 inch PC Impacted by 1.25 inch Steel Flyer Plate Incident at 600 cm/sec	99
A.8	Predicted One Dimensional Stress Wave Response for 0.25 inch PC Impacted by 1.25 inch Steel Flyer Plate Incident at 6,000 cm/sec	100
A.9	Predicted One Dimensional Stress Wave Response for 0.25 inch PC Impacted by 1.25 inch Steel Flyer Plate Incident at 60,000 cm/sec	101
A.10	Predicted One Dimensional Stress Wave Response for 0.25 inch PC with 0.05 inch PMMA Coating Impacted by 1.25 inch Steel Flyer Plate Incident at 6,000 cm/sec	102
A.11	Predicted One Dimensional Stress Wave Response for 0.25 inch PC with 0.20 inch PMMA Coating Impacted by 1.25 inch Steel Flyer Plate Incident at 6,000 cm/sec	103
A.12	Predicted One Dimensional Stress Wave Response for 0.25 inch PC with 0.20 inch PMMA Coating and 0.01 inch RS1305 Silicone Adhesive Impacted by 1.25 inch Steel Flyer Plate Incident at 6,000 cm/sec	104

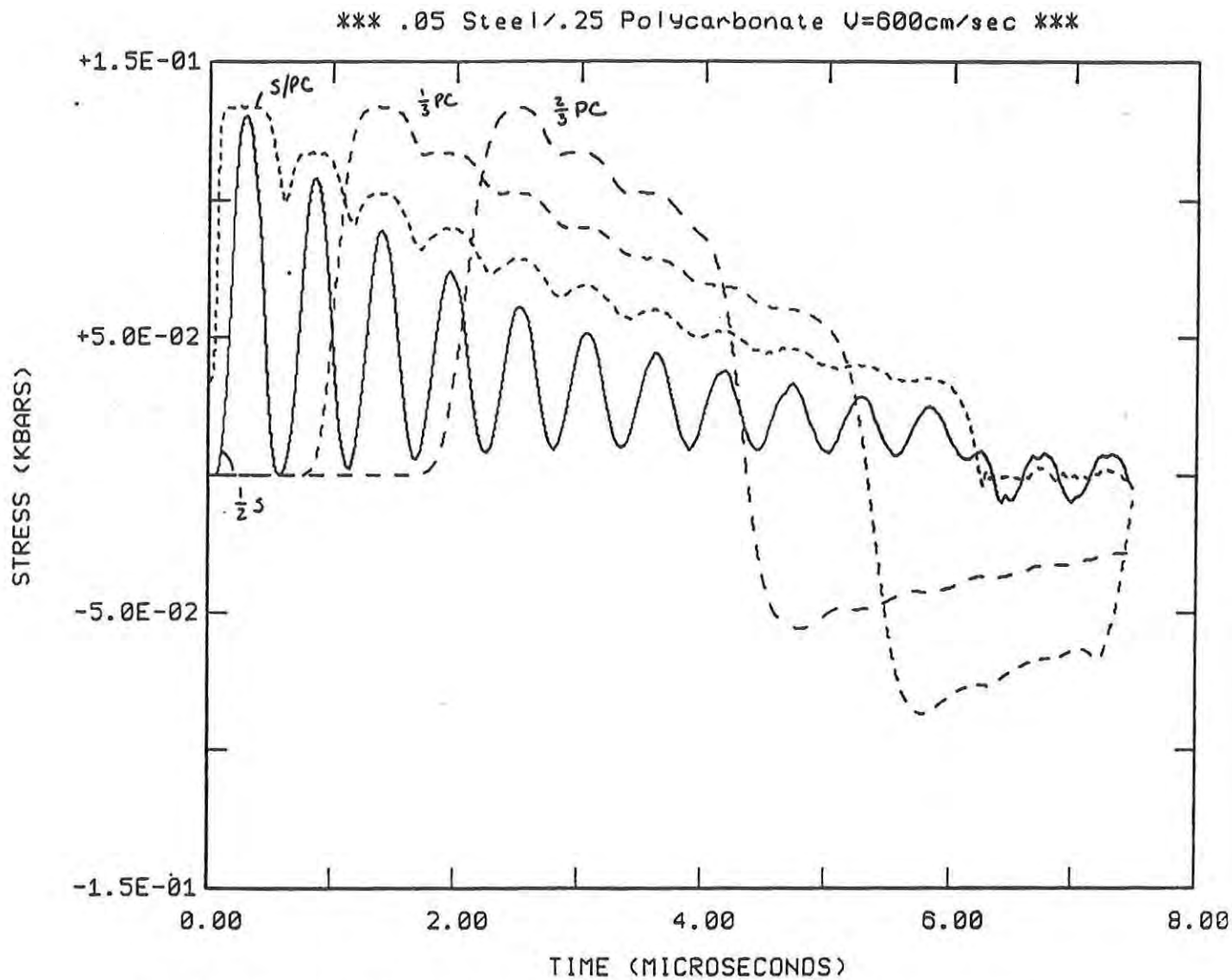


Figure A.1. Predicted One-Dimensional Stress Wave Response for
0.25 inch PC Impacted by 0.05 inch Steel Flyer Plate
Incident at 600 cm/sec

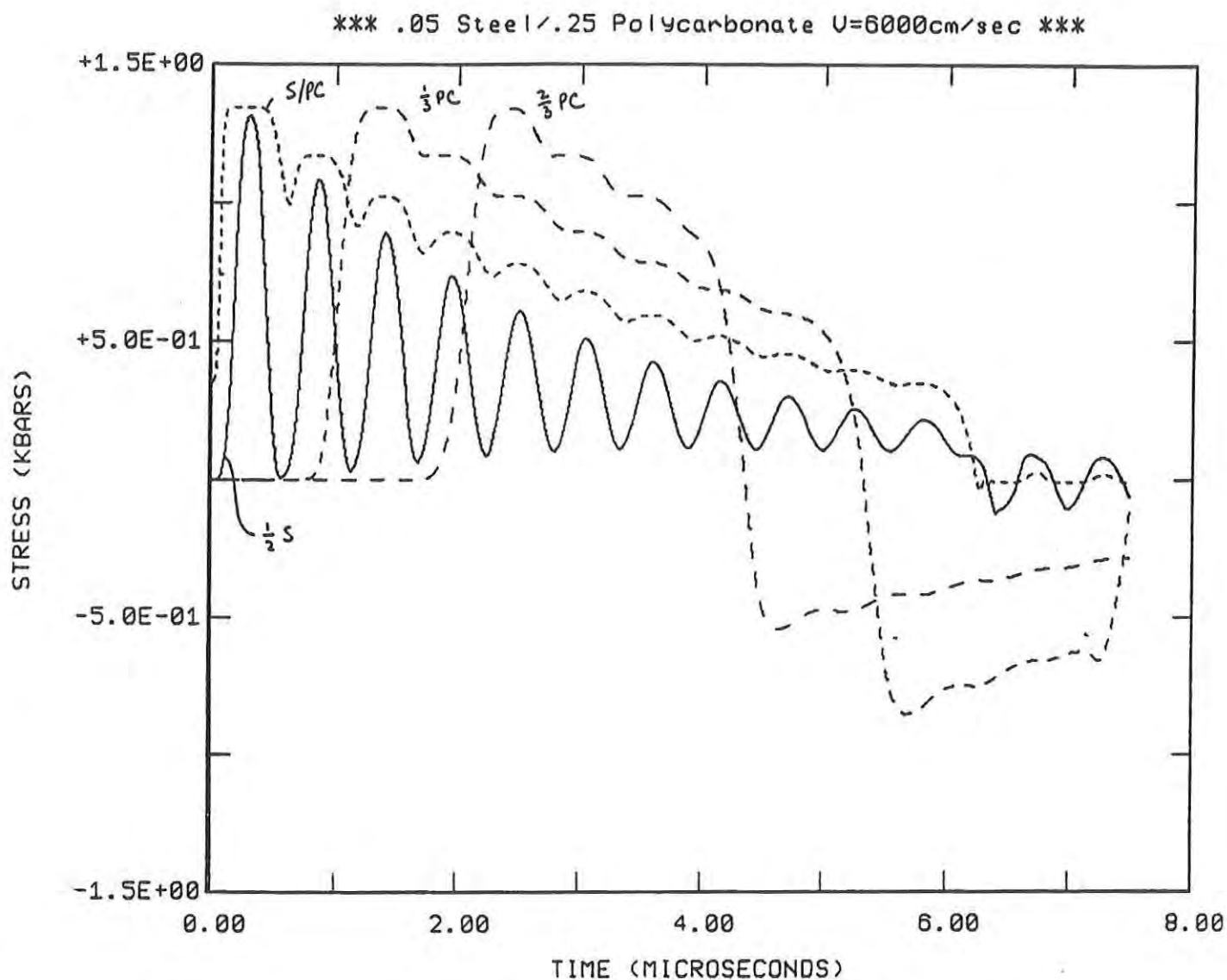


Figure A.2. Predicted One-Dimensional Stress Wave Response for
0.25 inch PC Impacted by 0.05 inch Steel Flyer Plate
Incident at 6,000 cm/sec

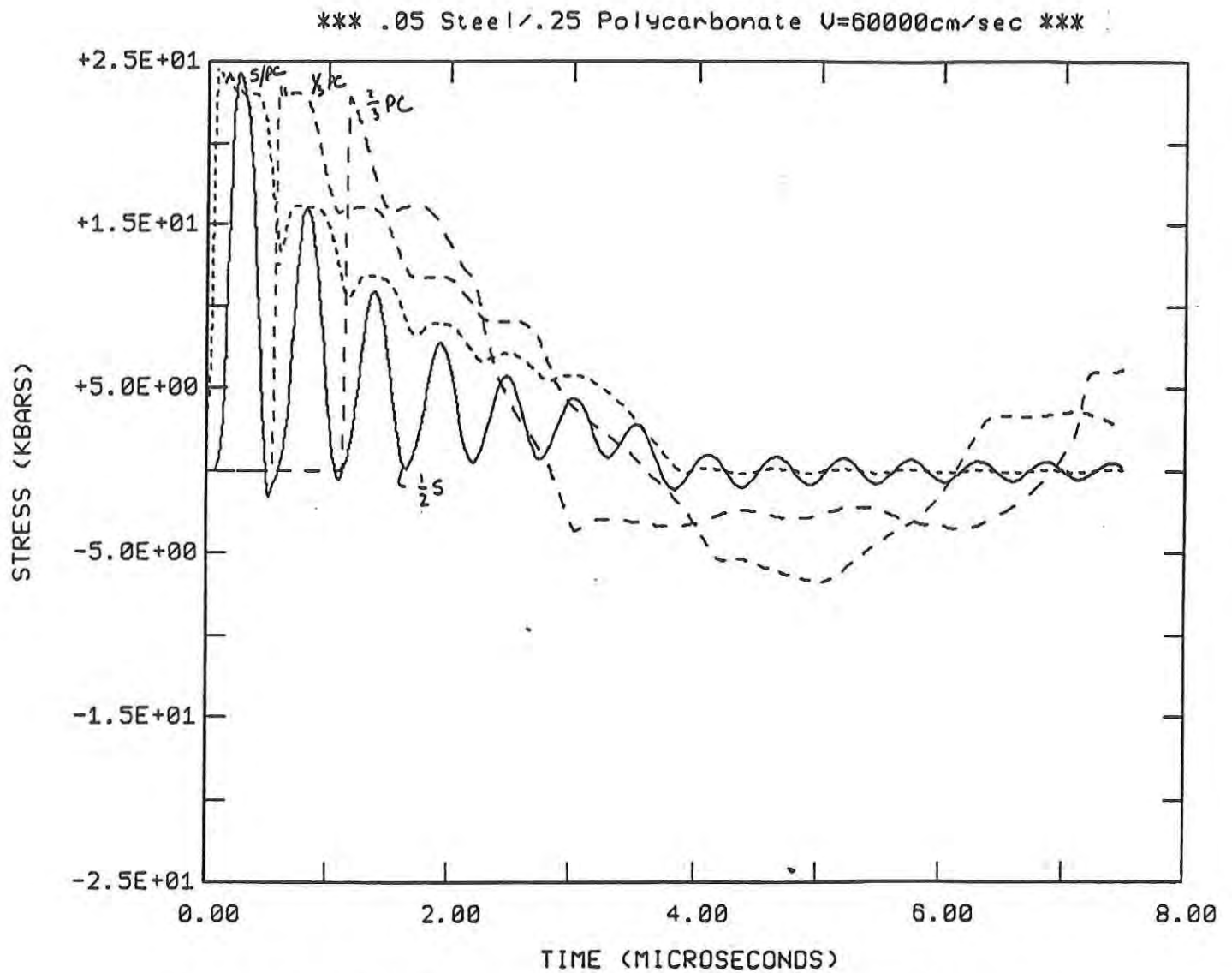


Figure A.3. Predicted One-Dimensional Stress Wave Response for 0.25 inch PC Impacted by 0.05 inch Steel Flyer Plate Incident at 60,000 cm/sec

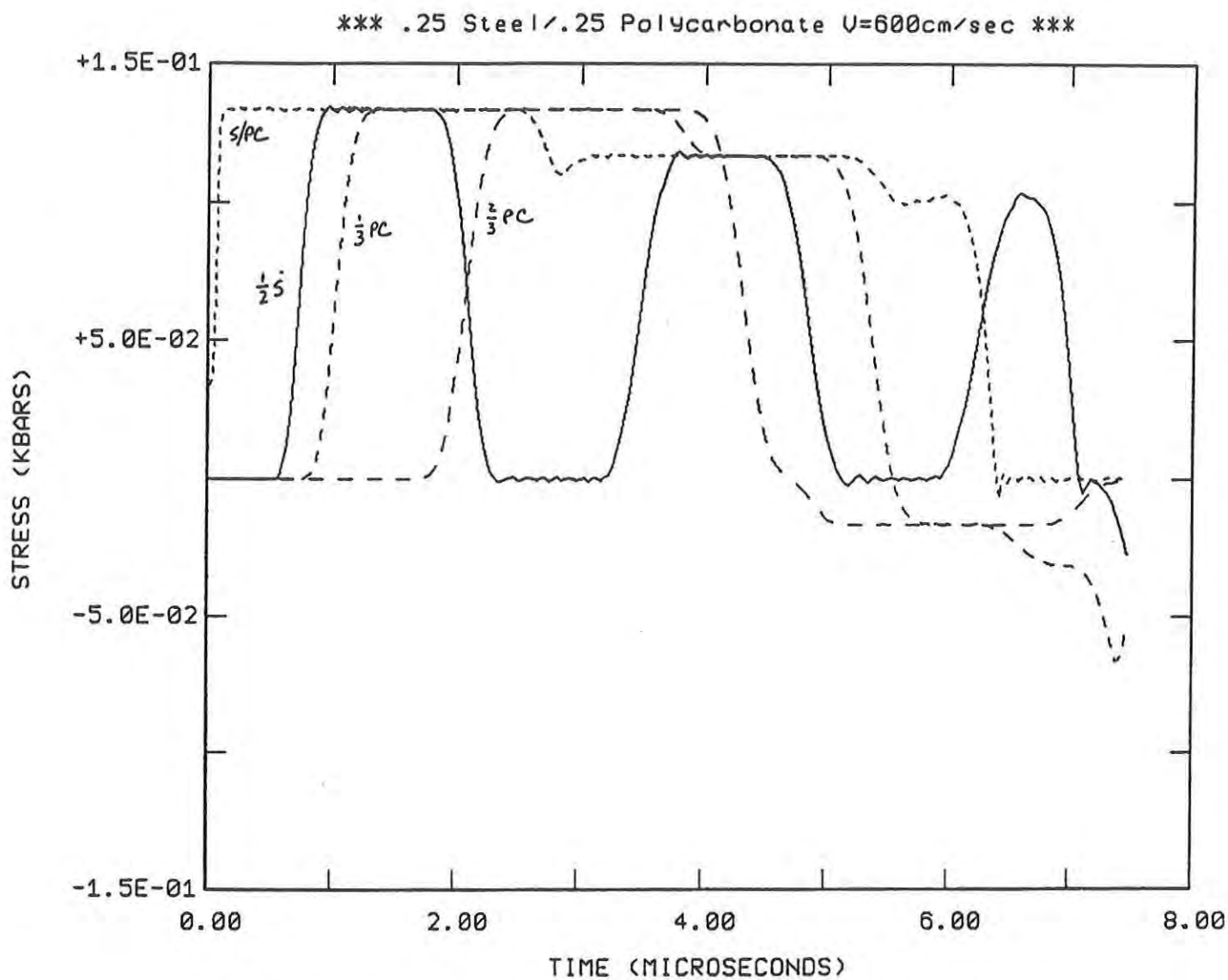


Figure A.4. Predicted One-Dimensional Stress Wave Response for
0.25 inch PC Impacted by 0.25 inch Steel Flyer Plate
Incident at 600 cm/sec

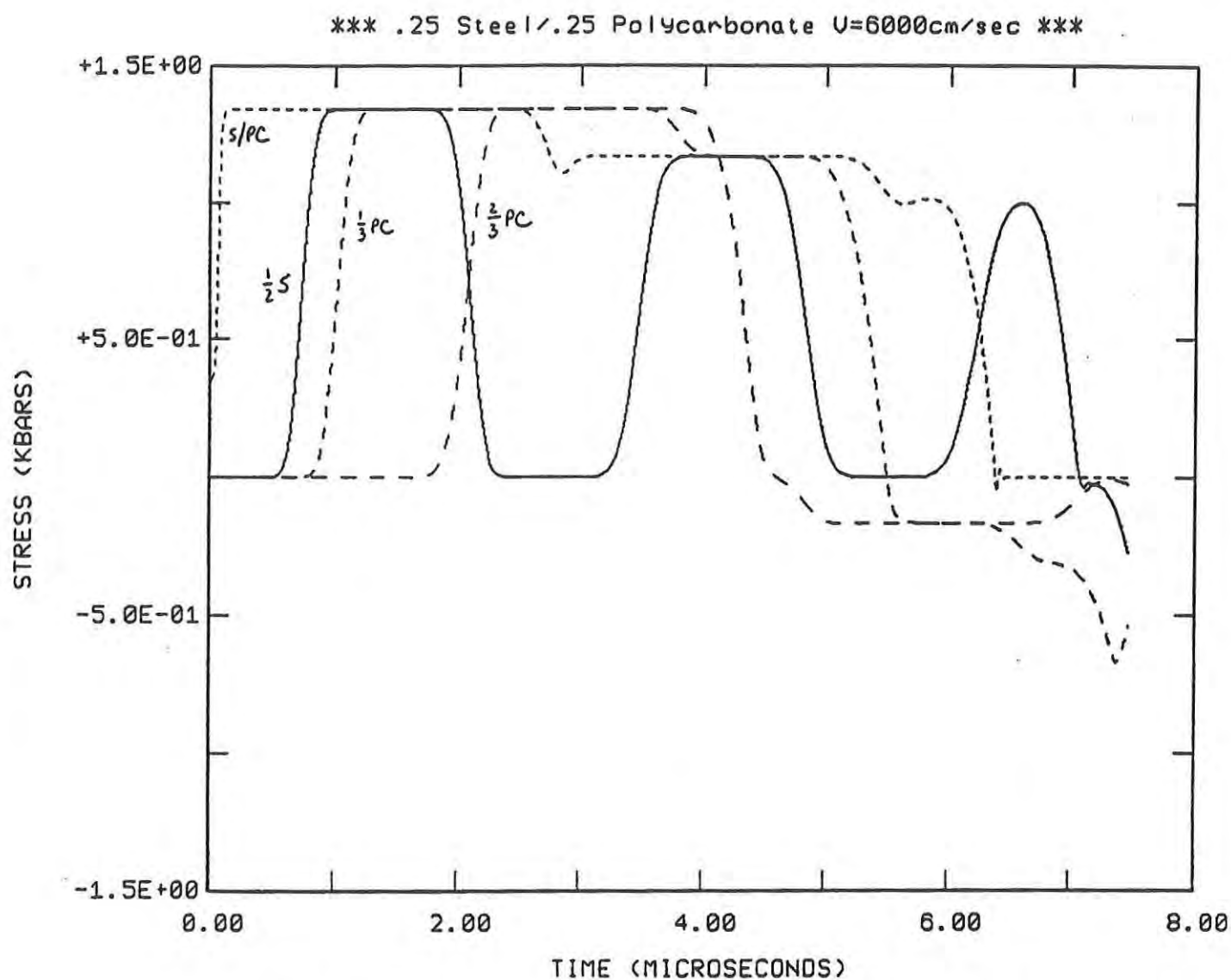


Figure A.5. Predicted One-Dimensional Stress Wave Response for
0.25 inch PC Impacted by 0.25 inch Steel Flyer
Plate Incident at 6,000 cm/sec

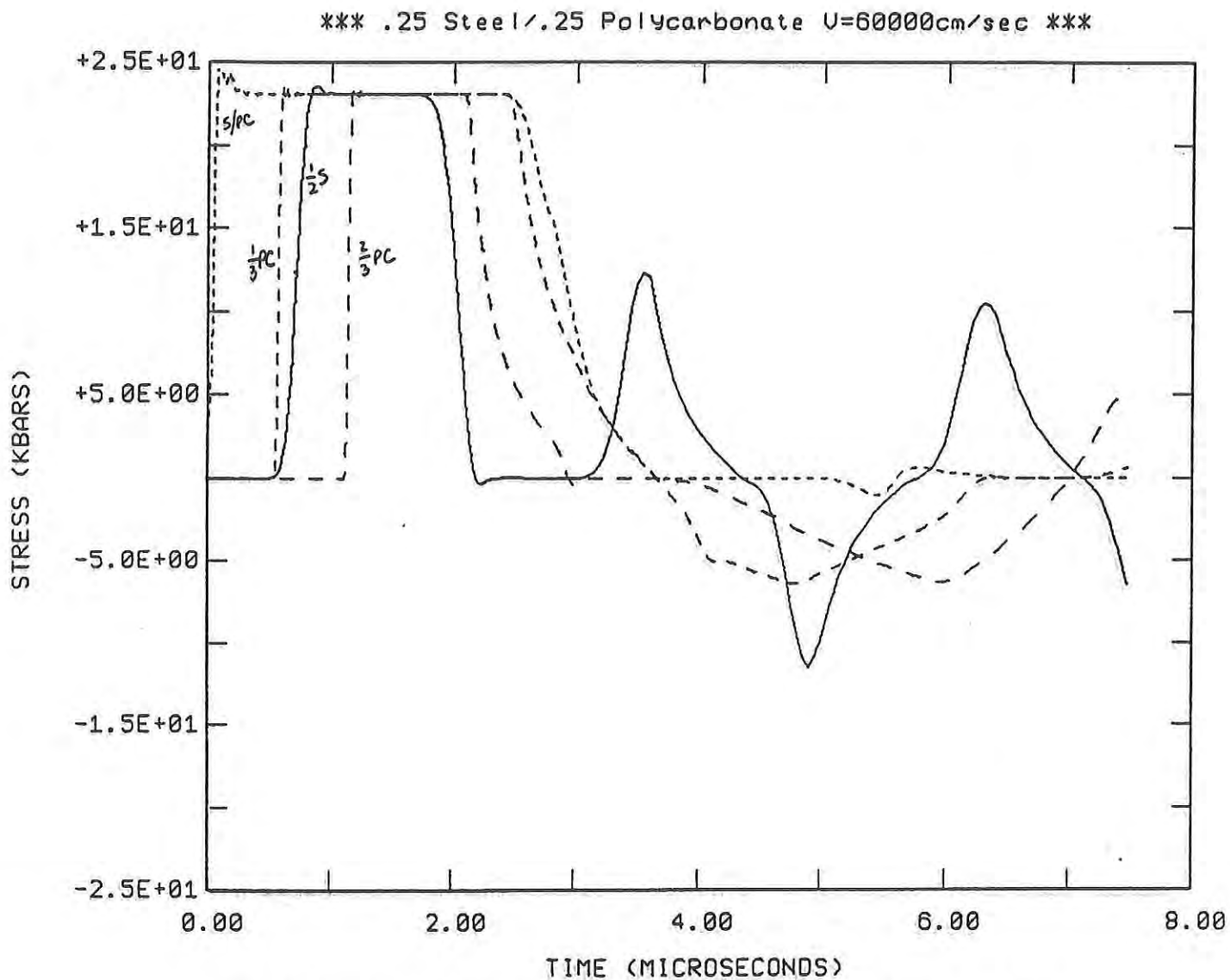


Figure A.6. Predicted One-Dimensional Stress Wave Response for
0.25 inch PC Impacted by 0.25 inch Steel Flyer Plate
Incident at 60,000 cm/sec

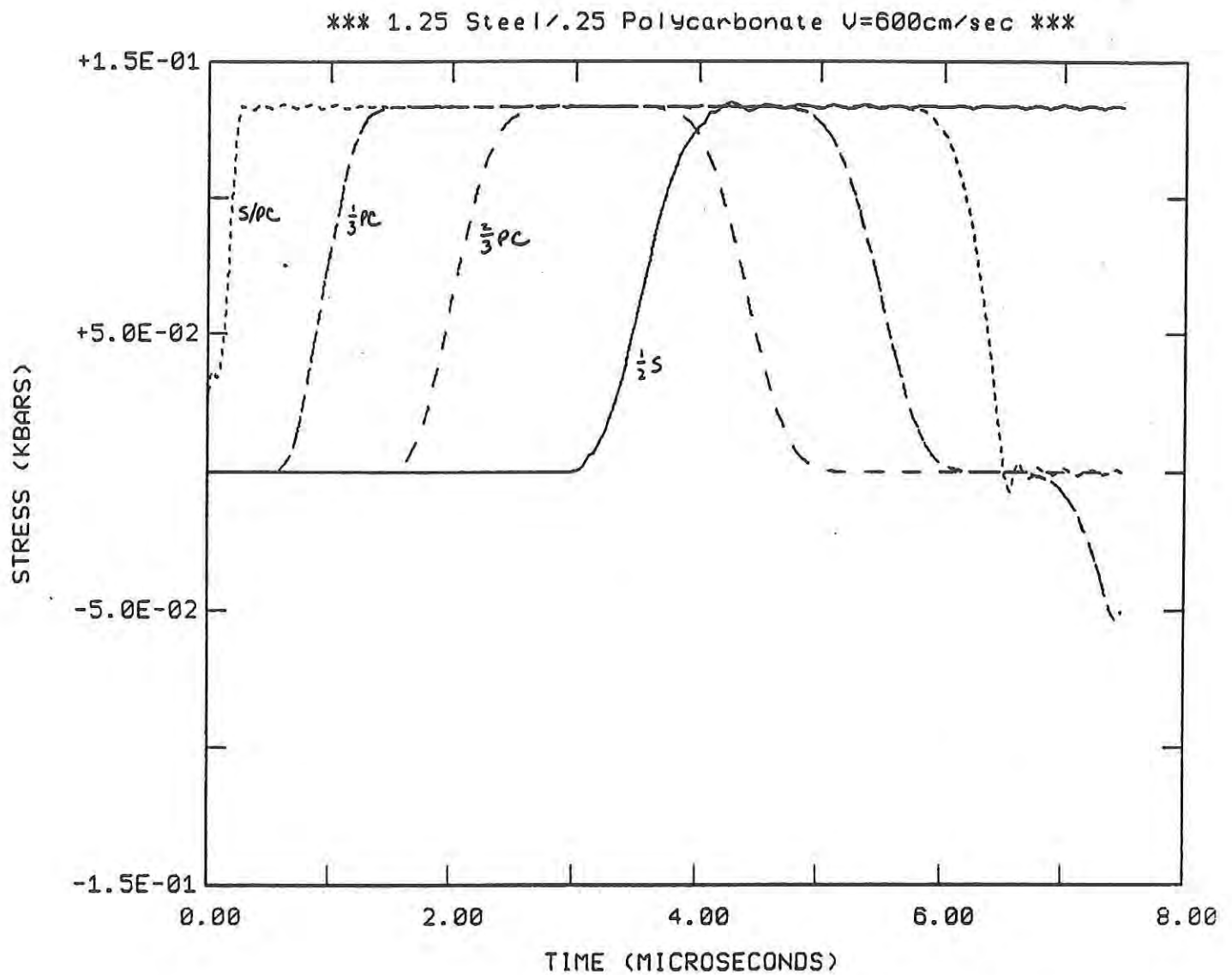


Figure A.7. Predicted One-Dimensional Stress Wave Response for 0.25 inch PC Impacted by 1.25 inch Steel Flyer Plate Incident at 600 cm/sec

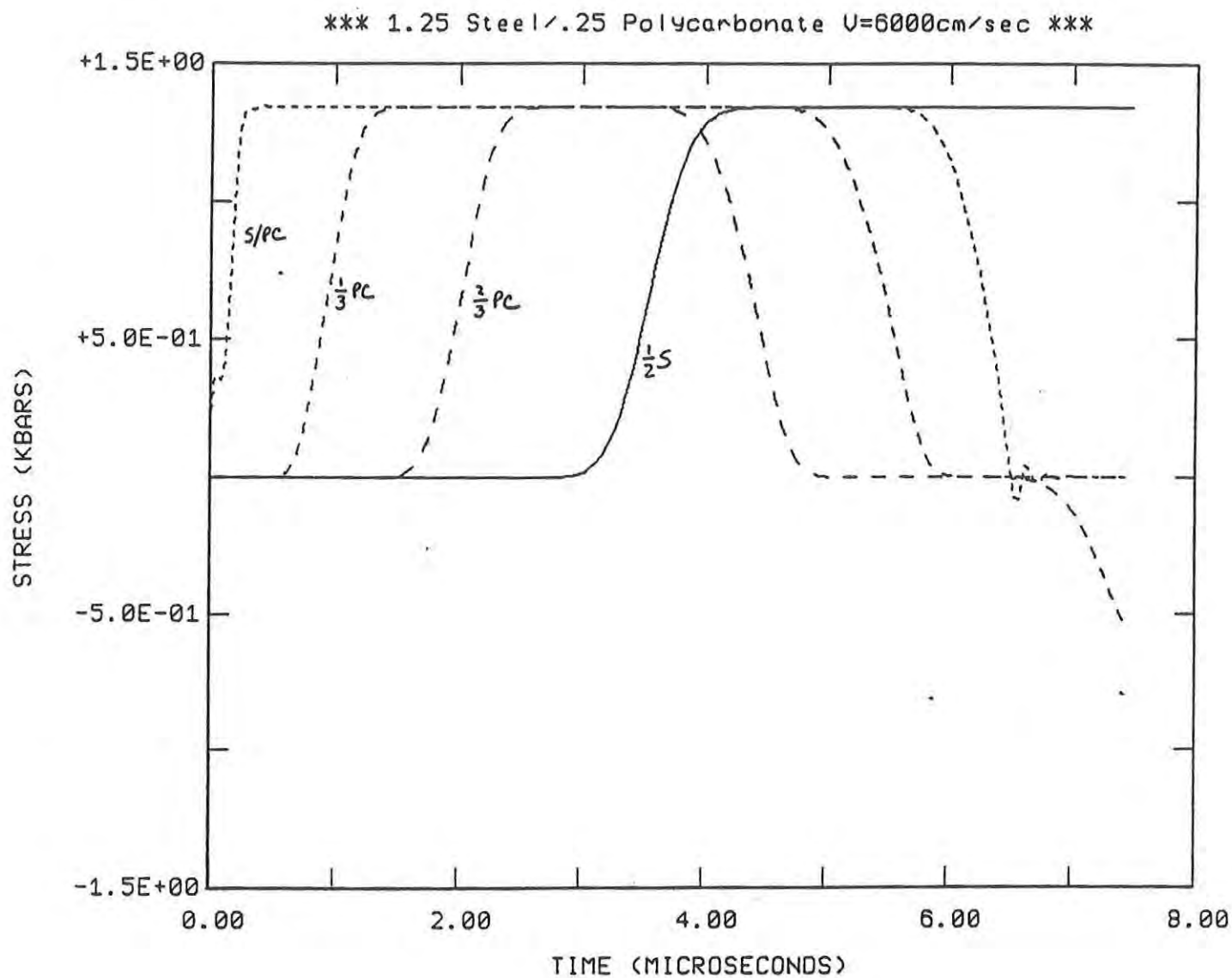


Figure A.8. Predicted One-Dimensional Stress Wave Response for
0.25 inch PC Impacted by 1.25 inch Steel Flyer Plate
Incident at 6,000 cm/sec

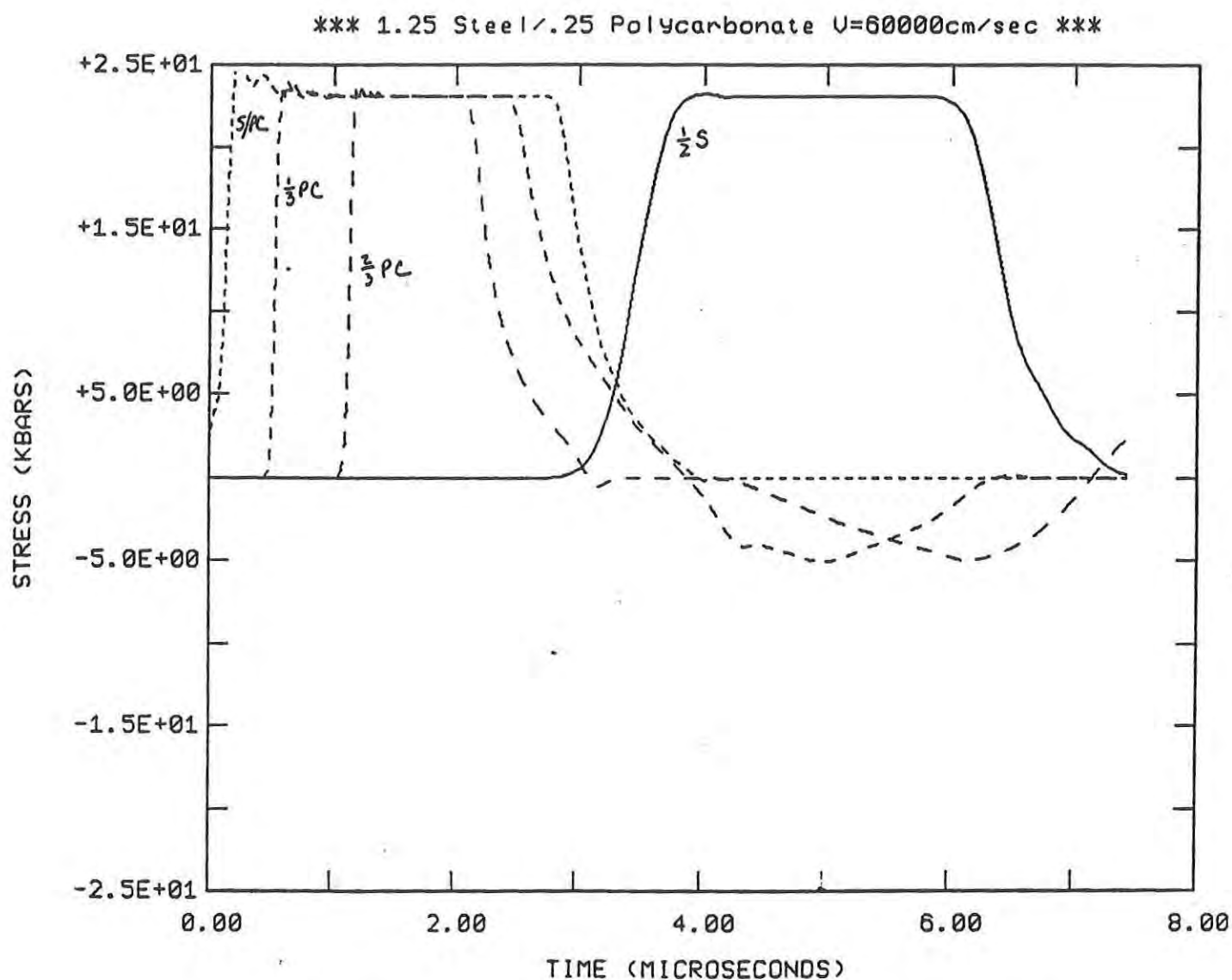


Figure A.9. Predicted One-Dimensional Stress Wave Response for
0.25 inch PC Impacted by 1.25 inch Steel Flyer Plate
Incident at 60,000 cm/sec

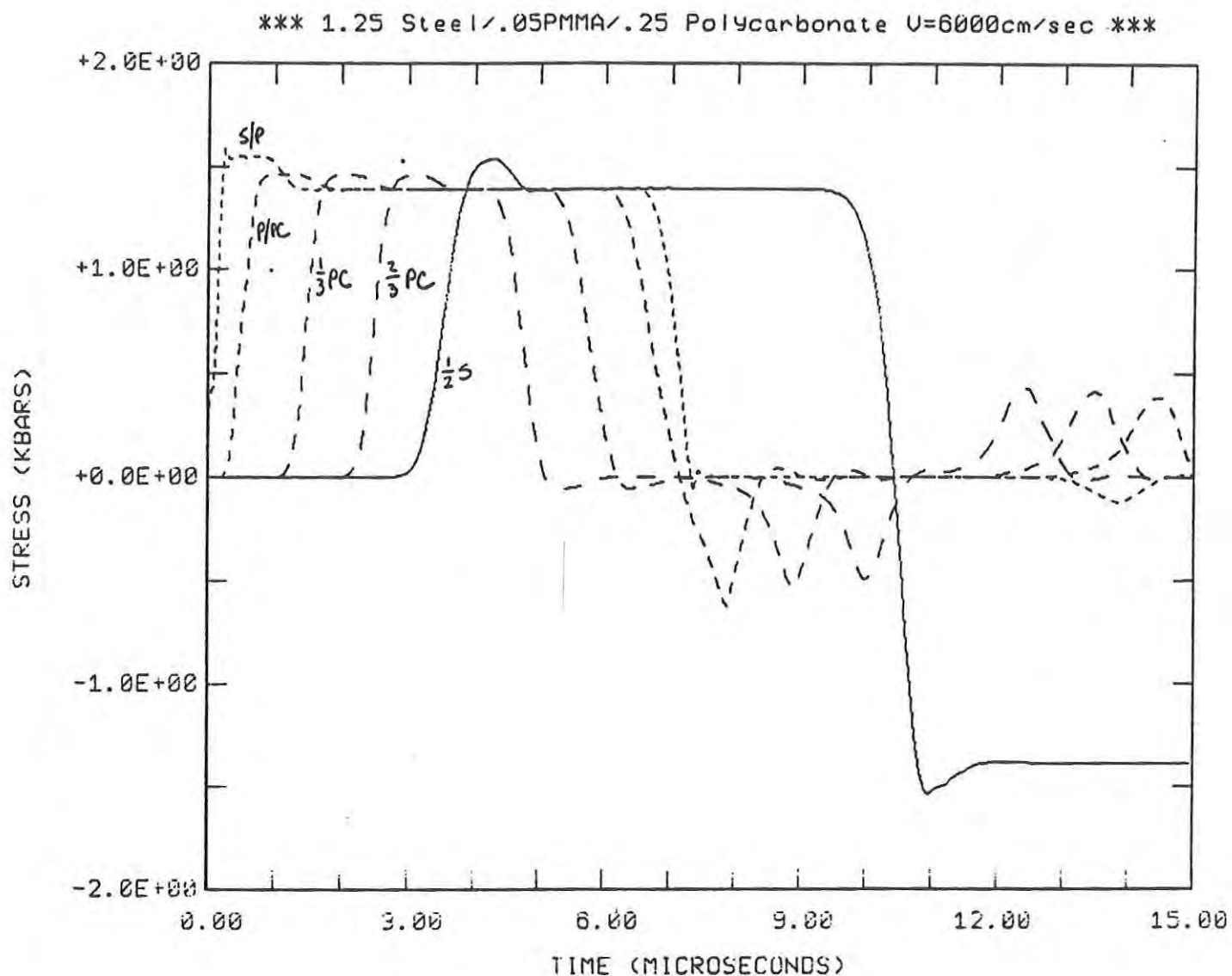


Figure A.10. Predicted One-Dimensional Stress Wave Response for 0.25 inch PC with 0.05 inch PMMA Coating Impacted by 1.25 inch Steel Flyer Plate Incident at 6,000 cm/sec

JEDIT * J= 51 M=1 FD=5.000E-01

*** 1.25 Steel/.20PMMA/.25 Polycarbonate U=6000cm/sec ***

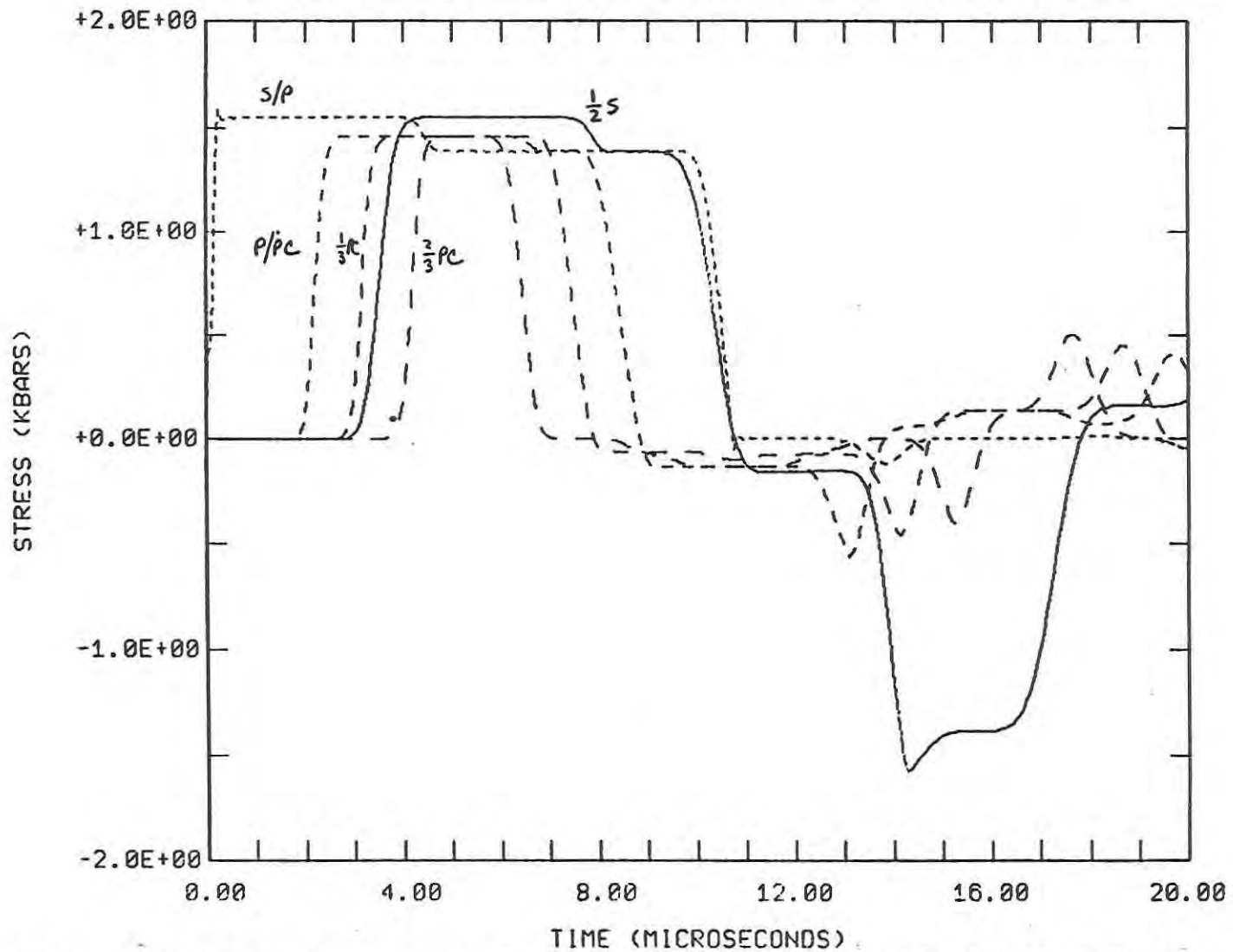


Figure A.11. Predicted One-Dimensional Stress Wave Response for 0.25 inch PC with 0.20 inch PMMA Coating Impacted by 1.25 inch Steel Flyer Plate Incident at 6,000 cm/sec

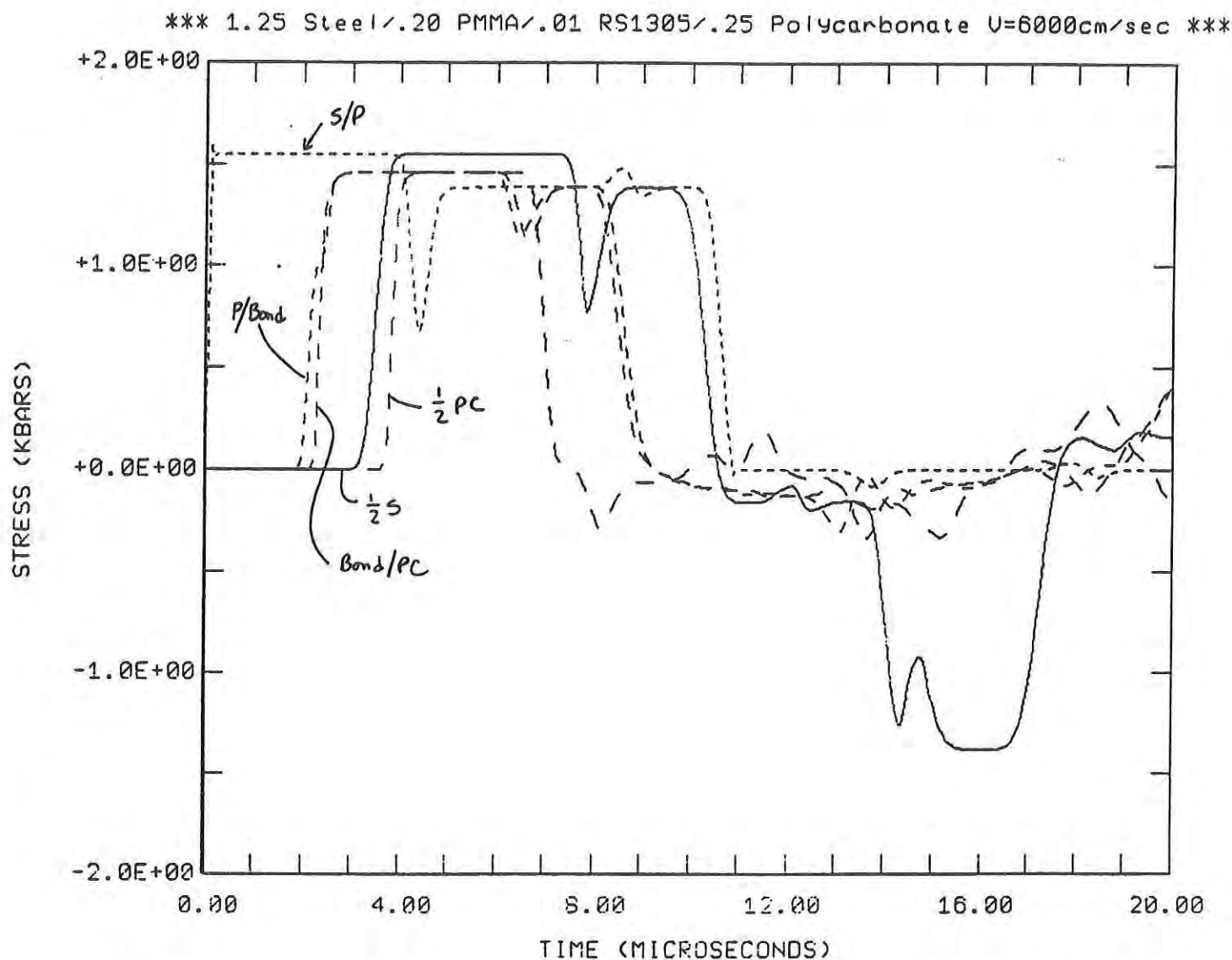


Figure A.12. Predicted One-Dimensional Stress Wave Response for 0.25 inch PC with 0.20 inch PMMA Coating and 0.01 inch RS1305 Silicone Adhesive Impacted by 1.25 inch Steel Flyer Plate Incident at 6,000 cm/sec

APPENDIX A.2.1 - 2D Stress Wave Analysis for High Velocity Impact

<u>Figure</u>		<u>Page</u>
A.13	Location of Target Points for Post Processing of High Velocity Impact Analysis	107
A.14	Projectile Particle Velocities in Impact Direction: (a) Near Impact Surface; and, (b) Near Back Surface of Projectile.	108 109
A.15	Comparison of Particle Velocities in Impact and Radial Directions for Coated and Uncoated PC near Impact Surface	110
A.16	Comparison of Particle Velocities in Impact and Radial Directions for Coated and Uncoated PC near Near the Midplane of the Substrate	111
A.17	Comparison of Particle Velocities in Impact and Radial Directions for Coated and Uncoated PC Near the Midplane and Back Surface of the Substrate	112
A.18	Comparison of Particle Velocities in Impact and Radial Directions for Coated and Uncoated PC Near the Back Surface of the Substrate and along the Midplane of the Substrate Outside the Impact Region	113
A.19	Comparison of Pressure and Stress in the Projectile along the Impact and Radial Directions.	114
A.20	Calculated Pressure for Coated and Uncoated PC through the Target Thickness.	115
A.21	Calculated Stress for Coated and Uncoated PC through the Target Thickness along the Radial and Impact Directions.	116
A.22	Calculated Stress for Coated and Uncoated PC through the Target Thickness along the Radial and Impact Directions.	117

LOCATION OF TARGET POINTS

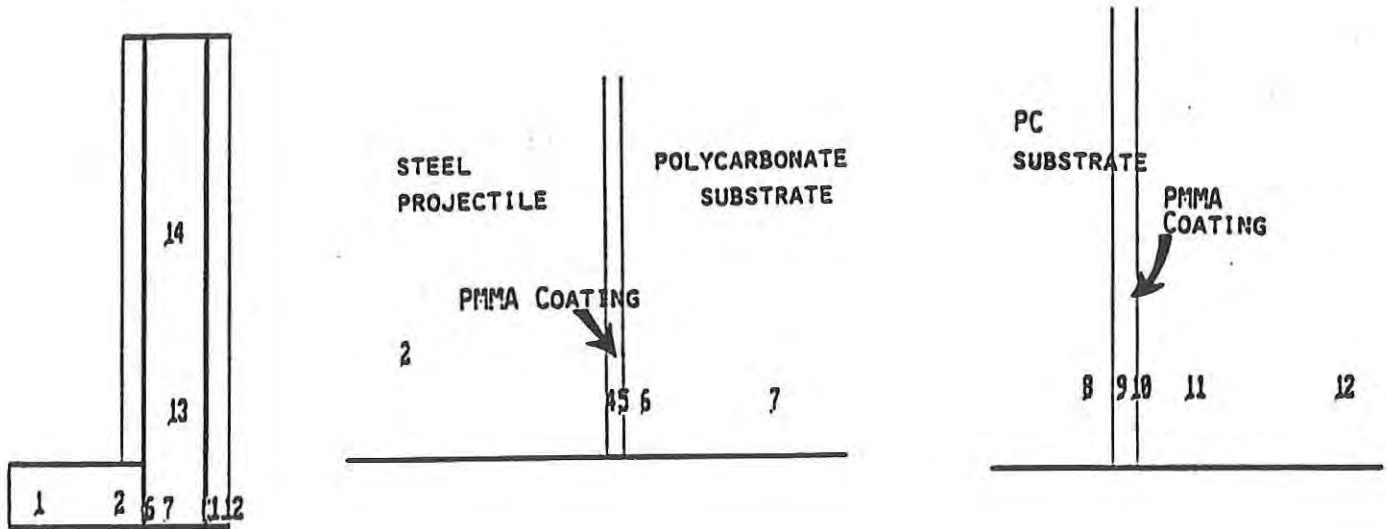


Figure A.13. Target Points for Post Processing: (a) Global View; (b) Impact Surface Detail; and, (c) Rear Surface Detail.

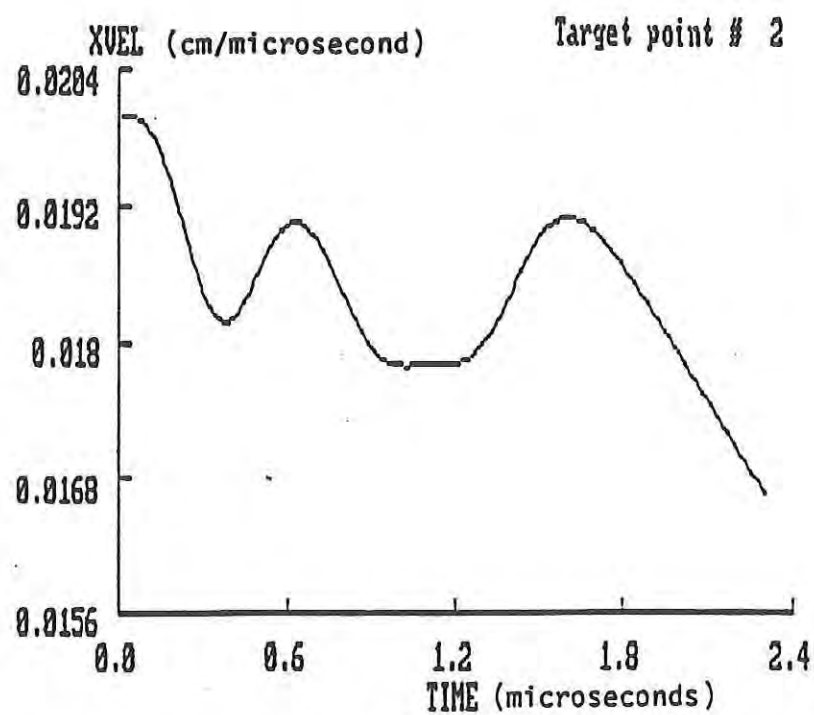


Figure A.14a. Projectile Particle Velocities in Impact Direction:
(a) Near Impact Surface of Projectile

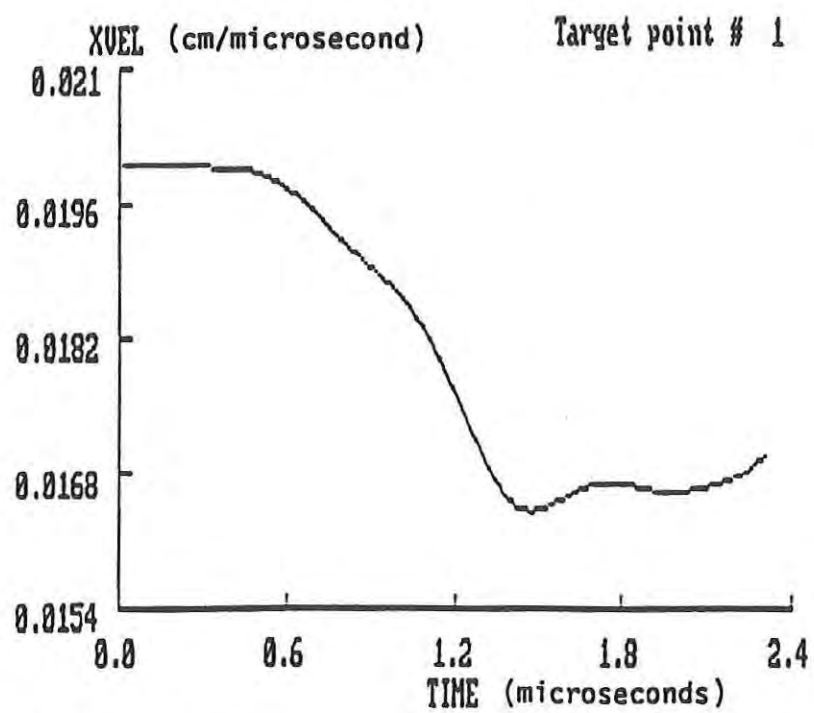


Figure A.14b. Projectile Particle Velocities in Impact Direction:
(b) Near Back Surface

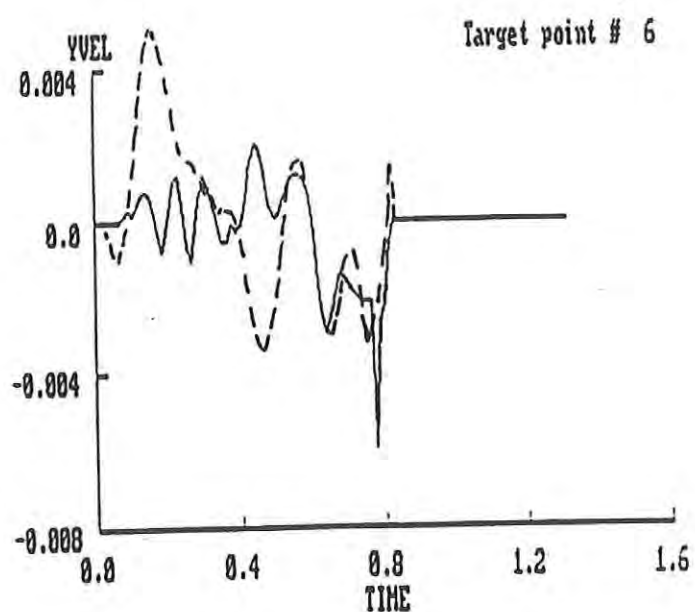
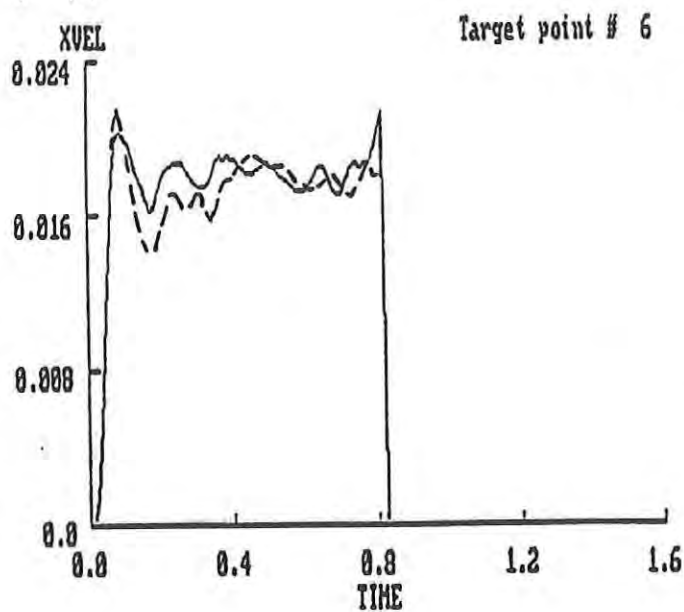
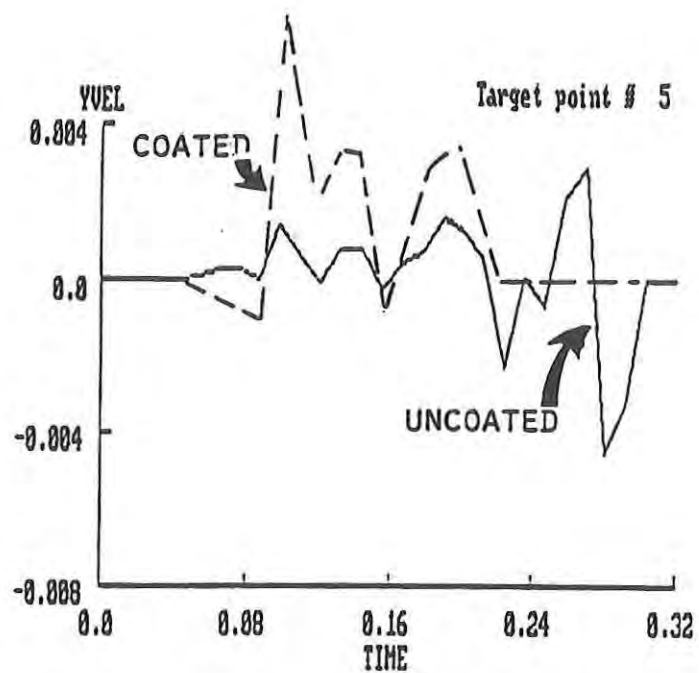
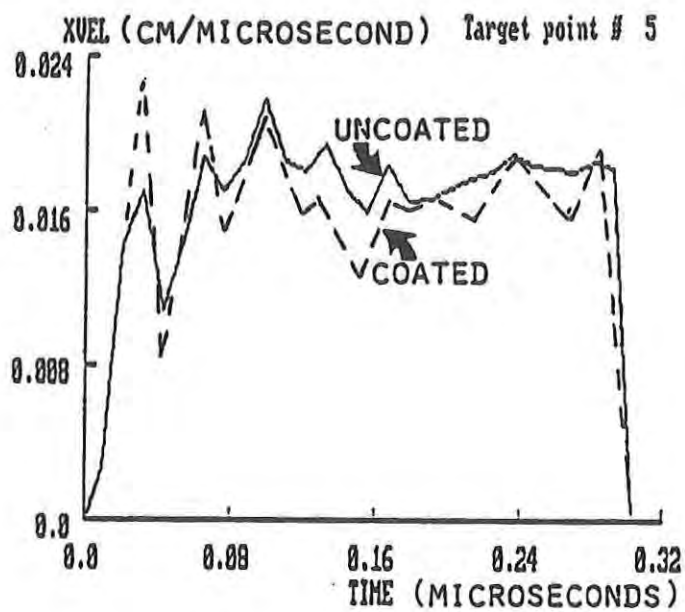


Figure A.15

Comparison of Particle Velocities in Impact and Radial Direction for Coated and Uncoated PC near Impact Surface.

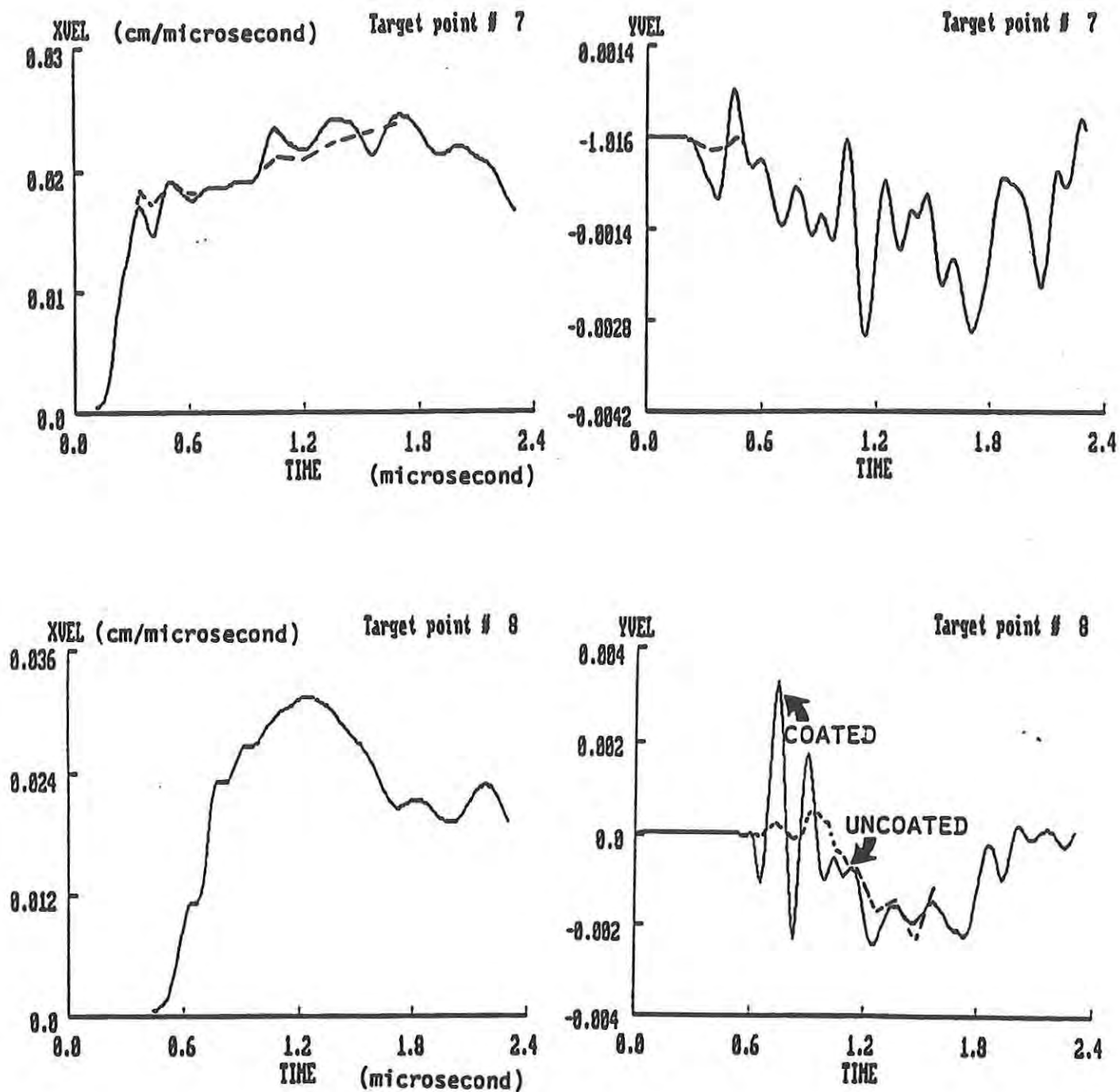


Figure A.16.

Comparison of Particle Velocities in Impact and Radial Directions for Coated and Uncoated PC Near Impact Surface

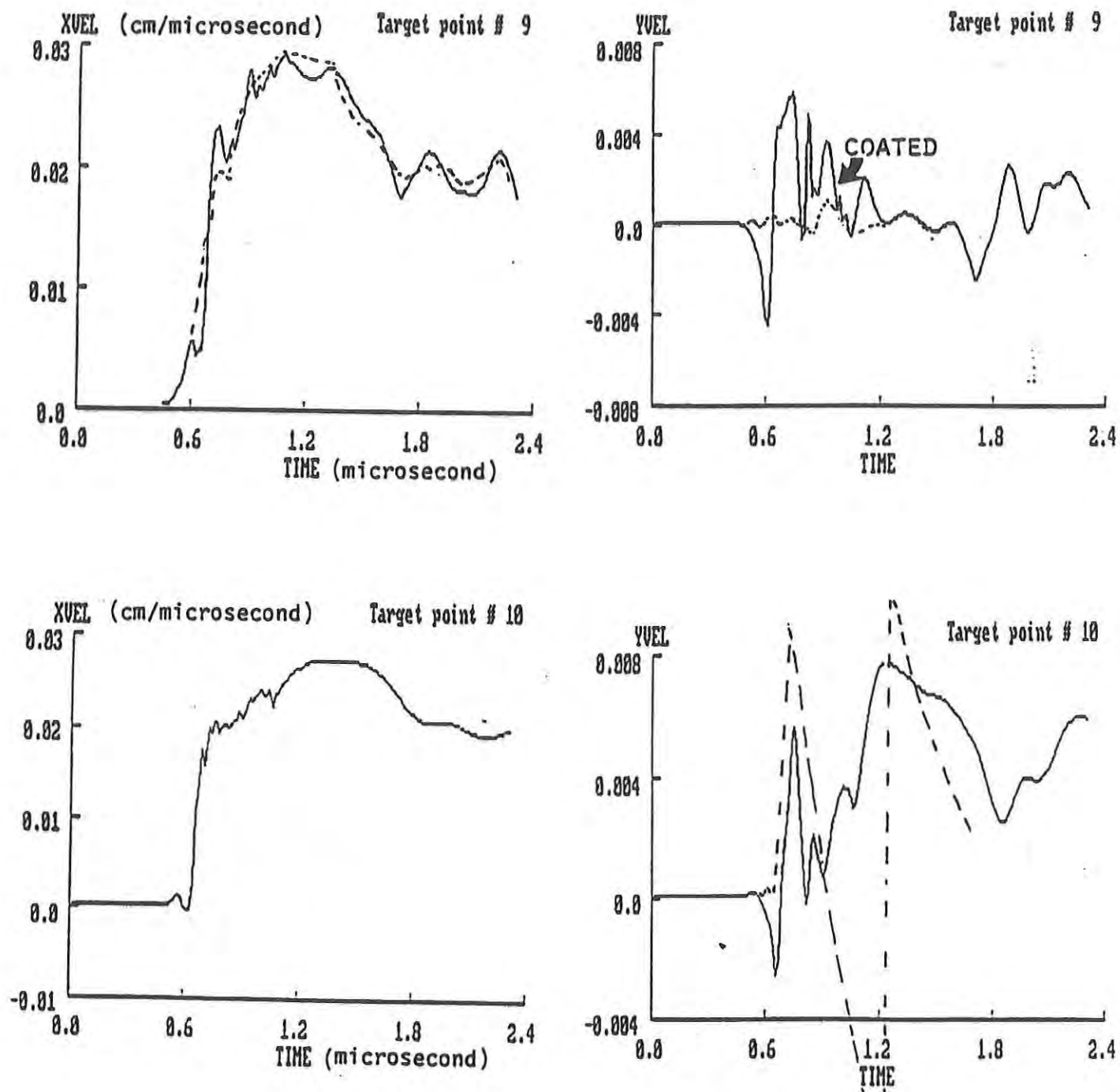


Figure A.17.

Comparison of Particle Velocities in Impact and Radial Directions for Coated and Uncoated PC Near the Midplane and Back Surface of the Substrate

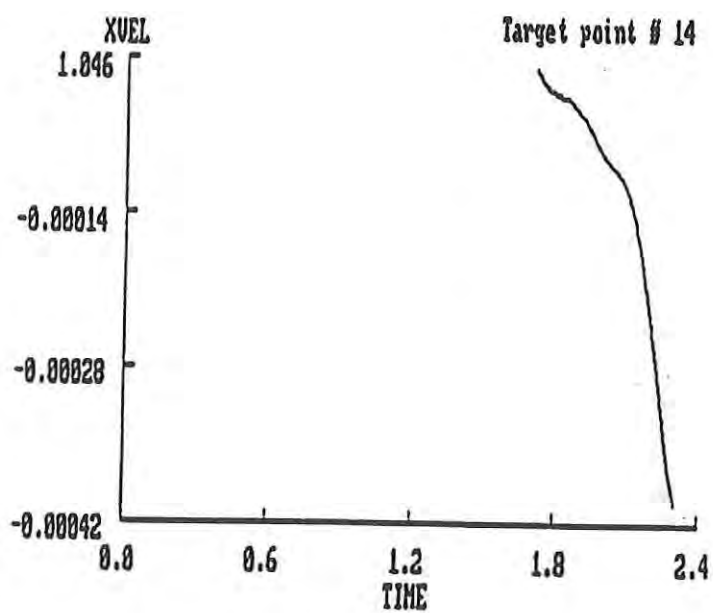
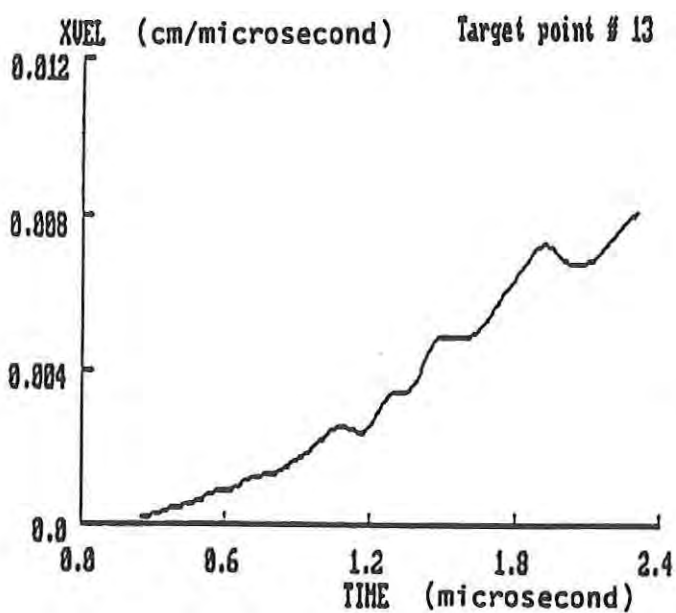
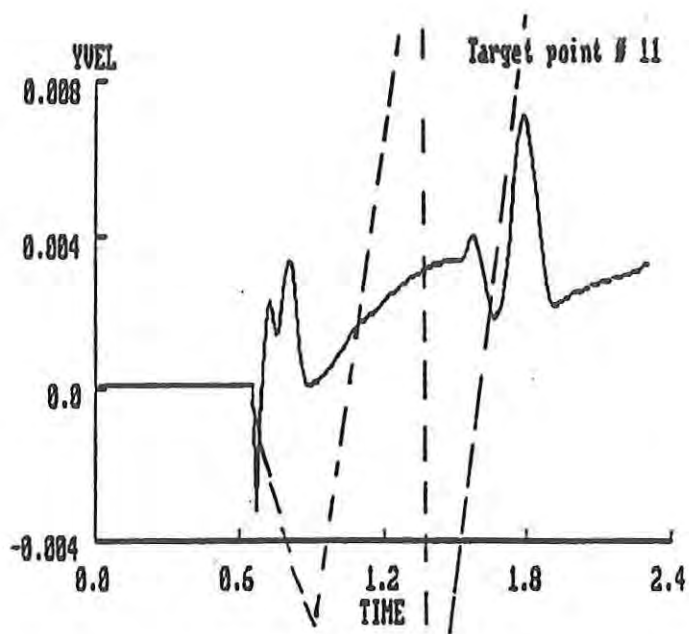
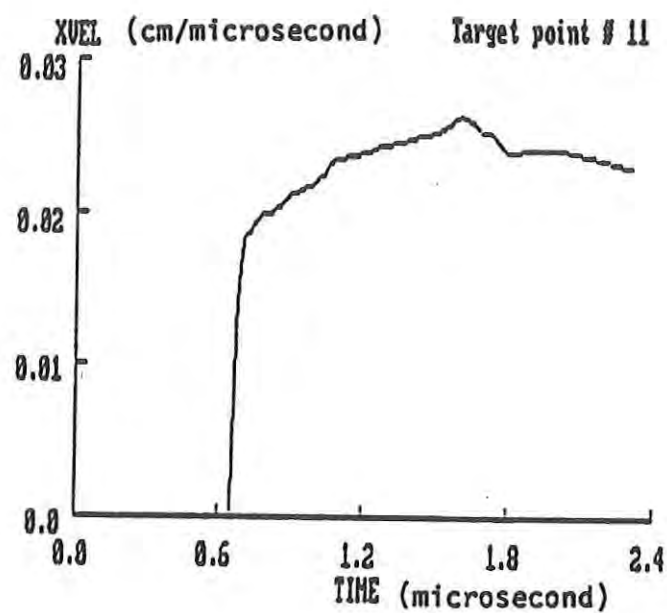


Figure A.18.

Comparison of Particle Velocities in Impact and Radial Directions for Coated and Uncoated PC Near the Back Surface of the Substrate and along the Midplane of the Substrate Outside the Impact Region

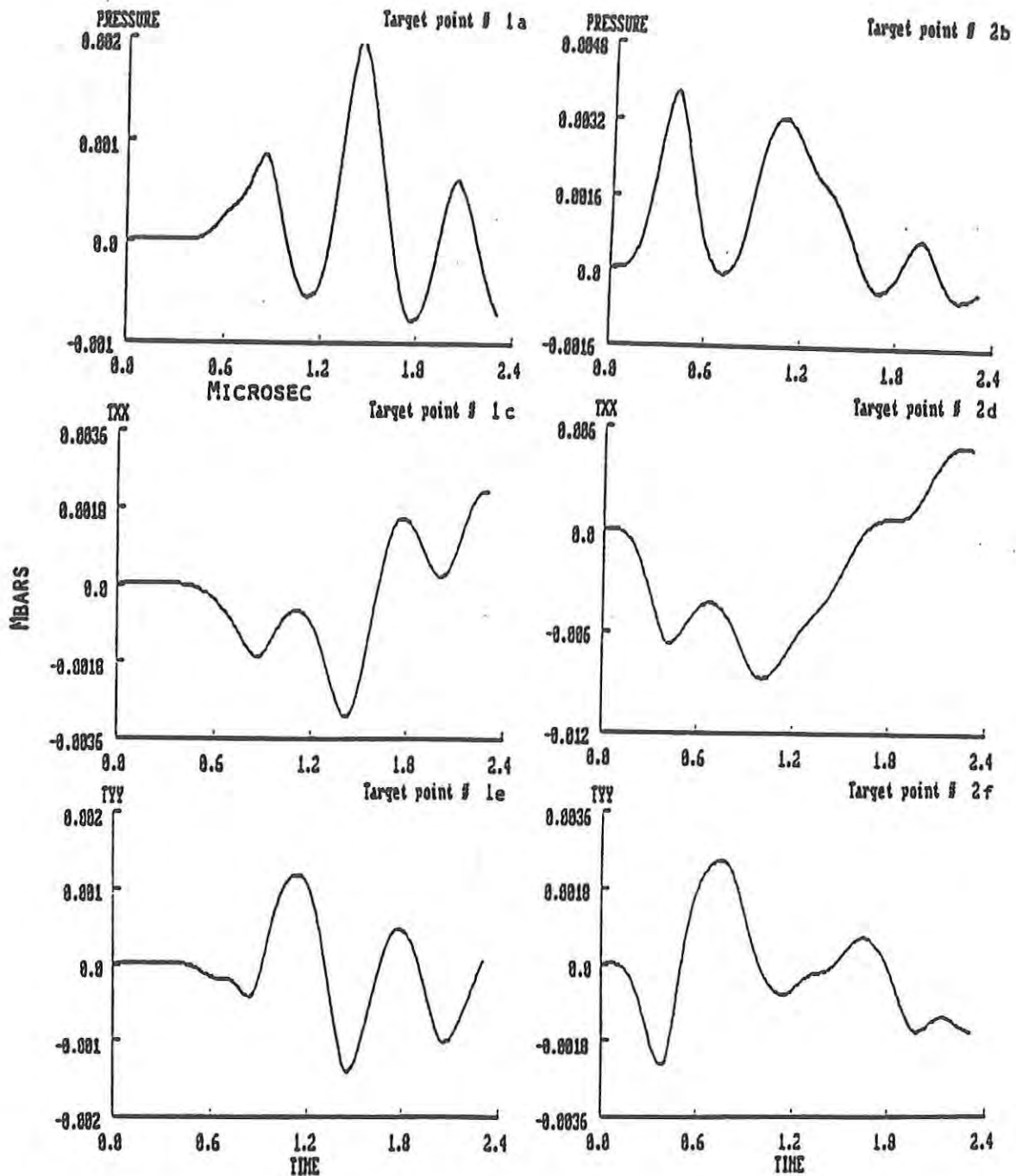


Figure A.19.

Comparison of Pressure and Stress in the Projectile along the Impact and Radial Directions

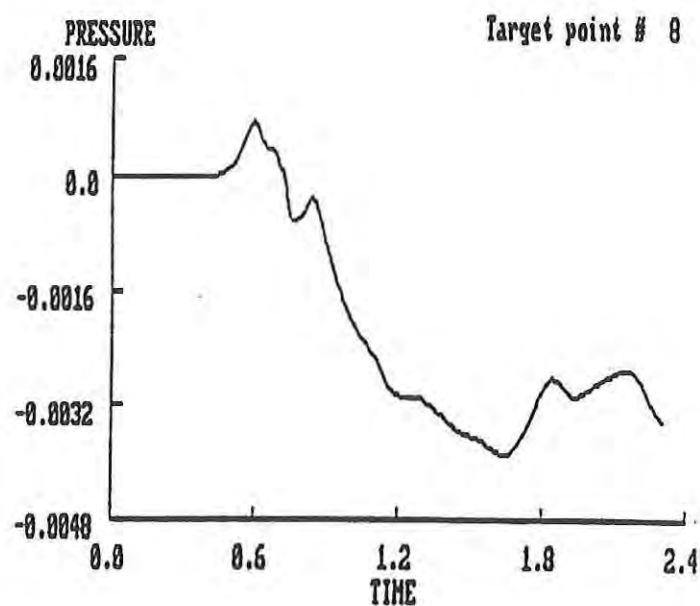
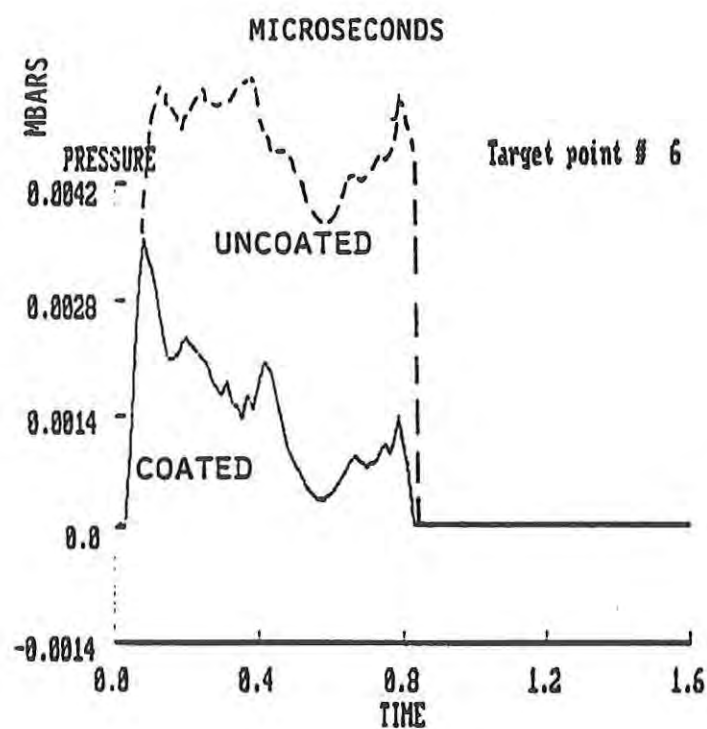
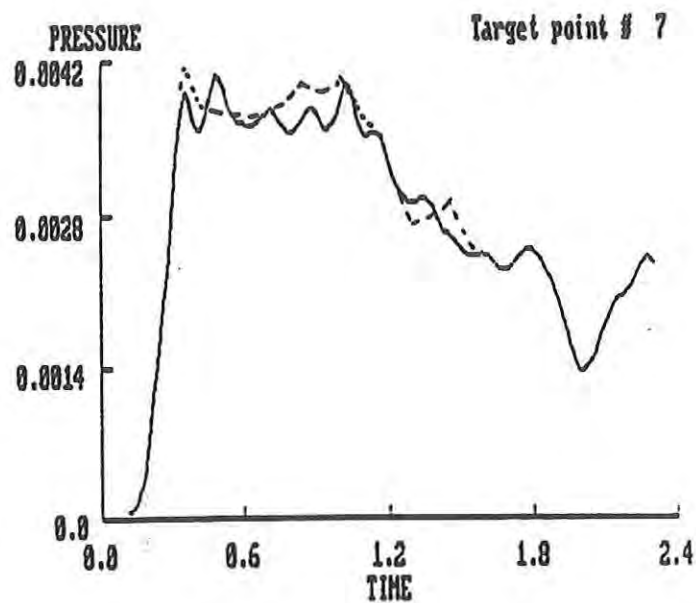
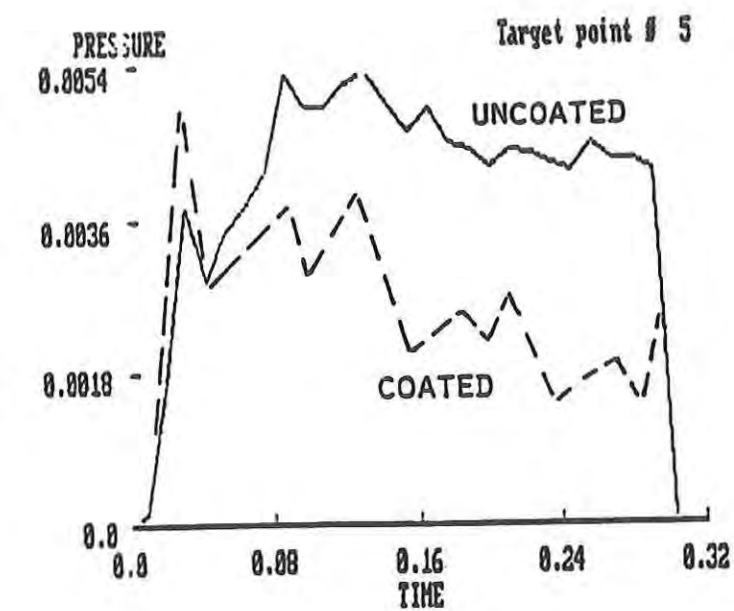


Figure A.20.

Calculated Pressure for Coated and Uncoated PC through the Target Thickness

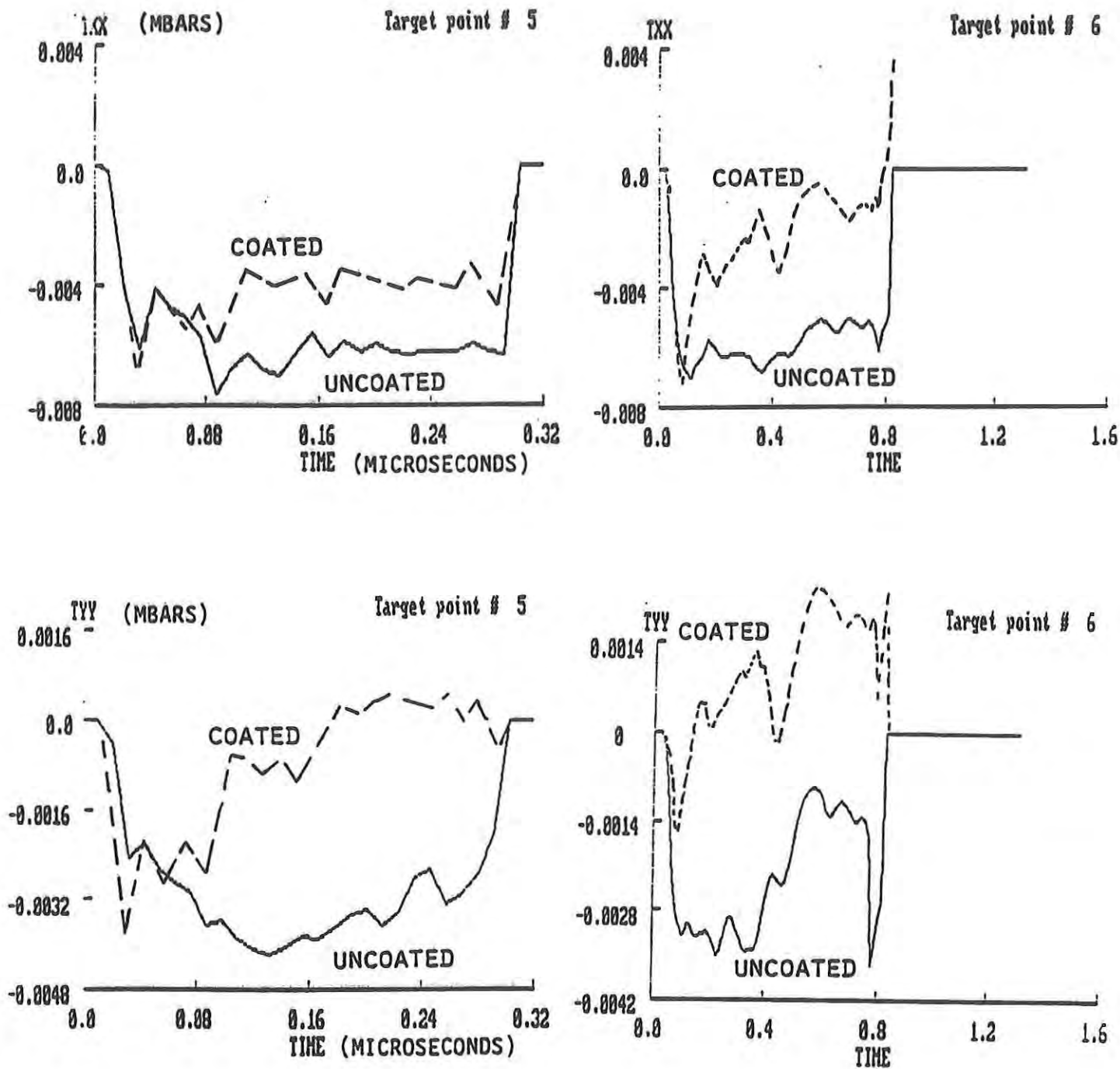


Figure A.21. Calculated Stress for Coated and Uncoated PC through the Target Thickness along the Radial and Impact Directions

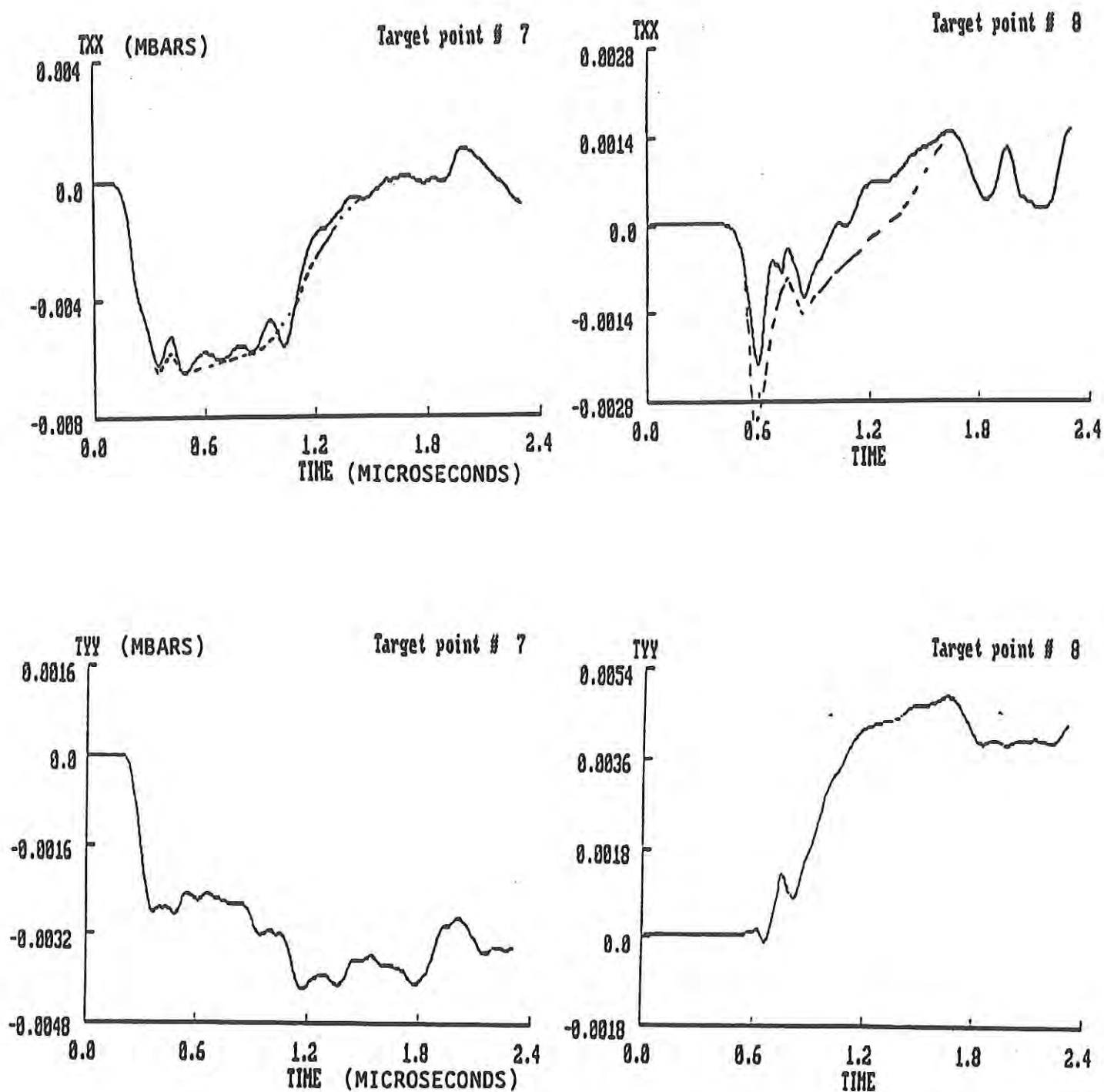


Figure A.22. Calculated Stress for Coated and Uncoated PC through the Target Thickness along the Radial and Impact Directions

APPENDIX A.2.2.1 - Two-Dimensional Stress Wave Analysis for Low Velocity Impact without Defects

<u>Figure</u>		<u>Page</u>
A.23	Location of Target Points for Post Processing of Low Velocity Impact Analysis	121
A.24	Projectile Particle Velocities in Impact Direction: (a) Near Impact Surface; and, (b) Near Back Surface of Projectile.	122
A.25	Projectile Pressures: (a) Near Impact Surface; and, (b) Near Back Surface of Projectile.	123
A.26	Stress Components in Projectile Near Impact Surface: (a) Impact Direction; and, (b) Radial Direction.	124
A.27	Stress Components Near Back Surface of Projectile: (a) Impact Direction; and, (b) Radial Direction.	125
A.28	Pressure in PC Substrate near Impact Surface	126
A.29	Radial Stress Near Impact Surface of PC Substrate	127
A.30	Stress in Impact Direction Near Impact Surface of PC	128
A.31	Pressure near Midplane of PC Substrate	129
A.32	Stress Component at Midplane of PC Substrate in Impact Direction	130
A.33	Stress Component at Midplane of PC Substrate in Radial Direction	131
A.34	Pressure near Rear Surface of PC Substrate	132
A.35	Stress Component near Rear Surface of PC Substrate in Impact Direction	133
A.36	Stress Component near Back Surface of PC Substrate in Radial Direction	134
A.37	Pressure near Midplane of PC Substrate Outside of Impact Region	135
A.38	Stress Component near Midplane of PC Substrate Outside of Impact Region in Impact Direction	136
A.39	Stress Component near Back Surface of PC Substrate Outside of Impact Region in Radial Direction	137

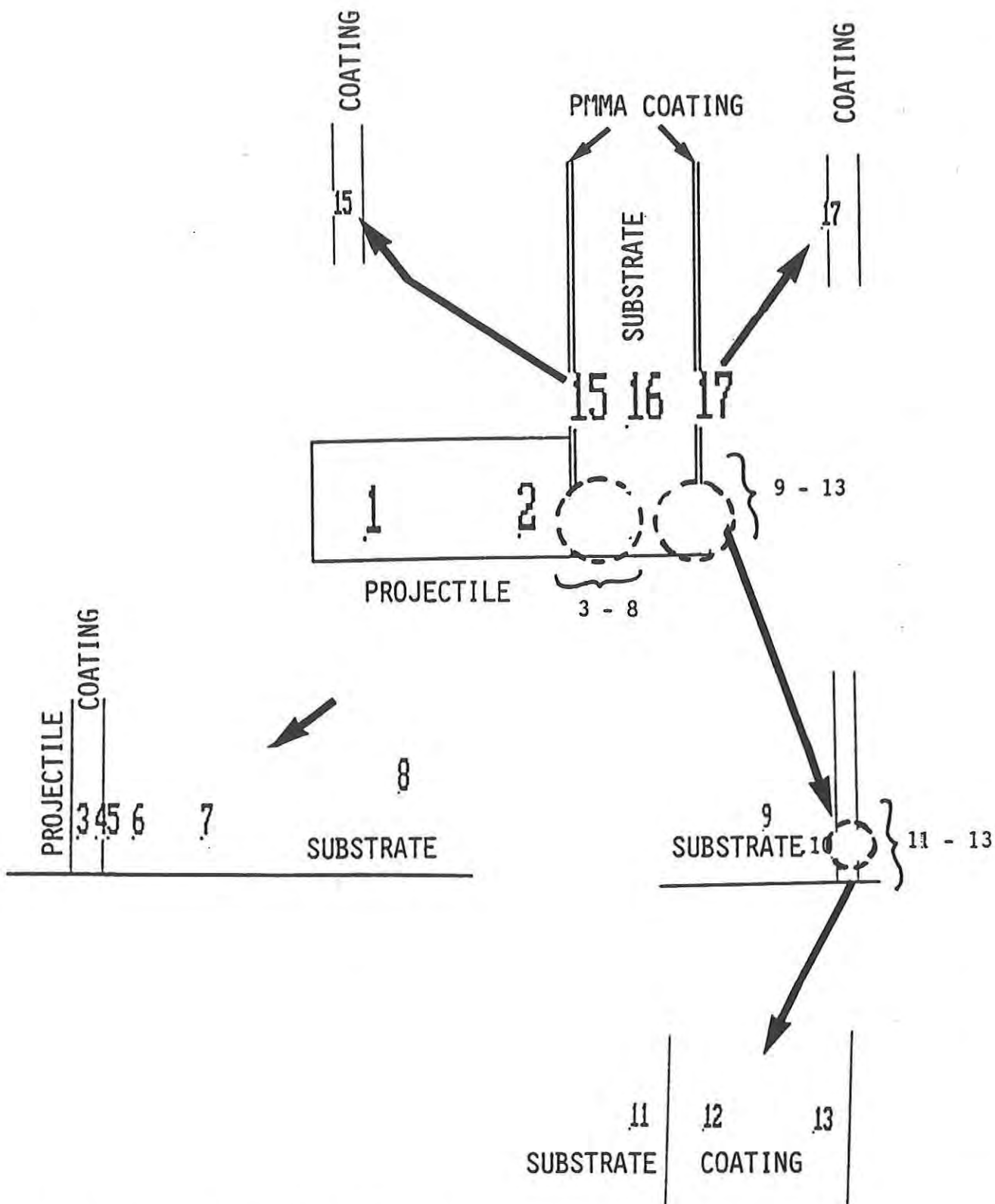


Figure A.23. Location of Target Points for Post Processing of Low Velocity Impact Analysis

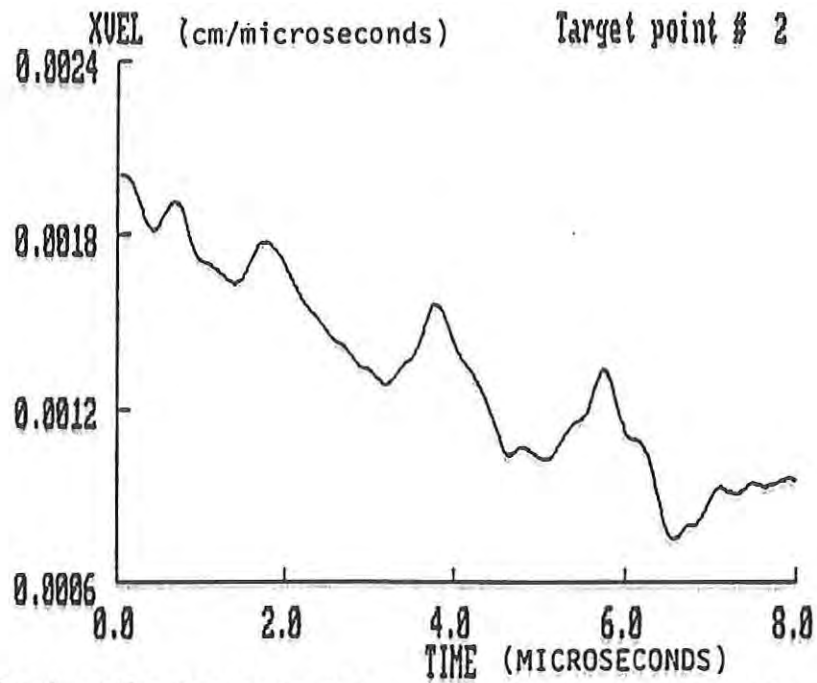


Figure A.24a. Projectile Particle Velocities in Impact Direction:
(a) Near Impact Surface of Projectile

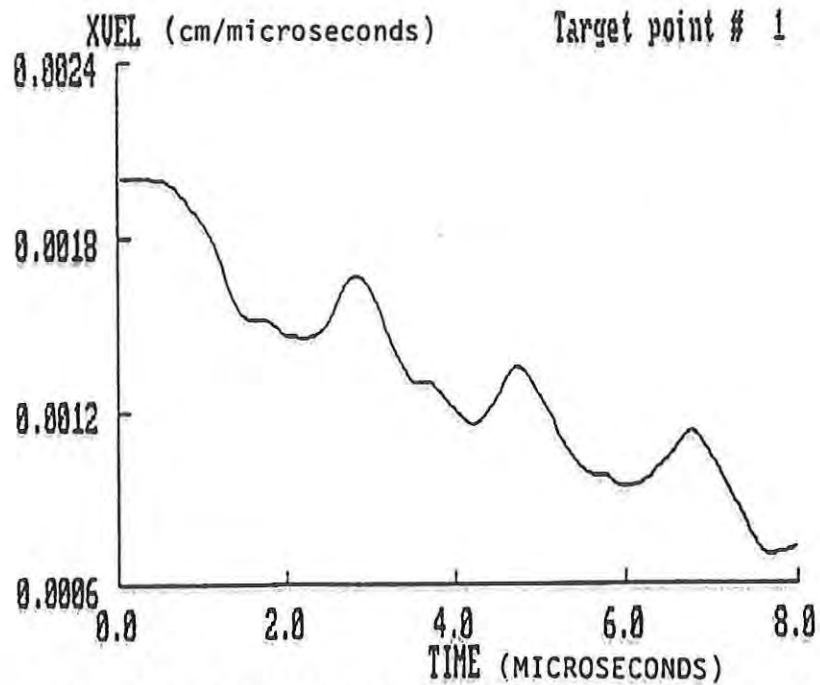


Figure A.24b. Projectile Particle Velocities in Impact Direction:
(b) Near Back Surface

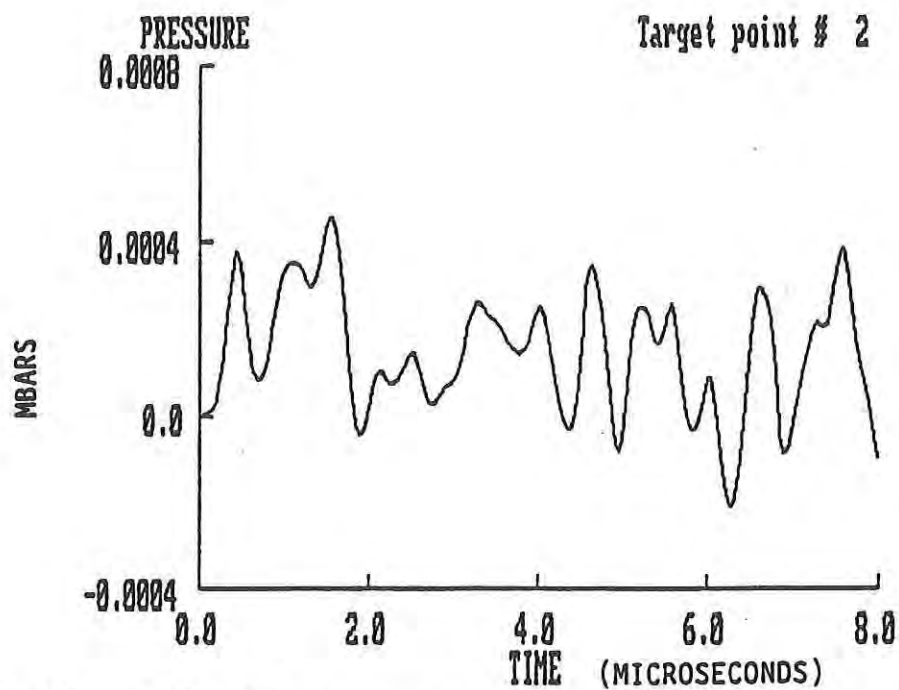


Figure A.25a. Projectile Pressures: (a) Near Impact Surface of Projectile

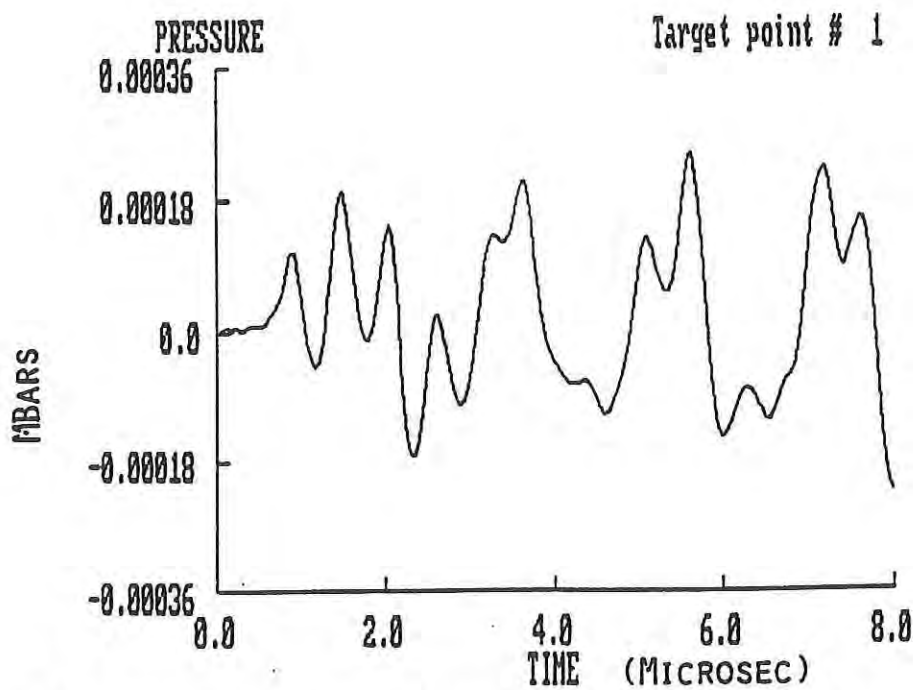


Figure A.25b. Projectile Pressures: (b) Near Back Surface

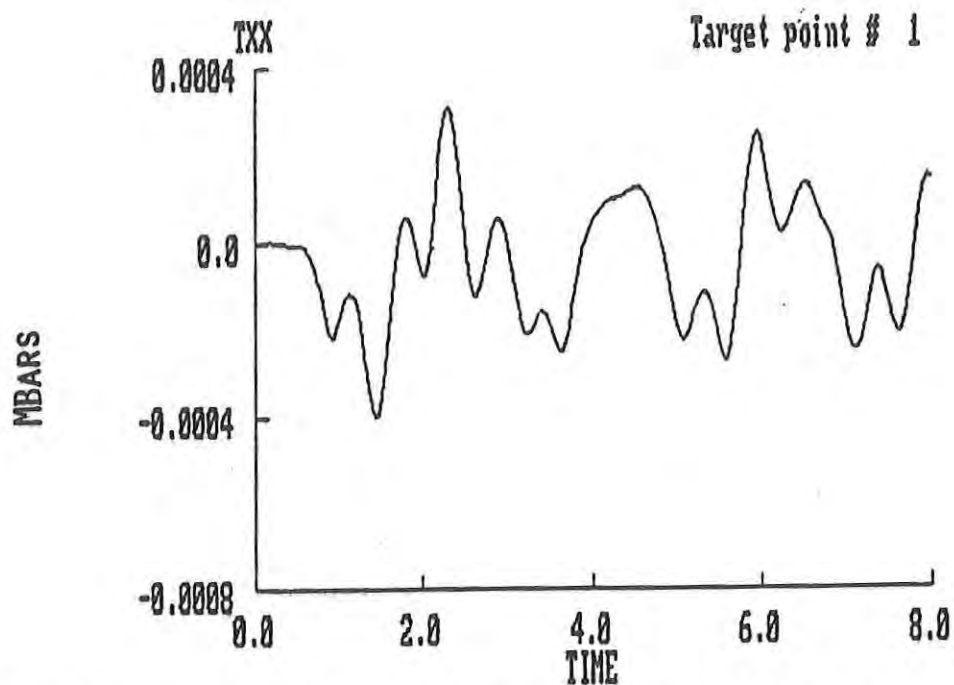


Figure A.26a. Stress Components in Projectile Near Back Surface:
 (a) Impact Direction

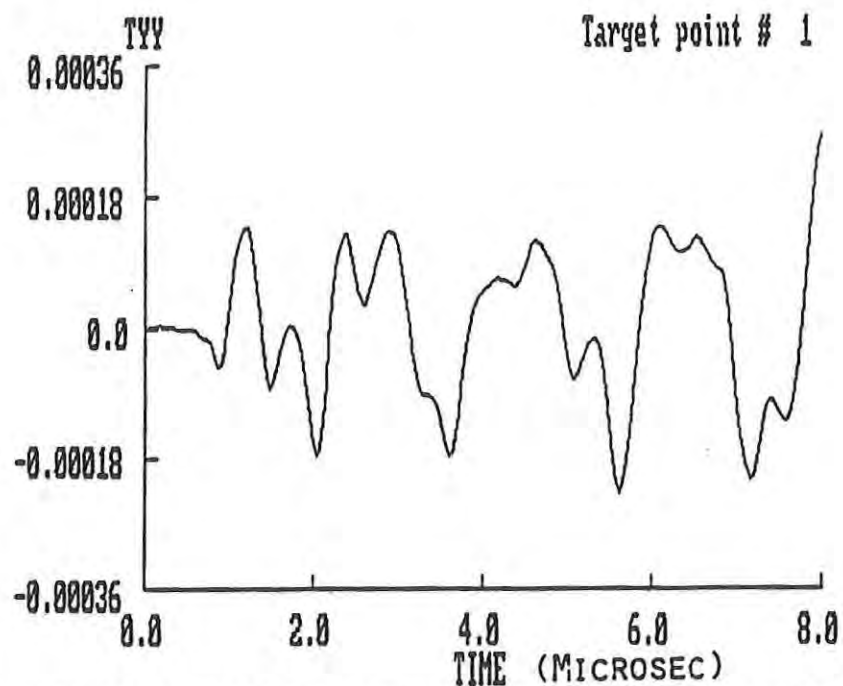


Figure A.26b. Stress Components in Projectile Near Back Surface:
 (b) Radial Direction

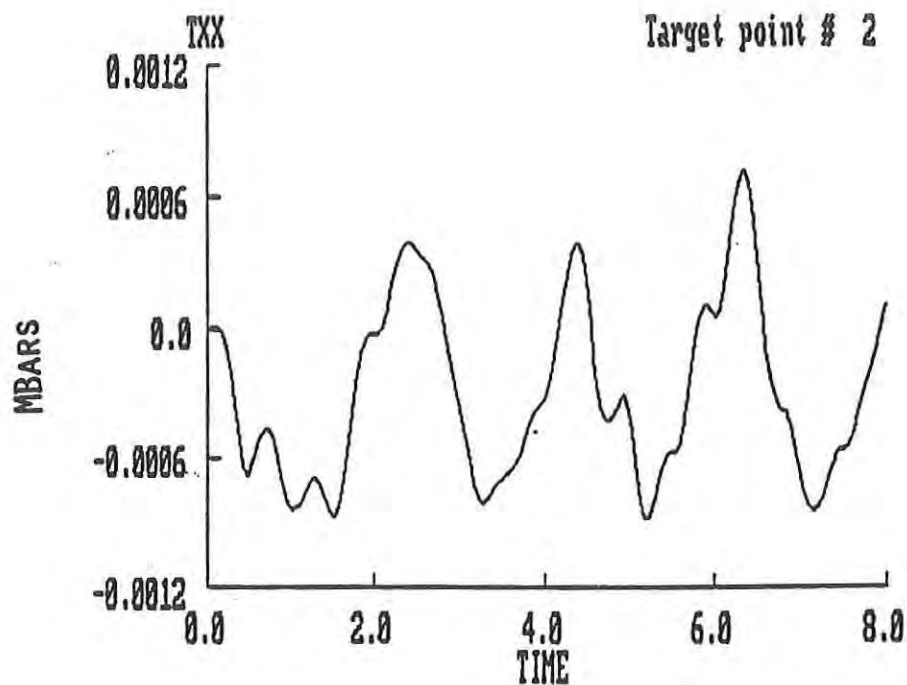


Figure A.27a. Stress Components Near Impact Surface of Projectile:
(a) Impact Direction

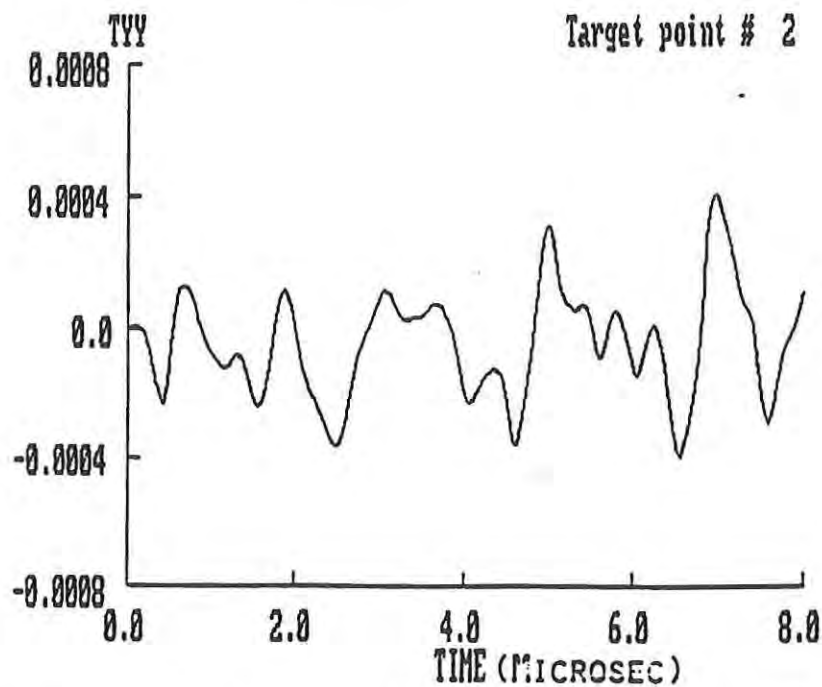


Figure A.27b. Stress Components Near Impact Surface of Projectile :
(b) Radial Direction

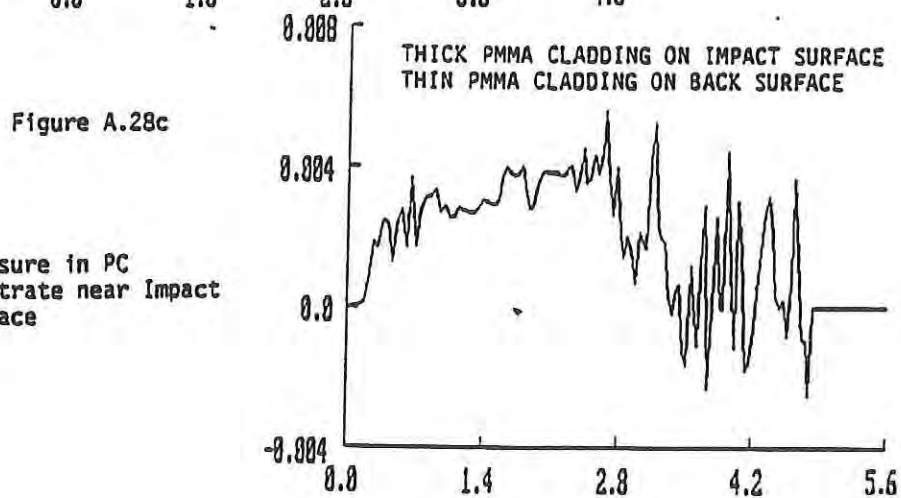
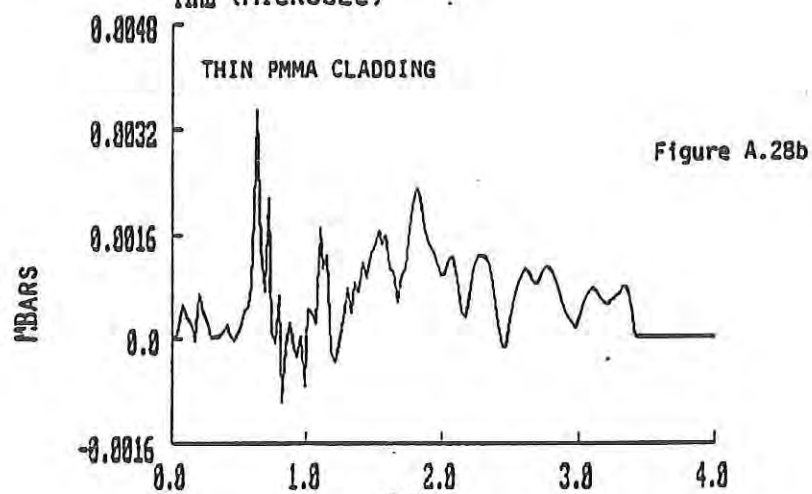
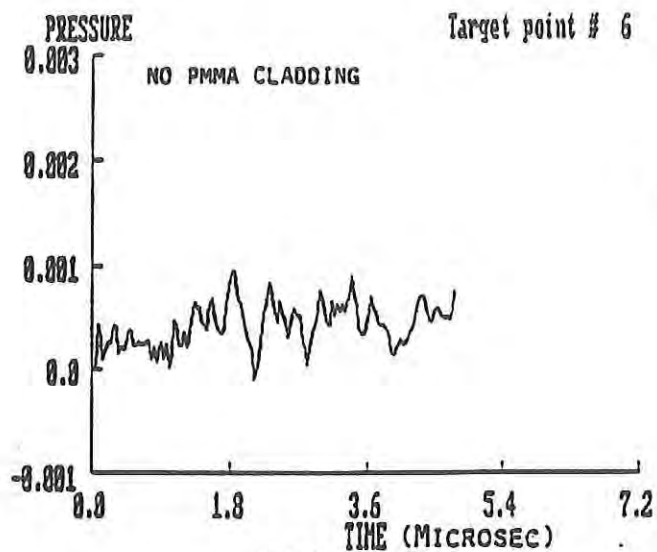


Figure A.28. Pressure in PC Substrate near Impact Surface

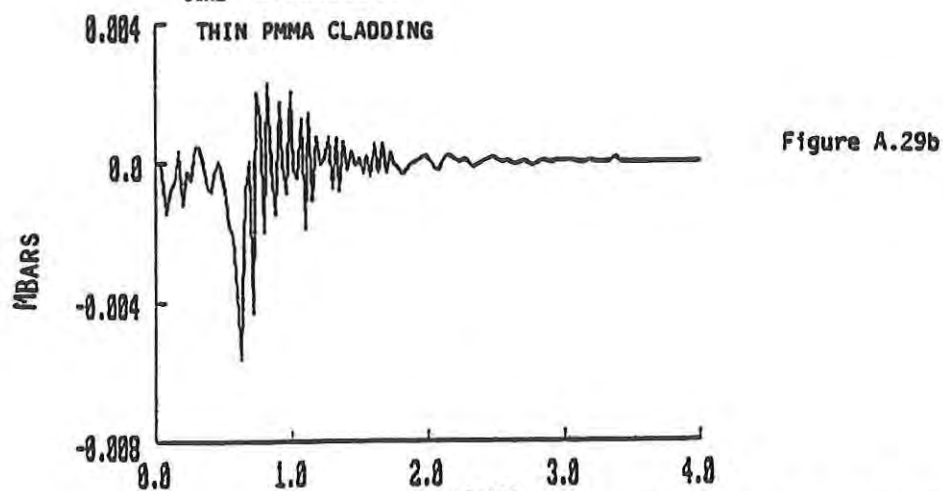
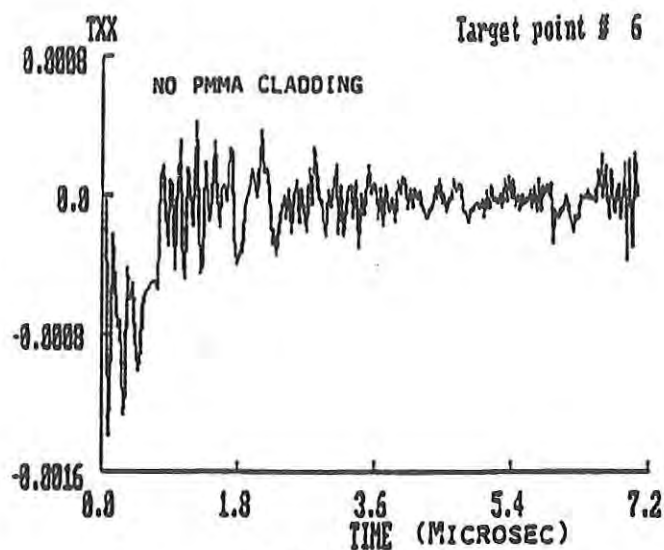


Figure A.29c

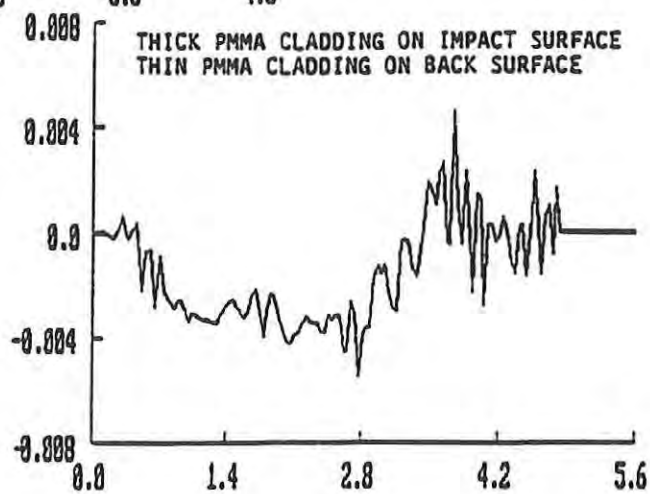


Figure A.29. Radial Stress Near Impact Surface of PC Substrate

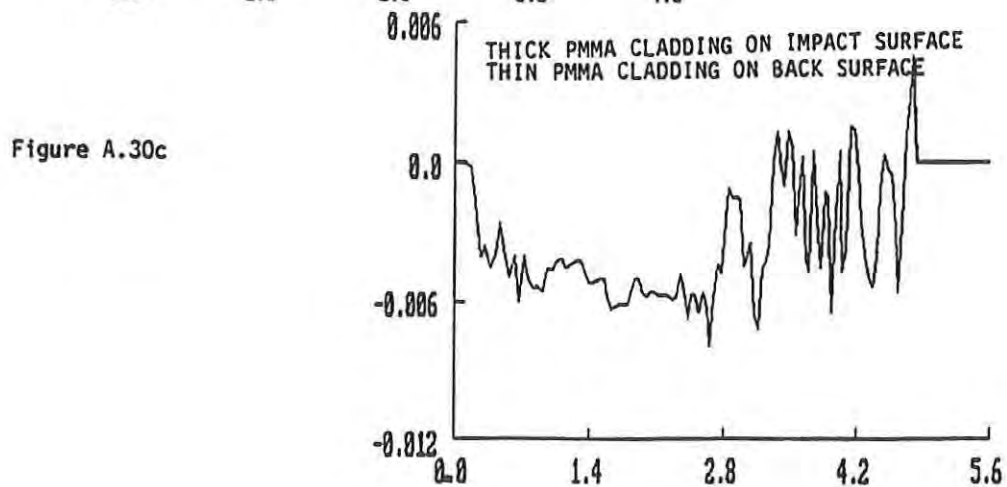
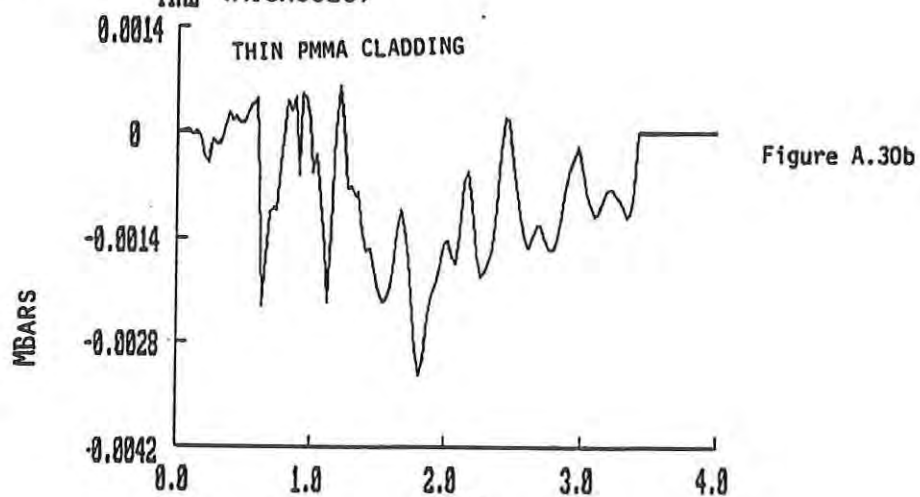
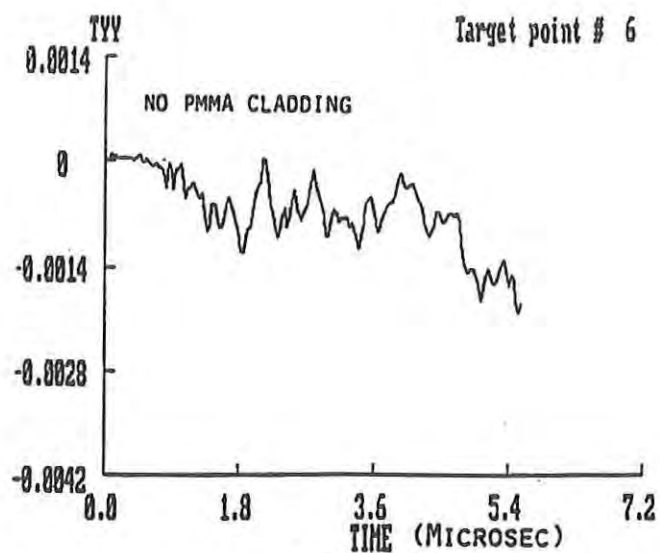


Figure A.30. Stress in Impact Direction Near Impact Surface of PC

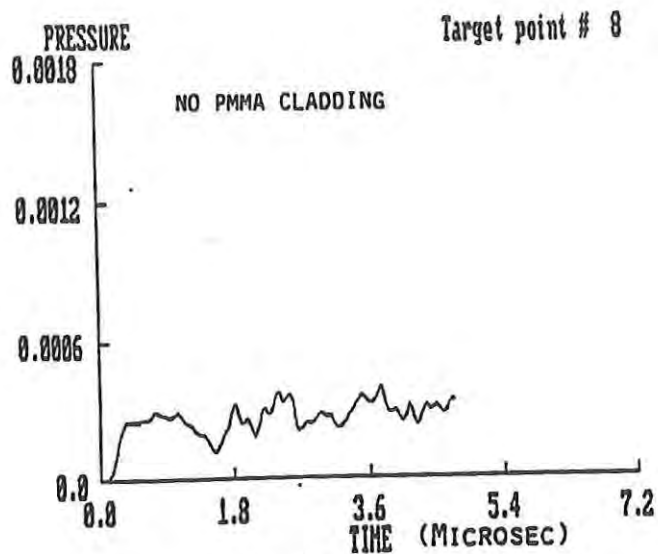


Figure A.31a

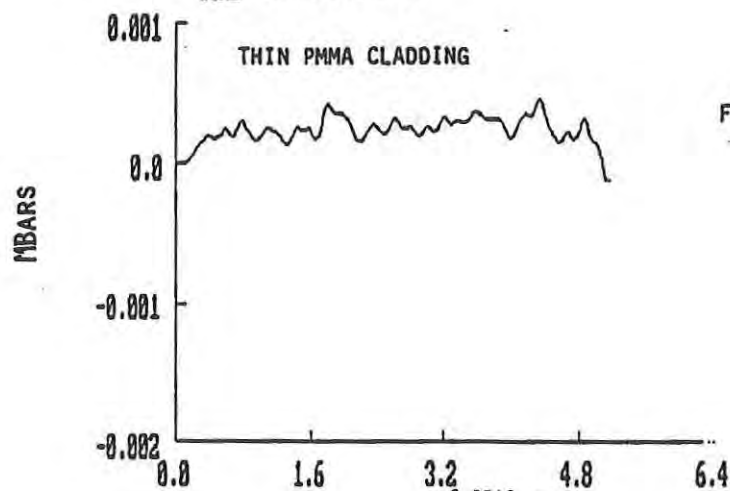


Figure A.31b

Figure A.31c

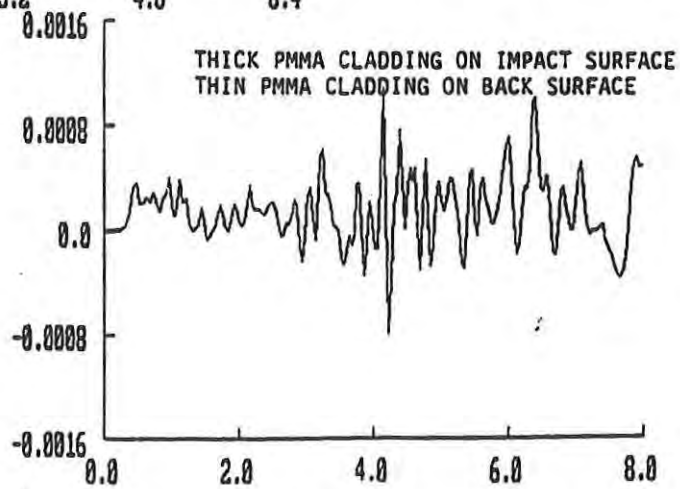


Figure A.31.

Pressure Near Midplane of PC Substrate

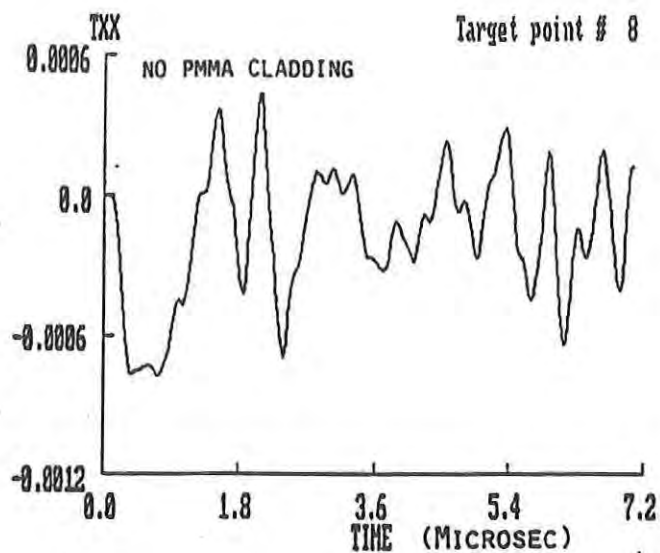


Figure A.32a

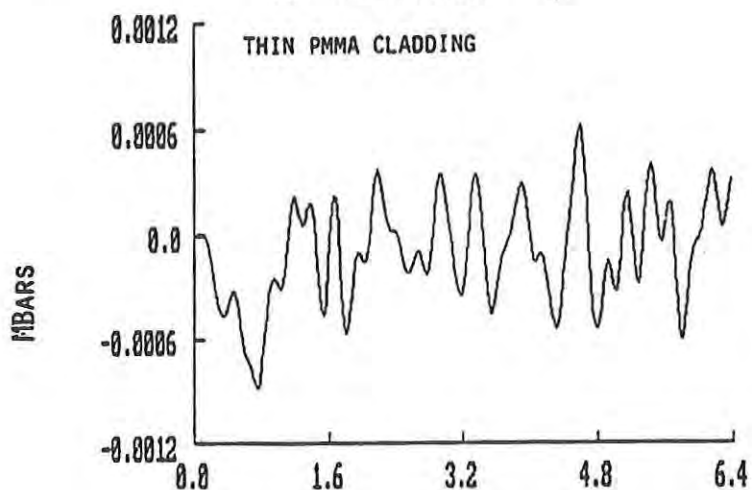


Figure A.32b

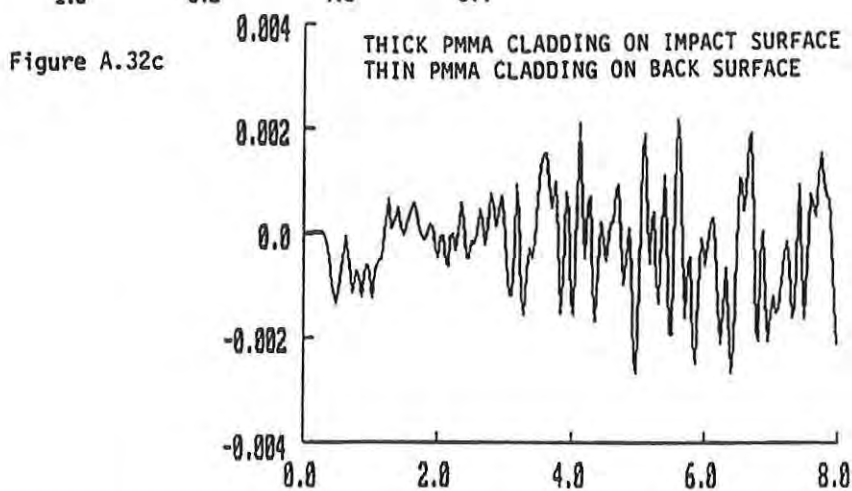


Figure A.32c

Figure A.32.

Stress Component at Midplane of PC Substrate in Impact Direction

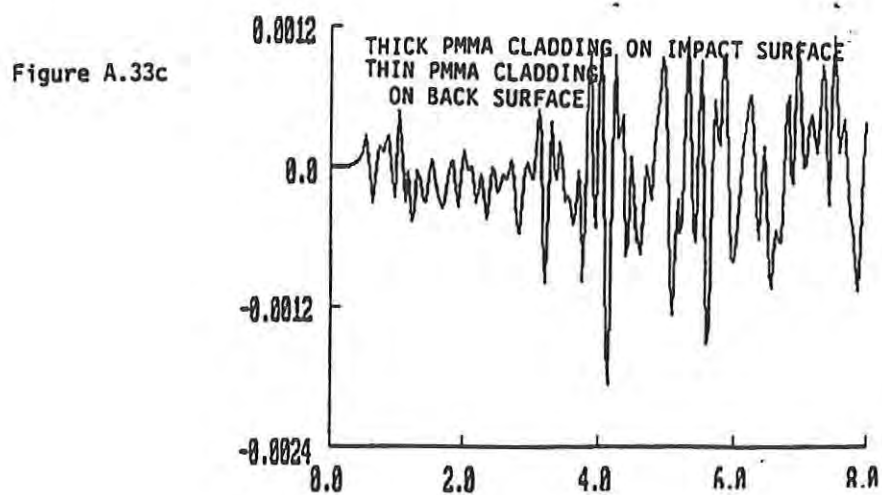
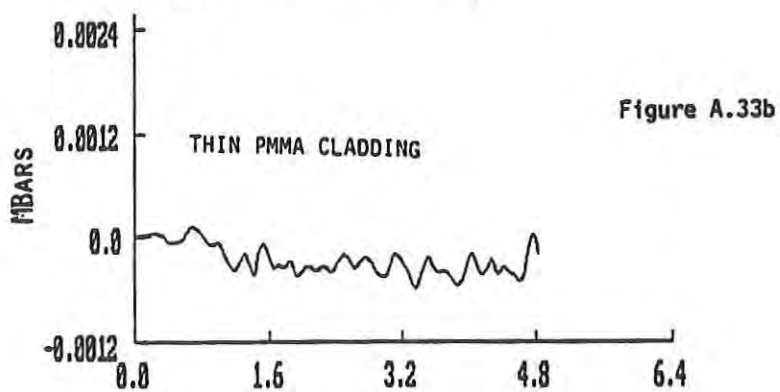
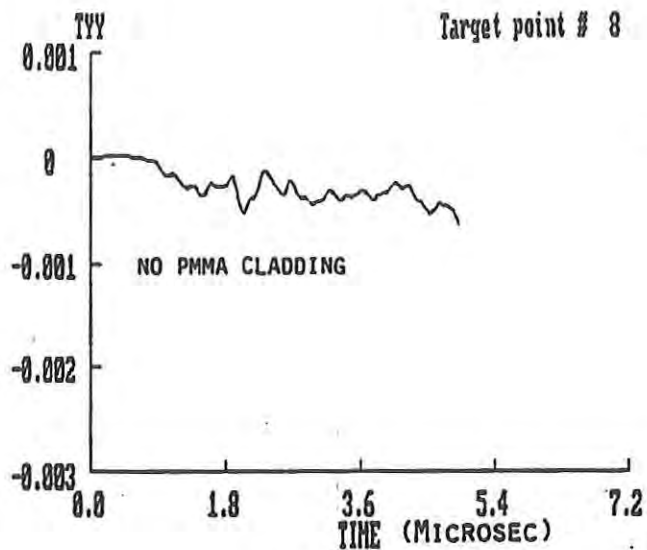


Figure A.33.

Stress Component at Midplane of PC Substrate in Radial Direction

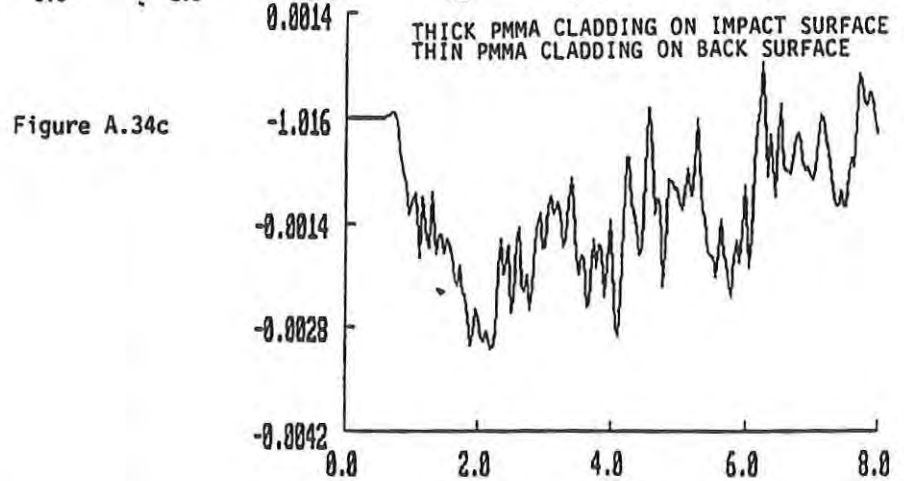
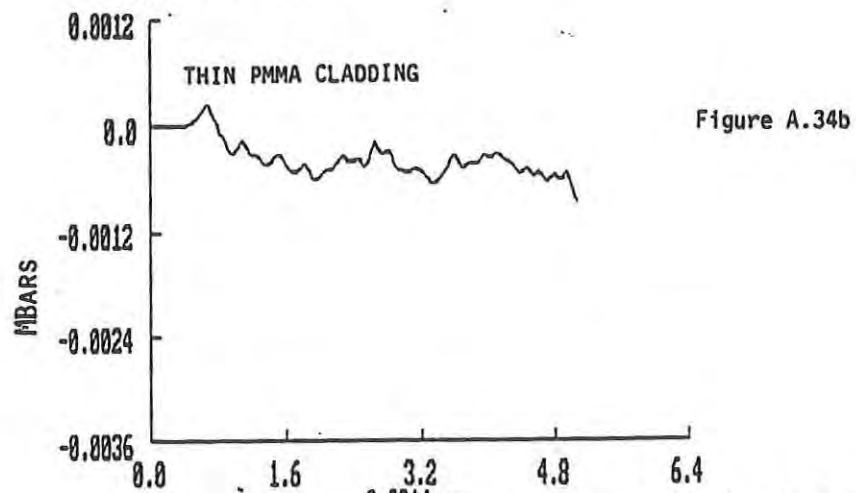
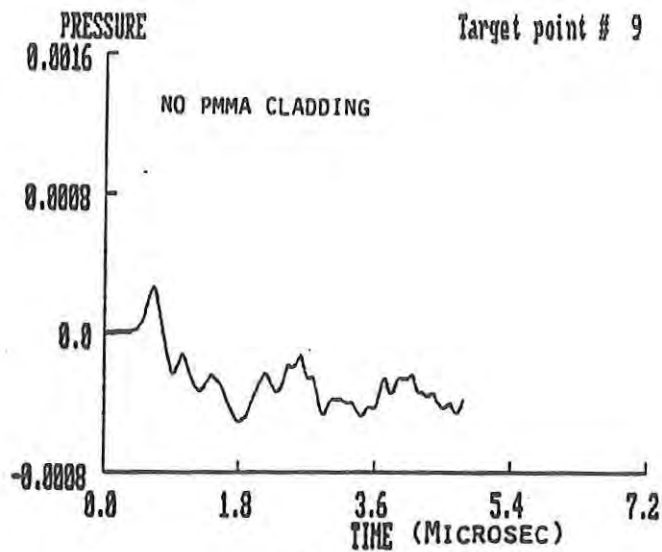


Figure A.34

Pressure Near Rear Surface of PC Substrate

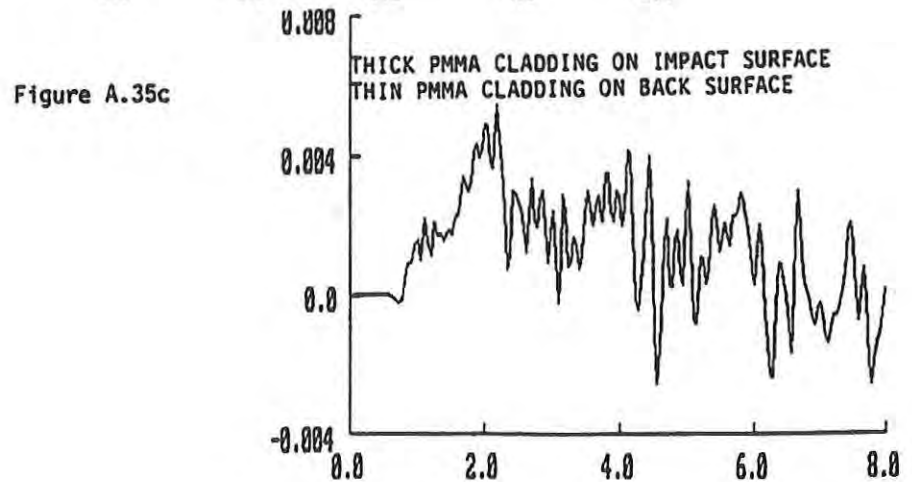
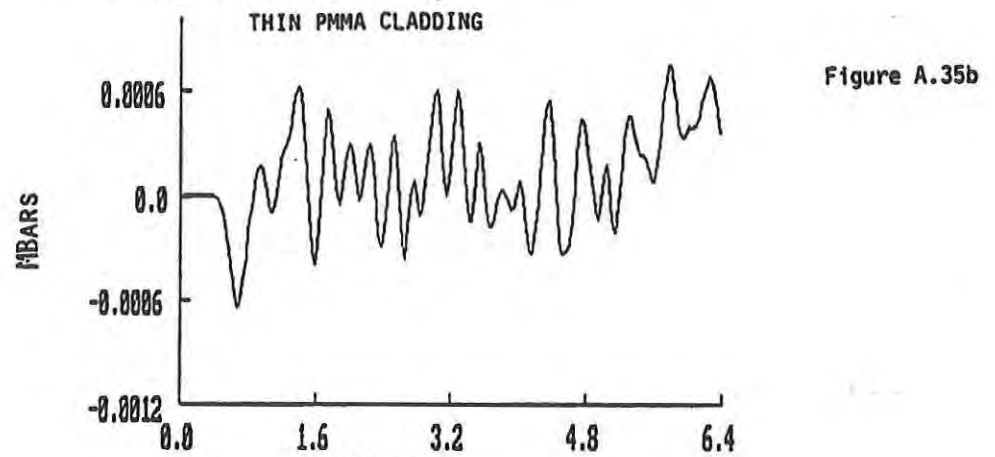
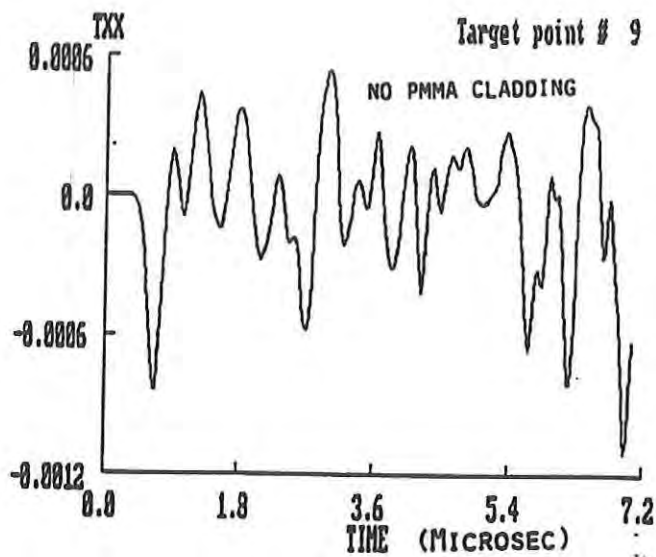


Figure A.35. Stress Component Near Rear Surface of PC Substrate in Impact Direction

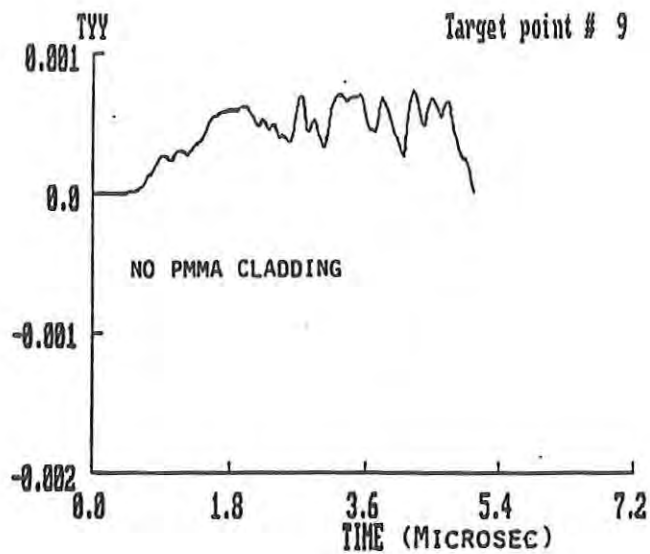


Figure A.36a

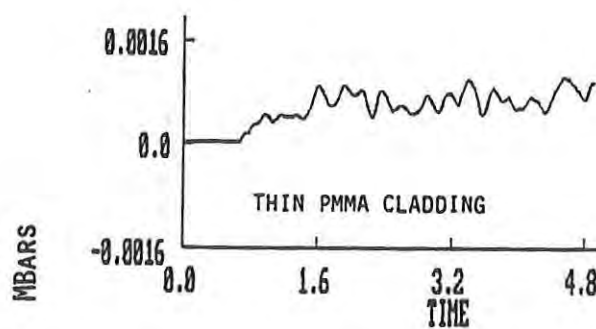


Figure A.36b

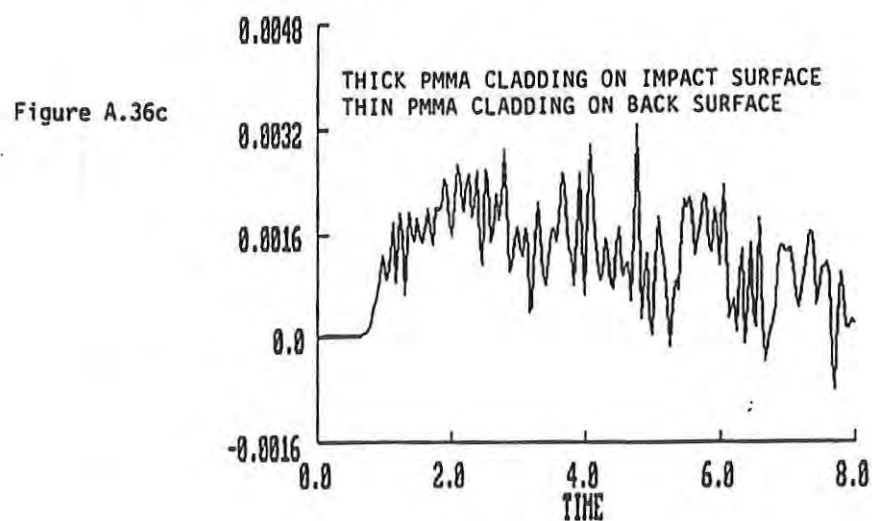


Figure A.36.

Stress Component Near Back Surface of PC Substrate in Radial Direction

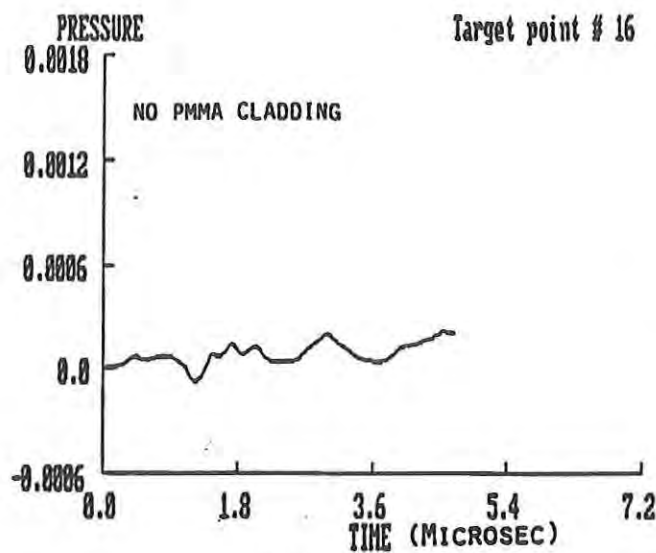


Figure A.37a

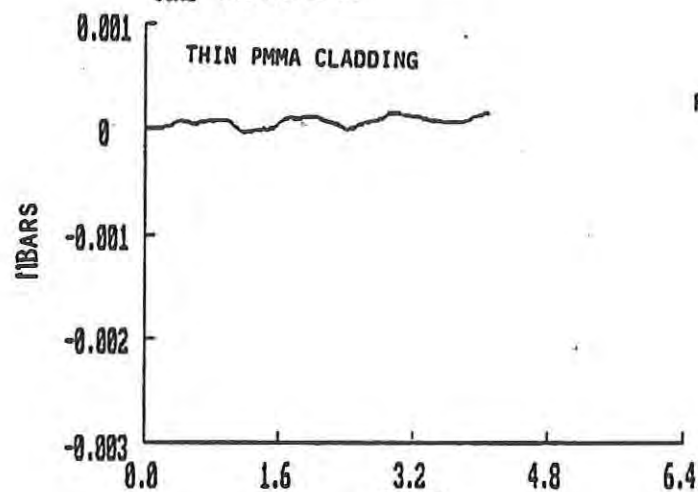


Figure A.37b

Figure A.37c

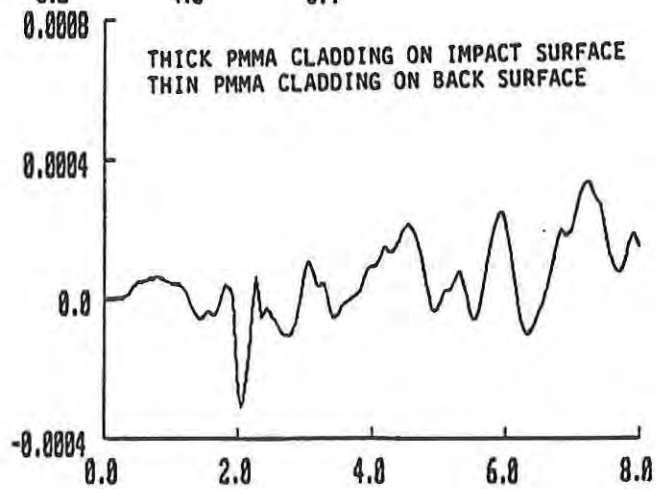


Figure A.37.

Pressure Near Midplane of PC Substrate Outside of Impact Region

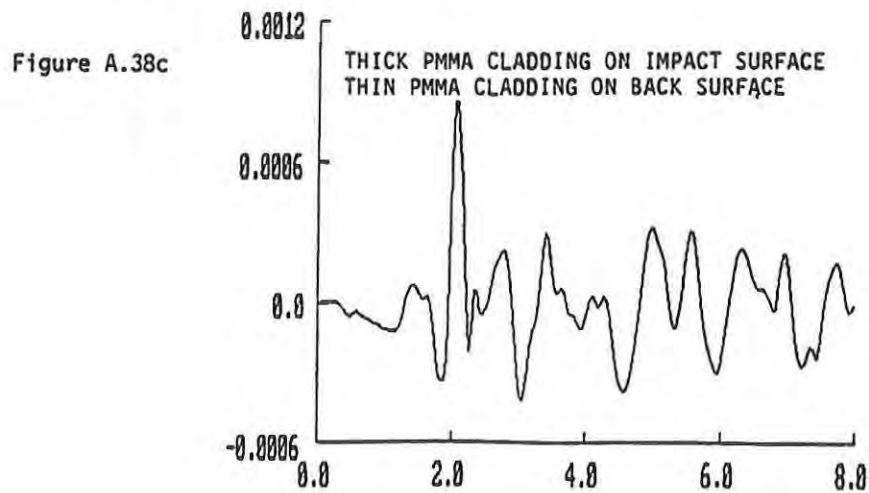
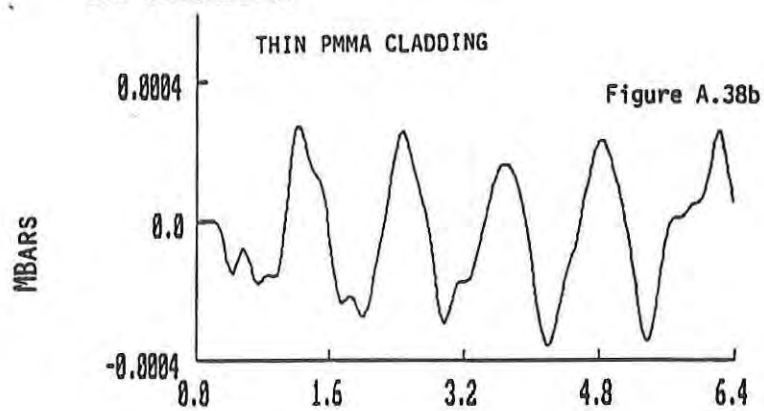
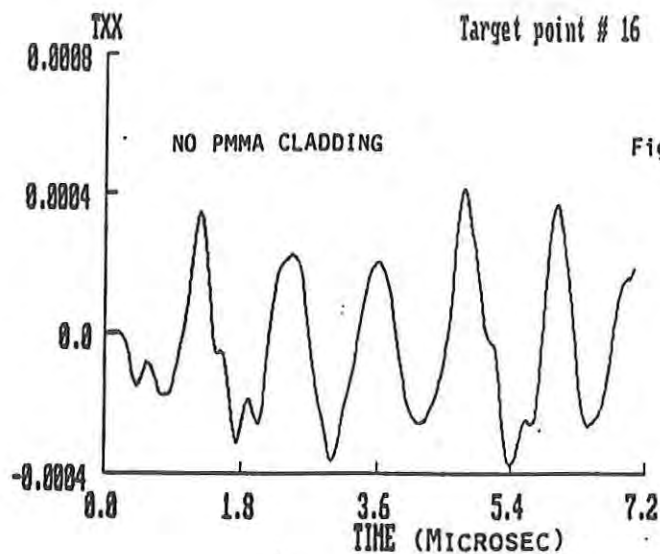


Figure A.38.

Stress Component Near Back Surface of PC Substrate Outside of Impact Region in Radial Direction

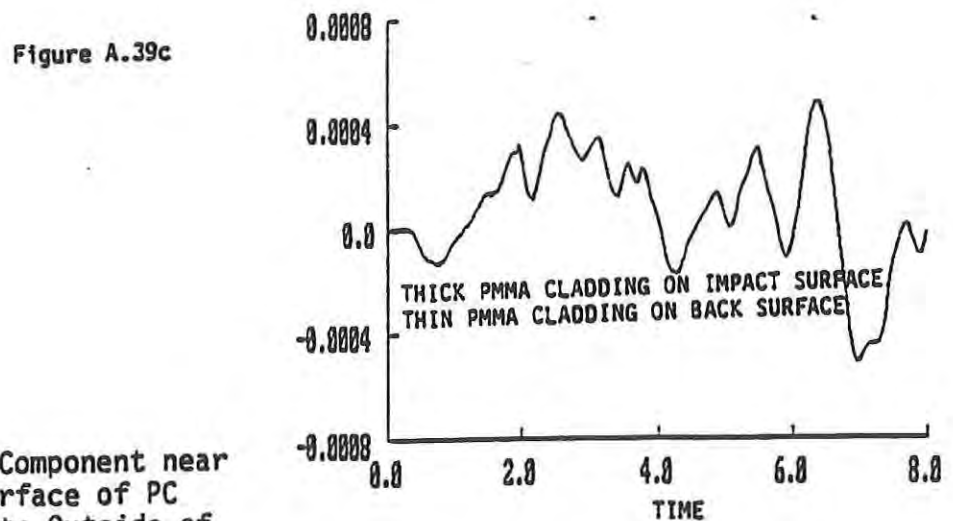
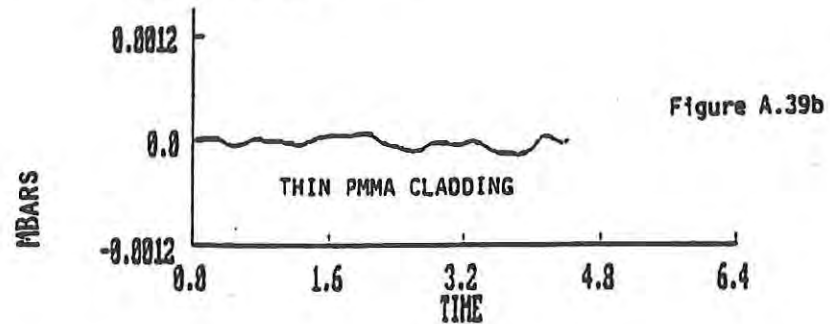
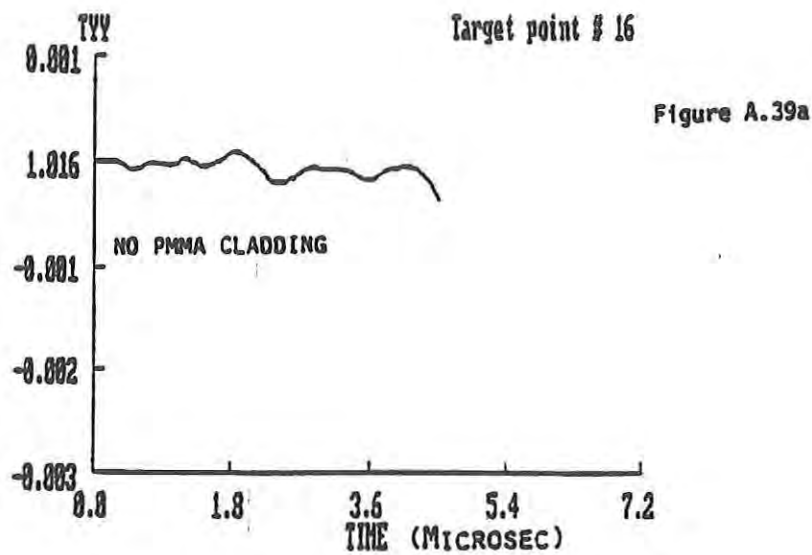


Figure A.39. Stress Component near Back Surface of PC Substrate Outside of Impact Region in Radial Direction

1850

1851

1852

1853

1854

1855

1856

1857

1858

1859

1860

1861

1862

1863

1864

1865

1866

1867

1868

1869

1870

1871

1872

1873

1874

1875

1876

1877

1878

1879

**APPENDIX A.2.2.2 - 2D Stress Wave Analysis
for Low Velocity Impact with Pre-Existing Geometric Discontinuity**

<u>Figure</u>		<u>Page</u>
A.40	Pressure near Midplane of PC Substrate: (a) No PMMA Cladding; and, (b) Thin PMMA Cladding.	141
A.41	Stress Components at Midplane of PC Substrate: (a) No PMMA Cladding in Impact Direction; (b) Thin PMMA Cladding in Impact Direction; (c) No PMMA Cladding in Radial Direction; and, (d) Thin PMMA Cladding in Radial Direction.	142
A.42	Pressure near Rear Surface of PC Substrate	143
A.43	Stress Components near Rear Surface of PC Substrate: (a) No PMMA Cladding in Impact Direction; (b) Thin PMMA Cladding in Impact Direction; (c) No PMMA Cladding in Radial Direction; and, (d) Thin PMMA Cladding in Radial Direction.	144
A.44	Pressure near Rear Surface of PC Substrate	145
A.45	Stress Components near Rear Surface of PC Substrate: (a) No PMMA Cladding in Impact Direction; (b) Thin PMMA Cladding in Impact Direction; (c) No PMMA Cladding in Radial Direction; and, (d) Thin PMMA Cladding in Radial Direction.	146
A.46	Pressure near Midplane of PC Substrate outside Impact Region	147
A.47	Stress Components near Midplane of PC Substrate outside of Impact Region: (a) No PMMA Cladding in Impact Direction; (b) Thin PMMA Cladding in Impact Direction; (c) No PMMA Cladding in Radial Direction; and, (d) Thin PMMA Cladding in Radial Direction.	148
A.48	Pressure near Rear Surface of PC Substrate outside Impact Region	149
A.49	Stress Components near Rear Surface of PC Substrate outside of Impact Region: (a) No PMMA Cladding in Impact Direction; (b) Thin PMMA Cladding in Impact Direction; (c) No PMMA Cladding in Radial Direction; and, (d) Thin PMMA Cladding in Radial Direction.	150

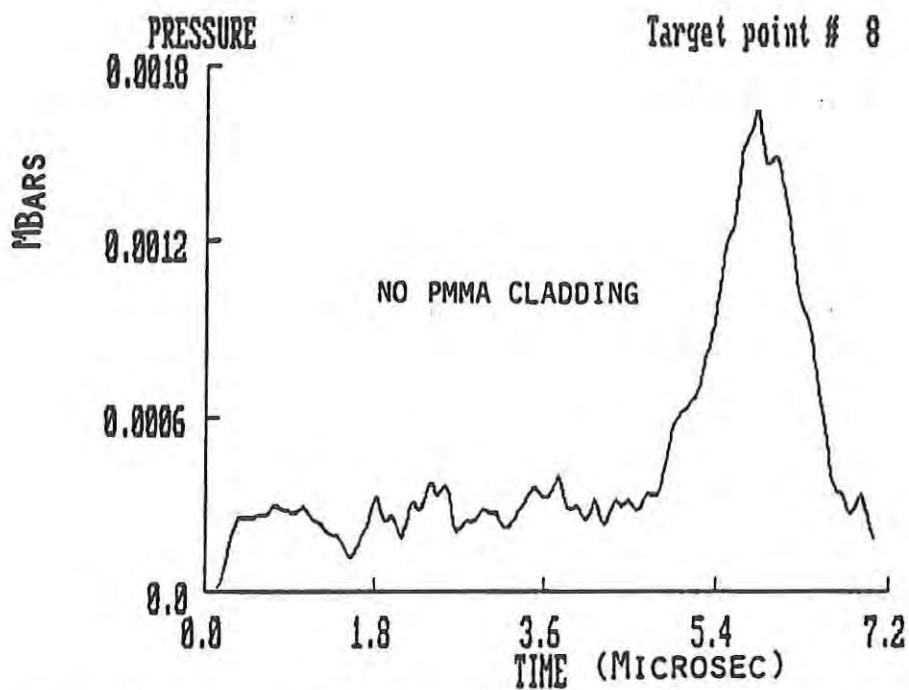


Figure A.40 (a) Pressure near Midplane of PC Substrate:
No PMMA Cladding

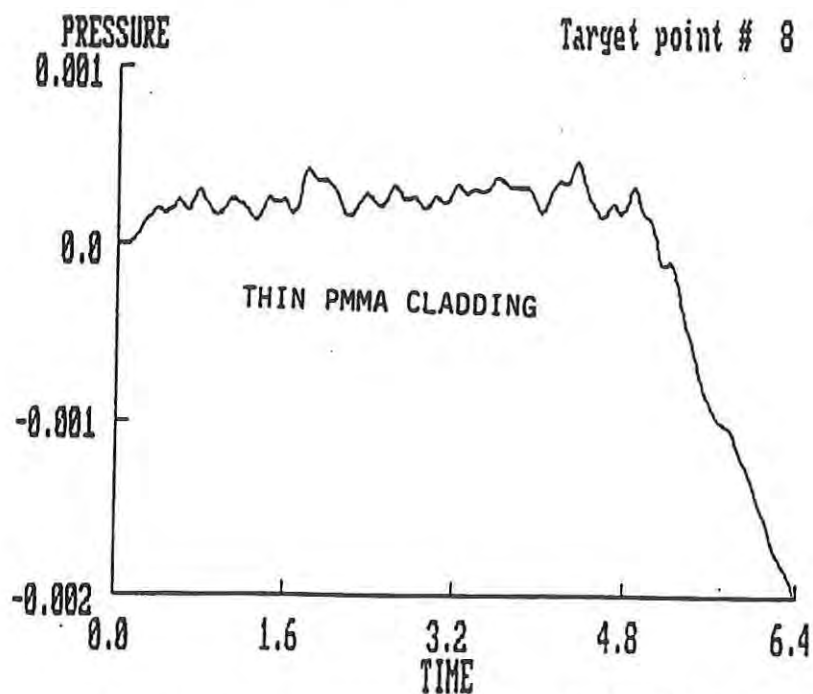


Figure A.40 (b) Pressure near Midplane of PC Substrate:
Thin PMMA Cladding

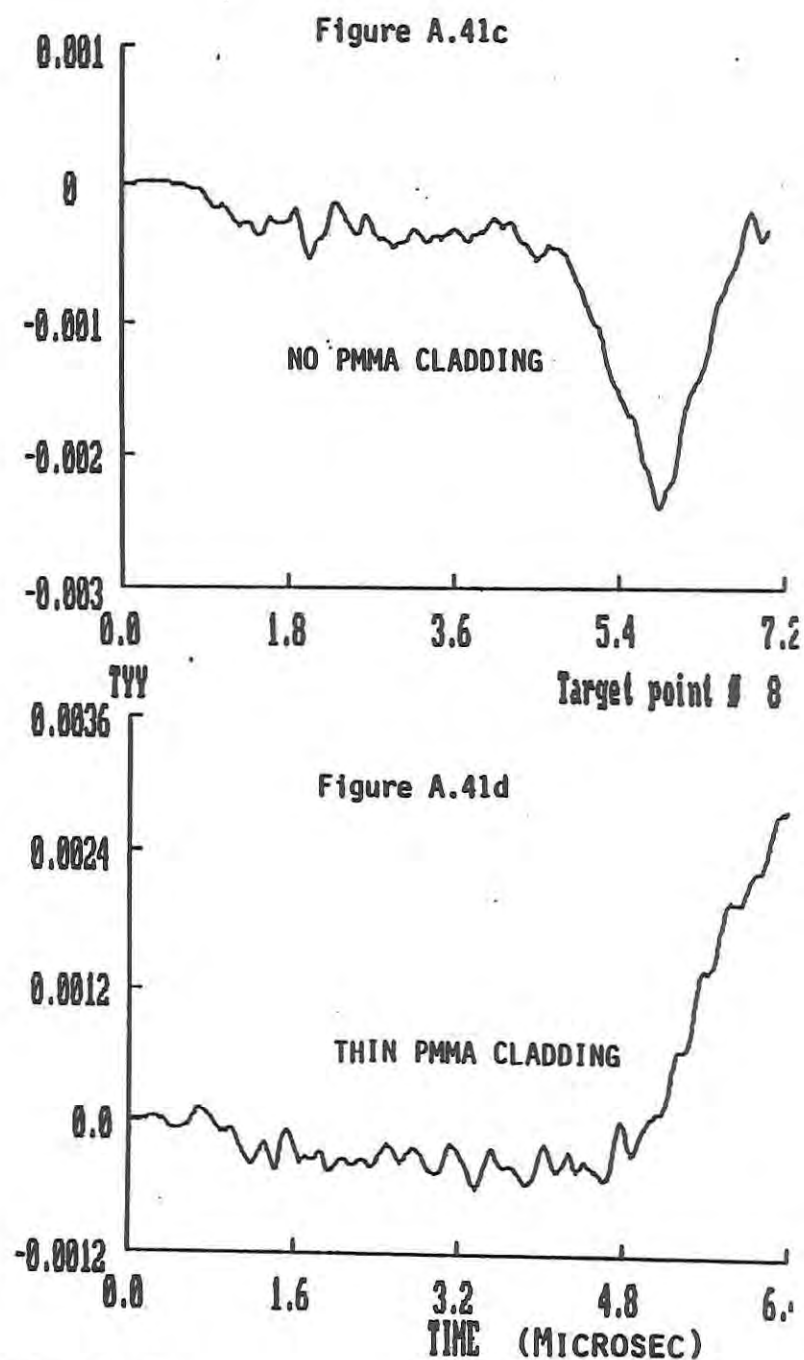
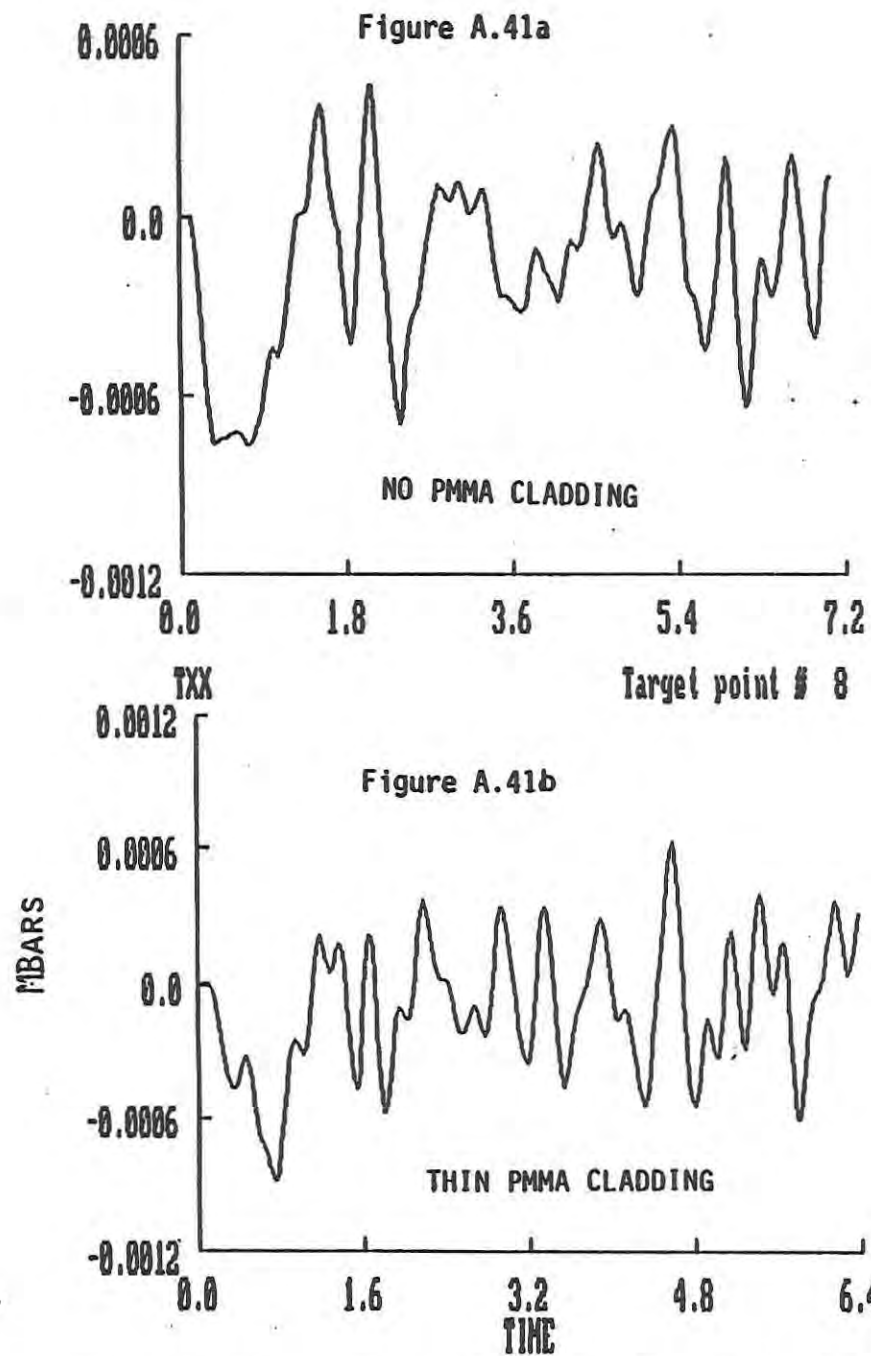


Figure A.41. Stress Components at Midplane of PC Substrate

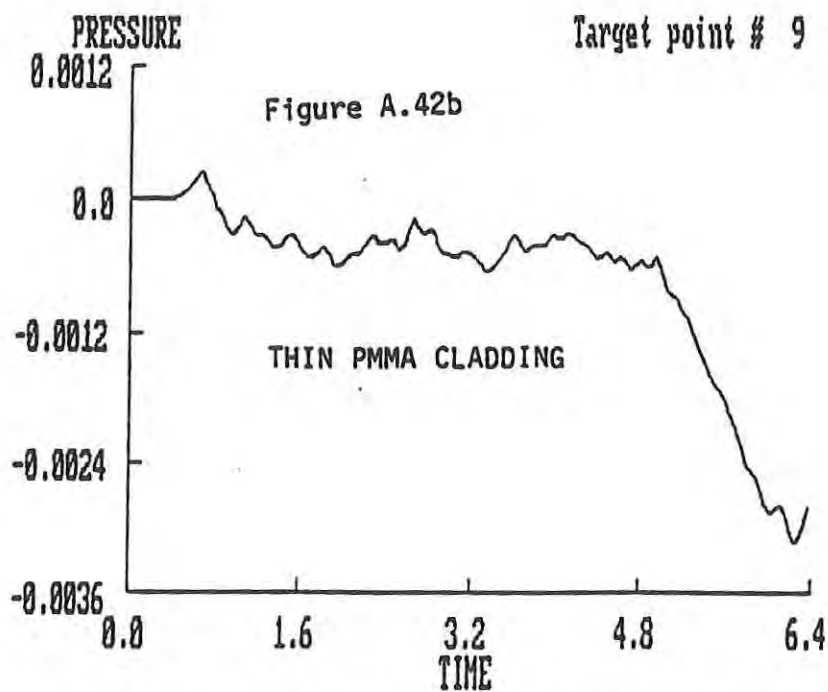
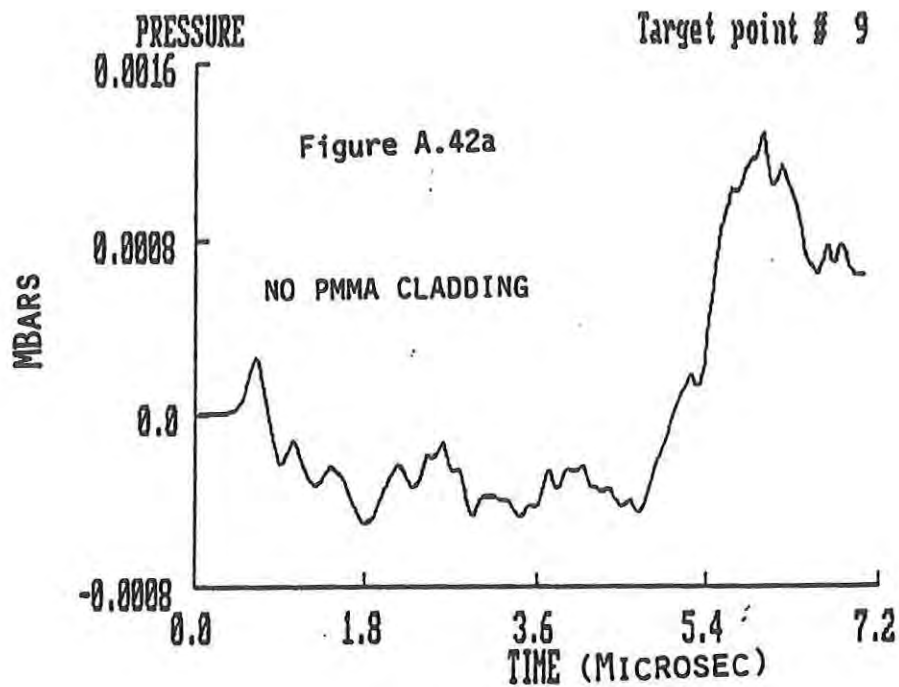


Figure A.42. Pressure near Rear Surface of PC Substrate

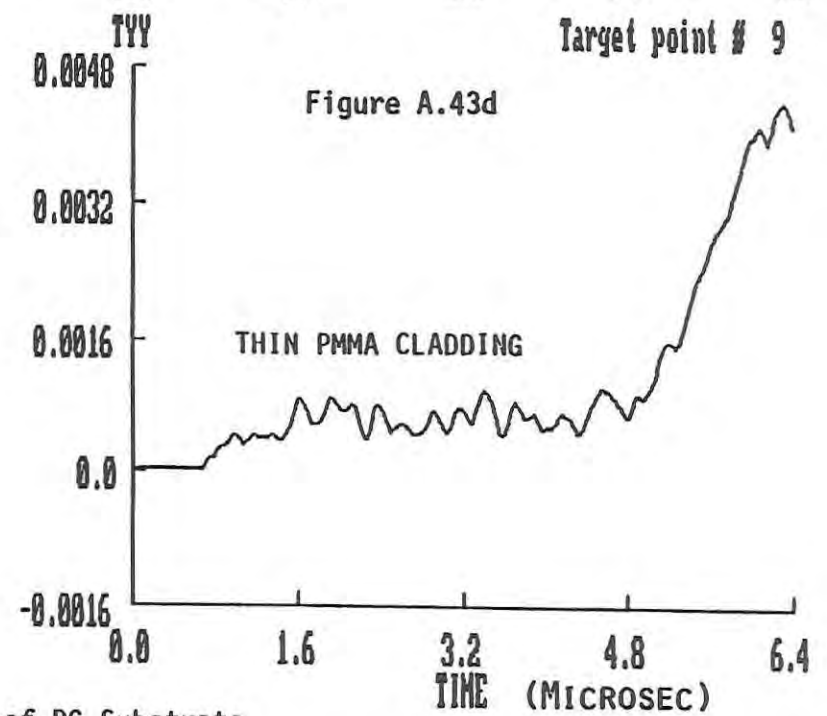
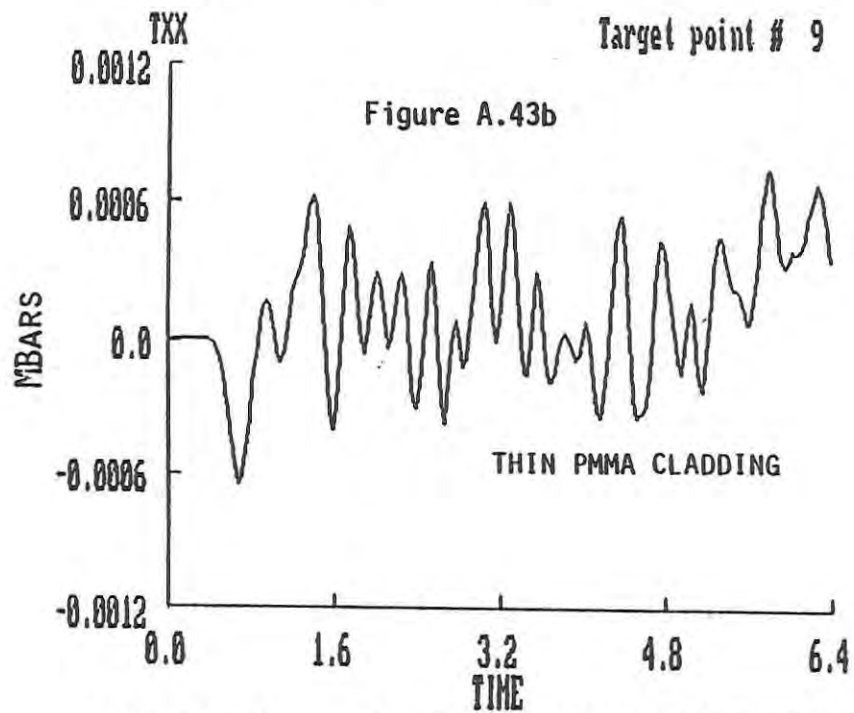
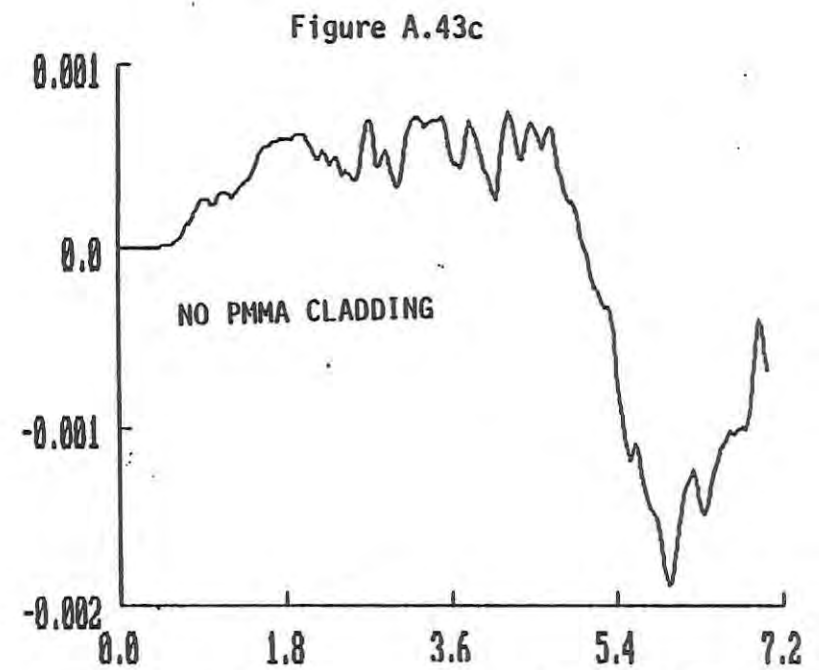
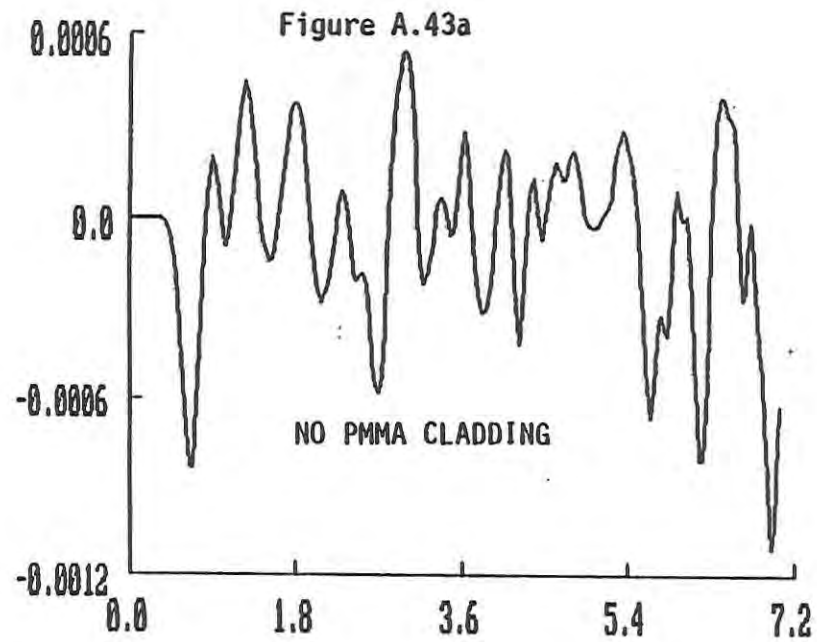


Figure A.43. Stress Components near Rear Surface of PC Substrate

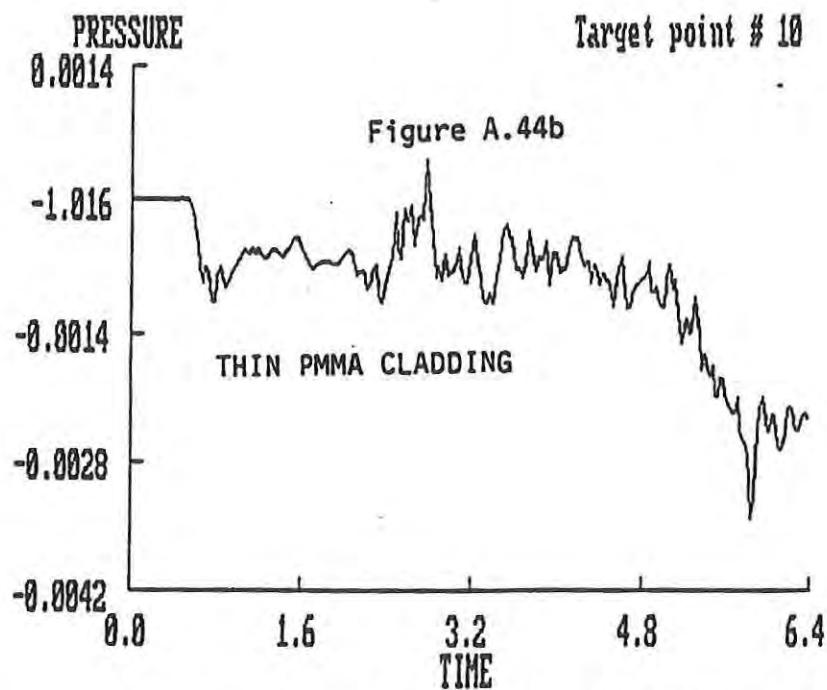
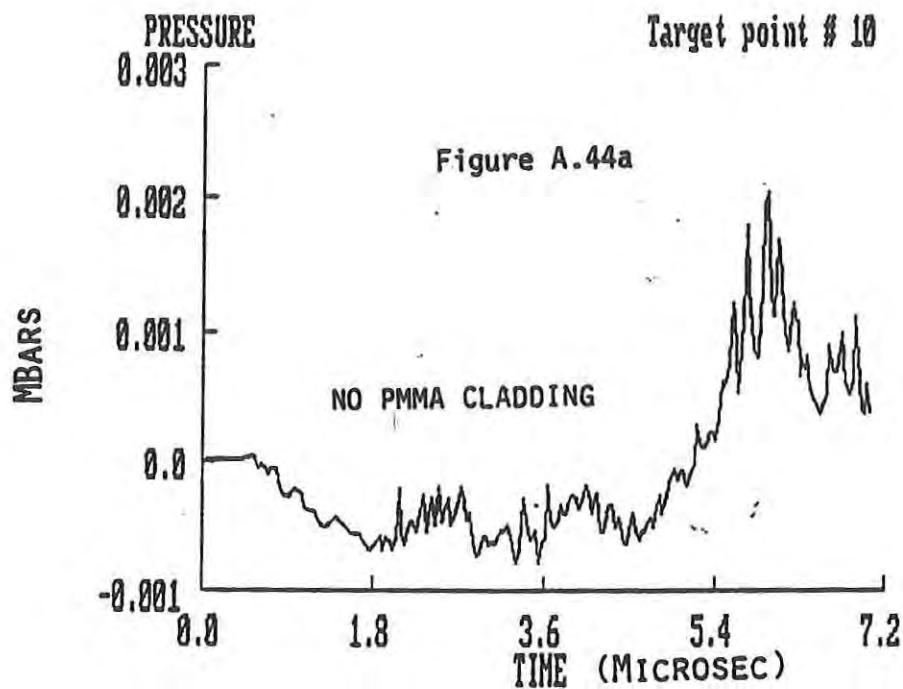


Figure A.44. Pressure near Rear Surface of PC Substrate

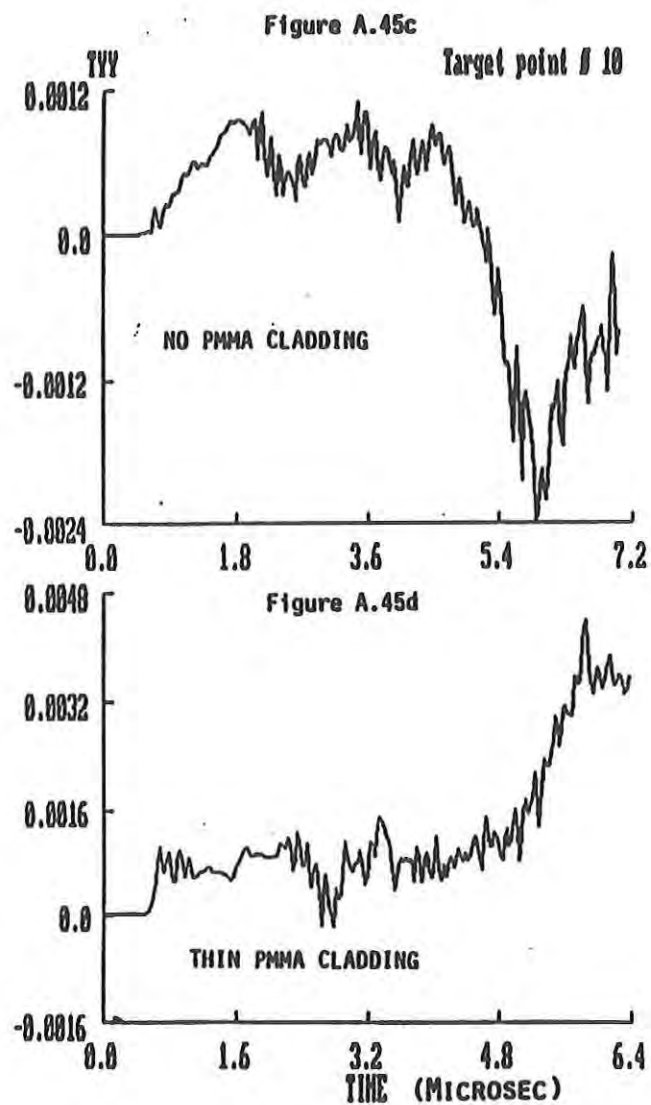
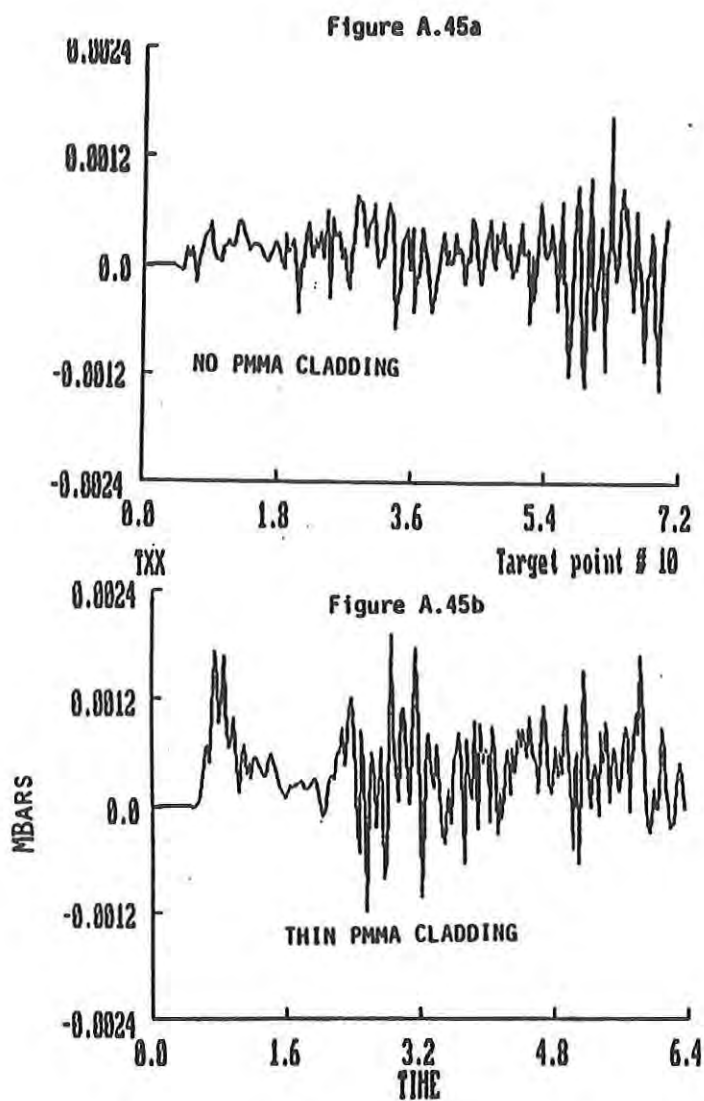


Figure A.45

Stress Components Near Rear Surface of PC Substrate

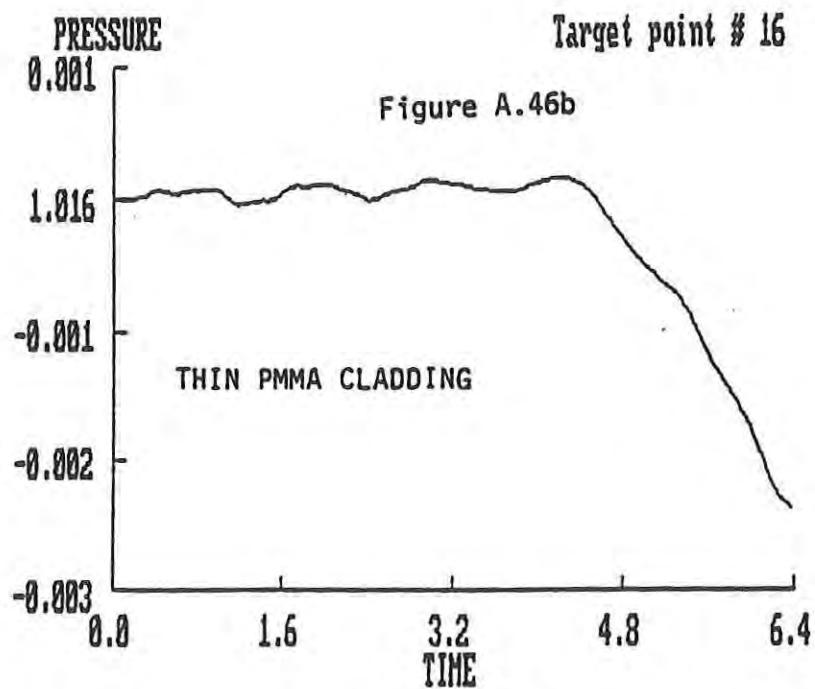
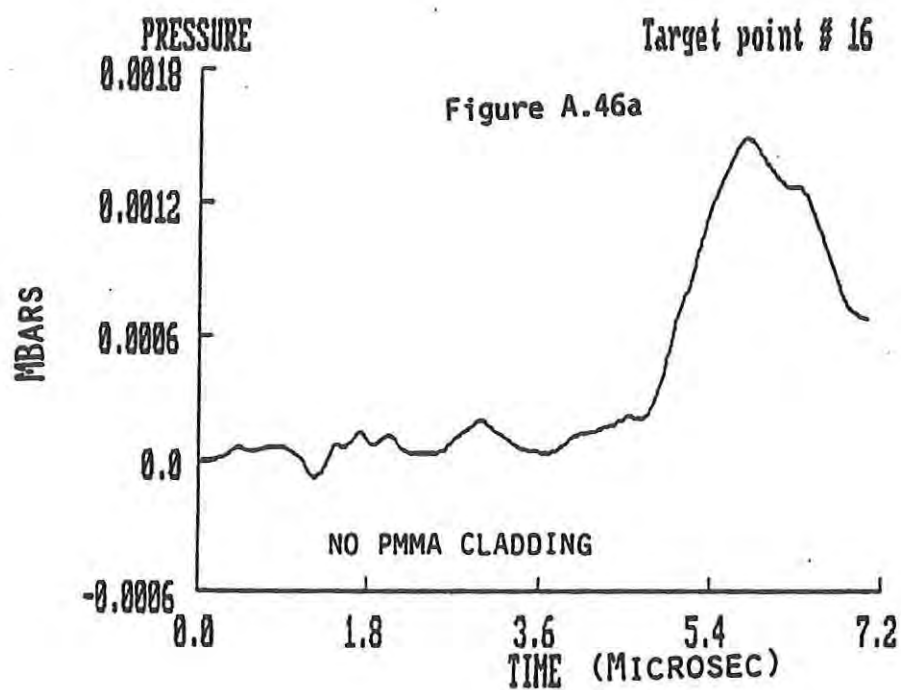


Figure A.46. Pressure near Midplane of PC Substrate Outside Impact Region

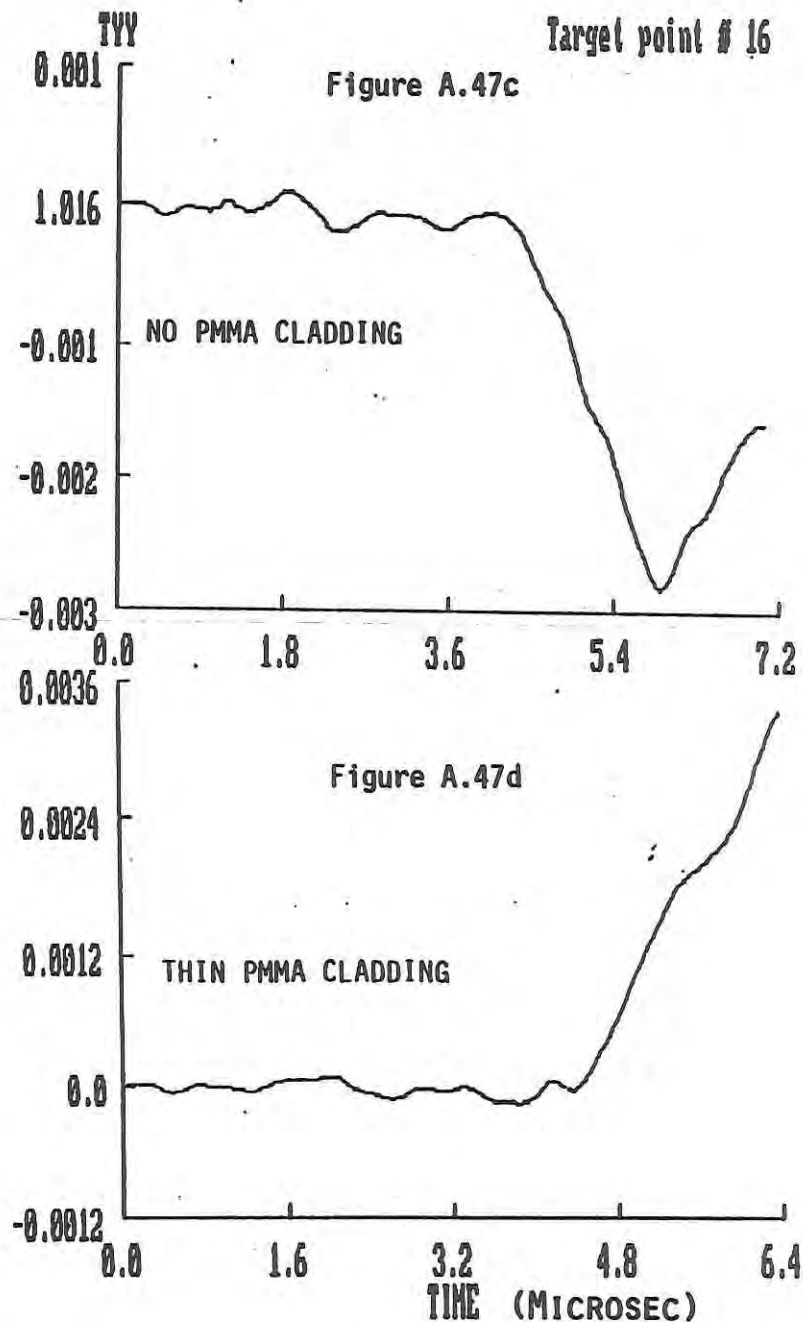
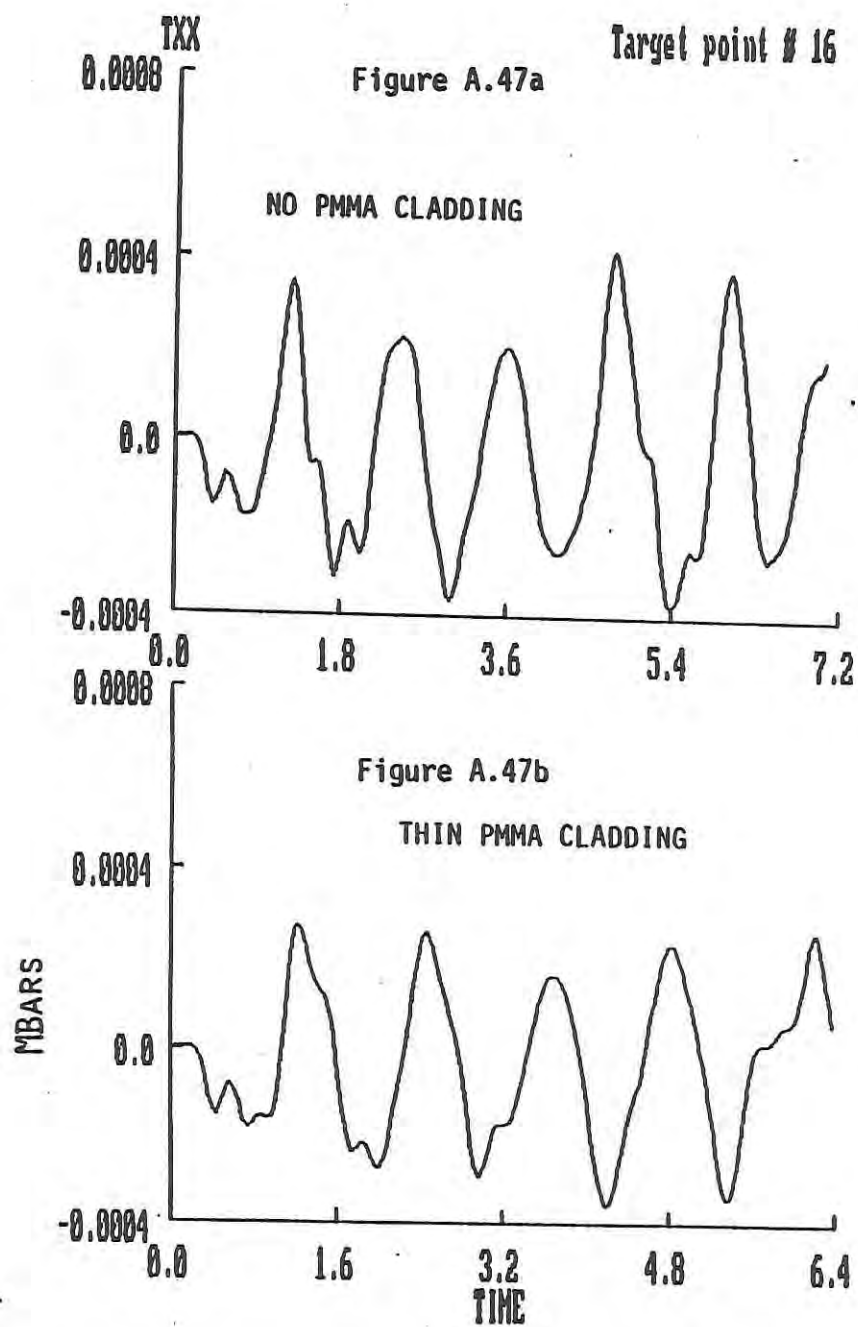


Figure A.47. Stress Components near Midplane of PCSubstrate Outside of Impact Region

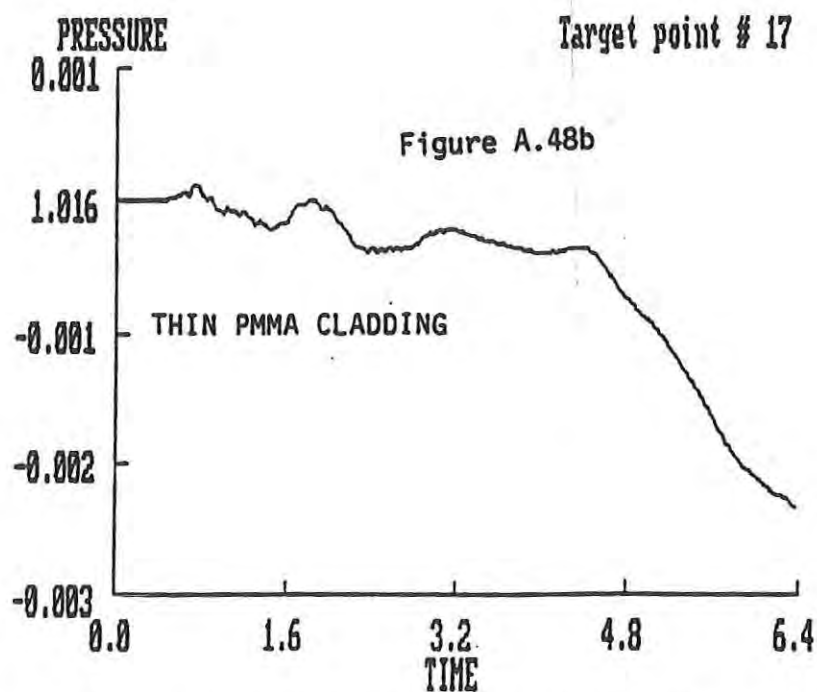
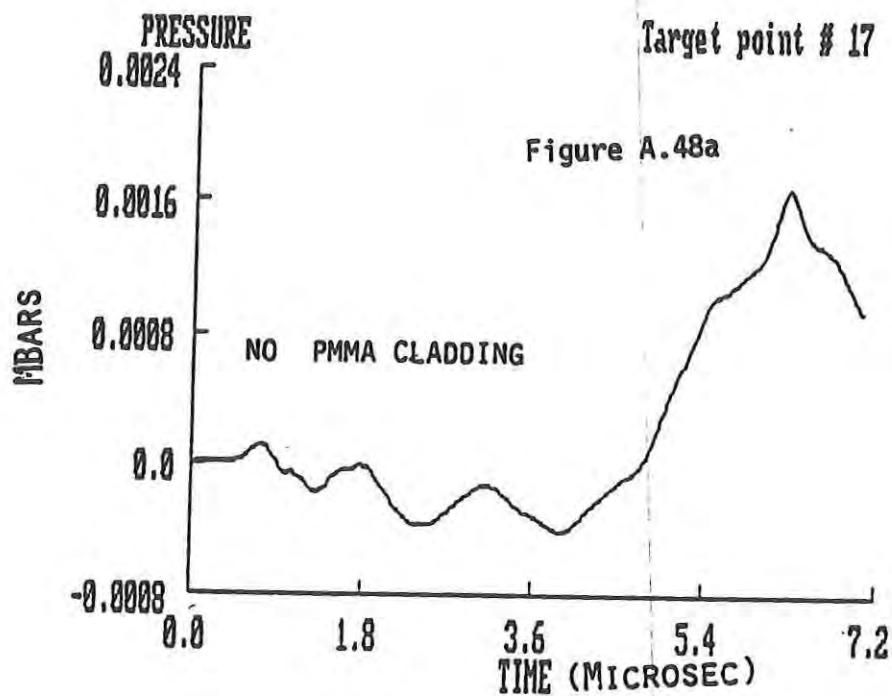


Figure A.48. Pressure near Rear Surface of PC Substrate Outside Impact Region

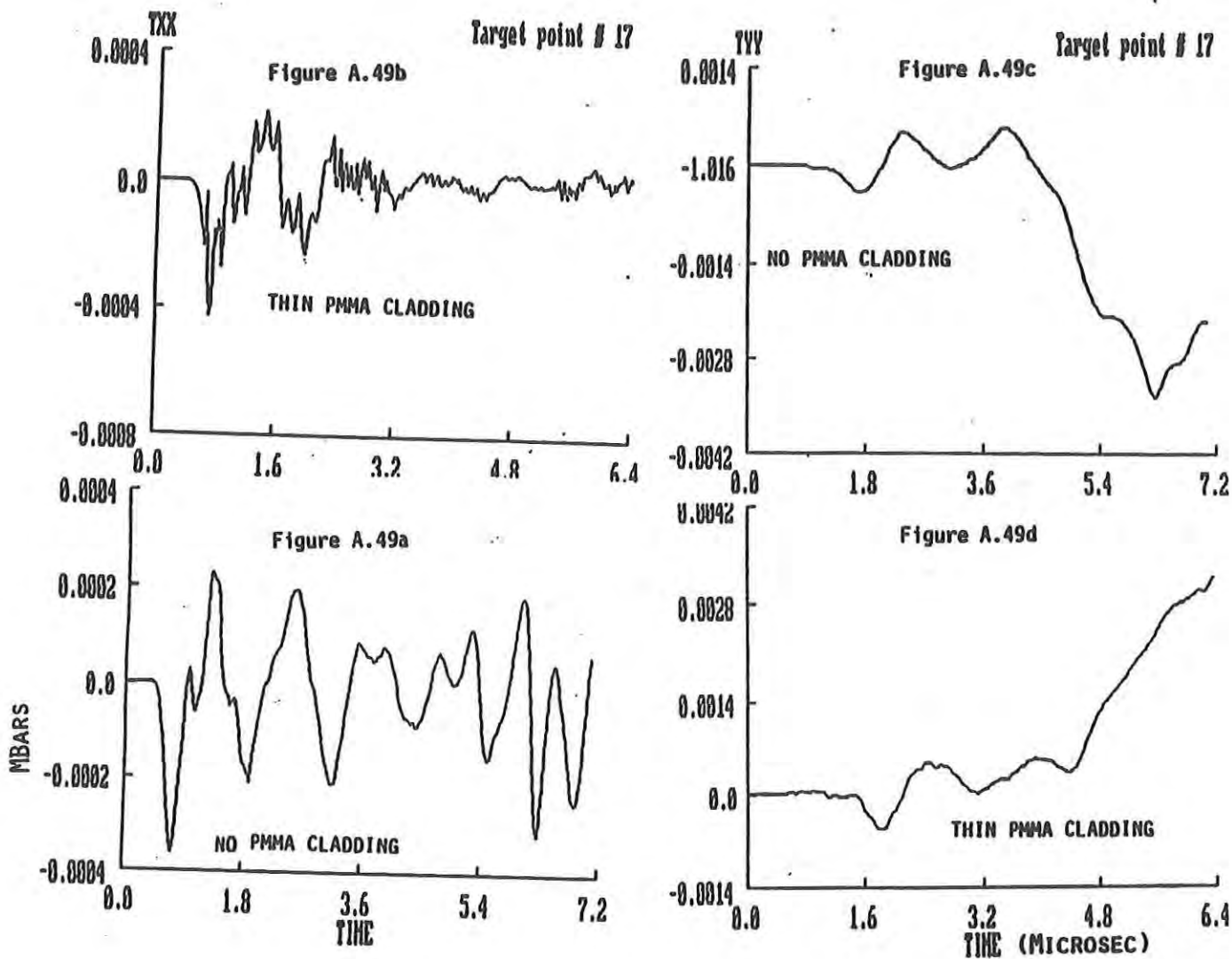


Figure A.49. Stress Components Near Rear Surface of PC Substrate Outside of Impact Region

APPENDIX B: STRUCTURAL ANALYSIS

B.1 Static Analysis

B.2 Frequency Analysis

APPENDIX B.1 - Static Analysis

<u>Figure</u>		<u>Page</u>
B.1	Finite Element Solution using Different Grid Refinements for: (a) Radial Stress in Uncoated PC; and, (b) Circumferential Stress in Uncoated PC.	155 156
B.2	Large Displacement Correction Factors for: (a) Uncoated Plate; and, (b) Coated Ballistic Lens.	157
B.3	Comparison of Small Displacement Solutions for: (a) Circumferential Stress in Coated and Uncoated Ballistic Lens; and, (b) Radial Stress in Coated and Uncoated Ballistic Lens	158
B.4	Maximum Principal Stress for Static Point Load Applied at the Center of the: (a) Uncoated Lens; and, (b) Coated Ballistic Lens	159
B.5	Maximum Principal Stress for Static Point Load Applied at the Edge of the: (a) Coated Lens; and, (b) Uncoated Lens	160 161

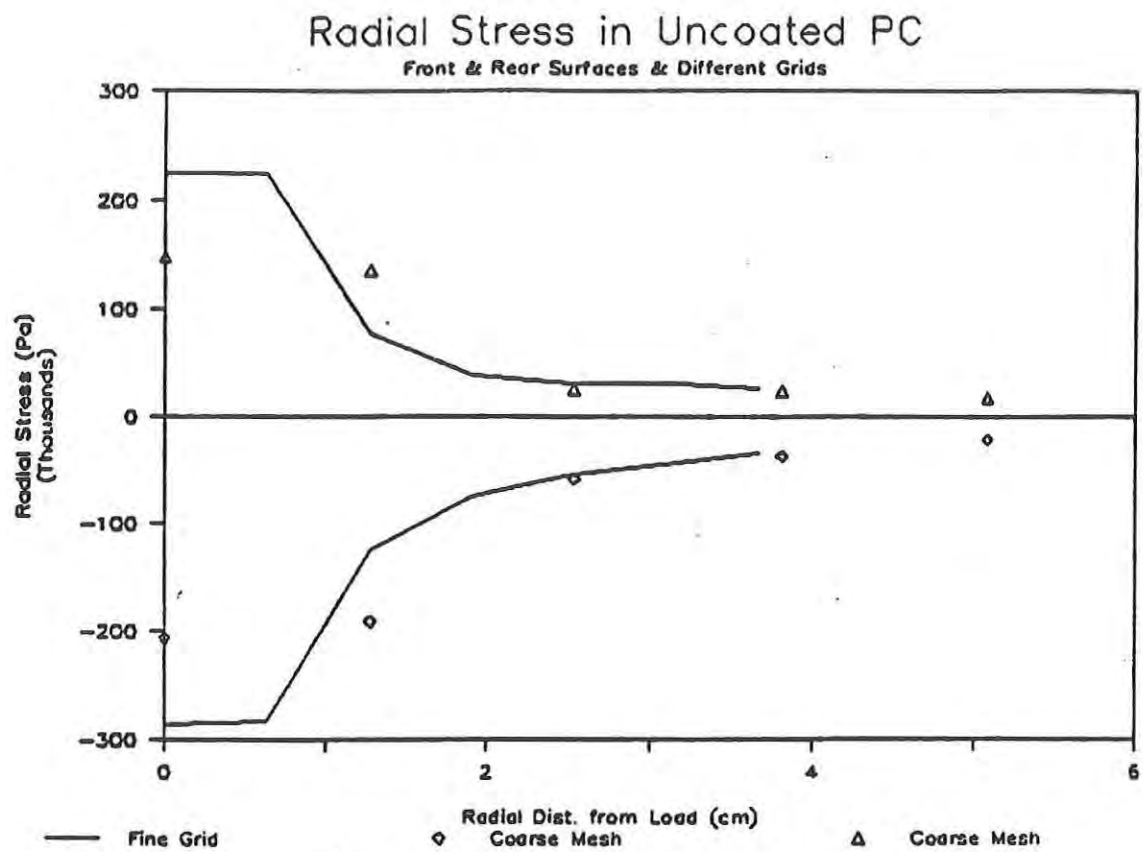


Figure B.1a

Finite Element Solutions for Different Grid Refinements.

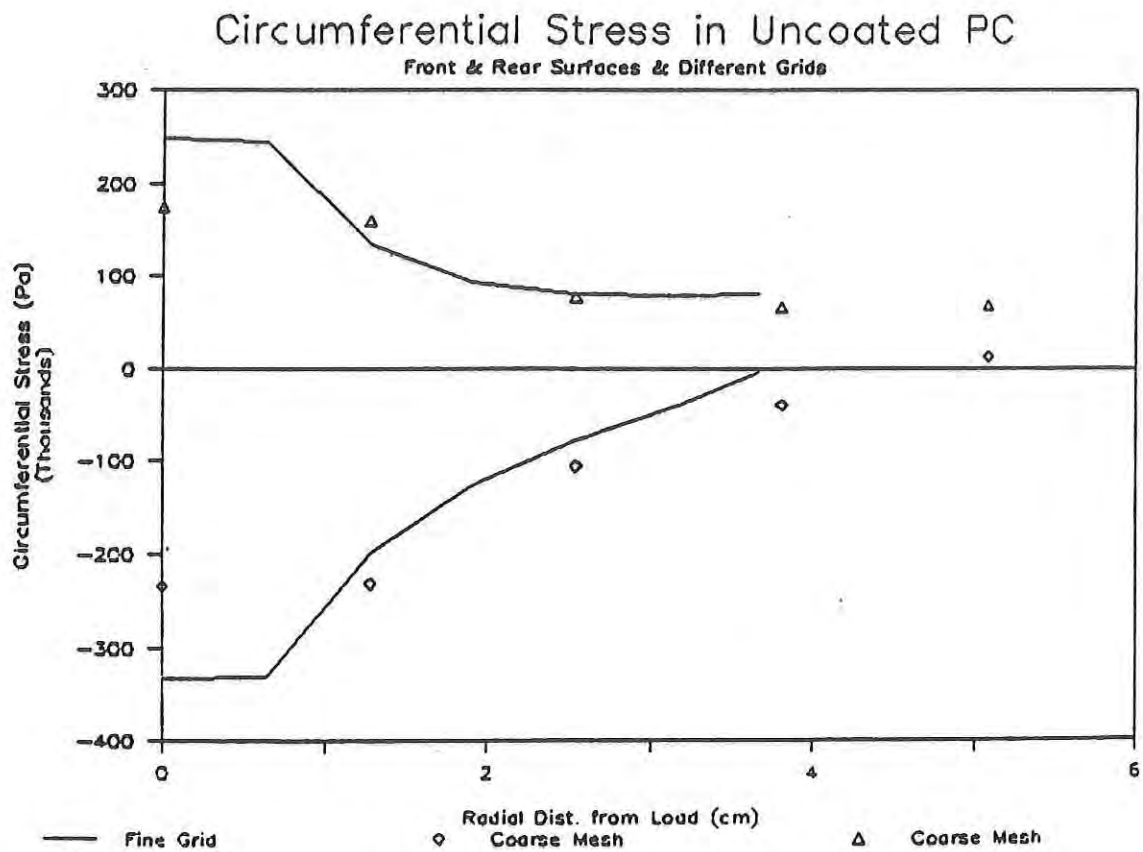


Figure B.1b

Figure B.1. Finite Element Solutions for Different Grid Refinements.

Large Displacement Correction Factors

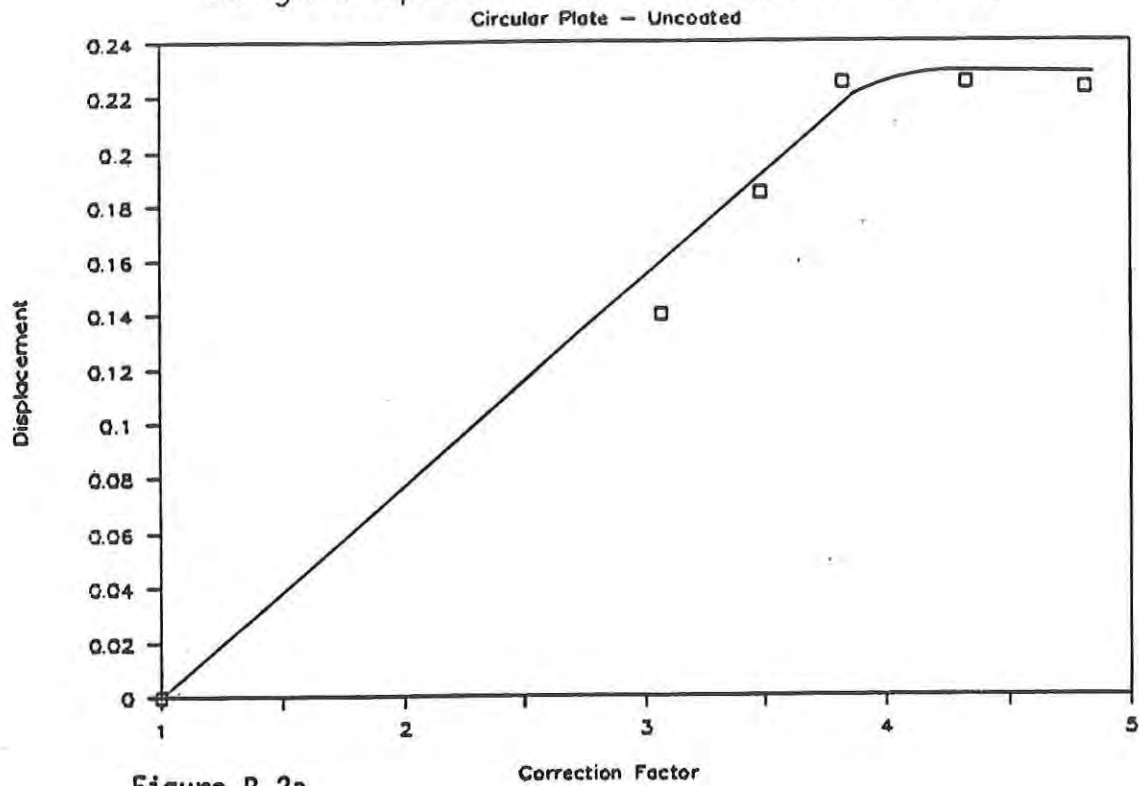


Figure B.2a

Large Displacement Correction Factors

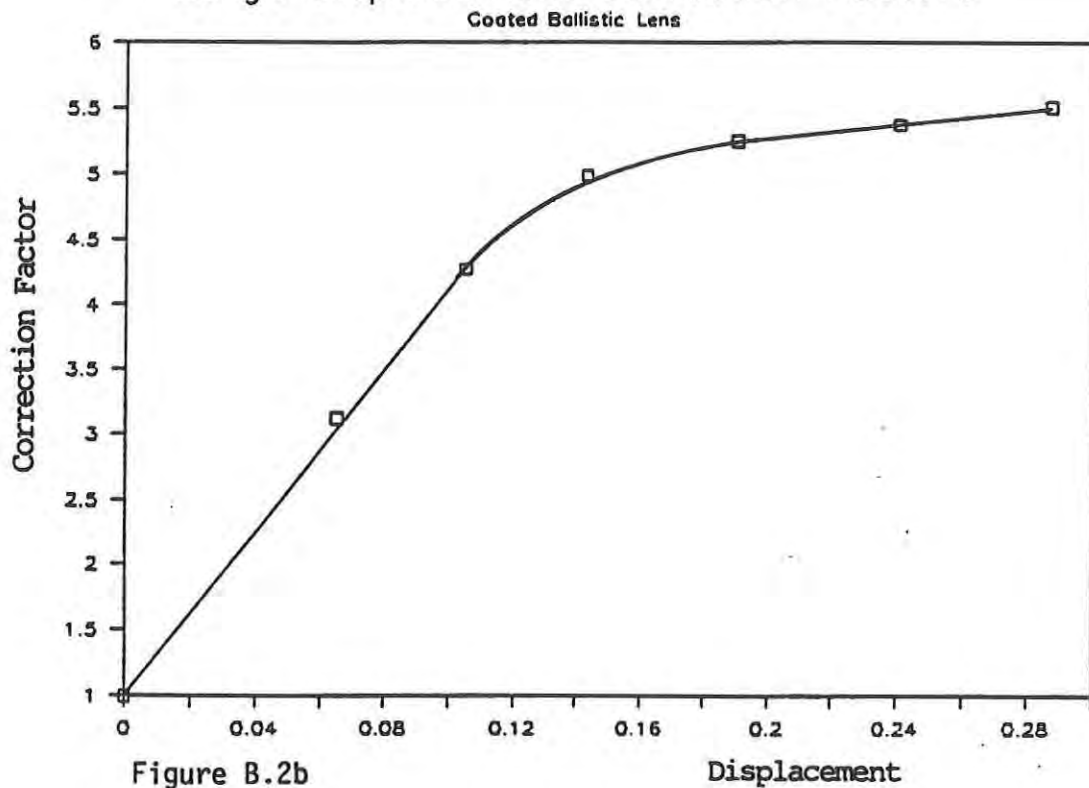
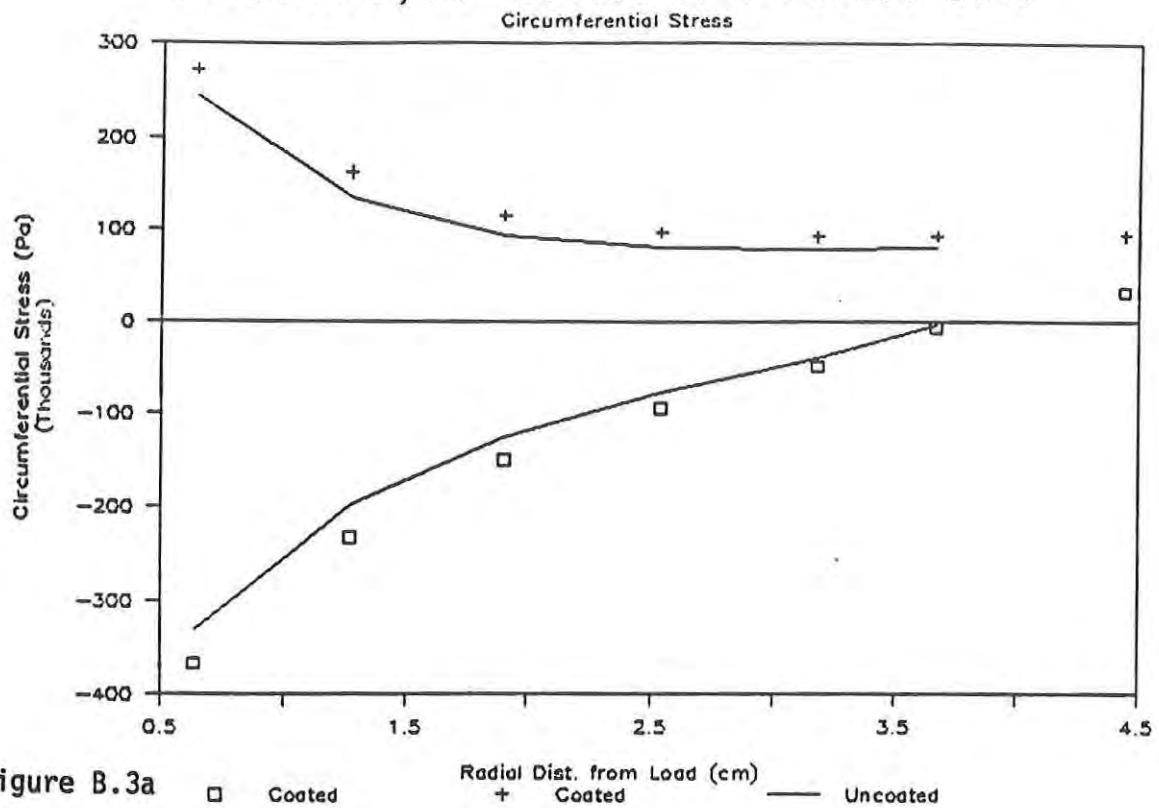


Figure B.2b

Figure B.2. Large Displacement Correction Factors.

Static Analysis—Coated & Uncoated Lens



Static Analysis—Coated & Uncoated Lens

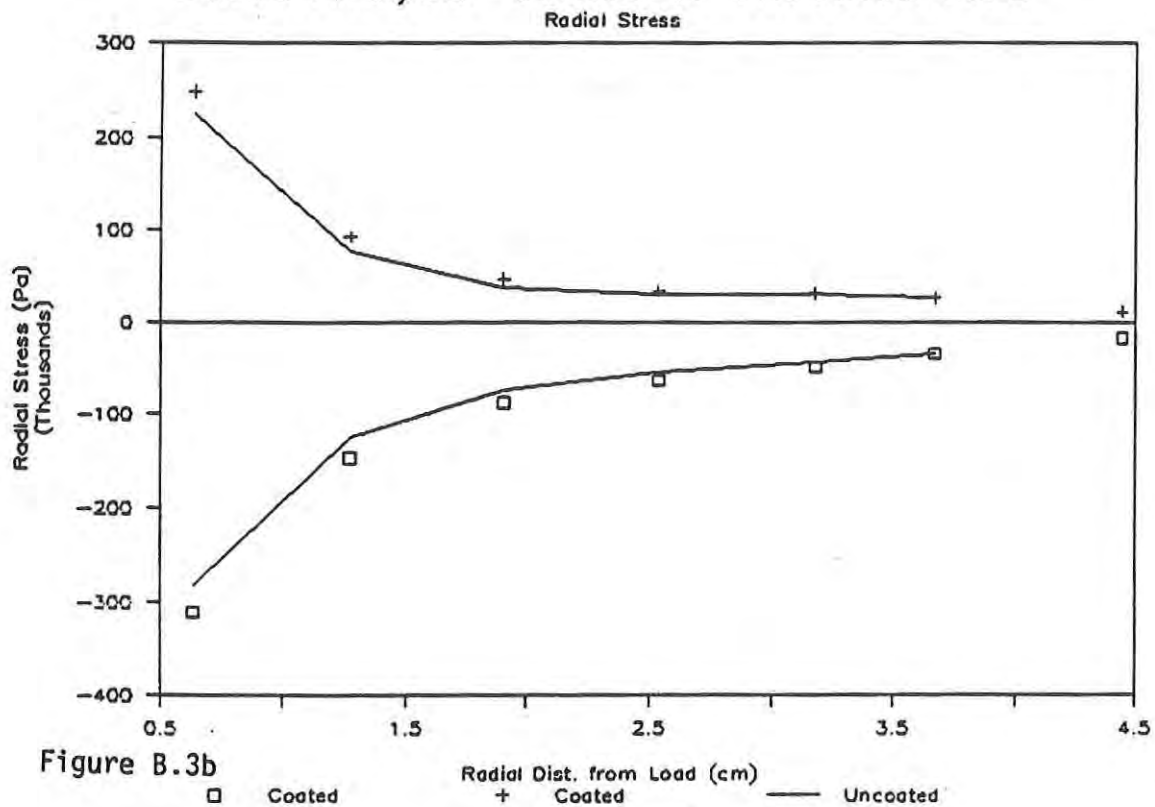
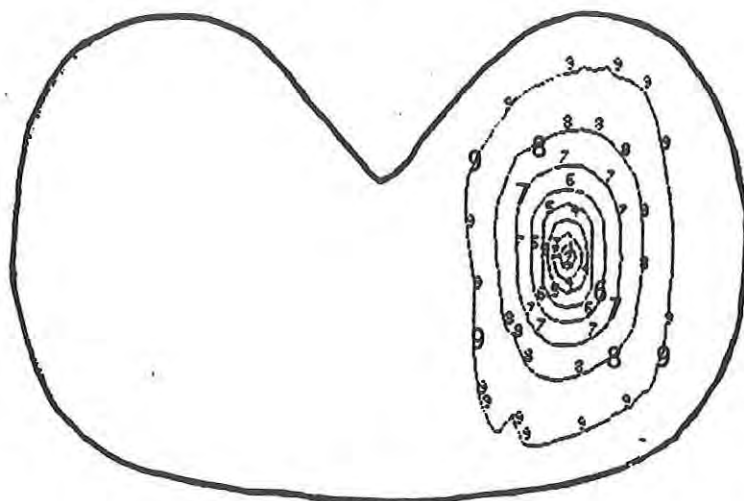


Figure B.3. Small Displacement Solutions.

PRINCZ

UNCOATED

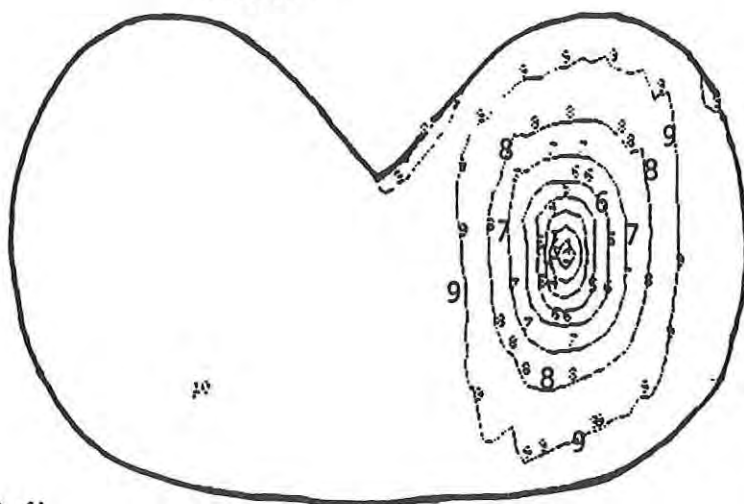


1	=	-384673.
2	=	-341931.
3	=	-299190.
4	=	-256448.
5	=	-213707.
6	=	-170965.
7	=	-128224.
8	=	-85482.9
9	=	-42741.4
10	=	0.03125

Figure B.4a

PRINCZ

COATED



1	=	-287229.
2	=	-255315.
3	=	-223401.
4	=	-191487.
5	=	-159573.
6	=	-127660.
7	=	-95746.2
8	=	-63832.4
9	=	-31918.5
10	=	-4.76172

Figure B.4b

Figure B.4. Maximum Principal Stress (Pa) for Static Point Load Applied at the Center of the Lens.

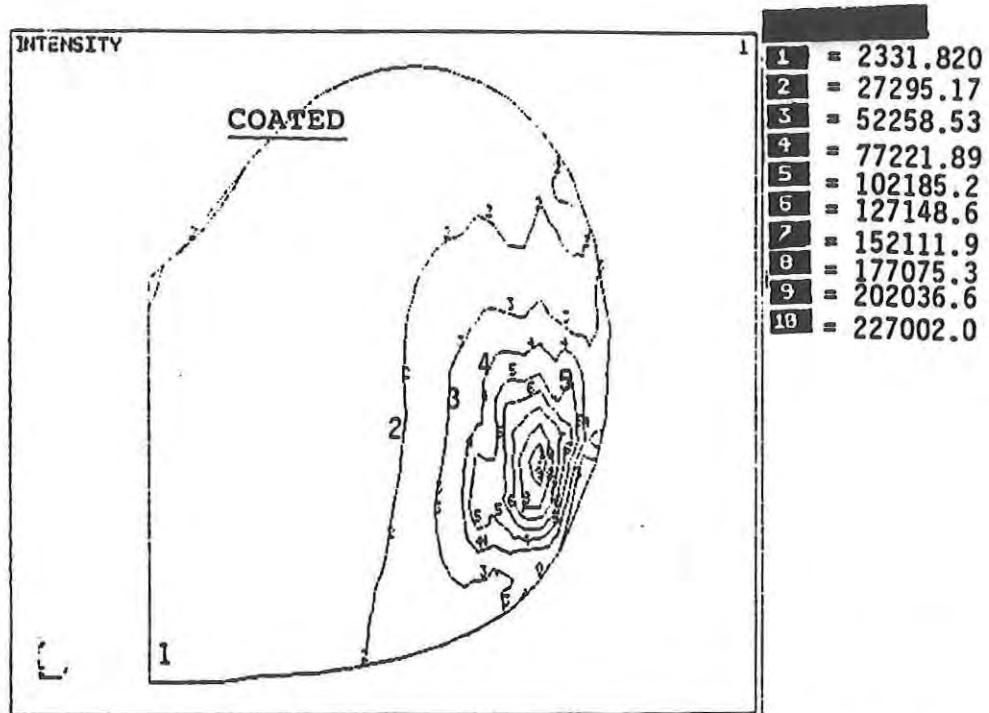


Figure B.5a Maximum Principal Stress (Pa) for Static Point Load Applied at the Edge of the Lens (Coated).

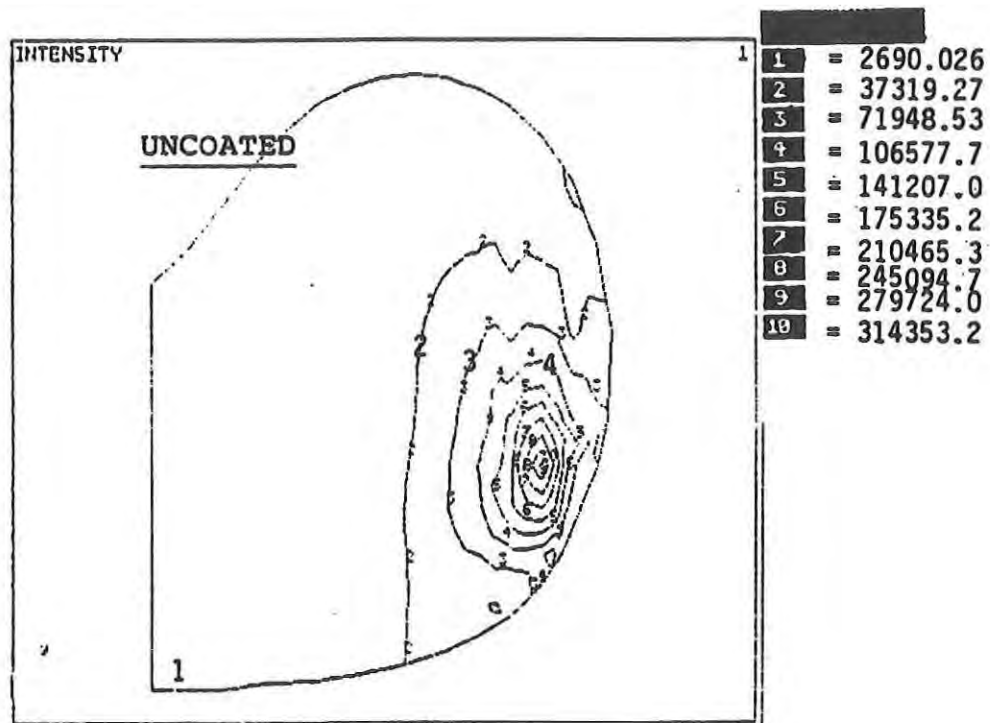
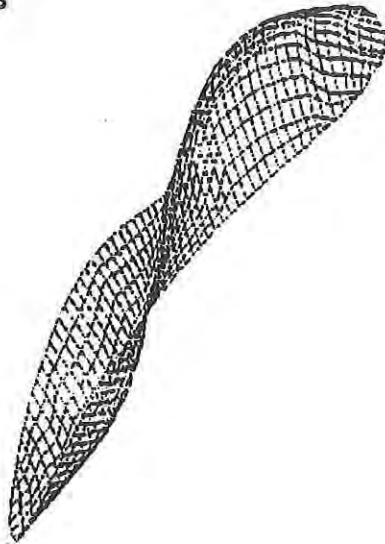


Figure B.5b. Maximum Principal Stress (Pa) for Static Point Load Applied at the Edge of the Lens (Uncoated).

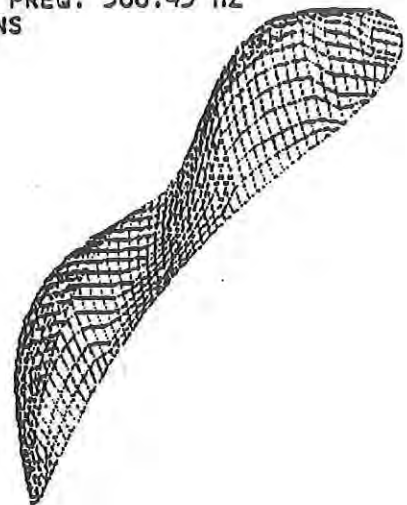
APPENDIX B.2 - Frequency Analysis

<u>Figure</u>		<u>Page</u>
B. 6	First Two Mode Shapes and Frequencies For Coated and Uncoated Ballistic Lens	164
B. 7	Third, Fourth and Fifth Mode Shapes and Frequencies	165

FUNDAMENTAL FREQ. 529.89 HZ
UNCOATED LENS



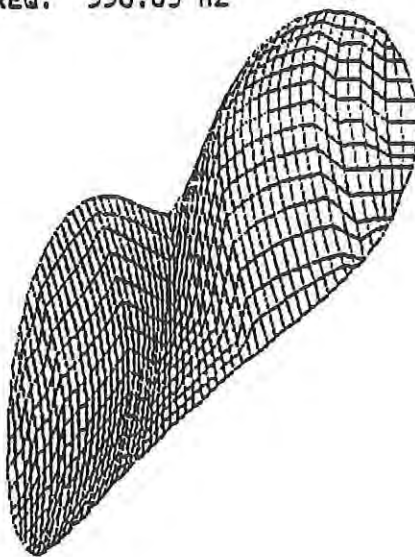
SECOND MODE FREQ. 566.43 HZ
UNCOATED LENS



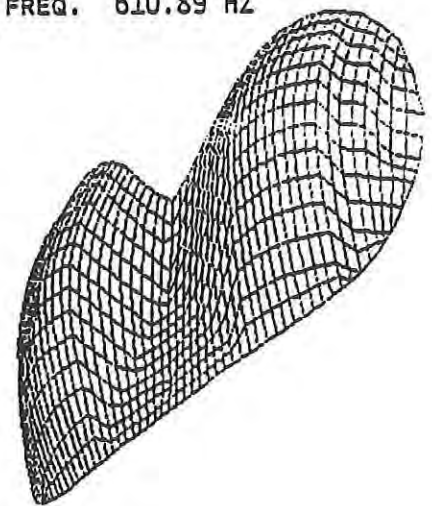
a.

b.

FUNDAMENTAL FREQ. 550.09 HZ
COATED LENS



SECOND MODE FREQ. 610.89 HZ
COATED LENS

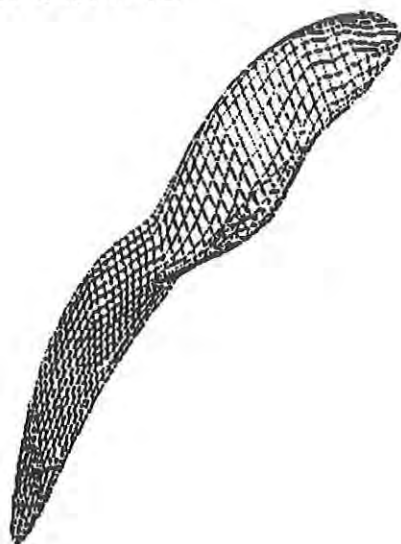


c.

d.

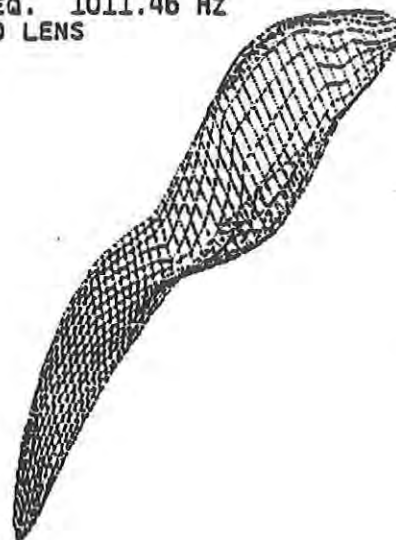
Figure B.6 First Two Mode Shapes and Frequencies
For Coated and Uncoated Ballistic Lens

THIRD MODE FREQ. 840.44 HZ
UNCOATED LENS



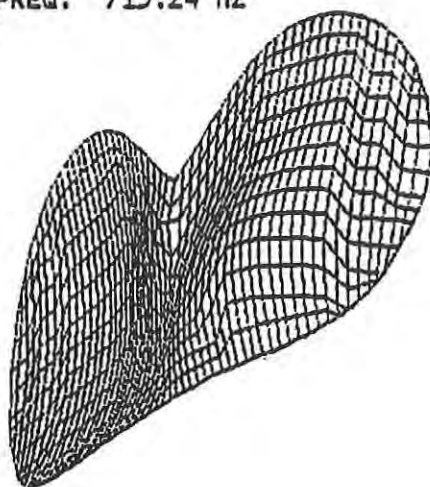
a.

FOURTH MODE FREQ. 1011.46 HZ
UNCOATED LENS



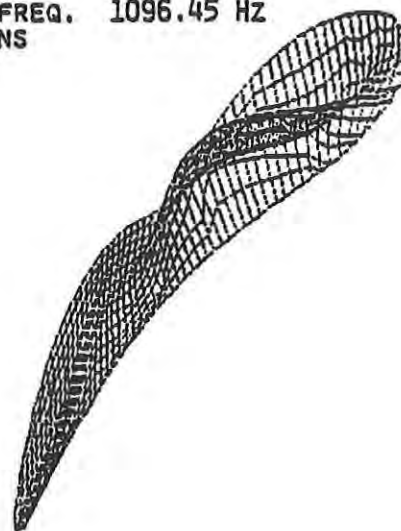
b.

THIRD MODE FREQ. 715.24 HZ
COATED LENS



c.

FIFTH MODE FREQ. 1096.45 HZ
UNCOATED LENS



d.

Figure B.7 Third, Fourth and Fifth Mode Shapes and Frequencies



APPENDIX C: Ballistic Test Data

- C.1 Natick RD&E Center Coated Ballistic Goggles**
- C.2 MRC Unclad Polycarbonate Flat Sheet**
- C.3 MRC PMMA Clad Polycarbonate Flat Sheet Sample**

APPENDIX C.1 - Ballistic Test Data on Coated Ballistic Goggles

Table

Page

C.1	Ballistic Test Data on Coated PC Ballistic Goggles Supplied by Natick	170
------------	--	------------

Table C.1
Ballistic Test Data

Coated Polycarbonate Ballistic Goggles Supplied by Natick

Date/Test	Sample Designation	Thickness (inches)	Mass (grams)	Penetration Depth (inches)	Crater Depth (inches)	Plug Thickness (inches)	Plug Mass (grams)	Residual Mass (grams)	Incident Velocity (ft/sec)	Residual Velocity (ft/sec)	Comments
6-15/04	I	0.0925	17.432	0.0163	0.0478	0.0762	0	17.432	640	0	
6-15/05	II	0.0889	17.021	0.0040	0.0501	0.0849	0	17.021	640	0	
6-15/06	III	0.0908	17.031	0.0133	0.0525	0.0775	0	17.031	650	0	
6-15/08	IV	0.0854	16.561	0.0854	0.0854	0.0798	0.0339	16.521	--	--	
6-16/01	V	0.0906	17.012	0.0140	0.086	0.0767	0	17.012	847	0	
6-16/02	VI	0.0863	16.682	0.0863	0.0863	0.0794	0.0353	16.646	735	486	
6-16/04	VII	0.0854	16.451	0.0304	0.105	0.055	0	16.438	680	0	
6-16/05	VIII	0.0882	17.085	0.0296	0.0814	0.0586	0	17.085	775	0	Scratch on Impact Surface 1 inch long, 2 mil deep, 100 microns thick
6-21/02	IX	0.0843	16.614	0.0843	0.0843	--	--	16.577	781	282	
6-21/03	X	0.0891	17.046	0.0408	0.0967	0.0483	0	17.039	741	0	
6-21/04	XI	0.0896	17.085	0.0199 ¹	0.0828 ¹	0.0697 ¹	1.697	15.504	757	0	Impacted 0.3934 inches from lateral free surface
6-21/05	XII	0.0865	16.471	0.0865	0.0865	--	--	16.431	830	--	Impacted 0.6582 inches from lateral free surface
6-22/01	XIII	0.0891	17.020	0.0211	0.0810	0.0680	0	17.015	759	0	Impacted 0.7732 inches from lateral free surface
6-22/02	XIV	0.0885	17.033	0.0070	0.0565	0.0815	--	17.026	795	--	Impacted 0.6046 inches from lateral free surface
6-22/12	XV	0.0853	16.620	0.0244	0.0516	0.0609	0	16.621	704	0	0.723 inch scratch on rear surface
6-22/13	XVI	0.0851	--	0.0129	0.0235	0.0722	0	16.496	581	0	Tested at 33°F

Note: 1. This sample failed in a brittle manner; i.e., a 180° segment, 1.735 inches along the major axis and 0.75 inches along the minor axis was removed from the goggles. The parameter values listed are associated with the ductile crater located approximately 0.39 inches from the edge of the failed sample segment.

APPENDIX C.2 - Ballistic Test Data on PC Flat Sheet Specimens

<u>Table</u>		<u>Page</u>
C.2	Ballistic Test Data on Uncoated PC Flat Plate Samples	175

Table C.2

Ballistic Test Data (6/14 - 2/22)

Uncoated Polycarbonate Flat Plate Samples ¹

Sample Description					Penetration Depth ² (inches±0.0005)	Crater Depth ³ (inches±0.00005)	Residual Mass of Sample (grams)	Plug Thickness ⁴ (estimated inches)	Velocities Incident (ft/sec)	Residual (ft/sec)	Failure Mode (D,B)
Date/Test	Sample Designation	Thickness (inches±0.0015)	Planar Dimensions (inches x inches)	Mass (grams)							
6-14/01	6-1	0.0719	3.3 x 3.3	--	0.0719	0.0719	--	0	678	0	D
6-14/02	6-2	0.0738	3.3 x 2.9	--	0.0238	0.0855	--	0.0500	655	N/A	0
6-14/03	6-3	0.0767	3.4 x 3.0	--	0.0222	0.0755	--	0.0545	655	N/A	D
6-15/02	4B	0.1027	3.1 x 3.1	19.023	0.0117	0.047	18.964	0.0910	655	N/A	D
6-15/03	4A	0.1147	3.2 x 2.9	19.679	0.0118	0.047	19.609	0.1029	655	N/A	D
6-15/07	6A	0.0762	3.2 x 2.2	13.222	0.0762	0.0762	13.196	0	840	450	D/B ⁵
6-21/01	2C	0.0636	3.1 x 3.0	11.492	0.0636	0.0636	11.427	0	655	N/A	D

Notes:

1. Compression Molded Specimens Fabricated by MRC from Caliber 300-22 general purpose polycarbonate pellets supplied by DOW chemical corporation.
2. Penetration depth is estimated by subtracting the measured crater depth from the deformed thickness of the sample and then subtracting the estimated depth of material beneath the crater from the initial undeformed material thickness. The deformed thickness is greater than the undeformed thickness by as much as 25 to 85 percent due to the formation of a bulge below the crater (the bulge is larger for thinner samples). The deformed thickness is determined using vernier calipers. Due to the fact that the bulge is highly curved, the estimated accuracy of the measurement is ± 0.0005 inches.
3. The crater depth is measured with a dial indicator equipped with a very fine point machined and microscopically examined by MRC. The crater is measured with respect to the impact surface which tends to be irregular close to the penetration.
4. The plug thickness is estimated by subtracting the measured crater depth from the deformed thickness of the sample (see note 2).

5. In addition to a ductile punch plug failure mode this sample manifested both asymmetrical through-the-thickness radial cracking and circumferential cracking on the impact surface.

A 0.344 inch radial crack was evident at 18°. At 0.116 inches the crack branched into 2 orthogonal segments that extended to the edge of the plate. The secondary branches evidenced unsuccessful branching attempts for approximately 0.6 inches and then transitioned into a smooth appearance.

Two circumferential cracks were evident within a radial distance of 0.09 inches. The farther thin crack subtended an angle of 44° - 124°. The closer thick crack subtended an angle of 142° - 215°. A lip was evident on the crater that subtended an angle which included the circumferential cracks. A terminus of the radial crack coincided with the terminus of the farther circumferential crack.

APPENDIX C.3 - Ballistic Test Data on PMMA Clad PC Targets

<u>Table</u>		<u>Page</u>
C.3	Ballistic Test Data on PC Flat Samples with PMMA Cladding	179
C.4	Ballistic Damage to PMMA Impact Layer	180
C.5	Ballistic Damage to PC Substrate	181
C.6	Ballistic Damage to Rear Surface PMMA Cladding	182
C.7	Posttest Residual Cracks in Sample 2-30	183
C.8	Posttest Residual Cracks in Sample 2-31	184
C.9	Posttest Residual Cracks in Sample 2-32	185
C.10	Posttest Residual Cracks in Sample 2-33	186
C.11	Posttest Residual Cracks in Sample 2-34	187
C.12	Posttest Residual Cracks in Sample 2-35	188
C.13	Posttest Residual Cracks in Sample 2-61	189
C.14	Posttest Residual Cracks in Sample 2-64	190
C.15	Posttest Residual Cracks in Sample 2-65	191

Table C.3

Ballistic Test Data

Polycarbonate Flat Plate Samples with PMMA Cladding

Date/Test	Sample Designation	Sample Description					Plug Description					
		Thickness		Planar Dimensions (Inches x Inches)	Mass (grams)	Velocities		Residual Mass of Sample (grams)	Thickness (Inches)	Mass (grams)	Diameter	
		PMMA Layer (Inches)	PC Substrate (Inches)			Incident (ft/sec)	Residual (ft/sec)				Front (Inches)	Rear (Inches)
6-22/03	2-35	0.031	0.068	3.1 x 3.5	22.166	>800	700	21.852	0.068	0.048 0.088	0.329 0.165	0.493 0.383
6-22/04	2-33	0.031	0.065	3.5 x 3.4	25.952	810	579	25.629	0.063	0.099	0.393	0.450
6-22/05	2-34	0.027	0.069	3.5 x 3.5	26.189	760	532	25.611	0.068	0.255	0.464	0.527
6-22/06	2-30	0.033	0.068	3.5 x 3.5	28.813	726	421	28.402	0.068	0.124	0.294	0.466
6-22/07	2-64	0.056	0.066	3.3 x 3.3	34.850	686	307	30.397	0.0	0.0	0	0
6-22/08	2-61	0.053	0.069	3.4 x 3.4	35.994	708	248	34.887	0.069	0.328	0.525	0.639
6-22/09	2-65	0.058	0.069	3.4 x 3.1	35.188	675	0	34.693	0.0	0.0	0	0
6-22/10	2-31	0.034	0.068	3.5 x 3.4	28.736	537	201	27.556	0.068	--	0.412	0.558
6-22/11	2-32	0.031	0.09	3.1 x 3.1	25.108	368	0	25.061	0.0	0.0	0	0
6-16/03	PMMA	0.086	0.0	3.4 x 3.4	--	647	--	19.578	--	--	--	--

Table C.4
Ballistic Test Data
Polycarbonate PMMA Impact Layer Damage

Date/Test	Sample Designation	Crater Region			Fractured Region					
		Depth (inches)	Diameter		Circumferential Cracks			Radial Cracks		
			Front (inches)	Rear (inches)	Region Size (inches)	Subtended Angle (degrees)	Number of Cracks	Region Size (inches)	Subtended Angle (degrees)	Number of Cracks
6-22/03	2-35	0.031	0.223	0.223	0.274	45° each	2	0.495	131, 253 0, 195, 270	2 3
6-22/04	2-33	0.031	0.160	0.219	Front Surface Adjacent to Crater	N/A	0	0.973	117, 149 0, 184	2 2
6-22/05	2-34	0.027	0.174	0.206	N/A	N/A	0	0.758	21, 64, 206, 316 0, 90, 174, 246	4 4
6-22/06	2-30	0.033	0.171	0.219	N/A	N/A	0	0.526	0, 34, 104, 180, 204, 236, 284	7
6-22/07	2-64	0.056	0.168	0.363	N/A	N/A	0	0.730	354 0, 94, 180, 274	1 4
6-22/08	2-61	0.053	0.218	0.371	N/A	N/A	0	1.371	98, 212, 238 0, 116, 191, 296	3 4
6-22/09	2-65	0.058	0.165	0.361	0.391	N/A	N/A	2.170	51, 81, 155 0, 62, 236, 286	3 4
6-22/10	2-31	0.034	0.530	0.530	0.608	0-36	1	0.925	0, 36, 102, 154, 180, 284	6
6-22/11	2-32	0.031	Not Measurable	Not Measurable	0	N/A	0	2.067	Cracks initiate from corners of impact area 0, 90, 180, 252, 293	5
6-16/03	PMMA	0.086	0.163	0.340	0.490	?	?	0.755	40, 58, 149, 198, 214 0, 69, 90, 180, 236, 271	5 6

Table C.5
Ballistic Test Data
Polycarbonate Substrate Damage

Date/Test	Sample Designation	Crater Region			Fractured Region					
		Depth (Inches)	Diameter		Circumferential Cracks			Radial Cracks		
			Front (Inches)	Rear (Inches)	Region Size (Inches)	Subtended Angle (degrees)	Number of Cracks	Region Size (Inches)	Subtended Angle (degrees)	Number of Cracks
6-22/03	2-35	0.068	0.355	0.431	0.491		3	N/A	N/A, Radial cracks in plug	0
6-22/04	2-33	0.065	0.321	0.469	0.592	180° each	2	0.715	282 Radial cracks in plug 0, 175, 216, 252, 298	1 5
6-22/05	2-34	0.069	0.535	0.611		90	1	0.706	356 No cracking observed in plug 44	1 1
6-22/06	2-30	0.068	0.365	0.510	0.545	90 multiple forming crater	1	N/A	Radial cracks in plug	0
6-22/07	2-64	0.0148	0.157	N/A	N/A	N/A	0	N/A	N/A	0
6-22/08	2-61	0.069	0.559	0.642	0.784	180	1	0.909	20, 128, 207, 238, 286	5
6-22/09	2-65	0.069		N/A	N/A	N/A	0	N/A	N/A	0
6-22/10	2-31	0.068	0.465	0.663	0.710	32-219, 50-223	2	1.055	Plug not recovered 23, 90, 180	?
6-22/11	2-32	0	0	0	N/A	N/A	0	2.151	33, 111, 210, 325 0, 80, 141, 189, 256, 295	4 6
6-16/03	PMMA	N/A	N/A	N/A	N/A	N/A	N/A	N/A	N/A	N/A

Table C.6

Ballistic Test Data

Polycarbonate Damage to Back Surface PMMA Cladding

Date/Test	Sample Designation	Crater Region			Fractured Region					
		Depth (inches)	Diameter		Circumferential Cracks			Radial Cracks		
			Front (inches)	Rear (inches)	Region Size (inches)	Subtended Angle (degrees)	Number of Cracks	Region Size (inches)	Subtended Angle (degrees)	Number of Cracks
6-22/03	2-35	0.031	0.580	0.580	N/A	N/A	0	1.26	0, 70, 145, 195, 253, 335	6
6-22/04	2-33	0.031	0.615	0.615	N/A	N/A	0	0.311	0, 37, 83, 154, 195, 240, 285, 322	8
6-22/05	2-34	0.027	0.937	0.937	0.937	40	1	0.420	30, 90, 124, 170, 220, 261, 321	7
6-22/06	2-30	0.033	0.606	0.606	0.839	180 - 219	1	1.491	190 and 213 (secondary cracks) 10, 91, 136, 185, 220, 253, 284	2 7
6-22/07	2-64	0.056	0.265	0.397	N/A	N/A	0	2.612	0,39,80,114, 147, 180, 211, 256, 285, 321	10
6-22/08	2-61	0.053	0.663	0.748	N/A	N/A	0	1.998	20, 68, 108, 153, 167, 228, 286, 311, 329	9
6-22/09	2-65	0.058			N/A	N/A	0	2.465	0, 32, 62, 102, 180, 236, 286, 321	8
6-22/10	2-31	0.034	1.409	1.409	N/A	N/A	0	0.652	24, 60, 110, 145, 180, 213, 259, 302	8
6-22/11	2-32	0	0	0	N/A	N/A	0	2.355	0, 36, 90, 118, 165, 194, 233, 279, 323	9
6-16/03	PMMA	N/A	N/A	N/A	N/A	N/A	N/A	N/A	N/A	N/A

Table C.7

Sample 2-30

Posttest Residual Cracks

Stress Concentration Group	PMMA Impact Layer	Polycarbonate Substrate	Rear Surface PMMA Layer	Comments
1	0	Radial Cracking		
2	34	← Observed →	10	
2	104	← Plug →	91	
			136	
3	180	← →	185	
3	204	← →	190	Secondary Branch off Impact Layer Circumferential Crack
4	236	← →	213	Secondary Branch off Impact Layer Circumferential Crack
			220	
			253	
4	284	← →	284	

Table C.8
Sample 2-31
Posttest Residual Cracks

Stress Concentration Group	PMMA Impact Layer	Polycarbonate Substrate	Rear Surface PMMA Layer	Comments
1	0	23 ← → 24		
1	36		60	
2	102 ← → 90		110	
			145	
3	154			
3	180 ← → 180		180	
			213	
			259	
4	284 ← → 302			

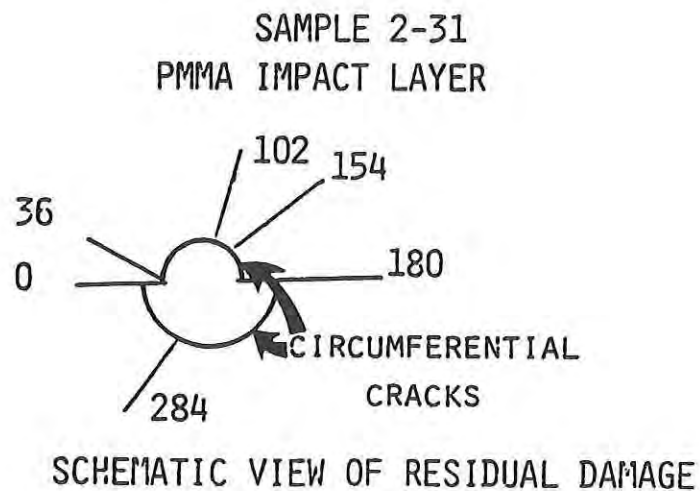


Table C.9

Sample 2-32

Posttest Residual Cracks

Stress Concentration Group	PMMA Impact Layer	Polycarbonate Substrate	Rear Surface PMMA Layer	Comments
1	0	0	0	
		33	36	
2	90	80	80	
		111	118	
		141		Secondary Branch off 325 Radial Crack
3	180	189	194	
		210		Secondary Branch off 33 Radial Crack
			233	
4	252	256		
			279	
4	293	295		
		325	323	

Table C.10
Sample 2-33
Posttest Residual Cracks

Stress Concentration Group	PMMA Impact Layer	Polycarbonate Substrate	Rear Surface PMMA Layer	Comments
1	0	0	0	
			37	
			83	
2	117			Secondary Branch Off Circumferential Crack
3	149			Secondary Crack Does Not Penetrate Through Layer, Starts at Interface
			154	
4	184	175		175 Substrate Crack Branches Off Circumferential in Substrate
		216	195	
		252	240	
		298	285	
			322	

Table C.11

Sample 2-34

Posttest Residual Cracks




Stress Concentration Group	PMMA Impact Layer	Polycarbonate Substrate	Rear Surface PMMA Layer	Comments
1	0			
	21			
			30	
		44		Secondary Branch Off Substrate Circum- ferential Crack
	64			Secondary Branch Off Impact Surface Circumferential Crack
2	90			90
			124	
3	174			170
	206			
			220	
4	246			261
			321	
		356		Secondary Branch Off Substrate Circum- ferential Crack

Table C.12
Sample 2-35
Posttest Residual Cracks

Stress Concentration Group	PMMA Impact Layer	Polycarbonate Substrate	Rear Surface PMMA Layer	Comments
1	0	←————→	0	
			70	
	131			2.6 mm Crack Does Not Penetrate, Starts at Interface
		138		Secondary Crack Branch Off Substrate Circumferential
			145	
2	195	←————→	195	
	253	←————→	253	Impact Layer Crack Starts at Impact Surface Interlayer and Does Not Penetrate Impact Surface
3	270			7 mm
			335	

Table C.13

Sample 2-61

Posttest Residual Cracks

Stress Concentration Group	PMMA Impact Layer	Polycarbonate Substrate	Rear Surface PMMA Layer	Comments
1	0			
		20 \longleftrightarrow 20		
			68	
	98			
			108	
2	116			
		128		
			153	
			167	
	191			
		207		Secondary Branch Off Substrate Circum- ferential Crack
	212 \longleftrightarrow 228			
	238 \longleftrightarrow 238			Radial Substrate Crack Which Branches Off Substrate Circumferential Crack
		286 \longleftrightarrow 286		Radial Substrate Crack Which Branches Off Substrate Circumferential Crack
			311	
			329	

Table C.14
Sample 2-64
Posttest Residual Cracks

Stress Concentration Group	PMMA Impact Layer	Polycarbonate Substrate	Rear Surface PMMA Layer	Comments
1	0			
	354	← Ductile Partial Penetration →	0	354 is Secondary Radial Branch Off 0 Radial
			39	
			80	
2	94	← →	114	
			147	
3	180	← →	180	
			211	
			256	
4	274	← →	285	
			321	

Table C.15

Sample 2-65

Posttest Residual Cracks

Stress Concentration Group	PMMA Impact Layer	Polycarbonate Substrate	Rear Surface PMMA Layer	Comments
1	0	← Ductile Partial Penetration →	0	
2	51			
2	62	← →	62	
2	81			
			102	
3	155			
			180	
3	236	← →	236	
	286	← →	286	
			321	

